
Equation of state of hot and dense matter in astrophysics and in the laboratory

Zustandsgleichung für heiße und dichte Materie in der Astrophysik und im Labor

Zur Erlangung des Grades eines Doktors der Naturwissenschaften (Dr. rer. nat.)

Genehmigte Dissertation von Sabrina Huth aus Lich

Tag der Einreichung: 7. Februar 2023, Tag der Prüfung: 26. April 2023

1. Gutachten: Prof. Achim Schwenk, Ph.D.

2. Gutachten: Prof. Dr. Almudena Arcones

Darmstadt, Technische Universität Darmstadt

Jahr der Veröffentlichung der Dissertation auf TUprints: 2023



TECHNISCHE
UNIVERSITÄT
DARMSTADT

Department of Physics
Institut für Kernphysik
Theoriezentrum



Equation of state of hot and dense matter in astrophysics and in the laboratory
Zustandsgleichung für heiße und dichte Materie in der Astrophysik und im Labor

Accepted doctoral thesis by Sabrina Huth

Date of submission: 7. Februar 2023
Date of thesis defense: 26. April 2023

Darmstadt, Technische Universität Darmstadt
Jahr der Veröffentlichung der Dissertation auf TUPrints: 2023

Bitte zitieren Sie dieses Dokument als:
URN: urn:nbn:de:tuda-tuprints-238446
URL: <http://tuprints.ulb.tu-darmstadt.de/23844>

Dieses Dokument wird bereitgestellt von tuprints,
E-Publishing-Service der TU Darmstadt
<http://tuprints.ulb.tu-darmstadt.de>
tuprints@ulb.tu-darmstadt.de

Die Veröffentlichung steht unter folgender Creative Commons Lizenz:
Namensnennung 4.0 International
<https://creativecommons.org/licenses/by/4.0/>
This work is licensed under a Creative Commons License:
Attribution 4.0 International
<https://creativecommons.org/licenses/by/4.0/>



Für Opa.
Ohne dich würde es diese Dissertation nicht geben.
Du bist für immer in meinem Herzen.



Abstract

For the interpretation of high-energy astrophysical phenomena such as supernova explosions or neutron star collisions, a thorough understanding of matter at supranuclear densities is necessary. Unfortunately, our current knowledge of dense matter as present in neutron star cores is limited. Novel constraints on the equation of state of neutron star matter are provided by gravitational wave observations of neutron star mergers such as GW170817 and measurements of neutron star radii by NASA's NICER mission. Recently, microscopic calculations of pure neutron matter are used as a basis for the construction of new equation of state parametrizations. However, extrapolations to high densities are required here as these calculations are only available up to about nuclear saturation density. Core-collapse supernovae and neutron star mergers probe an even broader range of temperature and electron fraction in comparison to cold isolated neutron stars. For astrophysical applications, commonly used equations of state are mostly not consistent with microscopic calculations and recent astrophysical observations. The construction of novel equation of state parametrizations that are in agreement with the latest constraints from nuclear physics and observations will facilitate significant advances in nuclear astrophysics.

In this thesis, we provide new equations of state for core-collapse supernova and neutron star merger simulations. To this end, we introduce a parametrization for the nucleon effective mass that reflects novel microscopic calculations up to twice saturation density. The effective mass is essential to accurately describe thermal effects, which govern the proto-neutron star contraction in core-collapse supernovae. To constrain the parameter range of the equation of state we use results from chiral effective field theory calculations at nuclear densities and functional renormalization group computations at high densities that are based on quantum chromodynamics. In addition, constraints from mass measurements of heavy neutron stars, the gravitational wave signal of GW170817, and the first NICER results are implemented as well. We investigate the results for the predicted ranges for the equation of state and neutron star properties such as the neutron star radius and maximum mass. From this equation of state functional, we choose a set of representative equations of state to systematically study the impact of the nucleon effective mass and nuclear matter properties in core-collapse supernova simulations. For this, equation of state tables can be computed using the liquid-drop model with a single nucleus approximation that cover a wide range of densities, temperatures, and electron fractions as required by astrophysical simulations.

Moreover, we combine information from astrophysical multi-messenger observations of neutron stars and from heavy-ion collisions of gold nuclei at relativistic energies with microscopic nuclear theory calculations via Bayesian inference to refine our knowledge of dense matter. Heavy-ion collision experiments offer complementary information at intermediate densities where theoretical calculations as well as observations are less sensitive to. Our results show an increase in the pressure in dense matter compared to previous studies when data from heavy-ion collisions is included. This leads to a shift in neutron-star radii towards larger values, similar to recent observations by the NICER mission. We conclude that constraints from heavy-ion collision experiments and multi-messenger observations are strikingly consistent with each other. This work highlights how joint analyses can shed light on the properties of neutron-rich nuclear matter over the density range probed in neutron stars.

Cover picture: Picture of the supernova 1987A in the Large Magellanic Cloud taken from the Hubble Space Telescope. Credit: NASA, ESA

Zusammenfassung

Die Interpretation hochenergetischer astrophysikalischer Phänomene wie Supernovaexplosionen oder Neutronensternkollisionen erfordert ein umfassendes Verständnis der Materie bei supranuklearen Dichten. Unser Wissen über dichte Materie, die in den Kernen von Neutronensternen zu finden ist, bleibt jedoch begrenzt. Gravitationswellenbeobachtungen von Neutronensternverschmelzungen wie GW170817 sowie Messungen der Radien von Neutronensternen im Rahmen der NICER-Mission der NASA liefern neue Hinweise für die Zustandsgleichung von Neutronensternmaterie. In den letzten Jahren wurden viele Bestrebungen unternommen, Parametrisierungen der Zustandsgleichung auf der Grundlage von mikroskopischen Berechnungen reiner Neutronenmaterie zu erstellen. Solche Berechnungen sind jedoch nur bis etwa zur Kernsaturierungsdichte verfügbar, so dass Extrapolationen zu höheren Dichten vorgenommen werden müssen. Im Vergleich zu kalten isolierten Neutronensternen weisen Kernkollaps-Supernovae und Neutronensternverschmelzungen einen viel größeren Bereich von Temperatur und Elektronenanteil auf. Die in astrophysikalischen Anwendungen üblicherweise verwendeten Zustandsgleichungen stimmen oft nicht mit mikroskopischen Berechnungen und aktuellen Beobachtungen überein. Die Konstruktion neuer Parametrisierungen von Zustandsgleichungen, die mit den neuesten Erkenntnissen der Kernphysik und astrophysikalischen Beobachtungen übereinstimmen, wird wichtige Fortschritte in der nuklearen Astrophysik ermöglichen.

Wir stellen neue Zustandsgleichungen für Anwendungen in Simulationen von Kernkollaps-Supernovae und Neutronensternverschmelzungen vor. Wir beginnen mit der Einführung einer Parametrisierung der effektiven Masse, die auf aktuellen mikroskopischen Berechnungen basiert. Dies ist wichtig, um die vorhergesagten thermischen Effekte zu erfassen, von denen gezeigt wurde, dass sie die Kontraktion des Proto-Neutronensterns in Supernova-Simulationen steuern. Der Parameterbereich der Zustandsgleichung zugrundeliegenden Energiedichtefunktional wird durch Ergebnisse der chiralen effektiven Feldtheorie bei Kerndichten sowie durch funktionale Renormierungsgruppenberechnungen bei hohen Dichten auf der Grundlage der Quantenchromodynamik bestimmt. Darüber hinaus werden Beobachtungen von schweren Neutronensternen, das Gravitationswellensignal von GW170817 und die ersten NICER-Ergebnisse berücksichtigt. Schließlich untersuchen wir die sich daraus ergebenden zulässigen Bereiche für die Zustandsgleichung und die Eigenschaften von Neutronensternen, einschließlich der vorhergesagten Grenzen für den Neutronensternradius und die maximale Masse. Aus diesem Zustandsgleichungsfunktional wählen wir eine Reihe repräsentativer Zustandsgleichungen aus, um die Auswirkungen der effektiven Masse der Nukleonen und der Kernmaterieeigenschaften in Kernkollaps-Supernova-Simulationen systematisch zu untersuchen. Zu diesem Zweck können Zustandsgleichungstabellen unter Verwendung des Flüssigkeitstropfenmodells mit einer Ein-Kern-Näherung berechnet werden, die einen breiten Bereich von Dichten, Temperaturen und Elektronenanteilen abdecken, wie sie für astrophysikalische Simulationen benötigt werden.

Wir verwenden zusätzlich Bayes'sche Verfahren, um Daten aus astrophysikalischen Multi-Messenger-Beobachtungen von Neutronensternen und aus Schwerionenkollisionen von Goldkernen bei relativistischen Energien mit mikroskopischen Kerntheorieberechnungen zu kombinieren, um unser Verständnis von dichter Materie zu verbessern. Wir finden heraus, dass die Einbeziehung von Schwerionenkollisionsdaten auf eine Erhöhung des Drucks in dichter Materie im Vergleich zu früheren Analysen hinweist,

wodurch sich die Radien von Neutronensternen zu größeren Werten hin verschieben, was mit den jüngsten Beobachtungen der NICER-Mission übereinstimmt. Unsere Ergebnisse zeigen, dass die Ergebnisse von Schwerionen-Kollisionsexperimenten eine bemerkenswerte Übereinstimmung mit Multi-Messenger-Beobachtungen aufweisen und ergänzende Informationen über Kernmaterie bei mittleren Dichten liefern. Diese Arbeit kombiniert Kerntheorie, Kernexperimente und astrophysikalische Beobachtungen und zeigt, wie gemeinsame Analysen Einblicke in die Eigenschaften neutronenreicher supranuklearer Materie über den in Neutronensternen untersuchten Dichtebereich geben können.

Contents

1	Introduction	1
1.1	History of neutron stars	2
1.2	The origin of neutron stars: Core-collapse supernovae	3
1.3	Neutron star structure	5
1.4	Neutron stars and the nuclear equation of state	7
1.5	Observations	8
1.5.1	Mass Measurements of heavy neutron stars	9
1.5.2	Neutron Star Interior Composition Explorer (NICER)	10
1.5.3	Gravitational waves and multi-messenger astronomy of neutron star mergers	12
1.6	Organization of this thesis	14
2	Equation of state of hot and dense matter	17
2.1	Microscopic description of the equation of state	18
2.1.1	Quantum chromodynamics and chiral symmetry	18
2.1.2	Chiral effective field theory	19
2.1.3	Functional Renormalization Group	21
2.1.4	Perturbative Quantum Chromodynamics	22
2.2	Matter at nuclear densities	23
2.3	Equation of state constraints from heavy-ion collision experiments	25
2.4	Nucleon effective mass and thermal effects	27
2.5	Liquid-gas phase transition in nuclear matter	29
2.6	Phenomenological equations of state for astrophysical applications	31
2.6.1	Traditional Equations of State	31
2.6.2	Equation of state effects in core-collapse supernovae	35
3	New equations of state constrained by nuclear physics, observations, and functional Renormalization Group calculations	39
3.1	Overview of equation of state constraints	39
3.1.1	Constraints from nuclear physics	39
3.1.2	Constraints from neutron star observations	42
3.1.3	Theoretical calculations at high densities	43
3.2	New Equation of state functional	44
3.2.1	Temperature dependence and nucleon effective mass	44
3.2.2	Equation of state functional	46
3.3	Equation of state variations	50
3.3.1	Variations of nuclear matter properties	50
3.3.2	Effective mass variation	51
3.3.3	High-density variations	54
3.4	Astrophysical equation of state	56
3.4.1	Neutron star properties	56

3.4.2	Thermal effects	60
4	Impact of the equation of state in astrophysical applications	65
4.1	Set of representative equations of state	65
4.2	Phase diagram of nuclear matter	68
4.3	Equation of state construction based on liquid-drop model	70
4.3.1	Single nucleus approximation	71
4.3.2	Equilibrium conditions	74
4.3.3	Comparison with Lattimer-Swesty equation of state	76
4.4	Impact of equation of state in astrophysical simulations	76
4.4.1	Neutron star mergers	76
5	Constraining neutron-star matter with microscopic and macroscopic collisions	79
5.1	Nuclear theory input	79
5.2	Multi-messenger astrophysics information	81
5.3	Data from heavy-ion collision experiments	82
5.3.1	Implementation of nuclear equation of state constraints from heavy-ion collisions	85
5.3.2	Uncertainty studies	89
5.4	Combination of the astrophysical and heavy-ion collision constraints	93
5.5	Combining information from micro- and macroscopic collisions	94
5.6	Impact of information from heavy-ion collisions on equation of state functional	96
6	Summary and outlook	99

1 Introduction

Neutron stars are one of the most compact objects in the universe aside from white dwarfs and black holes [1, 2]. A typical neutron star has as much as 1.4 times the mass of our sun, M_{\odot} , squeezed into a sphere with a radius of only 10 to 14 kilometers [3, 4, 5]. To date, massive neutron stars with masses of even $\sim 2 M_{\odot}$ have been observed with high precision [6, 7, 8, 9]. The exact maximum mass above which neutron stars collapse to black holes is still an open question. As such compact objects, neutron stars are bound by gravity and have to be treated as relativistic objects [10]. The density in their center exceeds several times the density in atomic nuclei on earth such that the conditions present in neutron star cores cannot be reproduced in terrestrial experiments yet [11, 3]. Consequently, many properties of matter in the center of neutron stars are still highly uncertain, including the constituents and their interactions that are governed by the strong force, see e.g. [1, 12, 13]. The equation of state (EOS) describes the state of matter across the wide range of densities from the surface to the center. Interestingly, there is a unique link between the EOS and the mass-radius relation of neutron stars [14]. This means that observations of neutron stars are able to inform the EOS and, thus, our knowledge about the underlying strong interaction at densities where modern microscopic calculations as well as experiments are not sensitive to.

Neutron stars are born in core-collapse supernova (CCSN) explosions that mark the end of live of stars of at least eight solar masses [15]. Very massive stars will collapse to a black hole, but the threshold mass is unknown to date. As soon as nuclear fusion reactions come to an end, the star cannot longer support its mass against gravity. The core collapses and transforms into a neutron star, while the surrounding material is ejected into space due to the triggered explosion [16, 17, 18, 19]. Elements heavier than iron are created via nucleosynthesis with the rapid and slow neutron capture process (r- and s-process) and enrich the stellar medium [20, 21, 22]. While the s-process mainly occurs in asymptotic giant branch stars, the r-process takes place in environments with higher fluxes of free neutrons. New stars and planets that form in the gas clouds contain the synthesized heavy elements. The enormous explosions of CCSNe can even be seen by the naked eye from earth if they are close enough, which can still be thousands of light-years away [23, 24]. In the left panel of Fig. 1.1, we show the Crab nebula that originates from a supernova explosion observed in 1054 [1]. Unfortunately, supernovae that are observed today are almost all too far away for detailed measurements and observations of emitted neutrinos. The investigation of the detailed mechanism behind CCSN explosions relies on numerical simulations where only specific parts of the physics input can be probed in experiments.

Neutron star mergers (NSMs) are another extreme astrophysical phenomenon. Here, two neutron stars that form a binary system spiral around each other until they eventually collide and merge [25, 26, 12], see right panel of Fig. 1.1. The mass of the remnant determines whether it collapses to a black hole or not. During the coalescence, matter is ejected from the neutron stars that either is directly expelled to space (dynamical ejecta) or stays gravitationally bound and forms an accretion disk around the central object that also generates outflows [27, 28, 29]. The ratio between these two ejecta components strongly depends on the fate of the remnant and consequently on the EOS [30, 31]. The expelled material is neutron-rich, especially for the dynamical ejecta, and is another site where heavy elements are produced via the r-process [32, 33, 34, 35, 36, 37, 38, 39, 40, 41, 28, 42]. However, the details of the nucleosynthesis in mergers of compact objects and also CCSN are still not resolved, see e.g. Ref. [43]. The multi-messenger

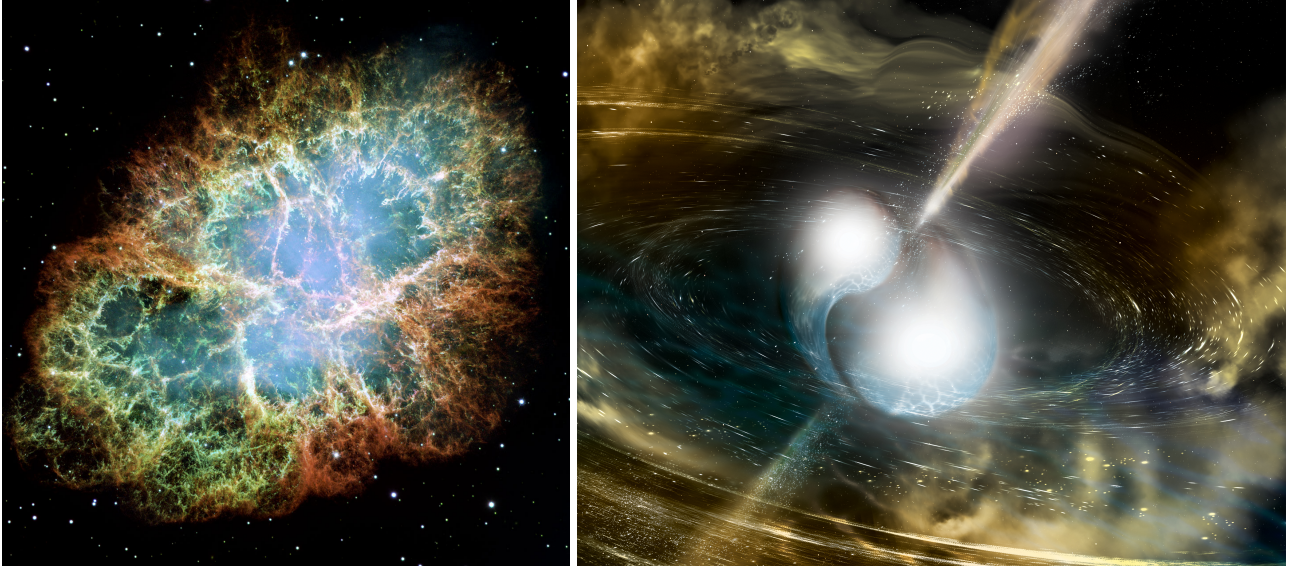


Figure 1.1: Crab nebula originating from a supernova observed in 1054 (left) as taken by Hubble Space Telescope [44] and illustration of a neutron star merger (right) taken from Ref. [45] and a courtesy of National Science Foundation, LIGO, Sonoma State University, Aurore Simonne.

observation of gravitational waves (GWs) and the corresponding electromagnetic counterpart offer a great opportunity to test our current understanding of the dynamics of the astrophysical phenomena and the involved fundamental forces.

The EOS is a key ingredient in CCSN and NSM simulations and highly influences the dynamics and outcome in both cases. A thorough description of the properties of matter at all relevant conditions is essential to explore these fascinating astrophysical environments and extract information from observations. However, we still rely on phenomenological models for simulations as the extreme conditions present in neutron stars, their mergers, and supernova explosions cannot be reproduced in terrestrial experiments yet. These phenomenological models are often not consistent with modern nuclear theory constraints or recent observations, see e.g. [46]. The aim of this work is to provide a new set of EOS for astrophysical simulations based on our current understanding from novel microscopic calculations including thermal effects that are especially crucial for the proto-neutron star evolution in CCSNe [47, 48]. In particular, uncertainties from nuclear theory as well as observations need to be reflected in the EOS to systematically study the sensitivity of specific nuclear physics properties in simulations. Moreover, heavy-ion collision experiments are a promising source of complementary information at intermediate densities where microscopic calculations are not applicable anymore and observations are not yet sensitive to. Our goal is to combine our knowledge from nuclear theory, observations, and current information from heavy-ion collision experiments to provide the most stringent constraint on the radius of a $1.4 M_{\odot}$ neutron star.

1.1 History of neutron stars

The first consideration of neutron stars can be dated back to 1932 by Lev Landau. He postulated that there are stars heavier than white dwarfs [49] only a month before Chadwick discovered the neutron [50]. Two years later, Baade and Zwicky assumed that neutrons are the main component of neutron stars and

anticipated that the massive stars are formed as remnants of supernova explosions [51, 52, 53]. While the first observation of a neutron star was still about three decades ahead, important progress has been made in the description of neutron stars. Tolman [54] and Oppenheimer and Volkoff [55] derived the structure equations of neutron stars independently from each other. These are now known as the Tolman-Oppenheimer-Volkoff (TOV) equations, see Sec. 1.4 for details. For their derivation, a noninteracting, relativistic neutron gas was assumed, which led to a first calculation of a maximum mass of neutron stars of $M_{\max} = 0.71 M_{\odot}$ [55].

Finally in 1968, Hewish and Bell detected the first pulsar with a period of 1.337 s [56]. Pulsars are fast rotating neutron stars with strong magnetic fields that emit radio signals, which can be precisely observed from earth as periodic pulses. Two years later, the intense radio source in the Crab nebula observed in 1965 [57], was identified as a pulsar [58, 59]. This marked the observational evidence that neutron stars are indeed born in supernova explosions [60]. The pulsar in the Crab nebula originates from a supernova explosion that was visible from earth in 1054 [1]. In 1987, the supernova SN1987A has been observed that took place in the Large Magellanic Cloud. It is the first event from which neutrinos were detected on earth, which validated the key role neutrinos play in these events [61], see also Sec. 1.2. To date, over 3300 pulsars have been observed [62, 63].

In 1974, the first binary system of pulsars has been detected [64]. This observation also indicated that GW exist. About four decades later, the era of GW astronomy started with the first detection of GW from a binary black hole merger [65]. In 2017, the LIGO/Virgo Collaboration detected the first direct GW detection from a binary NSM [66], which led to a series of new constraints on the equation of state [67, 68, 69, 70, 71, 72, 73]. see also Sec. 1.5.

1.2 The origin of neutron stars: Core-collapse supernovae

Neutron stars are the final stages of stellar evolution for massive stars with $M \gtrsim 8 M_{\odot}$, that explode in CCSNe, which are violent explosions driven by the release of gravitational energy. Low mass stars end up as white dwarfs while very massive progenitors and failed CCSN explosions lead to the formation of black holes [15]. The threshold mass after which all progenitors collapse to a black hole is not yet clear. In this section, we give a brief introduction starting from stellar evolution until the supernova explosion.

In the early stages of stellar evolution a star is mostly composed of hydrogen and helium. The star is stabilized against gravitational collapse by the pressure of the gas and degenerate electrons as well as by the energy that is released from fusion. Stars with masses of $8 M_{\odot}$ and more complete all burning stages leading to an iron core surrounded by specific burning layers that built an onion-like structure [17]. The fusion of elements in the core stops eventually since iron has the largest binding energy per nucleon. At the same time, the electron degeneracy pressure decreases due to electron capture reactions on either protons or ions that produce neutrons and neutrinos. The latter are only weakly interacting and escape the system. This prevents the inverse reaction and results in a deleptonization. At the surface of the core, silicon burning still produces iron nuclei, which lets the core grow further until the so-called Chandrasekhar mass $M_{\text{ch}} \approx 1.46 M_{\odot}$ [19]. Once the core reaches this value, the gravitational force cannot longer be balanced out and the core collapses. In less than a second, the core shrinks from around thousand kilometers in radius to only a few ten kilometers [74].

During the collapse, densities inside the core easily reach nuclear densities such that nuclei merge together and form homogeneous matter of neutrons, protons, and electrons. More and more neutrons are build via the electron capture reaction. Nucleons are packed so closely that the short-range interaction between them dominates and matter becomes almost incompressible. The collapse stops and infalling material bounces off the core. This so-called bounce initiates a shock wave that starts to propagate outwards, see left panel of Fig. 1.2. The former iron core and material that falls through the shock onto the core

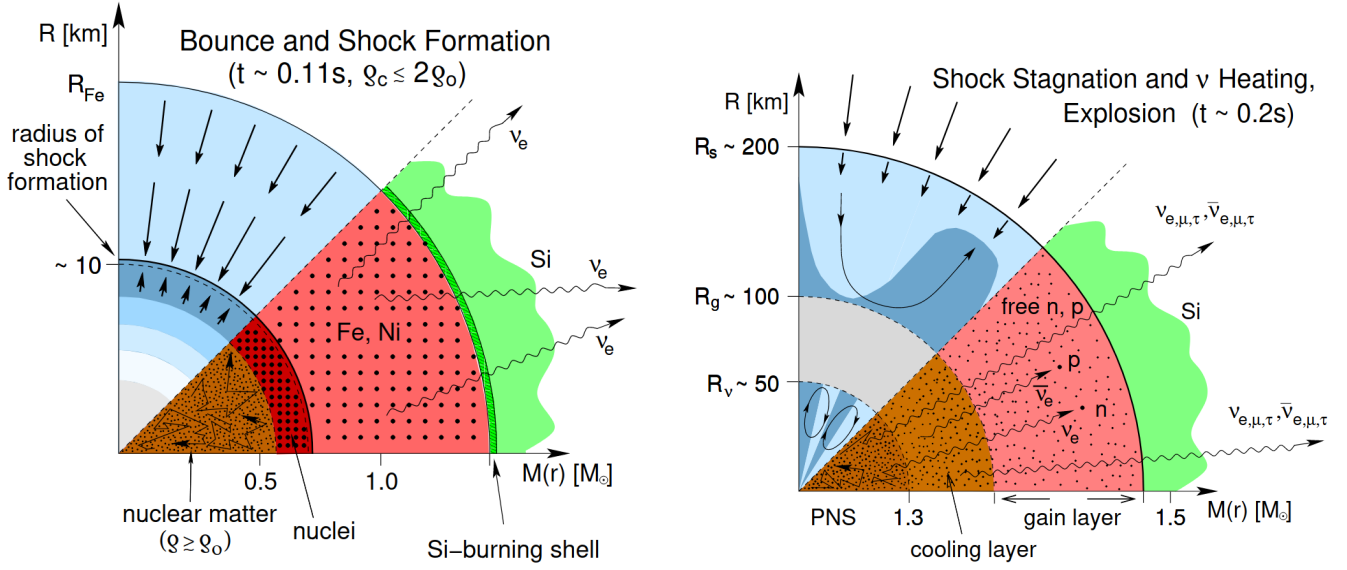


Figure 1.2: Schematic illustration of bounce and shock formation (left) and shock stagnation and neutrino heating (right) with dynamical conditions in the upper half and nuclear composition with nuclear and weak processes in the lower half. The x-axis represents the mass in units of the solar mass M_\odot and the y-axis refers to the radius where R_{Fe} , R_s , R_g , and R_ν stand for the the radius of the iron core, shock radius, gain radius, and neutrinosphere, respectively. From Ref. [15].

form a proto-neutron star (PNS). Here, the fraction of protons is approximately constant and about 30% of all baryons [16]. The reason for this is that electron capture reaction on protons, positron capture on neutrons, and the inverse reactions are in equilibrium as neutrinos are trapped in the prevailing dense matter of the PNS. In the meanwhile, the shock propagates further outwards where densities decrease and matter becomes transparent for neutrinos. This causes a neutrino burst shortly after bounce that takes away a lot of the energy. In the material that is heated up from the shock high-energy photons dissociate iron and nickel ions into protons and neutrons. The energy loss of the shock from this photodissociation process together with the escaping neutrinos results in a stagnation of the shock wave at a radius of about 100 to 200 km [15] and prevents a prompt supernova explosion.

In 1965, Colgate and White [75] were the first to propose that a few percent of the energy that is carried away by neutrinos is deposited behind the shock by neutrino absorption. Bethe and Wilson [76] postulated about twenty years later the delayed neutrino-heating mechanism. Here, the matter behind the shock wave in the so-called gain region is heated by the absorption of high-energy electron neutrinos and anti-neutrinos from neutrons and protons, see right panel in Fig. 1.2. These neutrinos become even more energetic since they are in thermal equilibrium with the PNS, whose temperature rises due to the ongoing contraction. In the cooling layer, which forms between the PNS and the gain region neutrinos are mostly emitted. At the same time, density and temperature at the position of the shock decrease as matter is still falling onto the PNS, which supports the shock revival as well. Simulations of CCSNe have shown that multi-dimensional instabilities further helps the shock propagation. In particular, Rayleigh-Taylor instabilities are induced when cold and heavy material in the gain region sinks towards the center while hot material expands [16] resulting in a longer duration of matter in the gain layer and, thus, higher neutrino absorption rates. In total, only a few percent of neutrinos are absorbed, which is enough to push the shock propagation and trigger a delayed explosion. [18]. If the deposited energy is not sufficient to revive the shock wave, the

PNS continues to accrete material until it eventually collapses to a black hole.

Less than a second elapses from the gravitational collapse to the delayed explosion [17]. The PNS in the center cools down mainly through the continuous emission of neutrinos. The conversion to a neutron star by neutronization and deleptonization is completed about 10 to 20 seconds after the core collapse of the progenitor star [11]. Days may pass by until the shock wave finally reaches the outer layers of the star and the explosion can be observed. As stated in Sec. 1.1, the supernova SN1987A was the first and so far the only one where a spectroscopy of the neutrino blast was possible. The observed neutrinos confirmed the delayed neutrino-heating mechanism [61]. However, only 24 neutrinos were detected such that statistics are weak. Neutrino observations enable a view directly to the dense matter in the core of the PNS as they do not further interact with matter in the outer layers of the star where densities are much lower than nuclear densities.

1.3 Neutron star structure

The composition of neutron stars varies considerably when going from the surface to the center where the density reaches its maximum. As a result, neutron stars are divided into several layers as illustrated in the schematic drawing in Fig. 1.3 from Ref. [77]. The atmosphere surrounds the neutron star with a thin layer of plasma and consists mostly of hydrogen and helium [1]. Its thickness depends on the temperature, but is at most a few ten centimeters [1]. The atmosphere is crucial for many observations as it emits thermal radiation that gives information on the effective surface temperature, the chemical composition and the magnetic field at the surface as well as neutron star properties like the mass and radius [12]. Thus, the atmosphere is essential in modeling neutron stars to extract these characteristics from observational data.

The outer crust is located beneath the atmosphere. It has a thickness of several 100 meters and is composed of a lattice of ions and degenerate electrons, where the latter dominate the pressure [1]. Towards the inner crust, the density increases progressively and with it the electron chemical potential. As

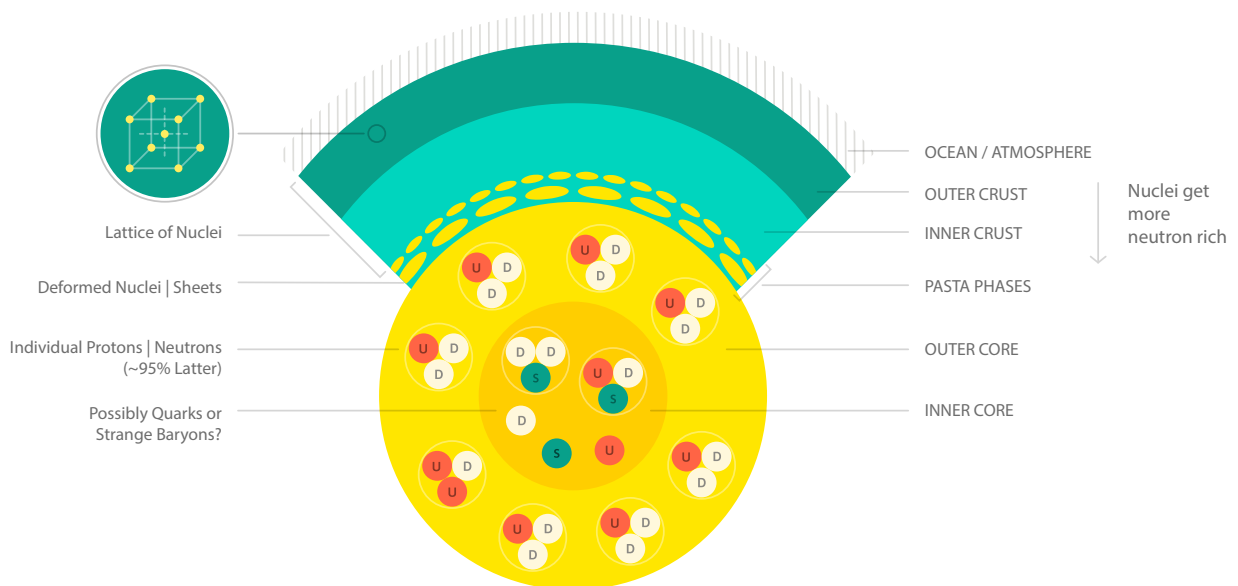


Figure 1.3: Schematic representation of a neutron star with the different layers and the corresponding constituents in each layer. Figure taken from [78].

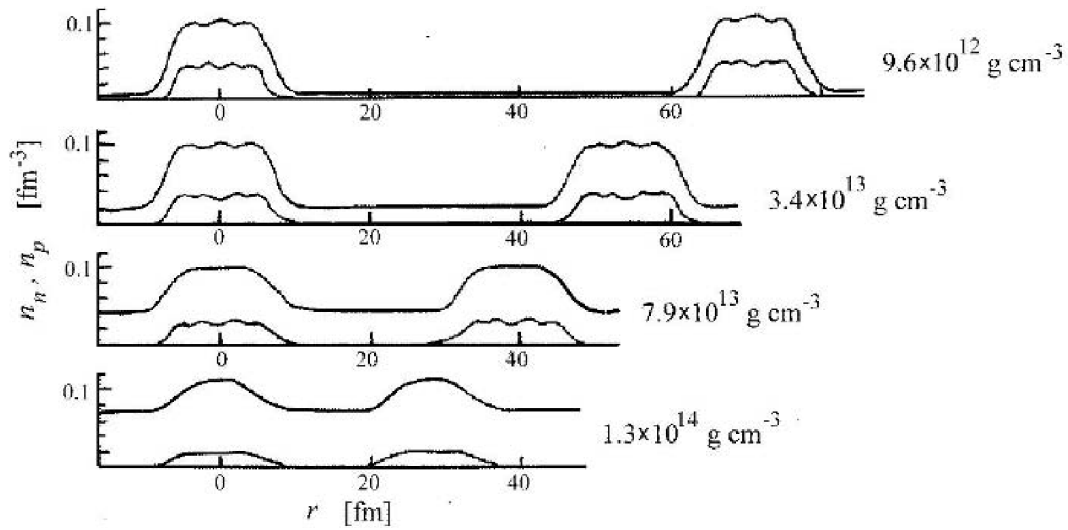


Figure 1.4: Neutron and proton density profiles for several average densities. Figure taken from Ref. [80], see also Ref. [1].

a consequence, electron captures on protons are energetically favorable, such that nuclei become more neutron-rich [79]. At a density of about $4 \cdot 10^{11} \text{ g cm}^{-3}$, nuclei are packed so close together that the neutron chemical potential becomes positive such that neutrons become unbound and drip out of nuclei [11]. At the same time, the electron chemical potential is high enough to hinder β -decay so that neutrons can exist freely. The density distributions of neutrons and protons are depicted in Fig. 1.4 for several average densities from Ref. [80] to illustrate the dripping of neutrons. The so-called neutron-drip density marks the beginning of the inner crust.

The inner crust is about 1 kilometer thick and extends from the neutron-drip density up to roughly half saturation density where the liquid-gas phase transition to nuclear matter is completed [12]. For details on the phase transition see Sec. 2.5. Matter in the inner crust is composed of neutron-rich nuclei surrounded by an electron gas and superfluid neutrons [1]. With increasing density, nuclei become heavier and the neutron density outside nuclei increases as well. Within this transition, nuclei might be deformed in a series of geometries including tubes, sheets, and bubbles [77]. These structures are similar to the shapes of pasta, which is why they are called nuclear pasta. The specific region in the inner crust where these structures are present is also depicted in Fig. 1.3. At the end of this transition at the crust-core boundary, the neutron density outside and inside nuclei are of same size, which means that all nuclei are completely dissolved to uniform matter [79], see Fig. 1.4.

About 99% of the matter in neutron stars is located in the core [12], which can be split into an outer and an inner core. Matter in the outer core consists mostly of neutrons, with a small admixture of about 5% protons as well as electrons and possibly muons [1]. The specific composition is determined by β -equilibrium and charge neutrality. The neutrons and protons form a strongly interacting Fermi liquid and might be both in superfluid state [11]. The outer core is several kilometer thick and reaches densities up to roughly $2n_0$ at the boundary to the inner core [1]. The inner core has a thickness of several kilometers, similar to the outer core. The maximum density that is reached in the center of the neutron star might be as high as $10n_0$ [12]. However, it is still an unknown quantity and very model dependent. In addition, different forms of matter may be present like deconfined quark matter, pion and kaon condensates or hyperons [11, 1]. A lot of efforts are currently put into studies about phase transition to these more exotic phases that lead to a softening of the equation of state, see e.g., Refs. [13, 81, 82, 83, 84, 85].

1.4 Neutron stars and the nuclear equation of state

Neutron stars can be described via the TOV equations for hydrostatic equilibrium that are based on general relativity. These are two coupled differential equations for a non-rotating and spherically symmetric body [54, 55]

$$\frac{dP}{dr} = -(\epsilon + P) \frac{m + 4\pi r^3 P}{r^2} \left(1 - \frac{2m}{r}\right)^{-1}, \quad (1.1)$$

$$\frac{dm}{dr} = 4\pi r^2 \epsilon, \quad (1.2)$$

with the pressure P , energy density ϵ , radius coordinate r , and mass m within a sphere of radius r^1 . The mass and the radius of a neutron star is obtained by integrating from the center to the surface of the star. To this end, the equation of state $P(\epsilon)$ is required to close the system of equations. The initial conditions are defined at the center, where the enclosed mass m as well as the radius r are zero. One chooses a value for the central pressure $P_c = P(r = 0)$ and integrates from there until $P = 0$, which is the condition of the surface. Here, the radius coordinate is identified with the radius of the neutron star, $r = R$, which then determines the neutron star mass as $M = m(r = R)$. This procedure is performed for various central pressures resulting in the mass-radius relation, see Fig. 1.5. Every point on this line corresponds to a specific central pressure and, thus, to a certain maximum density. With increasing central pressures, the maximum density increases as well and the corresponding neutron star becomes heavier. This describes the condition for stable neutron stars, $dM/dn > 0$, which holds up to the maximum mass. If this mass threshold is exceeded, the neutron star becomes unstable and collapses to a black hole.

There is a unique link between EOS and mass-radius relation, meaning that every $M - R$ relation corresponds to exactly one EOS [14]. The EOS describes the properties of matter across many orders of magnitude in density including various types of interactions and degrees of freedom. The conditions in the crust are rather well understood and can be probed in experiment resulting in low uncertainties for the EOS. However, with increasing density nuclei become neutron-rich and are often not accessible with experiments anymore. Towards the center of the star, uncertainties increase rapidly as also microscopic calculations break down above nuclear densities and extrapolations to the maximum density are needed. The constituents in the inner core are still unknown, which is also reflected in the enlarged EOS uncertainties. The space of possible EOS is reduced by the requirement that the speed of sound $v_s = \sqrt{dP/d\epsilon}$ does not exceed the speed of light. Another condition is that the EOS has to support masses of observed neutron stars. To date, a few massive neutron stars with masses of about $2 M_\odot$ have been precisely measured [6, 7, 9], see Sec. 1.5 for more details. These two general assumptions constrain the radius of a $1.4 M_\odot$ neutron star to approximately 12 ± 2 km [3, 4, 5]. A reduction of EOS uncertainties especially at densities above saturation density results in a smaller uncertainty for neutron star radii and vice versa. Consequently, observations are a key tool to constrain the equation of state at high densities where terrestrial experiments and microscopic calculations are not yet feasible.

In Fig. 1.5, we show the EOS and the resulting mass-radius relation from Ref. [4]. The EOS is based on microscopic calculations up to roughly saturation density (dark blue band) and a polytropic expansion to higher densities that only applies the two general assumption of causality and the $2 M_\odot$ neutron star and, thus, exhibits a broad uncertainty band. Soft EOS that have lower pressures at a given energy density feature smaller neutron star radii and larger central densities for a given neutron star mass compared to stiff EOS. The maximum mass also strongly depends on the EOS and is an important quantity to constrain the radius uncertainty [86, 87]. A lower bound on the maximum mass is given by the most massive neutron

¹Throughout this thesis, we use natural units with $c = \hbar = k_B = G = 1$.

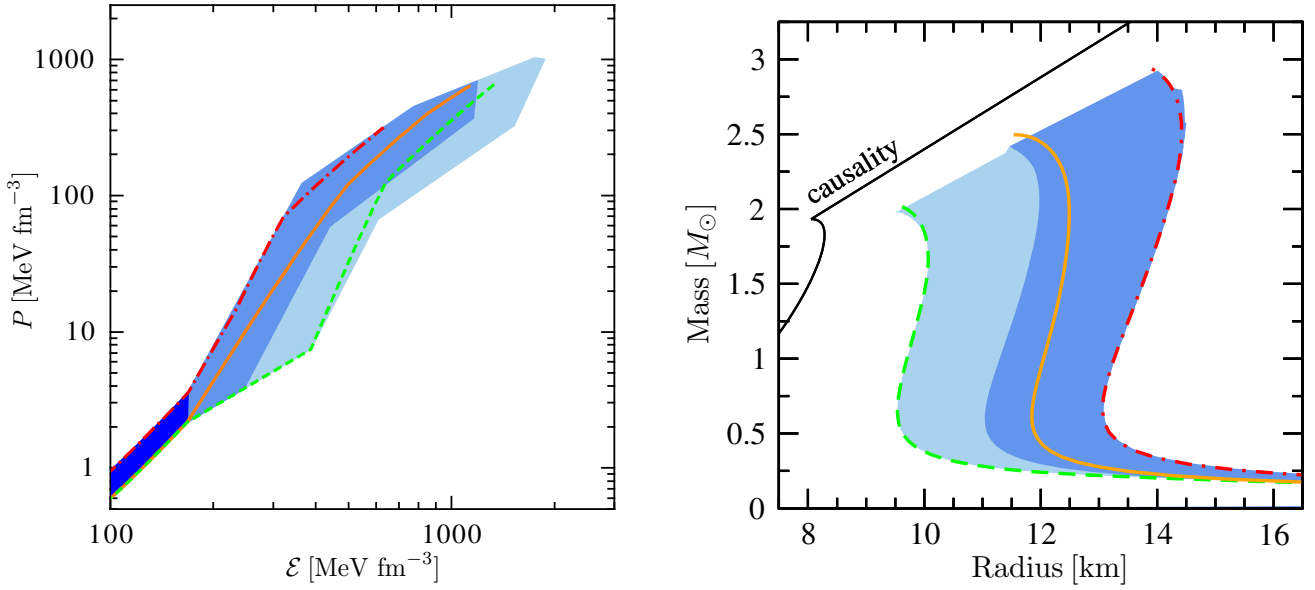


Figure 1.5: Equation of state (left) and mass-radius relation (right) from microscopic calculations up to roughly saturation density and a polytropic expansion to higher densities. Figure taken from Ref. [4].

star known so far, while an upper bound can be inferred by the multi-messenger detection of NSMs, e.g., Refs. [88, 89, 90, 91], see Sec. 1.5 for details. The radius of neutron stars are correlated with the pressure. In fact, the radius of a canonical neutron star is sensitive to the pressure around 1-2 times saturation density [92, 87]. This specific radius and the maximum mass are the key parameter that characterize the mass-radius relation [11].

In general, the EOS describing cold neutron stars does not only depend on density, but also on temperature and the proton fraction. However, the proton fraction is set by the condition of β -equilibrium. The temperature is of the order of 10^8 K, which corresponds to a thermal energy of about 10 keV [86, 93]. This is small compared to the Fermi energy of neutrons at nuclear densities, which is several MeV and increases with density [94]. Consequently, isolated neutron stars can be considered at zero temperature. We use this description of the EOS with $P = P(n)$ only for cold neutron stars. In the case of proto-neutron stars born in supernova explosions and NSMs, temperature effects are relevant and the general description with $P = P(n, x, T)$ is necessary for a thorough characterization of the EOS.

1.5 Observations

The observation of neutron stars is essential for our understanding of dense matter as conditions that are present inside neutron star cores cannot be produced in terrestrial experiments yet. In our galaxy, there are an estimate of $10^8 - 10^9$ neutron stars, but only a small fraction of them have been observed so far [1]. Observations provide information about various properties of neutron stars. In particular, masses of pulsars in binaries can be measured with incredible precision, while measurements of the radius still have large uncertainties. However, a promising tool to constrain the radius to a high degree in the future is the measurement of the moment of inertia for a neutron star with a well-known mass [95, 96]. In this section, we will focus on the types of observations that we use in the upcoming chapters of this thesis to

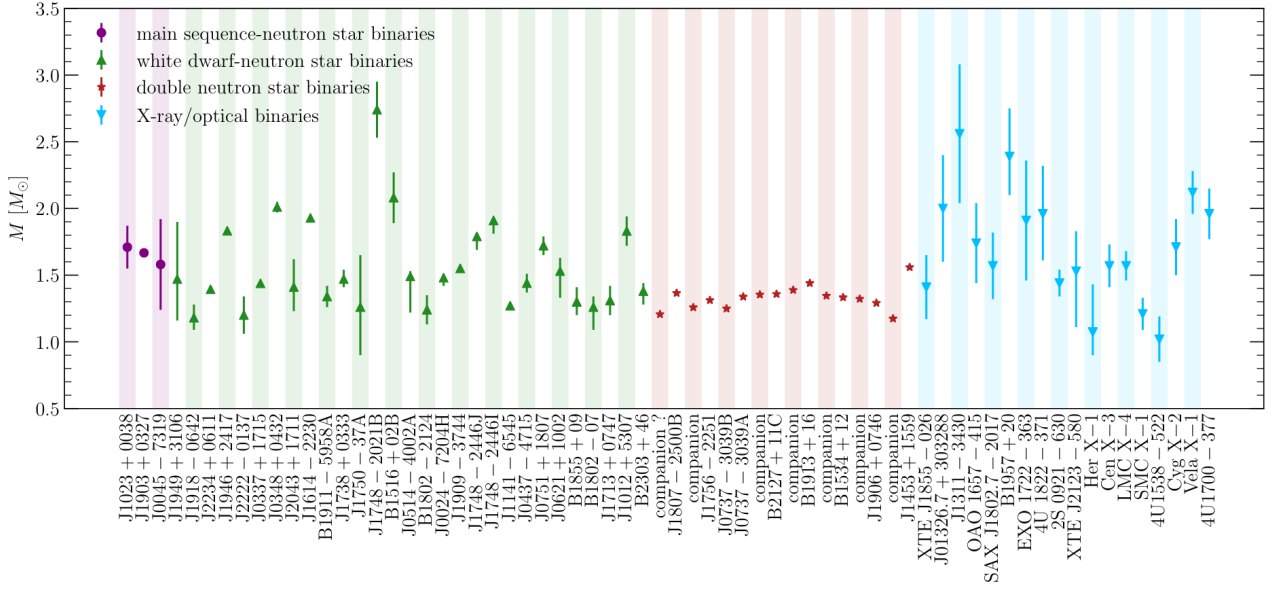


Figure 1.6: Observed neutron star masses with 1σ uncertainty from various binary systems as indicated by the different colors and symbols. From Ref. [96] with data from [98], see also [98, 99, 3].

study the dense matter inside neutron stars.

1.5.1 Mass Measurements of heavy neutron stars

Precise measurements of neutron star masses are especially possible when observing pulsars in binary systems [3]. Pulsars have an almost constant rotational period. Their axis of magnetisation and rotation are in general misaligned resulting in a small decrease of rotation. Nevertheless, the rotation as well as its derivative can be measured accurately, such that any deviation of their predicted pulse profile due to gravitational interaction with a companion star gives information about the mass of the pulsar [97]. The accuracy of the mass measurement increases with the compactness of the companion such that double neutron star binaries offer the most precise mass measurements to date where relative uncertainties of the order of 10^{-4} are possible, see, e.g., the Hulse-Taylor pulsar with a mass of $M = 1.4408 \pm 0.0003 M_{\odot}$ [64]. In Fig. 1.6, a summary of observed neutron star masses from various binary systems including main sequence-neutron star binaries, white dwarf-neutron star binaries, double neutron star binaries, and X-ray/optical binaries. The chart also demonstrates that most known neutron stars have a mass of about $1.4 M_{\odot}$, which is known as the canonical value.

Obtaining neutron star masses with long-term radio pulsar timing is done in two steps. First, the offset between the standard profile of a pulsar that is observed and the detected pulse profile give information about the pulsar position, the period with its derivative, and the dispersion measure [100]. Then, in binary systems, five Keplerian orbital parameters are fitted with the mass of the pulsar and the mass of the companion as the only unknown parameters [3]. In the case of double neutron star binaries, five post-Keplerian (PK) parameters are fit to the pulse profile. These are the rate of the periastron advance, the time-dilation and gravitational-redshift parameter, the rate of the orbital period decay, and the two Shapiro delay parameters. These parameters characterize the change of the expected pulse times-of-arrival due to relativistic effects of the two stars orbiting each other [101]. Each of the PK parameter is a function of the two stellar masses in a given theory of gravity [102, 103]. Consequently, to obtain the mass of the

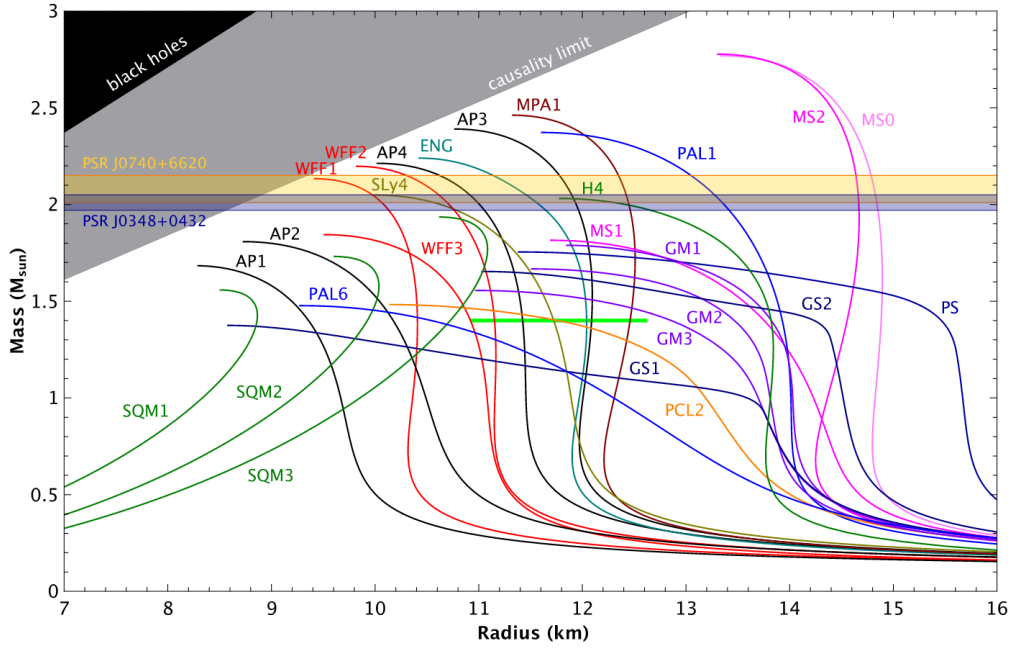


Figure 1.7: Mass-radius relation for various EOS. The horizontal bands are the 1σ uncertainty band of the two most massive neutron stars known to date [7, 9]. The green bar is the result of the 90% confidence limit of the radius of a $1.4 M_{\odot}$ neutron star from the multi-messenger analysis of Ref. [72]. Figure created by Norbert Wex from Ref. [104] with EOS tabulated in Ref. [92].

neutron stars one needs to measure two PK parameters. The observation of three or more PK parameters offers the possibility to test the theory of gravity [97].

Masses of heavy neutron stars are especially interesting as they constrain the maximum mass of neutron stars, i.e. the mass that can be still supported against gravitational collapse to a black hole. To date, there have been several precise observations of neutron stars with about two solar masses [6, 7, 8, 9]. These discoveries provided valuable information about the behavior of dense matter as it excludes exotic degrees of freedom in neutron star cores that lead to a drastic softening of the EOS and, thus, cannot support such a high mass. This is reflected in Fig. 1.7, which depicts the mass radius relation of neutron stars for various EOS. The horizontal bands show the 1σ uncertainty of the two most massive pulsars observed so far [7, 9]. This rules out many EOS that predict maximum masses smaller than the current limit. The green bar represents the 90% confidence limit of the radius of a $1.4 M_{\odot}$ neutron star from the multi-messenger analysis of Ref. [72].

1.5.2 Neutron Star Interior Composition Explorer (NICER)

Neutron stars are small, faint, and far away, which makes measurements of neutron star radii very complicated. However, a NASA mission was launched in 2017 in which the soft X-ray telescope NICER (Neutron Star Interior Composition Explorer) has been installed on the International Space Station with the purpose to measure the mass and radius of a neutron star simultaneously for the first time [105, 106, 107, 108]. This is done via pulse profile modeling of the observed X-rays that are emitted from regions with high radiation levels on the surface of the star. These regions are called hot spots and appear as pulsation due to the rotation of the pulsar. Relativistic effects are essential for the pulse profile since the

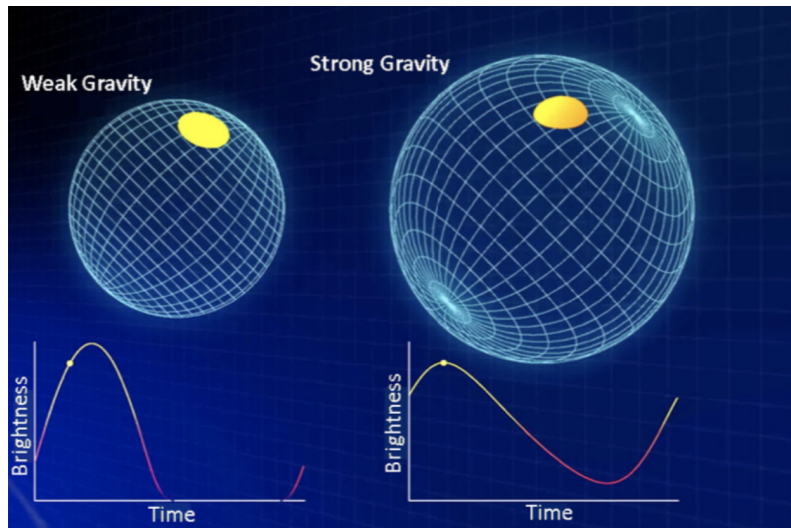


Figure 1.8: Illustration of the relativistic effects of the pulse profile that are sensitive to the compactness of the neutron star. Figure credit Morsink/Moir/Arzoumanian/NASA.

emitted photons travel through the curved exterior space-time of the star. Consequently, the amplitude of the pulsation and the photon time delays from different points on the surface depend strongly on the compactness M/R [78]. For a more compact neutron star with a strong gravitational field, the light bending leads to the detection of X-rays even for the far-side hot spot [105]. This is illustrated in Fig. 1.8 for pulse profiles of two stars with different compactness. There are also other effects of general relativity that are sensitive to the compactness and have to be taken into account, e.g., gravitational redshifting of photons that impacts the energy-dependent normalisation [109, 110, 111, 112, 113, 114, 115, 116, 117]. The pulse profile itself also depends on other parameters like the emission direction, the emission from the stars surface in general as well as geometrical parameters of the hot spots including its size and shape. In order to infer the mass and radius of the observed neutron star one has to reconstruct the pulse profile. All parameters from the surface emission model including the surface temperature pattern and the inclination angle of the observer and all parameters of a given exterior space-time that is characterized by the mass, radius, and spin frequency enter in this modeling [118]. The pulse profile model is then sampled and matched to the observed data to obtain posterior probability distributions for the mass and radius via Bayesian inference.

There are three different pulsar types with hot spots for which mass and radius can be inferred via pulse profile modeling, namely rotation-powered pulsars, accretion-powered pulsars, and thermonuclear burst oscillation sources. The NICER mission focuses on rotation-powered millisecond pulsars, because they provide a very stable pulse profile that also allows for multiple distinct observation runs [78]. Future X-ray observation missions like the enhanced X-ray Timing and Polarimetry (eXTP) [119] and the Spectroscopic Time-Resolving Observatory for Broadband Energy X-rays (STROBE-X) [120] utilize the next generation of telescopes with a larger area such that more photons can be detected, which ultimately leads to tighter constraints. Here, also measurements from fainter rotational-powered pulsars as well as accretion-powered pulsars, and thermonuclear burst oscillation sources are possible, resulting in more constraints on the equation of state.

Up to now, NICER has reported on the measurements of two pulsars. The data have been analysed by two groups independently from each other. The assumptions for the pulse profile modeling vary in some

aspects, among others the configuration of hot spots, leading to different results for the inferred mass and radius. For the observation of the pulsar PSR J0030+0451, the mass and radius have been determined to be $M = 1.34_{-0.16}^{+0.15} M_{\odot}$ and $R = 12.71_{-1.19}^{+1.14}$ km by Ref. [121] and $M = 1.44_{-0.14}^{+0.15} M_{\odot}$ and $R = 13.02_{-1.06}^{+1.24}$ km by Ref. [122]. The second target was the most massive neutron star known to date, PSR J0740+6620. Here, the mass is known *a priori* such that the accuracy of the radius can be generally higher. The group of Riley *et al.* published for their analysis $M = 2.07_{-0.066}^{+0.067} M_{\odot}$ and $R = 12.39_{-0.98}^{+1.30}$ km [123], whereas the group of Miller *et al.* reported $R = 13.7_{-1.5}^{+2.60}$ km [124]. Both analyses are based on combined data from NICER and from the X-ray Multi-Mirror (XMM-Newton) mission. The latter was needed to obtain information on the mass and background, which was not constrained precisely enough from NICER alone. For more details on the implication of the results from NICER on the EOS see, e.g., Refs. [125, 126, 127].

1.5.3 Gravitational waves and multi-messenger astronomy of neutron star mergers

GWs have been predicted by Albert Einstein [128] based on his works on general relativity [129, 130]. They are small deformations of spacetime that travel with the speed of light [25]. Their interaction with matter is very weak, which makes the detection rather complicated. However, with mergers of two massive objects like black holes and neutron stars direct detection is possible [131, 132, 133, 134, 135]. Such a merger has three phases. In the inspiral phase, the two objects orbit each other, slowly approaching one another. GWs are emitted due to the loss of energy resulting in the reduction of the orbital distance between the two objects [25]. When they get closer, the frequency and the amplitude of the GWs increase, where the latter is characterized by the masses of the objects [26]. In the case of a binary NSM, tidal forces become relevant at the end of the inspiral phase [12]. The second phase is the merger itself, i.e. the coalescence of the two objects, which is followed by the post-merger phase.

The first direct detection of GWs was in September 2015 from a binary black hole merger [65]. About two years after on August 17, 2017, GWs of a binary NSM were detected and named GW170817. Furthermore, a short gamma-ray burst, GBR170817A, and a kilonova, AT2017gfo, were observed in the days after the merger [66, 136]. We show the detected frequency as a function of time from the merger as well as the observed lightcurves featuring the short gamma ray burst in Fig. 1.9. This event marks the beginning of the era of neutron star multi-messenger astronomy. The GWs were detected by two ground-based interferometers from LIGO (Laser Interferometer Gravitational-Wave Observatory) [137, 138], whereas there was no detection visible in the Virgo [139, 140] interferometer. These laser interferometers consist of two arms that are a few kilometers long to detect the very weak interaction of matter with GWs. A laser beam that enters the interferometer is split by a beam splitter and reflected by mirrors at the end of the interferometer arms. After recombining the beam, the intensity is detected via a photodiode. In the case of an incoming GW, the interference of the recombined laser beam is altered due to the modification of the arm length [137, 141]. Since these changes are very small and the detectors are sensitive towards all kinds of disruptions, there are several GW detectors distributed across earth to allow for coincidence measurements. In addition, this network of detectors helps to locate the GW source in the sky so that the possible electromagnetic counterpart might be detected as well [25].

Currently, detectors are only sensitive to the GW signal of the inspiral phase where frequencies are below 1000 Hz [133, 142]. Here, the intensity as well as the phase of the GW is measured. In practice, the observed waveform is matched to a theoretical model of the GW signal with fit parameters that depend on the observables of interest [143]. For the early inspiral phase, the objects are far apart from each other and are treated as point particles. Here, the chirp mass is a key quantity and imprinted in the evolution of the frequency [25]. It is given by $\mathcal{M} = (M_1 M_2)^{3/5} / (M_1 + M_2)^{1/5}$, with M_1 and M_2 being the masses of the binary system components [144]. The mass ratio $q = M_2/M_1$ where $M_1 \geq M_2$ becomes relevant with increasing gravitational interaction towards the end of the inspiral phase. Here, the approximation of point

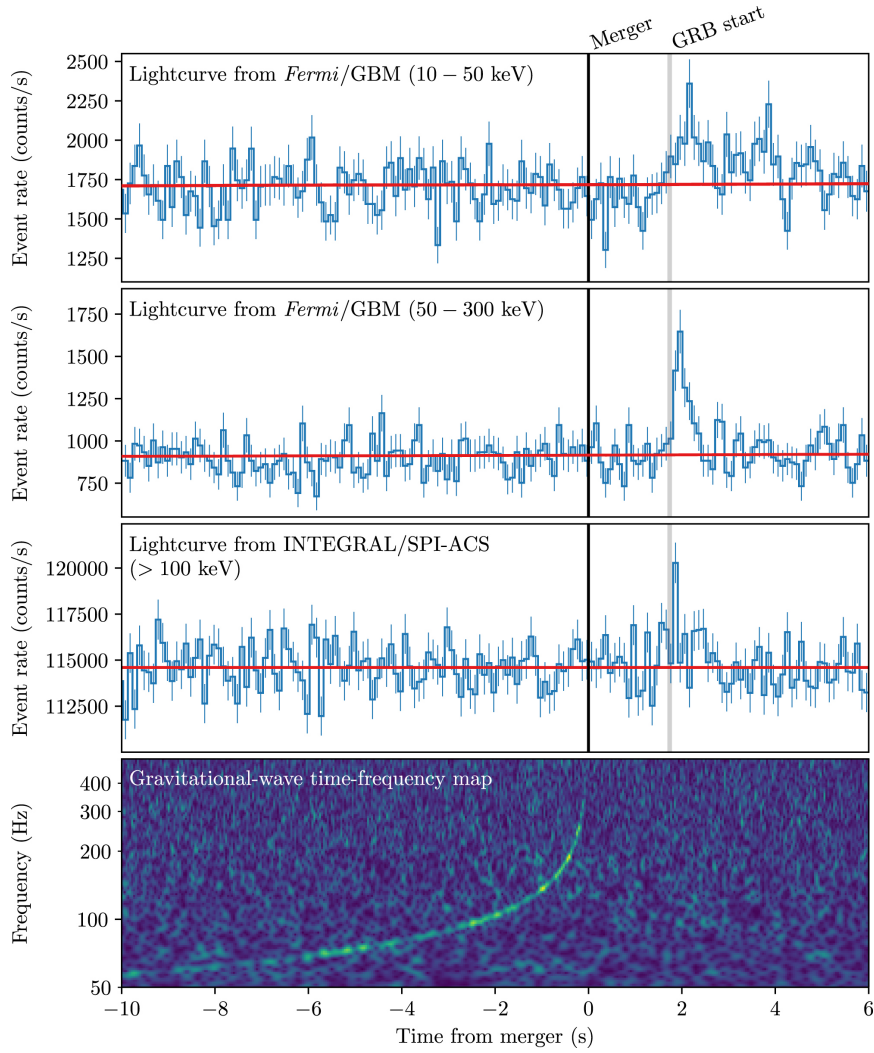


Figure 1.9: Multi-messenger detection of GW170817 and GRB170817A. The lowest panel shows the detected frequency as a function of time from the merger combined from the data of the two LIGO observatories. The upper panels show the lightcurves for different energy ranges with the clear imprint of the gamma ray burst associated with the gravitational wave signal. Figure from Ref. [136].

like particles is not valid anymore. The phase of the GW signal is now set by the binary tidal deformability $\tilde{\Lambda}$ as a function of the masses and tidal deformabilities of the individual binary participants [143]. The tidal deformability λ is defined as the ratio of the induced quadrupole moment over the perturbing tidal field of the companion and sensitive to the EOS [12]. Right before the merger, the frequency of the GW signal increases rapidly and lies outside the sensitivity band of current detectors [145]. Also the post-merger signal that entails information about the properties of matter at high densities lies outside of the current frequency band of the detectors. However, next generation telescopes like the Einstein Telescope [146, 147] or the Cosmic Explorer [148, 149] aim to deliver the required sensitivity.

The first detection of GW from a binary NSM, GW170817 [66], with its corresponding short gamma-ray burst GRB170817A and the kilonova AT2017gfo [136] already led to numerous constraints on the EOS


for neutron stars [67, 68, 69, 70, 150, 71, 72, 151, 124, 152, 73]. In particular, estimates for the tidal deformability of a $1.4 M_{\odot}$ neutron star and the binary tidal deformability favor softer EOS compared to NICER, while stiff EOS corresponding to large neutron star radii are excluded. This is also in line with constraints on the upper bound of the maximum mass of neutron stars inferred from the observation. The observed gamma ray burst and the subsequent kilonova indicate that the remnant collapsed to a black hole shortly after the merger. The time delay between the merger and the collapse supports about $2.2 - 2.3 M_{\odot}$ for the upper bound of the maximum mass [88, 89, 90, 91]. The observed kilonova in the days after the merger revealed that heavy elements are in fact produced in NSMs via the r-process, e.g. [153, 154, 155, 156].

In 2019, the GW signal GW190425 was detected in one of the LIGO interferometers [157]. The total mass $M_{\text{tot}} = 3.4_{-0.1}^{+0.3} M_{\odot}$ and the chirp mass $\mathcal{M} = 1.44_{-0.02}^{+0.02} M_{\odot}$ are both rather large, but the system is likely to be a binary NSM [157, 158]. It was not possible to detect an electromagnetic counterpart, see e.g. Refs. [159, 160]. The distance of the coalescence to earth was larger than that of GW170817 and the localisation was only poorly constrained. However, the missing kilonova could also hint at a prompt collapse to a black hole due to the high mass of the system [161, 162]. Therefore, the inferred constraint on the EOS from GW190425 is only weak.

In conclusion, observations are a crucial part to explore the equation of state above nuclear densities. Mass measurements of massive neutron stars, the first detection of gravitation waves, and results from NICER have already led to many insight into the properties of matter in neutron stars. In the next decade, we can expect many more observations that will ultimately result in more stringent constraint for the mass-radius relationship and hopefully shed some light on the constituents of neutron star cores.

1.6 Organization of this thesis

This thesis is structured as follows: In Chap. 2, we focus on the description of the EOS for hot and dense matter. We start with a short introduction to Quantum Chromodynamics (QCD), which is the underlying theory of strong interactions, and sketch microscopic approaches to the EOS at densities relevant for neutron stars. This is followed by a description of the theoretical concept of infinite nuclear matter to establish important properties of the EOS at nuclear densities. We then briefly discuss the extraction of information about the EOS from heavy-ion collision experiments. This is followed by a description at finite temperature with the interplay between the nucleon effective mass and thermal effects as well as the liquid-gas phase transition. We conclude with phenomenological EOS for astrophysical simulations and effects of the EOS in CCSNe. A new EOS functional consistent with results from nuclear theory, observations, and high-density QCD calculations is established in Ch. 3. After a summary about relevant EOS constraints, we discuss the new EOS functional with the corresponding nucleon effective mass and systematically study the impact of specific properties on the EOS. We then construct EOS for neutron star matter that reflect the uncertainties of the constraints from nuclear theory and observation. The work presented in this chapter is published in Ref. [73]. In Ch. 4, we construct EOS for astrophysical applications based on the EOS functional derived in Ch. 3. To this end, we introduce a set of representative EOS and discuss results for the liquid-gas phase transition. We then detail our construction of the EOS for simulations based on the liquid-drop model and the single-nucleus approximation, which can be used to built EOS tables. This is followed by an exploration of EOS effects in NSM simulations. We present an interdisciplinary study of neutron star matter in Ch. 5, which is published in Ref. [163]. Hereto, we detail the information from nuclear theory, multi-messenger observations and heavy-ion collision experiments that we use in a Bayesian framework to arrive at a combined constraint on the EOS from all of these complementary sources. We also discuss the implementation of data from heavy-ion collisions and detail numerous tests we have conducted that ensure that our result for the radius of a $1.4 M_{\odot}$ neutron star is robust. In Chap. 6, we conclude our work



and provide an outlook.

2 Equation of state of hot and dense matter

To describe neutron stars, their formation and mergers, the EOS across a wide range of density, temperature, and electron fraction is required. In the core of neutron stars, the density exceeds several times the nuclear saturation density n_0 . The dynamics of the interaction between the constituents are governed by the strong force. The strong interaction is one of the four fundamental forces in nature and is described by quantum chromodynamics (QCD). The phase diagram of QCD, showing the individual states of matter depending on density in units of the saturation density n/n_0 with $n_0 = 0.16 \text{ fm}^{-3}$, temperature T , and the density difference of neutrons to protons $n_n - n_p$, is depicted in Fig. 2.1. At low densities or baryon chemical potentials and temperatures below roughly 170 MeV [164], quarks as elementary particles are confined to hadrons. In this hadronic phase, a liquid-gas phase transition occurs just below nuclear saturation density, which we will detail in Sec. 2.5. Nucleons are bound to nuclei only in the coexistence region of this phase transition: this is where we and the matter around us that makes up our world live in the QCD phase diagram. Increasing the density and/or the temperature, hadrons become deconfined into their constituents, quarks and gluons. The exact location and behavior of this transition is topic of current research, see e.g. Ref. [165]. There are several experiments worldwide that are dedicated to study the nature of the state of matter across different densities and temperatures.

In the phase diagram, neutron stars are mostly located at the zero temperature plane. It is still unclear if and to which extent quark matter is present in neutron star cores due to the missing knowledge of

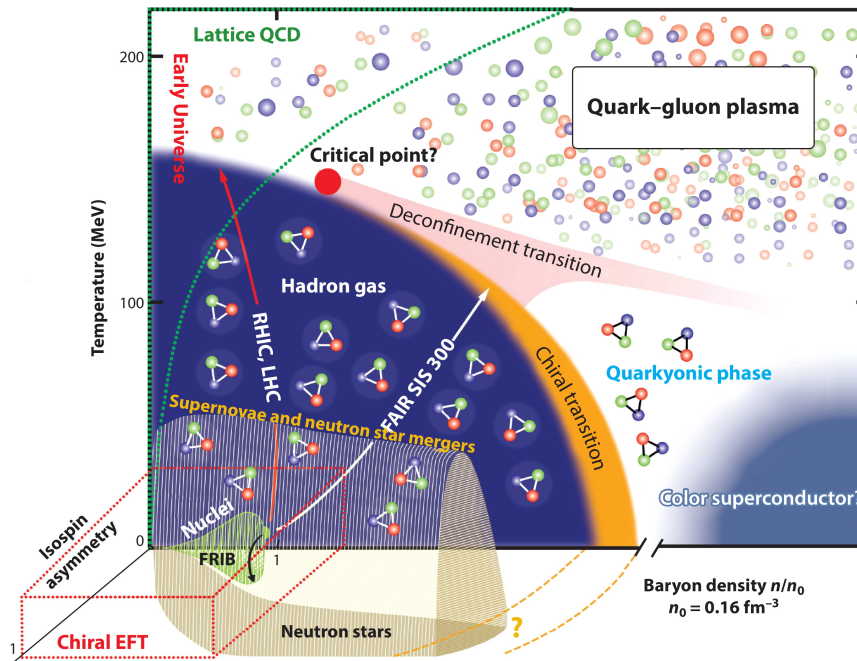


Figure 2.1: Phase diagram of quantum chromodynamics. Figure taken from Ref. [166].

the location of the phase transition and the maximum density in neutron star cores. The latter depends strongly on the EOS, which is itself only poorly known so far at densities well above saturation density. For astrophysical applications such as CCSNe and NSMs, the state of matter at finite temperatures is relevant as outlined in Fig. 2.1. In this Chapter, we describe different microscopic methods for calculating the equation of state of neutron stars and detail finite temperature effects as well as the liquid-gas phase transition that are relevant for astrophysical simulations.

2.1 Microscopic description of the equation of state

In this section, we introduce microscopic methods to calculate the equation of state. Since neutron stars and their astrophysical applications cover a broad range of densities, different methods have to be applied. Up to $1-2n_0$, chiral effective field theory (EFT) offers microscopic calculations of the EOS [4, 167, 168, 169, 170]. In the intermediate density regime, which also includes central densities of neutron stars, first results from functional Renormalization Group (fRG) became recently available [171, 172]. At very high density, perturbative QCD (pQCD) calculations are available [173, 174]. Currently, most EOS that are used to study cold isolated neutron stars are based on microscopic calculations up to nuclear densities and need a polytropic expansion [175, 4] or a speed of sound model [176, 177] to extrapolate the EOS up to central densities, where no reliable microscopic calculations for neutron star matter are available yet. These EOS are typically not suitable for simulations as they do not cover the required range for temperature and electron fraction.

2.1.1 Quantum chromodynamics and chiral symmetry

The underlying theory of the strong interaction is quantum chromodynamics (QCD). The fundamental degrees of freedom are quarks and gluons, which are the constituents of nucleons and the building blocks of hadrons in general. There are six different quark flavors in the standard model. The three light quarks up, down, and strange have masses from a few to roughly 100 MeV, while the three heavy quarks charm, bottom, and top cover a mass range from 1 to about 170 GeV [178]. In addition to a fractional electric charge, all quarks also carry a strong charge called color, where we distinguish between red, green and blue. Anti-quarks, which are the antiparticles of quarks, carry the corresponding anticolors. In nature, only systems that are color neutral have been observed so far. Color neutrality is realized by either a system made up of a quark and an anti-quark (mesons like the pion) or by three quarks (baryons like a nucleon). Gluons, which are also elementary particles, are gauge bosons that mediate the strong interaction.

The binding of nucleons to nuclei results from the interaction between nucleons that is a residual force of the strong interaction similarly as the van der Waals force for molecules. The coupling constant α_s of QCD is highly dependent on the energy [179, 180]. At high energies or equivalently small distances, α_s is sufficiently small making perturbative calculations possible. This behavior is called asymptotic freedom of QCD. At low energies or large distances, however, α_s is of order 1 and the system is highly non-perturbative. Direct calculations of nuclear forces from QCD in the energy scale of interest for nuclear physics are currently not feasible [181].

Based on Ref. [182], we briefly explain an important symmetry for low-energy nuclear physics, which is chiral symmetry. The QCD Lagrangian for the three light quark flavors up, down, and strange reads

$$\mathcal{L}_{\text{QCD}} = \sum_{i=1}^3 (\bar{q}_i i \not{D} q_i - m_i \bar{q}_i q_i) - \frac{1}{2} \text{Tr} G_{\mu\nu} G^{\mu\nu}, \quad (2.1)$$

with the quark fields q_i , their masses m_i , the covariant derivative $\not{D} = \gamma^\mu D_\mu = \gamma^\mu (\partial_\mu + igA_\mu)$, where g is related to the strong coupling constant via $\alpha_s = g^2/(4\pi)$ and A_μ are the gluon fields, and the gluon field

strength $G_{\mu\nu}$. The first term of Eq. (2.1) is the kinetic term and can be decomposed into left-handed and right-handed quarks leading to

$$\sum_{i=1}^3 \bar{q}_i i \not{D} q_i = \sum_{i=1}^3 (\bar{q}_{Li} i \not{D} q_{Li} + \bar{q}_{Ri} i \not{D} q_{Ri}) , \quad (2.2)$$

where $q_{Li} = 1/2(1 - \gamma_5)q_i$ and $q_{Ri} = 1/2(1 + \gamma_5)q_i$. From this splitting, one can see that the kinetic term is invariant under independent rotations of left-handed and right-handed quarks. This property is called chiral symmetry and is broken explicitly and spontaneously. The explicit symmetry breaking is due to the mass term in the QCD Lagrangian since it couples left-handed with right-handed quarks. Thus, chiral symmetry is broken explicitly due to non-zero quark masses. In addition, chiral symmetry is broken spontaneously as no parity doublets exist, i.e. there are no two particles with same mass which have the exact same quantum numbers except for parity. The difference of the particle masses leads to the symmetry breaking. Owing to Goldstone's theorem, every symmetry that is spontaneously broken generates a so-called Goldstone boson, which are massless excitations of the vacuum. In the case of chiral symmetry, the pions are the non-strange Goldstone bosons. In fact, pions are not massless because of the explicit breaking of chiral symmetry but have rather small masses compared to other hadrons, which is why they are called pseudo Goldstone bosons.

2.1.2 Chiral effective field theory

In this section, we give a brief introduction to chiral EFT based on Refs. [183, 184, 185, 181]. More details can be found there.

Chiral EFT is a systematic approach to calculate the interactions between nucleons, which was pioneered by Steven Weinberg in the early 1990's [186, 187, 188, 189]. At the low-energy scales of interest for nuclear matter, quarks and gluons are not resolved. Instead, nucleons and pions are the relevant degrees of freedom. Short-range interactions are described by contact interactions of two or more nucleons, while pion exchanges mediate the intermediate and long-range physics. The breakdown scale Λ_b is approximately the mass of the heavier ρ meson. Above this scale, new physics enters, that cannot be described by nucleons and pions. An effective theory is based on the separation of scales, which is in the case of chiral EFT the gap between the pion mass (soft scale $q \sim m_\pi \sim 140$ MeV) and the ρ meson mass (hard scale $\Lambda_b \sim 500$ MeV).

In order to come up with the expression of the nuclear force within an effective theory, one starts with the most general Lagrangian that is consistent with the symmetries of QCD as the underlying theory of the strong interaction. In the case of chiral EFT the Lagrangian reads

$$\mathcal{L}_{\text{EFT}} = \mathcal{L}_{\pi\pi} + \mathcal{L}_{\pi\text{N}} + \mathcal{L}_{\text{NN}} + \dots , \quad (2.3)$$

where $\mathcal{L}_{\pi\pi}$ accounts for interactions among pions, $\mathcal{L}_{\pi\text{N}}$ nucleon-pion interactions, and \mathcal{L}_{NN} nucleon-nucleon interactions. The Lagrangian itself has an infinite number of terms where two or more nucleons and/or pions contribute. The terms of the Lagrangian can be organized with the expansion parameter defined by the ratio of soft and hard scale, $Q \sim q/\Lambda_b$, which is approximately 1/3. In case of the Weinberg power counting scheme all interaction diagrams are ordered corresponding to Q^ν , where ν is an integer. There are also other alternative countings available like pionless EFT, where the only degrees of freedom are nucleons and the breakdown scale is of the order of the pion mass. The diagrams for the two-, three-, and four-nucleon force up to fifth order are shown in Fig. 2.2 [190]. At leading order (LO) with $\nu = 0$ are the most simple diagrams: a contact interaction and a pion exchange. The second order called next-to-leading order (NLO) has $\nu = 2$, followed by next-to-next-to-leading order (2 LO) with $\nu = 3$ and so on. Some diagrams are accompanied by so called low energy constants (LECs) that have to be fit to data,

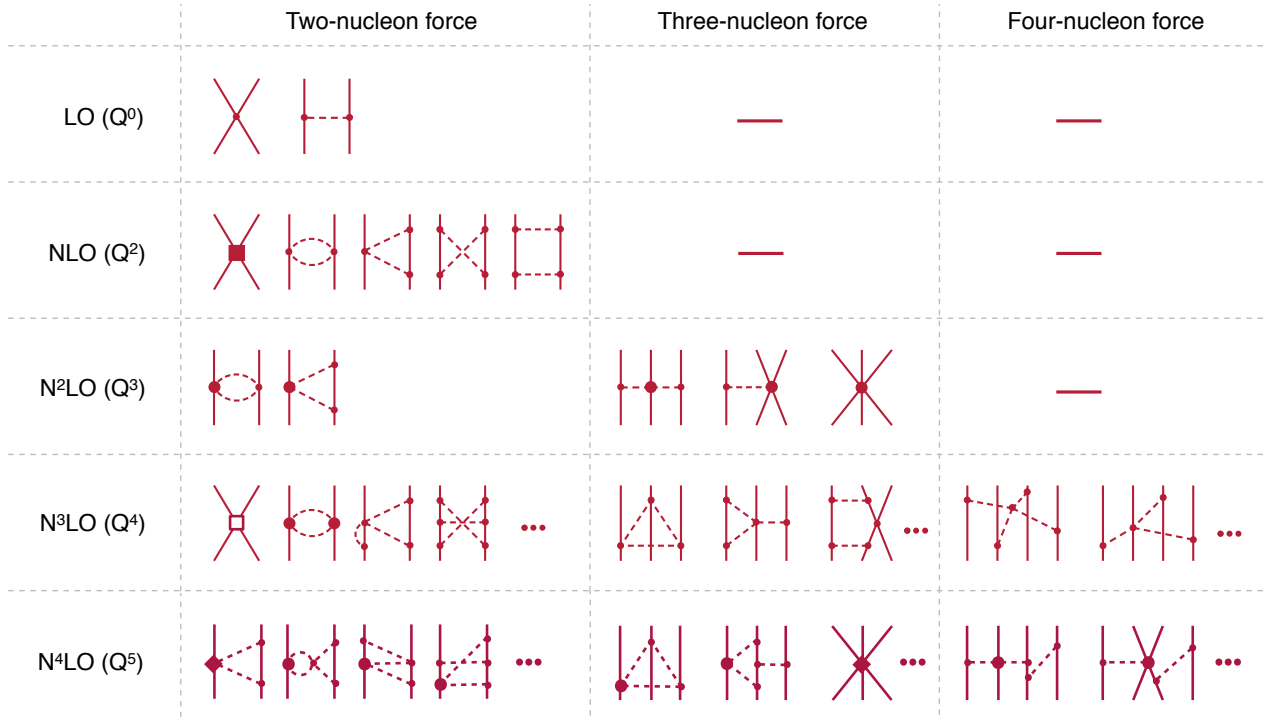


Figure 2.2: Diagrams of nuclear forces in chiral EFT ordered according to Weinberg power counting. Solid lines represent nucleons and dashed lines pions. Figure taken from Ref. [190].

e.g., few-body scattering data. The high-energy or short-distance information that cannot be resolved is contained in these LECs. Contributions from diagrams at higher orders become less and less important. In principle, infinite orders give the exact solution, which means that with increasing order the precision of the calculations can be systematically improved if the series converges. As visible in Fig. 2.2, many-body interactions arise naturally in the hierarchy and appear at subleading orders. One major advantage of chiral EFT is that one can systematically estimate uncertainties at a given order by evaluating what has been left out at higher orders.

Once the nuclear force is established from chiral EFT, one has to solve the Schrödinger equation to calculate the EOS. Here, many-body methods are required to solve this many-body problem. Various methods are available, amongst others Many-Body Perturbation Theory (MBPT) [191, 192, 193], in-medium Similarity Renormalization Group (IM-SRG) [194, 195], self consistent Green's function (SCGF) [196], quantum Monte Carlo (QMC) [197, 198, 199], and Coupled Cluster theory (CC) [200, 201]. Due to the breakdown scale of chiral EFT, calculations are only possible up to $1-2n_0$. In Fig. 2.3, we show results for the energy per particle of neutron matter from different chiral EFT interactions using various many-body methods [202]. In the left panel, all calculations are based on the EM 500 MeV N³LO NN interaction from Ref. [183]. The results with uncertainty bands are based on MBPT including N²LO 3N forces (red-dashed lines), N³LO 3N plus 4N forces (cyan band), and Renormalization Group (RG) evolved NN plus N²LO 3N forces. The size of the band is mainly given due to the uncertainties in the LECs of the 3N forces. In addition, results from SCGF, CC, and MBPT without uncertainties are displayed. The overlap of the different calculations demonstrates that constraints on the EOS for neutron matter do not strongly depend on the choice of the many-body method. In the right panel, complete N³LO calculations with NN, 3N, and 4N forces that employ different chiral interactions at N³LO are compared with each other. Other results at low density (NLO lattice, QMC) or based on phenomenological potentials lie within the uncertainty bands, which

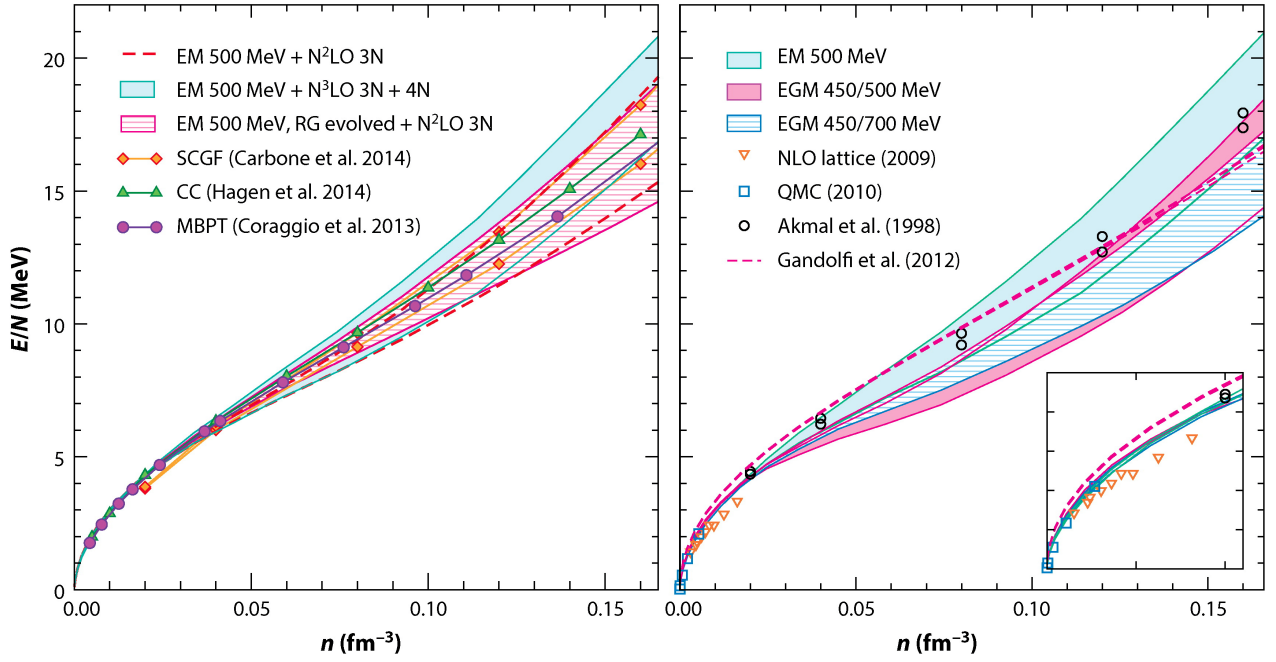


Figure 2.3: Energy per particle of neutron matter as a function of density for various many-body methods (left panel) and different chiral interactions (right panel). Figure taken from Ref. [202].

highlights the overall consistency of the calculations. We refer the reader to Ref. [202] for more details. More insights into current constraints on the EOS from chiral EFT are given in Sec. 3.1.

2.1.3 Functional Renormalization Group

Since chiral EFT constrains the EOS only for $n \lesssim 2n_0$, one needs another non-perturbative approach to describe matter at densities that are present in neutron star cores. Here, the densities are still too small for the perturbative regime due to the large coupling constant α_s . The functional Renormalization Group (fRG) provides such calculations from first principles via computing the effective potential of a field theory for a variable length scale [203]. The only input are fundamental parameters of QCD, which are the quark masses and the value of the strong coupling constant in the perturbative regime [204].

The fRG that is currently used to calculate the EOS for neutron stars uses the Wilsonian RG in combination with a functional approach for quantum field theory [205, 206, 207]. In general, an RG pictures the dependence of physical quantities from a length scale. The fRG introduces an effective average action which interpolates between microscopic (quarks and gluons) and macroscopic (nucleons) degrees of freedom and describes the evolution. One starts at high momenta k and evolves down to the infrared regime where $k = 0$. During this evolution, quantum and thermal fluctuations emerge that are absorbed into an effective Lagrangian. One step in the RG evolution is infinitesimal small such that a continuous change of the correlation functions is obtained for concatenation of many steps [208]. During the transition from the weakly coupled quark gluon plasma in the high energy regime to the strongly coupled nuclear matter at lower energies the relevant degrees of freedom, symmetries and many more can change [209]. The fRG is able to capture these effects and helps to identify the underlying physical processes. This framework is also applicable to finite temperature.

Constraints for the pressure and speed of sound of symmetric matter [171] as well as for the speed of sound of neutron star matter [172] at densities relevant for neutron stars became available only recently.

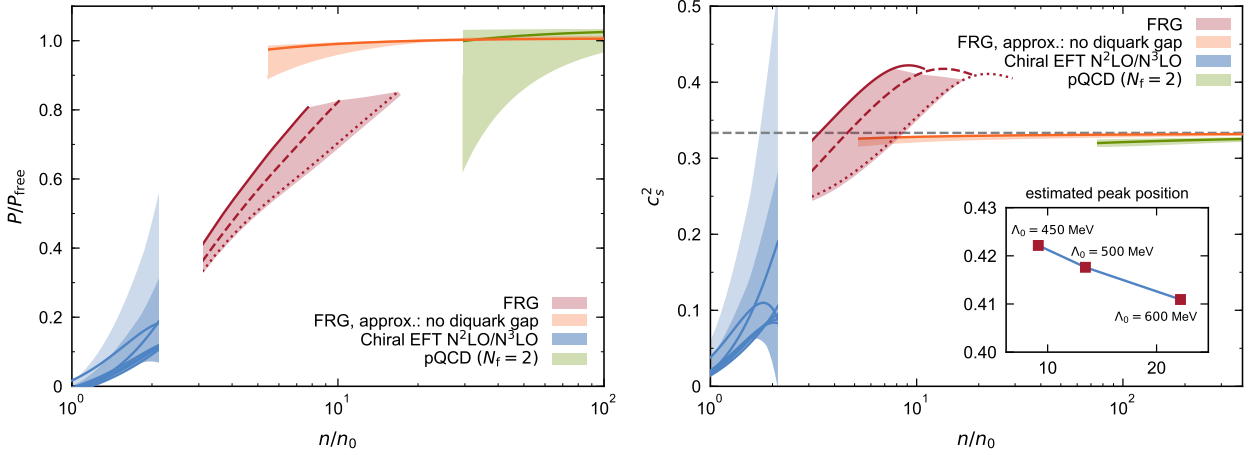


Figure 2.4: Results for the pressure and speed of sound as a function of density from fRG calculations compared to chiral EFT and pQCD computations. Figure taken from Ref. [171].

Both fRG calculations involve two massless quark flavors and provide an uncertainty due to the variation of the employed RG scheme. Other sources of uncertainties such as a third light quark or quark masses in general are not yet included. In Fig. 2.4, we show results from Ref. [171] for the pressure (left) and the speed of sound (right) as a function of density for symmetric matter. Notably, the calculations from fRG are consistent with chiral EFT computations at lower densities. The results indicate that the speed of sound has a maximum at intermediate densities $n \lesssim 10n_0$, which is in agreement with considerations of neutron-star masses [210, 177, 176, 13]. See Ch. 3 for implications on the EOS from the fRG results for symmetric matter.

2.1.4 Perturbative Quantum Chromodynamics

Calculations from perturbative QCD (pQCD) are reliable in the high-density regime with $n \gtrsim 50n_0$ [173, 211, 212] where quarks are deconfined. Here, perturbative approaches are possible due to asymptotic freedom. The current state-of-the-art are calculations in the weak-coupling expansion with contributions of a subset at $N^3\text{LO}$ of cold quark matter with massless quarks [211, 212]. Even though the densities of applicability are far above densities inside neutron stars, the pQCD results are often used to construct EOS for neutron star studies by interpolating between the chiral EFT band and the pQCD region [68, 213, 13, 214, 215, 216, 217, 218, 219, 220, 221, 222]. In Fig. 2.5 an example for this interpolation from Ref. [214] is shown. The blue bands refer to the uncertainty bands for the EOS from chiral EFT at nuclear densities and pQCD at high densities, where $\epsilon_0 \approx 150 \text{ MeV fm}^{-3}$ is the nuclear saturation energy density. Central energy densities as present in maximally massive non-rotating neutron stars are marked by the gray shaded region (ϵ_{TOV}). From observations, only the constraint of a two solar mass neutron star and the upper bound on the tidal deformability from GW170817 are imposed. The color coding corresponds to the maximum value of the speed of sound for each EOS. It has been predicted by Ref. [13], that smaller maximum values of the speed of sound are compatible with sizable quark matter cores of neutron stars. Note that in this study, the existence of massive neutron stars does not imply that the speed of sound has to have values above the conformal bound of $c_s^2 = 1/3$, which is approached from below in the high-density limit. This can be attributed to the fact that calculations from chiral EFT are only used up to saturation density in this study.

Topic of current research is the influence of the pQCD constraint on the EOS at neutron star densities. In

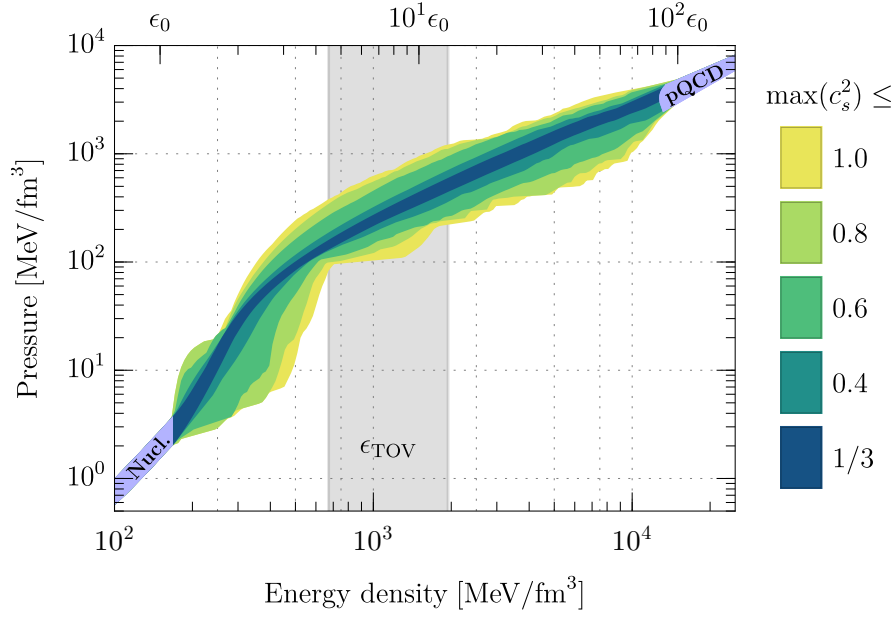


Figure 2.5: Interpolation of the equation of state between the chiral EFT and perturbative QCD calculations (blue bands). The color coding is due to the maximum value of the speed of sound of each EOS. The gray shaded region (ϵ_{TOV}) corresponds to the range of central energy densities inside maximally massive neutron star cores and $\epsilon_0 \approx 150 \text{ MeV fm}^{-3}$ refers to the nuclear saturation energy density. Figure taken from Ref. [214].

Refs. [223, 224] a sizeable impact at high densities is found whereas in Ref. [215] the influence on the EOS seems to be small. The size of the impact on the EOS beyond the constraints we have from astrophysical observations needs to be investigated more closely in the future.

2.2 Matter at nuclear densities

Nuclear matter is an idealized system of a homogeneous mixture of neutrons and protons that interact only via the strong force. Coulomb interactions are neglected. The system is extended to infinite mass number A and volume V , such that the total density $n = N/V$ is finite. The share of neutrons and protons is characterized by the proton fraction

$$x = \frac{n_p}{n_n + n_p} = \frac{n_p}{n} \quad (2.4)$$

or likewise the asymmetry parameter $\beta = (n_n - n_p)/n = 1 - 2x$. One extreme case of nuclear matter is pure neutron matter (PNM) where the proton fraction vanishes, $x = 0$. The energy per particle as well as the pressure of neutron matter is positive, which means that there are no self-bound states of neutrons only. Symmetric nuclear matter (SNM) is also of particular interest. Here, the density of neutrons is equal to the density of protons leading to $x = 1/2$. Symmetric matter is a bound system and exhibits an energy minimum at the so called saturation density n_0 . As a consequence, the pressure of SNM vanishes at this specific density. The energy per particle E/A of neutron matter and symmetric matter as a function of density are shown schematically in Fig. 2.6.

One can expand the energy per particle of nuclear matter with respect to the asymmetry parameter

around SNM as

$$\frac{E}{A}(n, \beta) \approx \frac{E}{A}(n, 0) + S(n)\beta^2, \quad (2.5)$$

where $E(n, 0)$ is the energy of SNM and $S(n)$ is called the symmetry energy. Here, we consider only contributions up to quadratic order. If higher orders are neglected, one can identify the symmetry energy as the energy difference between neutron matter and symmetric matter,

$$S(n) = \frac{E}{A}(n, 1) - \frac{E}{A}(n, 0). \quad (2.6)$$

Note that the symmetry energy is also given by the second derivative of E/A with respect to β , which is identical to the energy difference only if higher order terms in Eq. (2.5) are neglected. Expanding the energy per particle further in terms of the relative density difference $\chi = (n - n_0)/3n_0$ around n_0 yields

$$\frac{E}{A}(n, \beta) \approx -B + \frac{1}{2}K\chi^2 + (E_{\text{sym}} + L\chi)\beta^2. \quad (2.7)$$

Here, B is the binding energy and corresponds to the energy minimum of symmetric matter at saturation density. Since the pressure $P = n^2\delta_n E/A$ vanishes in SNM at saturation density, the next term in the expansion is of order χ^2 and is characterized by the incompressibility K . At saturation density, it is proportional to the second derivative of the energy per particle with respect to density,

$$K = 9 \left. \frac{\partial P}{\partial n} \right|_{n_0, \beta=0} = 9n_0^2 \left. \frac{\partial^2 E/A}{\partial n^2} \right|_{n_0, \beta=0}, \quad (2.8)$$

and describes how nuclear matter responds to compression. The incompressibility sets the steepness of the EOS. Soft EOS refer to small values for the incompressibility compared to stiff EOS with larger K . The leading terms of the density expansion of the symmetry energy $S(n)$ in Eq. (2.7) correspond to the symmetry energy coefficient $E_{\text{sym}} = S(n_0)$ and the slope parameter L . The latter is especially crucial in the description of neutron stars. It is proportional to the pressure of neutron matter at saturation density,

$$L = 3n_0 \left. \frac{\partial S}{\partial n} \right|_{n_0} = \frac{3}{n_0} P(n_0, \beta = 1), \quad (2.9)$$

and, thus, shows a high impact on the radius of neutron stars where large slope parameters lead to larger radii, e.g., [225]. The coefficients $n_0, B, K, E_{\text{sym}}$, and L are called nuclear matter properties and are depicted in Fig. 2.6.

The saturation density n_0 and binding energy B are very well constrained through the empirical saturation point with $n_0 = 0.164(7)$ and $B = 15.86(57)$ [169]. These ranges have been extracted by fitting selected Skyrme energy density functionals to properties of nuclei and nuclear matter [226] and include an additional systematic uncertainty for the binding energy [169, 227]. Microscopic calculations are able to reproduce these results within their uncertainties, which are in general rather large compared to the empirical saturation point [169, 228, 226].

Nuclear theory estimates for the incompressibility of SNM $K = 215 \pm 40$ MeV, which is a combination of the results from Refs. [228, 226, 169]. This is in agreement with information from heavy-ion collision (HIC) experiments [229]. The incompressibility can also be extracted from data of the isoscalar giant monopole resonance of finite nuclei, however, it is difficult to precisely capture finite-size effects. Here, experiments with doubly-magic nuclei like ^{208}Pb yield $K = 240 \pm 20$ MeV, but data from open-shell nuclei such as ^{120}Sn point towards lower values [230]. Similarly, there are also different predictions from nuclear models. Results using non-relativistic models like Skyrme forces have systematically lower values compared to relativistic mean-field models (see, e.g., Ref.s [231, 232] and references therein).

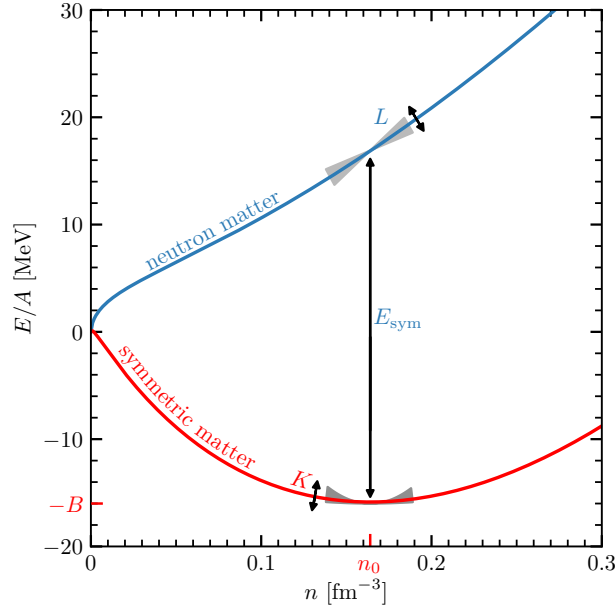


Figure 2.6: Energy per particle for pure neutron matter (blue) and symmetric matter (red) at zero temperature. At saturation density n_0 , the system is characterized by the nuclear matter properties, which are the binding energy B , the incompressibility K , the symmetry energy E_{sym} , and the slope parameter L .

Many efforts have been dedicated to determine the symmetry energy E_{sym} and the slope parameter L , which have a major impact in many aspects around neutron stars and astrophysical environments, see e.g. Ref. [233] for a recent review. In Fig. 2.7, results on the correlation between the symmetry energy parameters from theory as well as experiment are summarized. The tightest constraints come from microscopic calculations of neutron matter from Hebel *et al.* (H) [4], Drischler *et al.* (GP-B) [170], and Gandolfi *et al.* (G) [234]. The allowed region from the assumption that the unitary gas serves as a lower bound for the energy of PNM is also shown (UG) [235]. The boundary UG Analytic is stemming from the same work but includes some simplifications to obtain an analytical expression. In addition, Fig. 2.7 shows constraints from different experiments including mass measurements [236], giant dipole resonances (GDR) [237], neutron skin thickness of Sn [238], dipole polarizability of ^{208}Pb [239, 240], and HIC [241], which intersect in the white area. A constraint from isobaric analog states and isovector skins (IAS+ ΔR) is depicted as well [242]. Recently, the PREX collaboration extracted the neutron skin thickness of ^{208}Pb via parity violation in electron scattering [243]. The corresponding slope parameter $L = 106 \pm 37$ MeV [244], which is extracted from the correlation with the neutron skin thickness, is rather large compared to the microscopic calculations and not very tightly constrained.

2.3 Equation of state constraints from heavy-ion collision experiments

Constraining the EOS of neutron star matter via nuclear experiments is challenging since nuclei are mostly symmetric while matter in the core of neutron stars is very neutron rich. As a consequence, the sensitivity of the symmetry energy on the experimental data is oftentimes rather small leading to sizeable uncertainties, e.g., by extrapolating to small proton fractions. Here, we report on current experimental strategies with

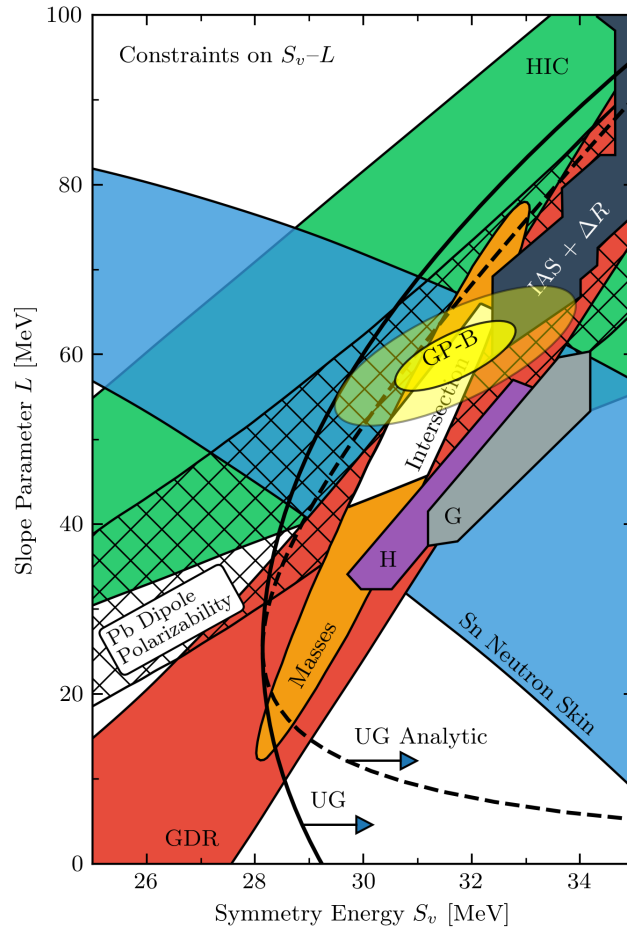


Figure 2.7: Correlation between the symmetry energy and the slope parameter for different microscopic calculations using chiral EFT and various experimental approaches. See text for details. Figure taken from [170], see also [225].

HICs to constrain the EOS of neutron star matter by combining results for symmetric matter and for the symmetry energy. This section is in parts based on Ref. [163], see also Ref. [245].

Over the last two decades, major experimental efforts have been devoted to measure the nuclear EOS with HIC experiments performed at relativistic incident energies [246, 247, 248]. These collisions of atomic nuclei form a hot, dense fireball of hadronic matter in the overlapping region, which expands in time and reaches the surrounding detectors as baryons and mesons. Due to the initial asymmetry of the non-central collision, the particles flowing out of the fireball in the expansion phase form an anisotropic flow. The distribution of these particles is largely determined by the compression achieved in the collision region, which in turn is given by the parameters of the EOS of the hot and dense nuclear matter produced during the collision. In addition, the flow asymmetry as well as the production of secondary particles is influenced by differences in neutron and proton potentials. The elliptic flow v_2 characterizes the azimuthal asymmetry and is the main observable to constrain the EOS of symmetric matter at supranuclear densities with HICs. It is given by the second coefficient of the Fourier expansion of the azimuthal distribution.

It has been shown that the elliptic flow of protons emitted at incident energies of several hundred MeV/nucleon offers the strongest sensitivity to the nuclear EOS [249, 246, 250], as evident from calculations

made with various transport models. This dependence on the nuclear EOS is predicted by QMD [249, 251, 250, 229] and Boltzmann-Uehling-Uhlenbeck [246] models. The origin of the phenomenon has been investigated in detail by Ref. [252]. As shown by Ref. [246], at higher beam energies between 1 and 10 GeV/nucleon, the sensitivity of the directed flow v_1 to the stiffness of the EOS of symmetric nuclear matter becomes comparable to that of v_2 . Overall, from HICs performed at incident beam energies of a few hundred MeV/nucleon up to around 10 GeV/nucleon, the flow data indicate an EOS for symmetric nuclear matter with an incompressibility K below 260 MeV, which is in agreement with chiral EFT calculations as shown in Sec. 2.2.

Experiments to constrain the symmetry energy and its density dependence are very challenging. With heavy-ion collisions the density-dependence of the symmetry energy can be studied where the probed density depends on the achieved compression originating from the collision energies. Since the neutron to proton asymmetry of the colliding ions is in general rather low, one often uses differences or ratios of observables to enhance the effect of the symmetry energy such as comparisons of the emitted neutrons and protons [253, 254]. At densities relevant for neutron stars, the elliptic flow ratio of particles with large isospin difference, ideally the ratio of neutrons over protons $v_2^{np} = v_2^n/v_2^p$ offers promising constraints [255, 256], see Ch. 5 for implications on the EOS. Recently, first results for the slope parameter with $42 < L < 117$ MeV from the S π rit collaboration became available [257]. They measure the spectra of charged pions that are produced in collisions of rare isotope Sn beams with an isotopic Sn target.

Transport models describe the evolution of the particles in HICs. Data from the experiment is then compared to the transport model calculations to constrain the EOS, which is an input of the transport codes. As a result, there are not only experimental uncertainties but also model dependencies that one has to account for to obtain reliable results.

2.4 Nucleon effective mass and thermal effects

In CCSN, temperatures of several tens of MeV can be reached [258, 18] and in NSMs even more [259, 260], see also Fig. 2.1. Thus, the temperature dependence of the EOS is key when studying these events. The so-called thermal index Γ_{th} is a useful tool to characterize thermal contributions to the equation of state and is defined as [261]

$$\Gamma_{\text{th}}(n, \beta, T) = 1 + \frac{P_{\text{th}}(n, \beta, T)}{\varepsilon_{\text{th}}(n, \beta, T)} = 1 + \frac{P(n, \beta, T) - P(n, \beta, 0)}{\varepsilon(n, \beta, T) - \varepsilon(n, \beta, 0)}. \quad (2.10)$$

Here, $\varepsilon_{\text{th}} = E_{\text{th}}/V$ denotes the internal thermal energy density and P_{th} the thermal pressure. For the right hand side of the equation, the pressure and the thermal energy density are split into a cold and a thermal part,

$$P = P_{\text{cold}} + P_{\text{th}}, \quad (2.11)$$

$$\varepsilon = \varepsilon_{\text{cold}} + \varepsilon_{\text{th}}. \quad (2.12)$$

Recently, the thermal index has been calculated using chiral EFT [262, 263]. In these calculations, it has been demonstrated that the nucleon effective mass $m^*(n, x)$ determines the thermal effects of the EOS to a high degree. That is, the expression for Γ_{th} of a free nucleon gas with a density-dependent but temperature-independent effective mass agrees accurately with the calculations of Γ_{th} from the thermal pressure and energy density derived from chiral EFT. The right panel of Fig. 2.8 shows the agreement between the thermal index obtained through direct calculations (solid lines) and the approximation with the effective mass (dashed lines) for PNM and a temperature of 30 MeV for two different interactions. The impact of 3N forces is also clearly visible and leads to a steep degrees of the thermal index.

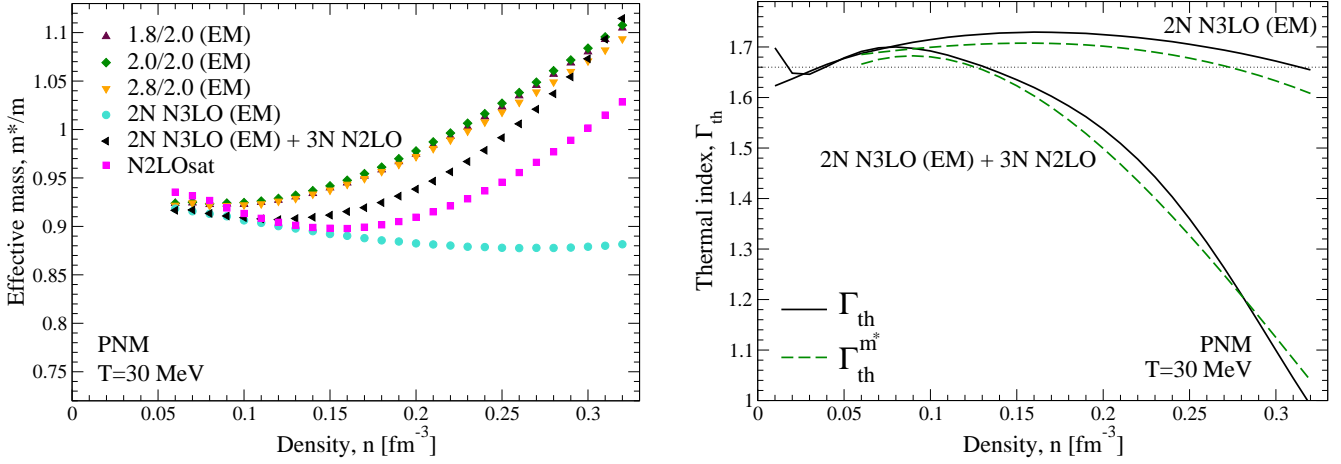


Figure 2.8: Effective mass and thermal index as a function of density for neutron matter from chiral EFT calculations. The different in interactions demonstrate that three-body forces lead to a significant increase of the effective mass after saturation density, which results in a decrease of the thermal index. Figure taken from Ref. [262].

The nucleon effective mass is based on a concept of Fermi liquid theory with quasiparticle/quasihole degrees of freedom close to the Fermi surface with an effective mass m^* . The energy and momentum dependence of the single-nucleon potential is mirrored by the effective mass. Due to the isospin dependence of the strong interaction, the effective masses for neutrons and protons differ. Results from chiral EFT indicate that the effective mass of neutrons m_n^* is larger at a given density than the effective mass of protons m_p^* [264, 262]. Novel microscopic calculations also show that the effective mass for both neutrons and protons first decreases with density, but after roughly saturation density it increases again and can even exceed the nucleon mass m [262, 263], see left panel of Fig. 2.8. This behavior is attributed to 3N forces. These findings have a significant impact on thermal effects and consequently on the dynamics in astrophysical applications, see Sec. 2.6.2.

The thermal index of a noninteracting nucleon gas with density-dependent effective mass $m_{n,p}^*(n)$ only depends on the effective mass and its density dependence. To derive the expression for Γ_{th} , we consider a canonical ensemble. This is a system with fixed particle number $A = N + Z$, where N, Z are neutron and proton number, respectively, in contact with an external heat bath at temperature T that determines the energy of the system. The Hamiltonian H is the sum over all single-particle energies ϵ_i and is given by

$$\begin{aligned}
 H &= \sum_{i=1}^N \left[\frac{k_{n,i}^2}{2m_n^*} + U(n) \right] + \sum_{i=1}^Z \left[\frac{k_{p,i}^2}{2m_p^*} + U(n) \right] \\
 &= \sum_{i=1}^N \frac{k_{n,i}^2}{2m_n^*} + \sum_{i=1}^Z \frac{k_{p,i}^2}{2m_p^*} + AU(n),
 \end{aligned} \tag{2.13}$$

with indices n, p for neutrons and protons, momentum \vec{k} , and density-dependent mean-field $U(n)$. To calculate the thermal pressure and energy density, we compute the partition function Z in the semi-classical

limit with the use of spherical coordinates and generalizations of Gaussian integrals:

$$\begin{aligned}
Z &= \text{Tr} e^{-\beta H} \\
&= \frac{1}{A! (2\pi)^{3A}} \int d^{3A}x d^{3A}k e^{-\beta \hat{H}} \\
&= \frac{V^A}{A! (2\pi)^{3A/2}} \frac{(m_n^*)^{3N/2} (m_p^*)^{3Z/2}}{3\beta A/2} e^{-\beta AU(n)},
\end{aligned} \tag{2.14}$$

where $\beta = 1/T$. Note that the integral over $d^{3A}x$ gives the volume to the A -th power.

With the partition function at hand, we calculate the energy density via the derivative

$$\begin{aligned}
\varepsilon &= \frac{E}{V} = -\frac{1}{V} \frac{\partial \ln Z}{\partial \beta} \\
&= nU(n) + \frac{3}{2}nT,
\end{aligned} \tag{2.15}$$

with the density $n = A/V$.

The pressure is proportional to the derivative with respect to the volume:

$$\begin{aligned}
P &= \beta^{-1} \frac{\partial \ln Z}{\partial V} \\
&= n^2 \frac{\partial U}{\partial n} + nT \left[1 - \frac{3}{2}n \left(\frac{1-x}{m_n^*} \frac{\partial m_n^*}{\partial n} + \frac{x}{m_p^*} \frac{\partial m_p^*}{\partial n} \right) \right].
\end{aligned} \tag{2.16}$$

The thermal pressure and energy density are obtained by subtracting the pressure and energy density at $T = 0$ from the expressions. Putting everything together, the thermal index of a nonrelativistic nucleon gas for arbitrary proton fraction x reads

$$\Gamma_{\text{th}}^{\text{n-rel}}(n, x) = \frac{5}{3} - \sum_{t=n,p} \frac{n_t(n, x)}{m_t^*(n, x)} \frac{\partial m_t^*(n, x)}{\partial n}. \tag{2.17}$$

The value $5/3$ is the thermal index of a free Fermi gas. Consequently, one can also interpret from the thermal index how close the system is to a free gas. Note that the thermal index only depends on the effective masses of neutrons and protons and their density dependence, but not on the temperature itself. According to Refs. [262, 263], this expression agrees remarkably well with the thermal index determined directly from chiral EFT. As a consequence, an accurate treatment of the effective mass in the EOS is necessary to capture thermal effects beyond the mean-field level. See Sec. 3.2.1 and 3.4.2 for the implementation of the effective mass based on chiral EFT and the implications for the thermal index.

2.5 Liquid-gas phase transition in nuclear matter

When a phase becomes unstable for certain thermodynamic conditions it undergoes a transition to a different phase. Such a phase transition is well known for a van der Waals fluid, where the interactions between molecules are repulsive at short distances and attractive at long distances. The interactions between nucleons in nuclei exhibit the same features, which lead to the assumption that a liquid-gas phase transition occurs in this system as well [265]. Since then, the existence of a liquid-gas phase transition has been confirmed in various experiments based on multifragmentation and fission [266, 267, 268]. To infer properties of the liquid-gas phase transition in nuclear matter from these experiments, one has to extrapolate

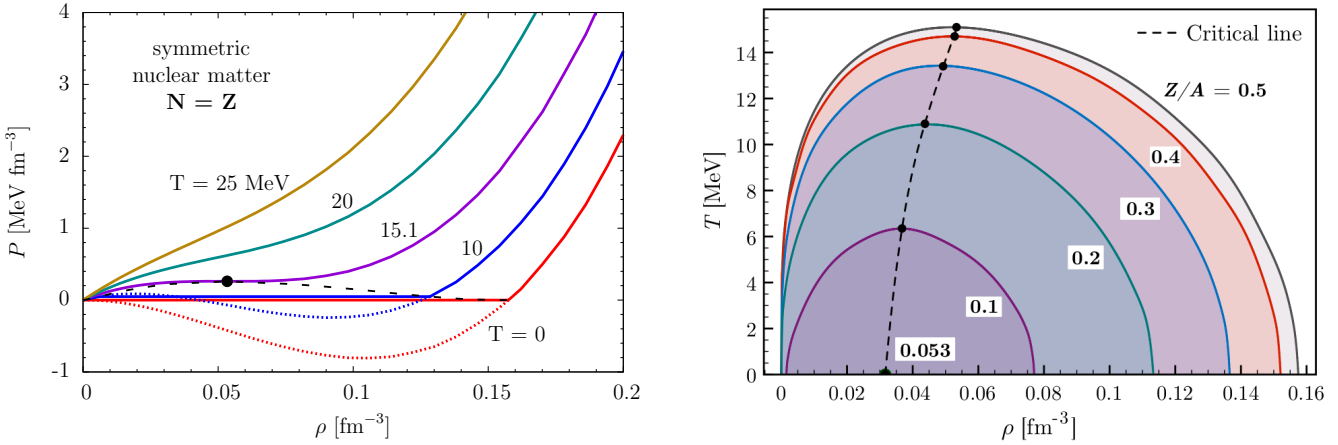


Figure 2.9: Left panel: Pressure as a function of density for several temperatures for symmetric matter. The solid lines correspond to the physical pressure obtained via a Maxwell construction. The dashed line is the coexistence curve with its maximum at the critical point (black dot). Right panel: Coexistence region for various proton fractions. The dashed line refers to the evolution of the critical points. Figure taken from Ref. [271].

from finite nuclei to infinite matter. The data predict the critical temperature to be $T_c \sim 15 - 20$ MeV, which is in agreement with microscopic calculations [269, 270, 271, 272].

The liquid-gas phase transition in nuclear matter can be visualized with the behavior of the pressure for different temperatures similar to the van der Waals case. The left panel of Fig. 2.9 shows pressure isotherms versus density for symmetric matter. Below the critical temperature there is an unphysical region, which is characterized by a negative slope of the pressure. The boundary of this area is called spinodal and is defined via $\partial_n P = 0$. Within the spinodal, matter is unstable and separates into two phases: a gas phase and a liquid phase. To obtain the physical pressure, one has to solve a system of equations, the so-called Maxwell construction:

$$\begin{aligned}
 P_g(n_g, x_g, T) &= P_l(n_l, x_l, T) , \\
 \mu_{n,g}(n_g, x_g, T) &= \mu_{n,l}(n_l, x_l, T) , \\
 \mu_{p,g}(n_g, x_g, T) &= \mu_{p,l}(n_l, x_l, T) ,
 \end{aligned}
 \tag{2.18}$$

where the subscript g and l stand for the gas and liquid phase. As a result of the Maxwell construction one obtains the coexistence curve, also called binodal (dashed line), which encloses the complete region of the phase transition, i.e. at its boundary the phase transition from gas to liquid starts and ends at a given temperature. The physical pressure is constant within the coexistence region (solid lines in Fig. 2.9). Matter that is located in the area between the binodal and the spinodal is metastable. With increasing temperature the densities of the coexistence curve n_g and n_l move closer together until they merge in the critical point at the critical temperature. Here, the pressure exhibits a saddle point. Above T_c matter is stable across all nuclear densities.

The right panel of Fig. 2.9 illustrates that the coexistence boundary shrinks when matter becomes more neutron rich. In the most extreme case for neutron matter there is no unstable region at all since the pressure increases monotonically even at zero temperature. When adding more protons to neutron matter, the pressure exhibits at some point an unstable region. This coexistence region then expands further until symmetric matter is reached. As a result of this behavior, also the critical temperature

increases when adding protons. For symmetric matter itself, the Maxwell construction simplifies as the chemical potentials of neutrons and protons are equal. One then has to solve the equations $P_g(n_g, 0.5, T) = P_l(n_l, 0.5, T)$, $\mu_g(n_g, 0.5, T) = \mu_l(n_l, 0.5, T)$ with the two unknowns n_g and n_l . See Ch. 4 for results on the phase transition for asymmetric nuclear matter with our EOS functional for astrophysical simulations.

2.6 Phenomenological equations of state for astrophysical applications

In astrophysical applications such as CCSNe or NSMs, the densities and temperatures that occur span several orders of magnitude. On top of that, the electron fraction covers everything from highly neutron-rich to slightly proton-rich matter. The conditions for the case of a one dimensional CCSN simulation of a $15 M_\odot$ progenitor star are illustrated in Fig. 2.10 for two EOS that have been widely used in these simulations, namely the Lattimer-Swesty (LS) EOS (left) and the Shen EOS (right). The color-coding represents the mass- and time-weighted occurrence of the specific conditions after core bounce, i.e. red indicates that the specific set of density and temperature (upper panels) or density and electron fraction (lower panels) are present for a large mass and/or a long time during the simulation. The density-temperature plane clearly shows that the temperature is proportional to the density. In particular, the dashed line represents the relation $T \sim n^{1/3}$. The proto-neutron star corresponds to the region with the highest density where most matter is accumulated as indicated by the dark red color. The maximum temperature does not appear in the center of the star as one might expect naively, but at its surface. Here, the shock wave is initiated from the core bounce and heats up the matter. The proto-neutron star has a relatively constant electron fraction of about 0.3 as neutrinos are trapped at high densities. With decreasing density in the mantle of the proto-neutron star, neutrinos that are produced in electron capture processes can escape rapidly resulting in a sharp decline of the electron fraction. Towards the shell structure of the progenitor star where nuclei are present at smaller densities, electron fractions increase again. The symbols correspond to the conditions where neutrinos decouple from matter with different symbols referring to different neutrino flavors and times after bounce. For more details see Ref. [273].

In Fig. 2.10 the influence of the EOS in the simulation is mostly visible in the density-temperature plane. The LS EOS has a smaller incompressibility compared to the Shen EOS and, thus, the proto-neutron star is more compact. This also results in higher temperatures and lower electron fractions in the core and causes larger maximum temperatures at the position of the core bounce as the same amount of material is squeezed into a sphere with smaller radius. The temperature at the surface of the star directly impacts the neutrino energies and with it the energy that is deposited behind the shock wave, which decides if it comes to an explosion or if the shock falls back onto the proto-neutron star and forms a black hole.

With the EOS being such a key factor in astrophysical applications, a microscopic description of matter at all occurring conditions is desirable. However, especially at densities above saturation density *ab initio* calculations for arbitrary proton fractions and finite temperature are not available yet even though there is some recent progress [263, 274]. As a consequence, phenomenological EOS are necessary for studying CCSN and NSM to describe the state of matter at all occurring conditions.

2.6.1 Traditional Equations of State

The two EOS that are most commonly used in CCSN simulations are the LS EOS and the Shen EOS, which have been constructed in 1991 and 1998, respectively. In recent years, many efforts have been undertaken to provide new EOS for astrophysical applications that are consistent with new constraints from microscopic calculations and observations. Here, we will give a brief overview of available phenomenological EOS and focus on the comparison of novel results from nuclear theory.

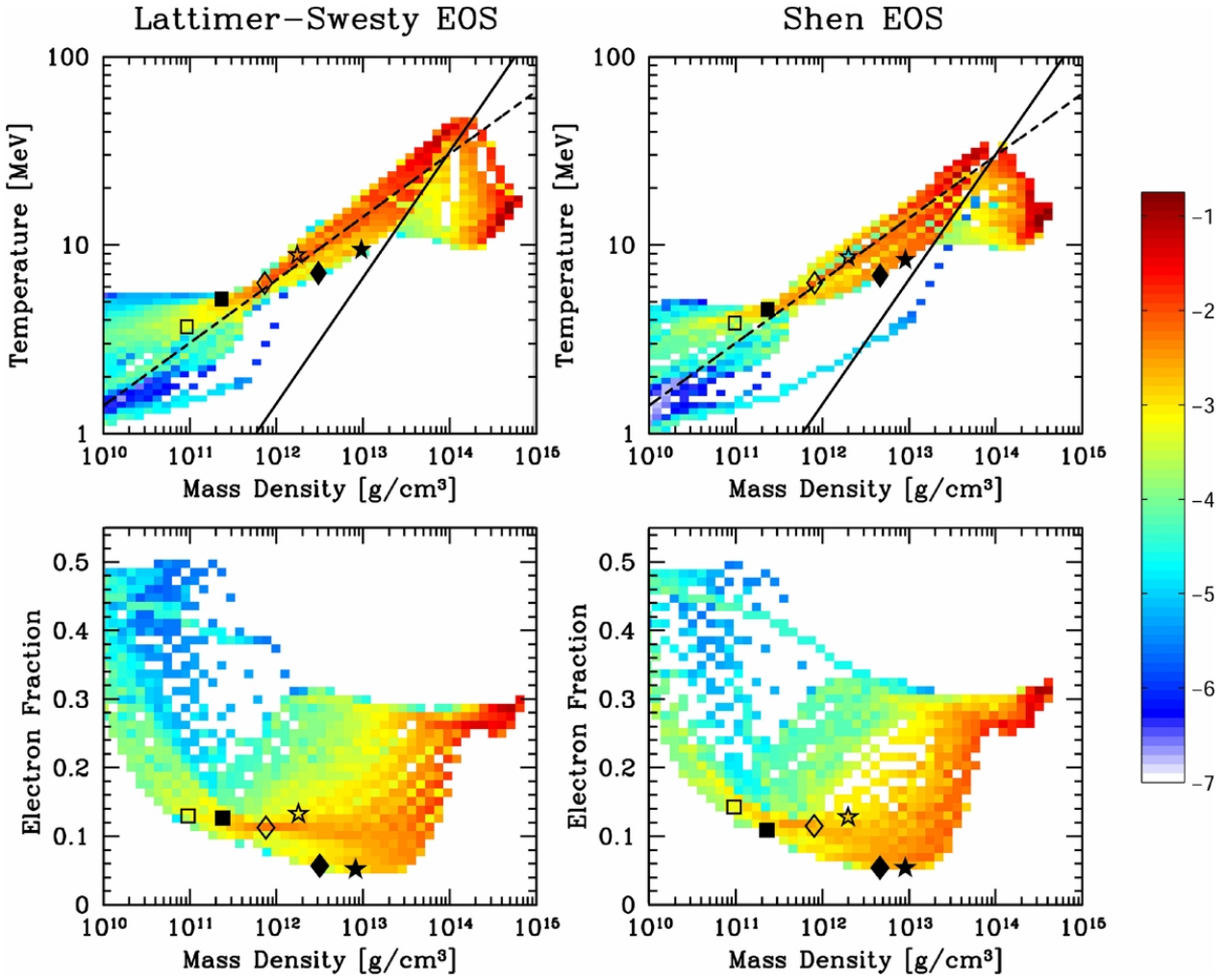


Figure 2.10: Conditions during a 1 dimensional supernova simulation of a $15 M_{\odot}$ progenitor star for the LS EOS (left) and Shen EOS (right). See text for details. Figure taken from Ref. [273].

Lattimer-Swesty Equation of State The LS EOS is based on a non-relativistic and momentum-independent Skyrme energy density functional in combination with a liquid-drop model [275, 276]. For inhomogeneous matter, the single nucleus approximation is used to describe heavy nuclei surrounded by alpha particles, unbound neutrons and protons as well as electrons, positrons, and photons. This means that one single heavy nucleus with varying mass and proton number represents all heavy nuclei. Similarly, the alpha particles account for all light nuclei with mass numbers smaller or equal than four. The distributions of the individual components is obtained in a thermodynamic consistent way via the minimization of the free energy density F , which is given by

$$F = F_o + F_{\alpha} + F_h + F_e + F_{\gamma}, \quad (2.19)$$

with the indices of outside (unbound) nuclei, alpha particles, heavy nuclei, electron-positron pairs, and photons, respectively. Nuclei are described within the compressible liquid-drop model [277], which considers nuclei as a drop of compressible nuclear matter. The free energy density of heavy nuclei consists of the bulk nuclear matter part together with contribution from Coulomb interactions, surface effects and

translational motion of the nucleus. In the LS EOS, the contributions from the nucleons inside nuclei and from the nucleon gas surrounding the representative heavy nucleus that also accounts for uniform matter are described by the same Skyrme energy density functional

$$\frac{E_{\text{bulk}}}{V}(n, x, T) = \sum_{t=n,p} \frac{\tau_t(n, x, T)}{2m_t^*(n, x)} + [a + 4bx(1-x)]n^2 + cn^{1+\delta} - xn\Delta. \quad (2.20)$$

The first term corresponds to the kinetic energy with the kinetic energy density τ and the nucleon effective mass m^* . The subscript denotes the isospin t , meaning that the sum runs over neutrons and protons. The Skyrme parameters a, b, c , and δ are fitted to the saturation density n_0 , binding energy B , the incompressibility K , and the symmetry energy E_{sym} . The last term in Eq. (2.20) takes into account the neutron-proton mass difference Δ .

The nucleon effective mass is parameterized using a simple density dependence with

$$\frac{1}{2m_t^*} = \frac{1}{2m} + \alpha_1 n_t + \alpha_2 n_{-t}, \quad (2.21)$$

where $-t$ denotes the nucleon with opposite isospin. The parameters α_i are fitted to specific values like the effective mass of neutron matter and symmetric matter at saturation density. While the description of the effective mass is included in the formulation of the LS EOS, in practice both fit parameters are set to zero leading to $m^* = m$ at all densities.

Within the LS EOS, alpha particles are described as a non-interacting gas where the particles themselves are considered as hard spheres with an effective volume $V_\alpha = 24 \text{ fm}^{-3}$. Electrons, positrons, and photons are assumed to be non-interacting and ultra-relativistic particles.

Shen et al. Equation of State The underlying theory of the Shen EOS is the relativistic mean-field (RMF) model [278, 279, 280], where nuclear interactions are described via meson exchanges of the isoscalar scalar σ meson, the vector ω meson, and the isovector vector ρ meson. To construct the EOS, one starts with the Lagrangian

$$\begin{aligned} \mathcal{L}_{\text{RMF}} = & \bar{\psi} \left(i\gamma_\mu \partial^\mu - M - g_\sigma \sigma - g_\omega \gamma_\mu \omega^\mu - g_\rho \gamma_\mu \tau_a \rho^{a\mu} - e\gamma_\mu \frac{1-\tau_3}{2} A^\mu \right) \psi \\ & + \frac{1}{2} \partial_\mu \sigma \partial^\mu \sigma - \frac{1}{2} m_\sigma^2 \sigma^2 - \frac{1}{3} g_2 \sigma^3 - \frac{1}{4} g_3 \sigma^4 - \frac{1}{4} W_{\mu\nu} W^{\mu\nu} + \frac{1}{2} m_\omega^2 \omega_\mu \omega^\mu + \frac{1}{4} c_3 (\omega_\mu \omega^\mu)^2 \\ & - \frac{1}{4} R_{\mu\nu}^a R^{a\mu\nu} + \frac{1}{2} m_\rho^2 \rho_\mu^a \rho^{a\mu} - \frac{1}{4} F_{\mu\nu} F^{\mu\nu}, \end{aligned} \quad (2.22)$$

with the nucleon field ψ , the photon field A^μ and the meson fields σ, ω^μ , and $\rho^{a\mu}$ with the corresponding nucleon mass M and meson masses m_σ, m_ω , and m_ρ . The coupling constants of the interactions between mesons and nucleons are denoted as g_σ, g_ω , and g_ρ , while g_2 and g_3 are the self-coupling constants for the σ meson and c_3 represents the self-coupling constant for the ω meson. All of these coupling constants and the meson masses are the parameters of the Lagrangian that are fitted to properties of finite nuclei. In the Shen EOS, the parameter set TM1 is used, see Tab. 2.1 for details. In the Lagrangian, $W^{\mu\nu}, R^{a\mu\nu}$, and $F^{\mu\nu}$ are the field tensors for the vector mesons ω and ρ and for the electromagnetic field, respectively, and are given by

$$\begin{aligned} W^{\mu\nu} &= \partial^\mu \omega^\nu - \partial^\nu \omega^\mu, \\ R^{a\mu\nu} &= \partial^\mu \rho^{a\nu} - \partial^\nu \rho^{a\mu} + g_\rho \epsilon^{abc} \rho^{b\mu} \rho^{c\nu}, \\ F^{\mu\nu} &= \partial^\mu A^\nu - \partial^\nu A^\mu. \end{aligned} \quad (2.23)$$

As a next step, the Dirac equation for nucleons and the Klein-Gordon equations for the mesons are derived, which refer to the equations of motion. In order to solve them for homogenous matter, a relativistic mean-field approximation is applied. In this approximation, the meson fields are assumed to be classical fields and the field operators σ, ω^μ , and $\rho^{a\mu}$ are replaced with their expectation values $\langle\sigma\rangle, \langle\omega^\mu\rangle$, and $\langle\rho^{a\mu}\rangle$. The effective mass is then defined as $M^* \equiv M + g_\sigma\langle\sigma\rangle$. The energy density of the RMF model is obtained with the well known Fermi-Dirac distribution. It consists of a kinetic term including the effective mass similar to the LS EOS, but with the relativistic single-particle energy $\epsilon_t = \sqrt{k^2 + M_t^*}$. The effective interaction consists of contributions containing the coupling constants, meson masses and meson fields derived from the Lagrangian.

The inhomogeneous phase where nuclei are present follows in many aspects a similar treatment as in the LS EOS, e.g. a single species to represent heavy nuclei together with a admixture of free nucleons and alpha particles. Leptons are again treated separately as non-interacting relativistic particles. An advancement compared to the LS EOS is the application of nucleon distribution functions within the Thomas-Fermi approximation [281]. The neutron distribution function is extended compared to the proton distribution function resulting in a neutron skin. The individual contributions of the different particle species are obtained via the minimization of the free energy that is given by the sum of bulk contributions from nucleons and alpha particles, the surface, and the Coulomb energy. Also in the Shen EOS, nucleons in the inhomogenous phase are described by the same RMF model as in uniform matter. The system is in uniform or non-uniform matter depending on which free energy density is lower. A Maxwell construction for calculating the coexistence boundary as in the LS EOS is not applied.

Further developments Since the construction of the LS and Shen EOS, a lot of effort has been put into generating new EOS for astrophysical applications as well as improving their description. Many of the more recently constructed EOS use an ensemble of nuclei in nuclear statistical equilibrium (NSE) instead of the SNA approximation to describe inhomogenous matter, such that the formation of light clusters is also accounted for, see, e.g., Ref. [282] for a description of the NSE model. Still, EOS for simulations are either based on the RMF framework or a Skyrme functional. For each of them, there are several parameter sets available that have been fitted in order to reproduce specific properties of nuclei. This results in a number of EOS that are based on the same theoretical groundwork, but differ considerably in their nuclear matter properties. In Tab. 2.1, we compare these nuclear matter properties of several EOS with the current estimates from nuclear theory, see Sec. 2.2 for details on chiral EFT results for nuclear matter properties. First, we list the properties for the LS and Shen EOS. The LS EOS is available for three different incompressibilities, namely 180, 220, and 375 MeV. We use the LS220 as the LS EOS with $K = 180$ MeV does not support a $2 M_\odot$ neutron star and $K = 375$ MeV does not agree with constraints for the incompressibility from nuclear theory. The SFHo and SFHx EOS are based on RMF and are constructed in order to agree with neutron star observations that were available at the time [283]. The DD2 [284] and FSUgold [285] EOS are two parametrizations for RMF models that have been used by Refs. [282, 286] to construct EOS for simulations. On the Skyrme side, Ref. [48] published various EOS with different Skyrme parameter sets, among others the SLy4 [287] parametrization.

In Tab. 2.1, we list the nuclear matter properties $n_0, B, K, E_{\text{sym}}$, and L as well as the nucleon effective mass at saturation density $m_{n_0}^*/m$ and the radius of a 1.4 solar mass neutron star $R_{1.4M_\odot}$. Note that the determination of the neutron star radius can differ slightly depending on the specific solver of the TOV equations. The binding energy and the incompressibility mostly agree with constraints from microscopic calculations across the listed EOS. The saturation density is for some RMF parametrizations quite low. Deviations from theory become larger for the symmetry energy and the slope parameter. Note that the published value of the symmetry energy for the LS EOS is about 1 MeV larger, because it is given as the energy difference of PNM to SNM. In Tab. 2.1, the symmetry energy for the EOS parametrizations are

EOS	n_0	B	K	E_{sym}	L	$m_{n_0}^*/m$	$R_{1.4M_\odot}$
Nucl. Theory	0.164(7)	15.86(57)	215(40)	32(3)	51(19)	0.9(2)	12(2)
LS220 [276]	0.155	16.00	220	28.6	73.7	1.000	12.7
Shen [278]	0.145	16.30	281	36.9	110.8	0.634	14.6
SFHo [283]	0.158	16.19	245	31.6	47.1	0.761	11.9
SFHx [283]	0.160	16.16	239	28.7	23.2	0.718	12.0
DD2 [284]	0.149	16.02	243	31.7	55.0	0.563	13.2
FSUgold [285]	0.148	16.27	230	32.6	60.4	0.611	12.5
SLy4 [287]	0.160	16.62	230	32.0	46.0	0.695	11.7

Table 2.1: Comparison of nuclear matter properties and radius of a typical neutron star for a selection of EOS that are available for astrophysical applications. The saturation density is given in fm^{-3} , binding energy B , incompressibility K , symmetry energy E_{sym} , and slope parameter L in MeV, and the radius of a $1.4M_\odot$ neutron star in km. Note that for all EOS, the value of the symmetry energy is determined via the second derivative of the energy per particle with respect to the asymmetry β . The effective mass is given at saturation density. For more details, see text.

defined via the second derivative of the energy per particle with respect to the asymmetry β . The LS220 has a rather low symmetry energy while its slope parameter is somewhat above the uncertainty estimate from chiral EFT. This combination leads to very low energies for PNM below the saturation density as visible in Fig. 2.11. Although SFHx has a similar symmetry energy, the slope parameter is very low, which results in the opposite behavior for E/N . The Shen EOS highly differs from microscopic calculations for many nuclear matter properties. The high slope parameter results in energies above the range of chiral EFT and in very large radii for neutron stars, see right panel of Fig. 2.11. The DD2 parameter set agrees quite well with chiral EFT constraints for the PNM energy and the mass-radius relationship for neutron stars is also reasonable. However, its effective mass is quite low at saturation density. In Ref. [288], a boundary of allowed $E_{\text{sym}} - L$ combinations is established from the assumption that the unitary gas is a lower bound for the PNM energy. The authors compared their constraint also to values from various astrophysical EOS.

Regarding the effective mass, the listed EOS use an isospin-independent parametrization, i.e. the effective mass for PNM and SNM are the same or only differ by the neutron-proton mass difference. Moreover, they use a mean-field description where the effective mass monotonically decreases with density. This is in contrast to results from chiral EFT, which show that in PNM the effective mass is larger compared to SNM and exhibits a turnover behavior after saturation density [262, 263], see also Sec. 2.4 for details.

2.6.2 Equation of state effects in core-collapse supernovae

There are numerous EOS available to study the impact in astrophysical applications such as CCSNe. However, most studies on EOS effects in simulations either compare EOS with different underlying theories, i.e. Skyrme functionals and RMF models or EOS that are based on the same framework but with parameter sets that differ for each nuclear physics input [282, 286, 283, 48]. As a result, it is not possible to test the sensitivity of a specific nuclear matter property in astrophysical simulations. As an exception, the LS EOS offers three individual EOS that are varied only for the incompressibility as discussed above. Only recently, in collaboration with Hannah Yasin, we carried out a study with EOS based on the LS EOS framework

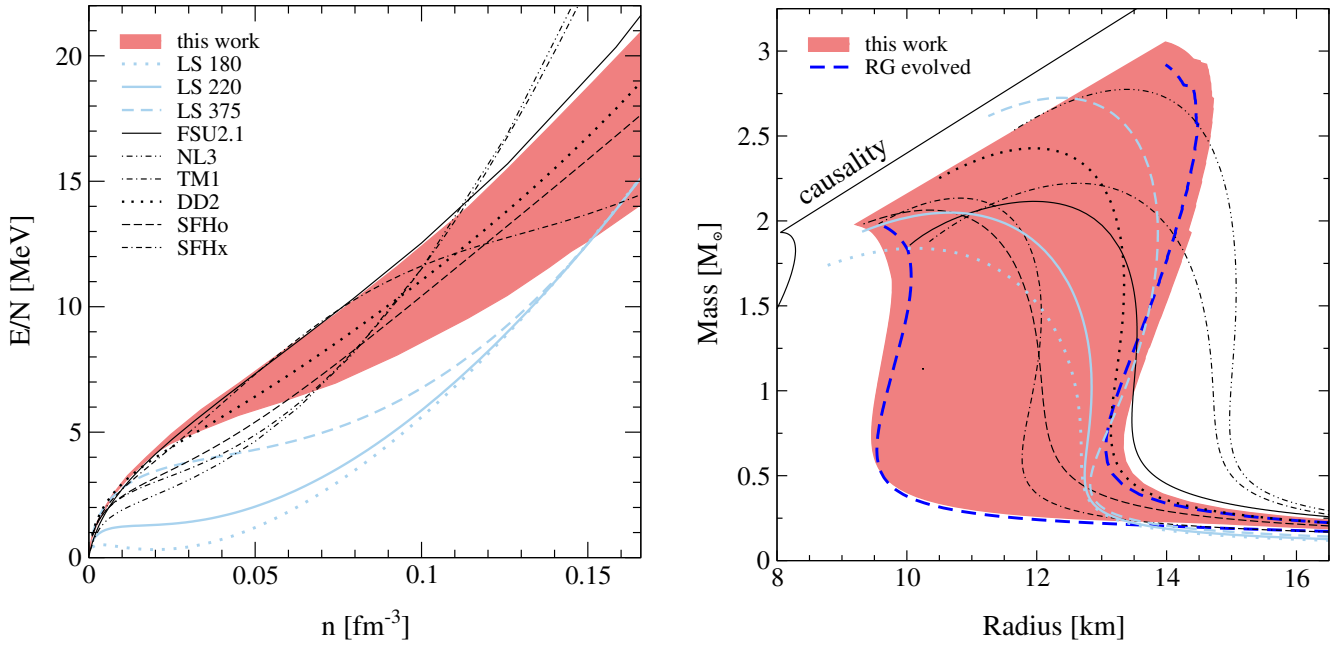


Figure 2.11: Energy per neutron as a function of density (left) and mass versus radius of neutron stars (right) from chiral EFT calculations in comparison with several astrophysical EOS. For the mass-radius relationship, the chiral EFT results are extended to higher densities via a polytropic expansion, see Ref. [4]. Figure taken from Ref. [46].

where we individually varied the nucleon effective mass, incompressibility, symmetry energy, and saturation point to determine the influence of these parameters in CCSNe [47].

The key finding of the study is that the PNS contraction is governed by the nucleon effective mass. This is illustrated in Fig. 2.12, which shows the PNS radius and the shock radius as a function of time. We compare the LS220 and Shen EOS with several EOS with varied effective mass and nuclear matter properties that are constructed using the SRO code [48, 289]. To this end, we refit the Skyrme parameters of the LS EOS to build EOS with effective masses with $m^*/m = 0.8$ at n_0 labelled $m_{0.8}^*$ and $m^*/m = 0.634$ (value of Shen) labelled m_s^* where all other nuclear matter properties are unchanged. On top of the effective mass, we vary the incompressibility $(m^*, K)_s$, the symmetry energy $(m^*, E_{\text{sym}})_s$, both $(m^*, K, E_{\text{sym}})_s$, and the saturation point. The latter is labelled SkShen. We find that in general lower effective masses lead to larger thermal contributions to the pressure that directly follow the behavior of the thermal index from Eq. (2.17). As a consequence, the PNS contraction slows down, which results in smaller temperatures at the PNS surface. This ultimately ends up in a deceleration of the shock evolution to a later explosion due to less energetic neutrinos.

From Fig. 2.12 it becomes clear that other nuclear matter properties do not effect the PNS contraction to a large extend as all EOS with the same effective mass end up in a narrow band of approximately the same radius. However, changing these parameters to the values of Shen further retards the shock evolution, such that the simulation with SkShen does not show an explosion, similar to the original Shen EOS. We conclude that nuclear matter properties are key when studying the PNS and high-density evolution in simulations rather than the underlying theory of the EOS.

From the comparison of the EOS available for astrophysical applications we have seen that many are not consistent with modern constraints from nuclear theory and observations. Especially novel results of the

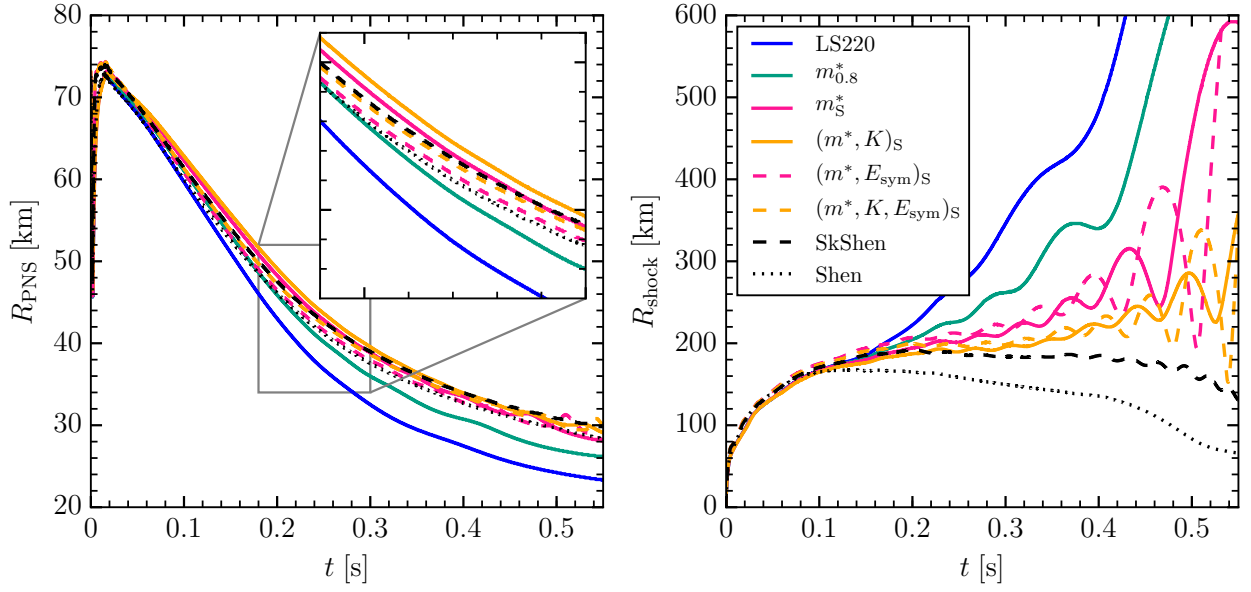


Figure 2.12: Evolution of the proto-neutron star and shock radius as a function of time for the LS220 and Shen EOS and several EOS that individually vary the nucleon effective mass and nuclear matter properties between the LS220 and Shen values. Figure adapted from Ref. [47].

nucleon effective mass detailed in Sec. 2.4 highly differ with the parametrizations used in current EOS. In this thesis, we incorporate these constraints including recent results from gravitational wave detection and NASA's NICER mission in a new EOS functional (see Ch. 3) and start to build EOS for astrophysical simulations with it (see Ch. 4). Moreover, we also study the influence of complementary information on the EOS from heavy-ion collisions (see Ch. 5).

3 New equations of state constrained by nuclear physics, observations, and functional Renormalization Group calculations

In the last years, novel constraints became available from both nuclear theory calculations and astrophysical observations, which ruled out many EOS that are suitable for astrophysical applications like CCSN and NSM simulations. In this chapter, we develop a versatile EOS functional that incorporates recent microscopic results for the nuclear matter properties and the nucleon effective mass. To this end, we fit the parameters of the EOS functional to theoretical calculations at low and high densities as well as observational constraints from mass measurements, GW170817, and NICER. By varying all parameters of the functional within the allowed uncertainties, we obtain comprehensive uncertainty bands for the EOS and for neutron star properties. This framework also allows us to easily include new constraints and update the uncertainties according to it.

This work is performed in collaboration with Corbinian Wellenhofer and published in Ref. [73]. It provides the basis for new EOSs of hot and dense matter for CCSN and NSM simulations, see Ch. 4.

3.1 Overview of equation of state constraints

In this section, we briefly summarize presently available constraints on the EOS of dense nuclear matter. First, we examine constraints from nuclear physics on the properties of neutron-rich matter at densities up to 1–2 times nuclear saturation density. Then, we discuss high-density constraints inferred from recent neutron star observations. Finally, we discuss the results of a recent fRG study of SNM at higher densities.

3.1.1 Constraints from nuclear physics

Here, we summarize constraints on the EOS from nuclear theory and experiment. In particular, we discuss constraints on various characteristic parameters of the EOS around saturation density n_0 : the binding energy B , the incompressibility K , the symmetry energy coefficient E_{sym} , and the slope parameter L . (The effective mass is discussed in Sec. 3.2.1.) Further, we discuss constraints from theoretical calculations on the EOS of PNM.

Neutron matter constraints

The modern approach to the description of the strong interaction at nuclear energy scales is based on chiral effective field theory (EFT) and renormalization group (RG) methods [184, 290, 181]. From general EFT convergence restrictions as well as regulator and many-body convergence considerations, the viability of this approach is restricted to densities $n \lesssim 2n_0$. The theoretical uncertainties in current implementations of chiral interactions in a given many-body framework arise from the interplay of finite-regulator artifacts, many-body and EFT truncation errors, and parameter-fitting ambiguities.

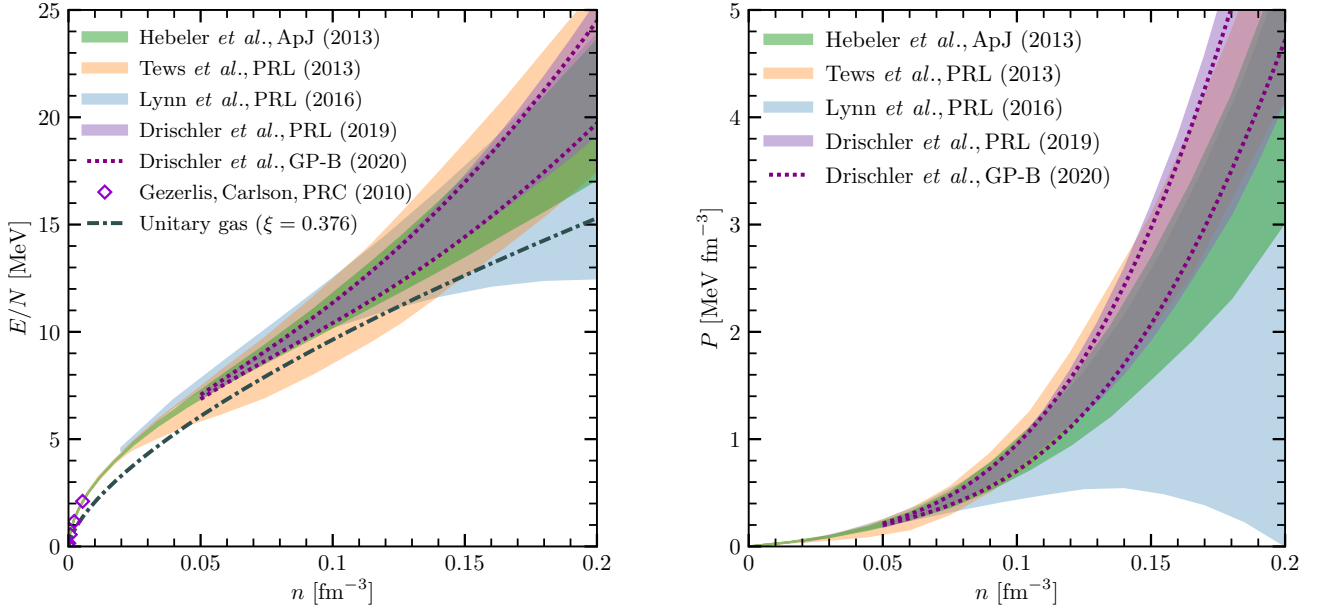


Figure 3.1: Energy per particle E/N (left panel) and pressure P (right panel) of PNM as a function of density n from various many-body calculations with chiral EFT interactions [4, 167, 168, 169, 170]; see text for details. In the left panel, we also show the low-density quantum Monte Carlo results by Gezerlis and Carlson [291] as well as the conjectured lower bound given by the energy per particle of a unitary Fermi gas of neutrons [235].

Because nuclear forces are weaker in PNM, the theoretical uncertainties are under better control compared to SNM. In Fig. 3.1 we compare the results for the energy per particle and pressure of PNM obtained from several recent nuclear many-body calculations with chiral EFT interactions. The results by Hebeler et al. [4], Tews et al. [167], and Drischler et al. [169, 170] are based on many-body perturbation theory, while the results by Lynn et al. [168] were obtained from auxiliary-field diffusion Monte Carlo computations using local chiral interactions. In each case, the results include uncertainty estimates, shown as bands in Fig. 3.1. These are based on EFT truncation errors and different regulators in Refs. [168, 169, 170], while they are mainly due to uncertainties in the low-energy couplings that enter three-nucleon forces in Refs. [4, 167]. The uncertainty band of Drischler et al. PRL (2019) [169] is based on simple EFT truncation errors. The results of Drischler et al. GP-B (2020) [170] are constructed from the same calculations (from Ref. [169]) but based on a Bayesian uncertainty analysis using Gaussian processes, which leads to a very similar band for the combined GP-B (450) and (500) results. One sees that while overall the results from these calculations are in good agreement, the uncertainties become sizable for densities $n \gtrsim n_0$.

At densities near and above saturation density the uncertainties associated with the effective description of the nuclear interactions dominate over many-body truncation effects. At low densities $n \ll n_0$, the nuclear interactions are less intricate, but here the many-body accuracy may be inflicted by the sensitivity to large-scattering length physics. Still, as shown in Fig. 3.1, the various chiral EFT-based many-body calculations discussed above are in reasonable agreement with the low-density results from precise quantum Monte Carlo computations by Gezerlis and Carlson [291].

Finally, in Fig. 3.1 we also show the energy per particle of a unitary Fermi gas of neutrons $E_{\text{UG}}(n) = \xi E_{\text{FG}}(n)$, where $E_{\text{FG}}(n)$ is the free neutron gas energy and the Bertsch parameter is $\xi \approx 0.376$ [292]. In Ref. [235], it was argued that $E_{\text{UG}}(n)$ can be used as a lower bound for the PNM energy. As seen in Fig. 3.1,

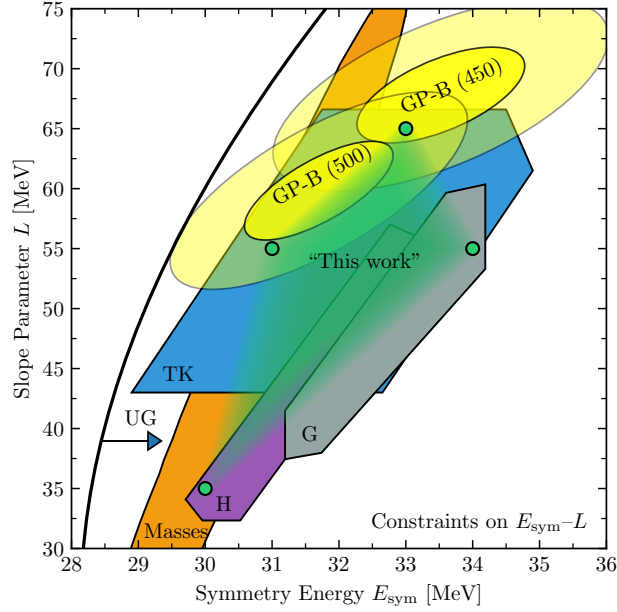


Figure 3.2: Theoretical constraints on the symmetry energy E_{sym} and the slope parameter L from Refs. [4, 234, 167, 170], see text for details. Also shown are constraints extracted from fits to nuclear masses (orange band) [236] and the conjectured unitary gas (UG) bound [235]. The corners (green dots) of the green shaded area (“This work”) correspond to the four representative (E_{sym}, L) pairs adopted in this work. The figure is adapted from Refs. [225, 170] using the Jupyter notebook provided in Refs. [297, 170].

the unitary gas bound reduces the uncertainties in the results by Tews *et al.* [167] and Lynn *et al.* [168], while the ones by Hebeler *et al.* [4] and Drischler *et al.* [169, 170] are unaffected.

Symmetry energy constraints

The symmetry energy coefficient E_{sym} and slope parameter L are crucial for a variety of phenomena in nuclear physics and astrophysics, ranging from nuclear masses [236], neutron skins and the dipole polarizability [239, 293, 294, 295, 296], to heavy-ion collisions [241], and CCSNe [47, 48], see also Sec. 2.2. In particular, the neutron star radius scales with the pressure of PNM at saturation density [225, 87], *i.e.*, with the L parameter.

Many experimental and theoretical efforts have been undertaken to constrain the symmetry energy. In Fig. 3.2, we show results for the correlation between E_{sym} and L obtained from the microscopic PNM calculations by Hebeler *et al.* (H) [4], Tews *et al.* (TK) [167], and Drischler *et al.* [GP-B (450), GP-B (500)] [170] discussed above. In addition, we show results from auxiliary-field diffusion Monte Carlo calculations by Gandolfi *et al.* (G) [234]. The uncertainties in the H, TK, and G results were obtained by using various (chiral) two- and three-nucleon interactions. The TK results involve the largest uncertainties, which stems in part from larger variations of the low-energy couplings in three-nucleon forces. In the GP-B case, we show results obtained from chiral potentials with two different cutoffs, GP-B (450) and (500), where in each case the uncertainties were obtained from a Bayesian analysis using Gaussian processes of the fixed-cutoff EFT systematics. Note that in Fig. 3.1 the two GP-B bands are combined in one single band.

The region of (E_{sym}, L) values spanned by these theoretical results overlaps with the constraints extracted

from various experiments; see, e.g., Refs. [225, 298, 170]. As an example, in Fig. 3.2 we show the constraint extracted from nuclear masses [236]. Also shown is the conjectured unitary gas (UG) bound [235]. The theoretical constraints (H,K,TK,GP-B) are all consistent with the UG constraint.

For the EOS constructed in this work we choose four representative (E_{sym}, L) pairs that lie within the combined theoretical constraints (H,K,TK,GP-B):

$$(E_{\text{sym}}, L)/\text{MeV} \in \{(30, 35), (31, 55), (33, 65), (34, 55)\}. \quad (3.1)$$

These four pairs are shown as green dots in Fig. 3.2 and the (green shaded) region spanned by them is labeled “This work”. Note that we exclude very large symmetry energies and slope parameters to avoid having too many EOSs exceed the PNM uncertainty band shown in Fig. 3.1. Even with (E_{sym}, L) values inside the GP-B region our EOS functional can still lead to PNM properties, which are incompatible with the theoretical PNM uncertainty band. This is because of higher-order terms in the density behavior. A detailed study of the EOS and neutron star properties associated with our four (E_{sym}, L) pairs is provided in Sec. 3.3.1.

3.1.2 Constraints from neutron star observations

Neutron star observations play a crucial role in constraining the dense-matter EOS. In particular, mass measurements of two-solar-mass neutron stars [6, 7, 8] have narrowed the uncertainties in the neutron star mass-radius relation considerably. To support neutron stars of such mass the EOS cannot be too soft, which challenges neutron star models that include substantial portions of exotic condensates or deconfined quark matter. The present lower bound for the maximal mass M_{max} is given by the mass of the heaviest observed neutron stars: PSR J0740+6620 with a mass of $M = 2.14^{+0.20}_{-0.18} M_{\odot}$ [8] at the 2σ level measured using relativistic Shapiro delay. This is in line with the radio-timing observation of the pulsar J0348+0432 with $M = 2.01 \pm 0.04 M_{\odot}$ [7]. In our work, we use the averaged lower bound of $M = 1.965 M_{\odot}$ as a constraint for the lower bound of the maximal mass.

The observation of the first NSM GW170817 [70, 299] by LIGO/Virgo together with the observation of the corresponding kilonova AT2017gfo and the short gamma-ray burst GRB170817A [300] led to many efforts to infer an upper bound on the maximum neutron star mass M_{max} from the remnant behavior. The suggested limits are generally in the range $M_{\text{max}} \lesssim 2.3\text{--}2.4 M_{\odot}$ [88, 301, 302, 89, 90, 303, 304, 305], which would rule out overly stiff EOS, in addition to the soft EOSs ruled out by the two-solar-mass constraint.

Even with a relatively narrow range on the maximal mass, the radius of a typical neutron star with $M = 1.4 M_{\odot}$ is uncertain, with a typical conservative range $10 \lesssim R/\text{km} \lesssim 14$; see, e.g., Refs. [4, 177, 176, 71]. Recently, a major step toward precise radius measurements was made by the NICER collaboration [121, 122], which simultaneously determined the radius and mass of PSR J0030+0451 via x-ray pulse-profile modeling.

Implications of this measurement on the EOS have been studied by Raaijmakers et al. [125] by applying two parametrizations for the neutron star EOS (in β -equilibrium): a piecewise polytropic (PP) model [4] and a speed of sound (CS) parametrization [176]. Raaijmakers et al. [126] performed a joint analysis of these models to infer implications on the EOS from the NICER measurement, GW170817, and the $2.14 M_{\odot}$ mass measurement. Their results for the pressure as a function of density are shown in Fig. 3.3 (green bands). While the PP and CS bands are consistent with each other, the PP model allows stiffer EOSs for densities $n \lesssim 4n_0$ and in general smaller maximal densities. Consequently, the M - R relation of the CS model involves somewhat smaller radii compared to the PP model. In our work, we use the combined PP and CS bands by Raaijmakers et al. [126] as a constraint for our EOS parametrization.

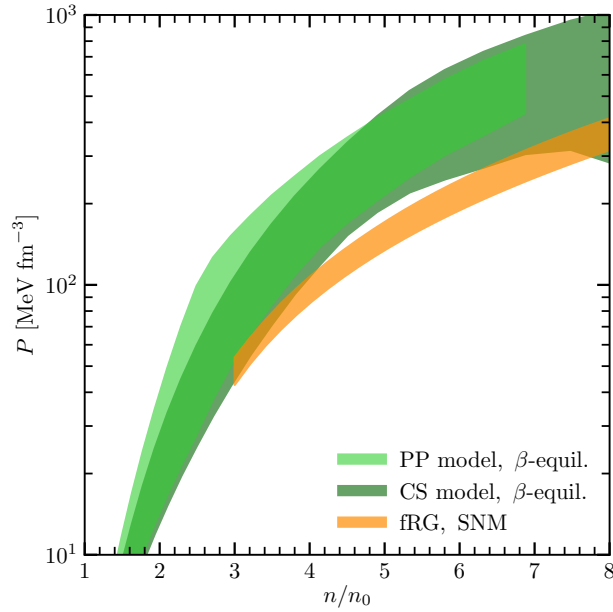


Figure 3.3: Constraints on the pressure of neutron star matter as a function of density n/n_0 (green bands) from a joint analysis [126] of the $2.14 M_\odot$ mass constraint, GW170817, and the NICER results, obtained using two different EOS models: piecewise polytropes (PP) and speed of sound model (CS). The bands are for the 95% credible regions. Also shown are the results for the pressure of SNM (orange band) from the fRG study of Ref. [171].

3.1.3 Theoretical calculations at high densities

The ultra-high-density regime ($n \gtrsim 50n_0$) of the EOS corresponds to deconfined quark matter. Perturbative QCD provides the expansion of the EOS about the high-density limit [211]. This expansion can be used to construct astrophysical EOSs from interpolating between the chiral EFT band for the EOS at nuclear densities and the perturbative QCD region [306, 68], see also Sec. 2.1.4. Here, we incorporate high-density constraints from neutron star observations explicitly. Moreover, we base the high-density extrapolation of the EOS of SNM on a recent fRG calculation at more relevant densities. Therefore, in our case the perturbative QCD expansion does not provide significant additional constraints on the dense-matter EOS.

At present no reliable and accurate method exists for computing the properties of strongly interacting matter at densities $n \gtrsim 2n_0$ (apart from the perturbative QCD limit). However, a notable step towards systematic high-density calculations was made by Leonhardt *et al.* in Ref. [171]. Starting from the QCD action, they use the fRG to derive a low-energy quantum effective action with effective four-quark interactions and diquark degrees of freedom, see Sec. 2.1.3 for details. The uncertainties in the results for the (zero-temperature) EOS of SNM from this approach have been estimated in terms of their RG scale dependence. Other sources of error are, e.g., due to neglected quark flavors and higher-order interaction effects.

The fRG results of Leonhardt *et al.* [171] for the pressure of SNM are shown in Fig. 3.3 (orange band). They span a band from $n = 3n_0$ to $n = 10n_0$. The band lies mostly below the observational neutron star matter constraints from Raaijmakers *et al.* [126], with small overlaps for densities near $n = 3n_0$ and near $n = 8n_0$. Note that the fRG band is significantly smaller than the neutron star matter bands of Raaijmakers *et al.*. We will see that neutron star constraints, in particular the maximum mass constraint with $M_{\max} \geq 1.965 M_\odot$, tend to favor a pressure of SNM that lies somewhat above the fRG band either

near $n = 3n_0$ or near $n = 8n_0$. Nevertheless, we find several EOS that are consistent with neutron star observations and for which the pressure of SNM lies within the fRG band for $n \gtrsim 5n_0$.

3.2 New Equation of state functional

We now come to the construction of a new EOS functional that takes into account the constraints from nuclear physics, neutron star observations and high-density QCD calculations. In Sec. 3.2.1, we examine recent microscopic calculations of the neutron and proton effective mass $m_{n,p}^*(n, \beta)$ in SNM ($\beta = 0$) and PNM ($\beta = 1$), and introduce a convenient parametrization of $m_{n,p}^*(n, \beta)$ to be implemented in our EOS functionals. The construction of the EOS functional is the subject of Sec. 3.2.2.

3.2.1 Temperature dependence and nucleon effective mass

Recently, Carbone and Schwenk [262] computed the finite-temperature EOS of PNM and SNM from chiral EFT interactions using the self-consistent Green's function method. In addition, they also calculated the effective masses $m_{n,p}^*(n, \beta = 0, 1)$. Based on these results they showed that the thermal index Γ_{th} obtained from the pressure and the energy density, see Eq. (2.10), can be accurately parametrized in terms of the effective mass, via the form given by Eq. (2.17). Recent microscopic neutron-matter calculations in many-body perturbation theory have confirmed this result [263]. Therefore, a reliable implementation of the effective masses of neutrons and protons $m_{n,p}^*(n, \beta)$ is crucial to capture thermal effects in astrophysical applications.

To this end, we introduce an effective mass parametrization that fits the results for $m_{n,p}^*(n, \beta = 0, 1)$ at densities $n \lesssim 2n_0$ from Ref. [262] based on the N³LO NN potential from Ref. [183] and N²LO 3N interactions constructed in Ref. [307]. The behavior of $m_{n,p}^*(n, \beta)$ at higher densities is uncertain. We explore different scenarios in this regime. Our effective mass parametrization as a function of density is given by

$$\begin{aligned} \frac{m_t^*}{m} = & 1 + \left(\alpha_1 n_t + \beta_1 n_{-t} + \alpha_2 n_t^{4/3} + \beta_2 n_{-t}^{4/3} + \alpha_3 n_t^{5/3} + \beta_3 n_{-t}^{5/3} \right) \frac{1}{1 + e^{5n}} \\ & + \left(\epsilon_t \frac{n_t}{n} + \epsilon_{-t} \frac{n_{-t}}{n} - 1 \right) \frac{1 - e^{-10n}}{1 + e^{-5(n-n_{\text{off}})}}, \end{aligned} \quad (3.2)$$

where the nucleon with opposite isospin is denoted by $-t$. The six parameters α_i, β_i with $i \in (1, 3)$ are fit to the SNM and PNM results of Ref. [262]. The factor $1/(1 + e^{5n})$ (sigmoid function) has the effect that the fitted part goes to zero with increasing density. The high-density behavior of $m_{n,p}^*(n, \beta)$ is then fixed by the parameters ϵ_t and ϵ_{-t} as well as by the offset n_{off} of the (modified) logistic function $(1 - e^{-10n})/(1 + e^{-5(n-n_{\text{off}})})$. For instance, for $\beta = 1$ the high-density limit of the neutron effective mass is given by ϵ_n , and for $\beta = 0$ the nucleon effective mass approaches the value $(\epsilon_n + \epsilon_p)/2$. Note that this implies that the high-density limit of the effective mass is constant and, hence, the thermal index is $\Gamma_{\text{th}} \rightarrow 5/3$; see Eq. (2.17). The correct ultrarelativistic limit is $\Gamma_{\text{th}} \rightarrow 4/3$, but this matters for the nucleonic part of the EOS only for densities far above those relevant for neutron stars.

In Fig. 3.4, we show the results for the nucleon effective mass in PNM and SNM from Ref. [262] and three representative effective mass parametrizations based on Eq. (3.2). In the PNM case we show the results for the neutron effective mass $m_n^*(n, \beta = 1)$. At low densities, the effective mass is a decreasing function of density (see also the recent auxiliary field diffusion Monte Carlo computations [308]), but starting at around nuclear saturation density it increases with density for both PNM and SNM mainly due to 3N forces. The effective mass in PNM is larger than the one for SNM (see also Ref. [264]) and for densities $n \gtrsim 1.5n_0$ it exceeds the bare nucleon mass.

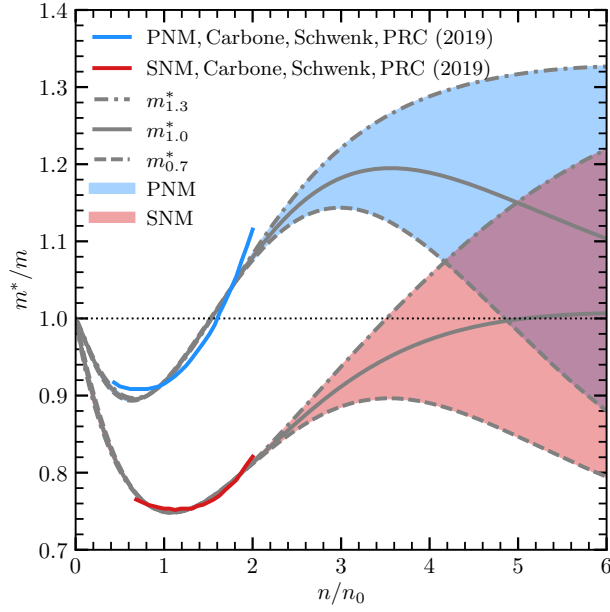


Figure 3.4: Effective mass m^*/m as a function of density n/n_0 for PNM and SNM. The blue (PNM) and red (SNM) solid lines up to $n/n_0 = 2$ show the results of Carbone and Schwenk [262]. The gray lines (connected by colored bands) correspond to the three representative effective mass parametrizations employed in this work. The associated high-density limits are given by $m^*/m \rightarrow 0.7$ (dashed lines), $m^*/m \rightarrow 1.0$ (solid lines), and $m^*/m \rightarrow 1.3$ (dash-dotted lines).

From Eq. (2.17) it follows that the thermal index is $\Gamma_{\text{th}} < 5/3$ in the density region where the effective mass increases with density. Depending on the form of the increase at higher densities it may even be that $\Gamma_{\text{th}} < 1$ at high densities. This would imply a negative thermal expansion coefficient [309], with a negative thermal pressure contribution so that the pressure at finite temperature would be smaller than the pressure at $T = 0$. While such a feature is not unphysical in general, it would still be somewhat peculiar to have $\Gamma_{\text{th}} < 1$ in nuclear matter. We therefore restrict the high-density extrapolations of the effective mass to a form that ensures that $\Gamma_{\text{th}} > 1$.

In this work, we set $n_{\text{off}} = 0.7 \text{ fm}^{-3}$ and restrict ourselves to cases where $\epsilon_t = \epsilon_{-t} = \epsilon$ in Eq. (3.2) such that the effective mass has the same high-density limit in SNM and PNM. We employ three representative values of the high-density limit, i.e., $\epsilon \in \{0.7, 1.0, 1.3\}$, denoted by $m_{0.7}^*$, $m_{1.0}^*$, and $m_{1.3}^*$ in Fig. 3.4. As seen in Fig. 3.4, these three scenarios span a reasonably wide range for the behavior of the effective mass at high densities. Note also that the fit below twice saturation density is unaffected by the high-density behavior (with our parametrization this holds true even for more extreme values of ϵ). Consequently, our effective mass scenarios only affect thermal properties at very high densities.

Regarding isospin-asymmetric nuclear matter, our effective mass parametrization ensures that the neutron effective mass $m_n^*(n, \beta)$ increases with β and satisfies $m_n^*(n, \beta) > m_p^*(n, \beta)$, in agreement with theoretical results [310, 311, 312, 313, 314]. In contrast to $m_n^*(n, \beta)$, which is constrained by fits to microscopic calculations for both PNM and SNM, in our approach the β dependence (at finite n) of the proton effective mass $m_p^*(n, \beta)$ is an outcome of the fit of $m_p^*(n, 0) = m_n^*(n, 0)$ to SNM after $m_n^*(n, 1)$ has been fit to PNM. We found that the β dependence of both m_n^* and m_p^* is largest at $n \approx 3 - 4n_0$ (the high-density limit ϵ is β independent). Moreover, our parametrization leads to a β dependence of $m_p^*(n, \beta)$ that is decreased compared to that of $m_n^*(n, \beta)$, which is consistent with the results from Refs. [311, 312]. For $m_{0.7}^*$, the

proton effective mass decreases with β at low densities $n \lesssim n_0$ and increases for $n \gtrsim n_0$. In the $m_{1.0}^*$ and $m_{1.3}^*$ case the proton effective mass decreases with β at all densities, with the decrease being significantly more pronounced for $m_{1.3}^*$. Here, the behavior for $m_{1.0}^*$ and $m_{1.3}^*$ is more in line with nuclear theory results [311, 312]. Future work may involve the construction of improved EOS functionals that incorporate additional theoretical constraints on the β dependence of $m_p^*(n, \beta)$.

3.2.2 Equation of state functional

We now introduce the new EOS functional that forms the basis for the investigations carried out in the remainder of this work. The microscopic results for the relation between the effective mass $m_t^*(n, \beta)$ and the thermal index $\Gamma_{\text{th}}(n, \beta)$ make clear that a reasonable approach to the temperature dependence of an effective EOS functional is to use a T -dependent kinetic term with density-dependent effective mass and a T -independent interaction part. This is also supported by the microscopic nuclear-matter calculations of Refs. [309, 315, 314, 262, 263], where it was found that the T dependence of the interaction contribution in many-body perturbation theory is small compared to the one of the noninteracting contribution.

In the usual (Skyrme) energy density functionals, the interaction part is modeled as a finite polynomial in fractional powers of density; see, e.g., Refs. [316, 48]. By construction, the high-density behavior of a polynomial EOS ansatz involves a highly fine-tuned balance between different density powers. In certain cases, i.e., for some judicious choices of the density powers, a reasonable high-density extrapolation can result from fits to microscopic calculations at nuclear densities [316, 317]. However, for the systematic construction of EOS functionals constrained by nuclear physics, neutron star observations, and high-density QCD calculations, a polynomial ansatz can clearly encounter difficulties.

We therefore choose a form of the interaction part that ameliorates this fine tuning. For the internal energy density as a function of density $n = n_n + n_p$, proton fraction $x = n_p/n$ and temperature T we use the following form:

$$\frac{E}{V}(n, x, T) = \sum_t \frac{\tau_t(n, x, T)}{2m_t^*(n, x)} - xn\Delta + \sum_i \left[\frac{a_i}{d_a + n^{(\delta_i-2)/3}} + \frac{4b_i x(1-x)}{d_b + n^{(\delta_i-2)/3}} \right] n^{1+\delta_i/3}. \quad (3.3)$$

Here, the second term gives the rest mass contribution (modulo the neutron mass energy), with Δ being the neutron–proton mass difference. The first term corresponds to the kinetic part of the internal energy density; it is modeled as a noninteracting gas of neutrons and protons with effective masses $m_{n,p}^*(n, x)$ given by Eq. (3.4). That is, the term τ_t is given by¹

$$\tau_t(n, x, T) = \frac{1}{2\pi^2} \int_0^\infty dp p^4 \frac{1}{1 + \exp \left[\frac{1}{T} \left(\frac{p^2}{2m_t^*(n, x)} - \tilde{\mu}_t(n, x, T) \right) \right]}, \quad (3.4)$$

where the auxiliary chemical potential $\tilde{\mu}_t(n, x, T)$ is defined via

$$n_t = \frac{1}{2\pi^2} \int_0^\infty dp p^2 \frac{1}{1 + \exp \left[\frac{1}{T} \left(\frac{p^2}{2m_t^*} - \tilde{\mu}_t \right) \right]}. \quad (3.5)$$

The $T \rightarrow 0$ limit of the kinetic part is given by $\tau_t(n, x, 0) = (3\pi^2 n_t)^{5/3}/(5\pi^2)$. The role of the auxiliary chemical potential is similar to the one in many-body perturbation theory at finite temperature [318]. The true chemical potential is obtained from the thermodynamic potential corresponding to the variables

¹We use the nonrelativistic quasiparticle dispersion relation for all densities. The high-density behavior of our EOSs is fit to observational and fRG constraints, so only thermal effects at very high densities are affected by this approximation, which is, however, a minor effect in comparison to the effective-mass uncertainties in that regime.

(n, x, T) , i.e., the free energy. Since the interaction part and the effective masses are T independent, the free energy is obtained by substituting the kinetic part of E/V with the free energy density of a (nonrelativistic) noninteracting gas of neutrons and protons with effective masses $m_{n,p}^*(n, x)$.

The third term in Eq. (3.3) is the interaction part. The crucial feature of the interaction part is that it is based on rational functions instead of density monomials. While the parameters a_i and b_i with $i \in (1, 4)$ are fit to low- and high-density results as specified below, the density exponents δ_i as well as d_a and d_b are not fit parameters but set to specific values. We choose two different sets for δ_i :

$$\delta_{k_F} = (3, 4, 5, 6), \quad \delta_n = (3, 6, 9, 12). \quad (3.6)$$

For the choice δ_{k_F} , the density exponents in the numerators of the interaction part are $(1, 4/3, 5/3, 2)$, corresponding to integer powers of the Fermi momentum k_F at zero temperature. The choice δ_n corresponds to integer powers of n in the numerators. The density dependence of the denominators is chosen such that in the high-density limit the interaction part becomes proportional to $n^{5/3}$. Note that the density dependence in the ultrarelativistic limit is $\sim n^{4/3}$, but this matters only for densities far above those relevant for neutron stars; see Sec. 3.2.1. The purpose of the denominators is to mitigate the fine-tuning between the different parts of the interaction term such that the EOS functional is stable under variations of the fit input. For a given choice of δ_i , the fit performance of the EOS functional is controlled by the two offset parameters d_a and d_b . We set $d_a = d_b = d$ and use for d the following values:

$$d_{k_F} \in \{1, 3, 5, 7\}, \quad d_n \in \{0.2, 0.4, 0.6, 0.8\}. \quad (3.7)$$

These choices provide a reasonably wide range of different density behaviors, as examined in detail below. The smaller values of d for δ_n are mandated by the large density exponents, i.e., the suppression of higher density powers must set in earlier there. We note that removing the restriction $d_a = d_b$ has no notable impact on our results.

We fix the eight parameters $a_{1,2,3,4}$ and $b_{1,2,3,4}$ by matching to the following input:

- the energy per particle of PNM at $n = 0.05 \text{ fm}^{-3}$, determined by the QMC result from Ref. [291] as $E/N(0.05 \text{ fm}^{-3}) = 2.1 \text{ MeV}$,
- the nuclear matter properties $(n_0, B, K, E_{\text{sym}}, L)$,
- the pressure of PNM at $n = 1.28 \text{ fm}^{-3} \approx 8n_0$,
- the pressure of SNM at $n = 1.28 \text{ fm}^{-3} \approx 8n_0$.

Here, the six nuclear-density inputs (first two items) are varied according to their uncertainties, as examined in Sec. 3.1.1. The high-density input for the pressure of PNM and SNM is taken such that the resulting EOS is consistent with constraints from neutron star observations (Sec. 3.1.2) and the pressure of SNM is in reasonable agreement with the fRG results (Sec. 3.1.3) (we allow a 10% deviation from the fRG band to account for further fRG uncertainties).

The results for the energy per particle E/A of PNM and SNM obtained for one particular input set are shown in Fig. 3.5. Here we set the nuclear matter properties to $(B, K, E_{\text{sym}}, L) = (15.29, 255, 30, 35) \text{ MeV}$ and $n_0 = 0.157 \text{ fm}^{-3}$, the pressure at $n = 1.28 \text{ fm}^{-3}$ to 600 MeV fm^{-3} for SNM and to 1000 MeV fm^{-3} for PNM, and use the effective mass scenario $m_{1.0}^*$. Figure 3.6 shows the corresponding results for the pressure P and the square of the speed of sound c_s^2 (in units where $c = 1$), which is given by the derivative of the pressure with respect to energy density. Variations of the input are investigated in Sec. 3.3. For each δ_i set from Eq. (3.6), we show the results for the smallest and the largest d in the corresponding set of possible d values of Eq. (3.7). One sees that the nuclear-density input has the effect that for densities up to roughly twice saturation density the functional is not very sensitive to the values of δ_i and d . At intermediate densities $2n_0 \lesssim n < 8n_0$, different choices of δ_i and d result in the following systematics:

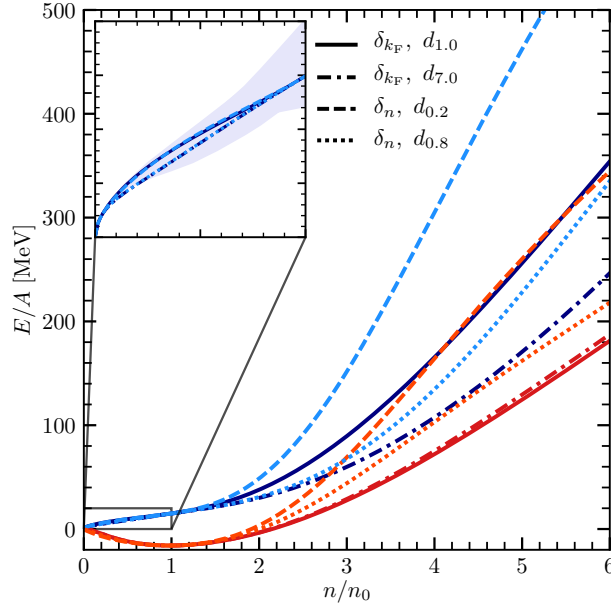


Figure 3.5: Results for the energy per particle of PNM (blue) and SNM (red) as a function of density n/n_0 obtained from the two δ_i sets with the minimal and maximal value of the corresponding d . We use the same set of low- and high-density fit points for all depicted EOS. The light blue band in the inset corresponds to the combined chiral EFT results from Fig. 3.1.

- $\delta_{k_F}, d = 1.0$ (solid lines): We find a soft EOS for SNM indicated by the rather small values of the square of the speed of sound, which only barely exceeds $c_s^2 \approx 0.5$. In the case of PNM, the EOS is stiffer to support a $2 M_\odot$ neutron star and c_s^2 shows a broad peak around $5n_0$.
- $\delta_{k_F}, d = 7.0$ (dash-dotted lines): An enhancement of the d parameter results in no notable changes for SNM. In contrast, increasing d softens the EOS of PNM for $n \lesssim 5n_0$, while at high densities it is significantly stiffer and c_s^2 almost reaches the speed of light at $8n_0$. Nevertheless, the energy per particle as well as the pressure of PNM is smaller in the given density range.
- $\delta_n, d = 0.2$ (dashed lines): Compared to the choice δ_{k_F} , the larger density exponents in δ_n lead to a rapid increase of the energy per particle and the pressure of both SNM and PNM at comparatively low densities. As the density increases the EOS becomes softer again to match the pressure fit point at $8n_0$. As a consequence, we find a pronounced peak for the speed of sound due to the stiffness of the EOS.
- $\delta_n, d = 0.8$ (dotted lines): Again, a larger d parameter softens the EOS. In comparison to δ_{k_F} , the sensitivity of the functional with respect to d is more pronounced for PNM as well as for SNM. In this specific case, the speed of sound has a second maximum at high densities; this feature depends on the chosen input values and is not present in most EOS.

These characteristics of the EOS functional are quite robust throughout the input parameter space. In line with this, our new approach (rational functions instead of density monomials) ensures that the fit parameters (a_i, b_i) remain of reasonable size (i.e., there is no “unnatural” fine-tuning) under comprehensive variations of the low- and high-density input. More precisely, for the 16,128 input sets considered in Sec. 3.4.1, those that are consistent with the imposed constraints from nuclear physics and observations

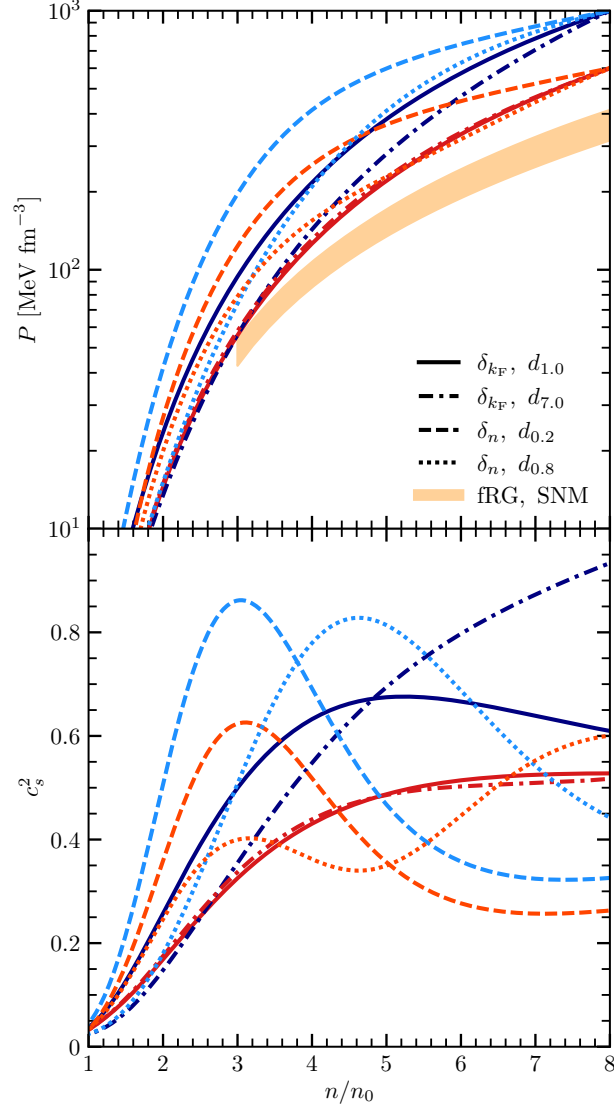


Figure 3.6: Same as Fig. 3.5 but here we show the pressure P (upper panel) and speed of sound c_s^2 (lower panel) of PNM (blue) and SNM (red). Note the pressure fit points at $8n_0$. The orange band corresponds to the fRG results of Ref. [171].

with the density exponents δ_n have absolute values of the dimensionless parameters of at most 2.6, with mean values between 0.2 and 1.1. For δ_{k_F} the parameters are in general larger due to the smaller density exponents in the numerators of the interaction terms, i.e., δ_{k_F} involves more tuning than δ_n . The mean values of the fit parameters for δ_{k_F} lie in the range 1.4 to 15.5. For the combined (δ_{k_F} and δ_n) parameter space, 80% of the constrained EOS have a_i and b_i in a range from -12 (lower bound b_2) to 20 (upper bound b_3), with five out of the eight fit parameters spanning only a range at most from -3 to 3 . Overall, as discussed in Secs. 3.2 and 3.3, our approach allows to generate (via variations of the low- and high-density input) a broadly populated range of EOSs that reflects well the uncertainties from nuclear physics, observations, and high-density QCD calculations.

3.3 Equation of state variations

With the energy density functional in place, we perform variations of the input choices to span a range of EOS that covers the uncertainties of the constraints discussed in Sec. 3.1. First, we discuss the variations of nuclear matter properties in Sec. 3.3.1. This involves the four representative (E_{sym}, L) pairs shown in Fig. 3.2 as well as three choices for the saturation properties of SNM. In Sec. 3.3.2, we then analyze the behavior of the EOS parametrization for the three effective mass scenarios introduced in Sec. 3.2.1. This is followed by high-density variations of the pressure for PNM and SNM in Sec. 3.3.3. These variations are performed for each set of expansion coefficients δ_i and each of the corresponding d values given by Eqs. (3.6) and (3.7), respectively. For each type of variation, we show the corresponding influence on the energy per particle, pressure, and speed of sound for PNM and SNM with an associated figure.

3.3.1 Variations of nuclear matter properties

To cover the uncertainties of the energy of PNM from many-body calculations based on chiral EFT, four combinations of the symmetry energy E_{sym} and the slope parameter L were identified, namely,

$$(E_{\text{sym}}, L)/\text{MeV} \in \{(30, 35), (31, 55), (33, 65), (34, 55)\}. \quad (3.8)$$

These values cover a reasonable range of the combined theoretical results for the $E_{\text{sym}}-L$ correlation; see Fig. 3.2. In fact, we have investigated a whole grid of (E_{sym}, L) pairs that encompasses and exceeds the green-shaded region in Fig. 3.2: the grid ranges are 28–36 MeV for the symmetry energy and 30–75 MeV for the slope parameter (with step sizes 1 and 5 MeV). We have examined the EOS and neutron star properties obtained from each (E_{sym}, L) pair in this grid for each (δ_i, d) choice, each effective mass scenario, and each of the different (n_0, B, K) values and high-density input specified in Sec. 3.3.3. For every (E_{sym}, L) pair we then counted the number of EOSs, which fulfill the constraints from nuclear physics and neutron star observations discussed in Secs. 3.1.1 and 3.1.2. Note that the high-density fRG results for SNM from Sec. 3.1.3 are not enforced as a strict constraint.

The results from this study are analyzed in Fig. 3.7 where one sees that larger slope parameters become disfavored the smaller the symmetry energy is. This feature, which is more pronounced for δ_{k_F} , is reflected also in the microscopic constraints on the $E_{\text{sym}}-L$ correlation, see Fig. 3.2. Our four choices for (E_{sym}, L) are based on the combined results from Figs. 3.2 and 3.7, and on the observation that they lead to EOSs that cover a broad range of neutron star properties.

For the saturation properties of SNM, we use the empirical saturation point $n_0 = 0.164(7) \text{ fm}^{-3}$ and $B = 15.86(57) \text{ MeV}$ [169] together with the constraint on the incompressibility $K = 215(40) \text{ MeV}$ determined from microscopic nuclear-matter calculations [228, 226, 169]. The uncertainties in (n_0, B, K) are covered by three combinations. The triple $(K, n_0, B)_{\text{central}}$ uses the central values. The two other triples combine the minimal (maximal) values of n_0 and B with the largest (smallest) incompressibility: $(K_{\text{max}}, (n_0, B)_{\text{min}})$ and $(K_{\text{min}}, (n_0, B)_{\text{max}})$. Overall:

$$(K_{\text{min}}, (n_0, B)_{\text{max}}) = (175, 0.171, 16.43), \quad (3.9)$$

$$(K, n_0, B)_{\text{central}} = (215, 0.164, 15.86), \quad (3.10)$$

$$(K_{\text{max}}, (n_0, B)_{\text{min}}) = (255, 0.158, 15.29), \quad (3.11)$$

in units MeV, fm^{-3} , and MeV, respectively. These combinations have a physical motivation: First, they follow the Coester-band correlation between n_0 and B values [169]. Second, if SNM saturates at small densities and energies, then one expects that the incompressibility increases, and vice versa.

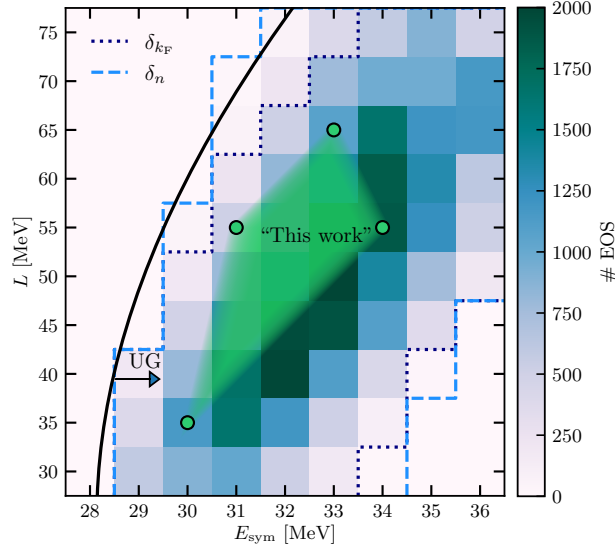


Figure 3.7: Grid of (E_{sym}, L) pairs used to determine the four representative pairs given by Eq. (3.8). The black line (labeled “UG”) corresponds to the constraint on (E_{sym}, L) obtained from the unitary gas boundary on the PNM energy [235]; see Sec. 3.1.1. The color coding gives the number of EOS that fulfill the theoretical and observational constraints discussed in Secs. 3.1; see text for details.

The four (E_{sym}, L) pairs and three (n_0, B, K) triples amount to twelve possible combinations of nuclear matter properties for each choice of (δ_i, d) . The corresponding results for the PNM energy at nuclear densities are examined in Fig. 3.8 where each of the four panels is for one of the four (E_{sym}, L) pairs. One sees that the chosen variations of the nuclear matter properties provide a thorough representation of the PNM uncertainty band from chiral EFT. The depicted EOS are for one particular choice of (δ_i, d) , $m_t^*(n, x)$ and the high-density input, as specified in the caption of Fig. 3.8. Variations of these properties broaden the covered area further. We use the unitary gas bound to rule out some of the EOSs (gray lines), in particular among those are $(K_{\text{min}}, (n_0, B)_{\text{max}})$, and δ_{k_F} . The EOS with intermediate symmetry energies and large slope parameters $(E_{\text{sym}}, L)/\text{MeV} = (31, 55)$ and $(33, 65)$ are most affected by this (conjectured) lower bound.

Finally, in Fig. 3.9, we show the analog of Fig. 3.8 for the pressure and the speed of sound of PNM and SNM. One sees that the nuclear matter properties have only a relatively small impact on the high-density behavior, which for a given high-density fit input is predominantly determined by the choice of δ_i and d .

3.3.2 Effective mass variation

As discussed in Sec. 3.2.2, we employ three different parametrizations of the nucleon effective mass, $m_{0.7}^*$, $m_{1.0}^*$, and $m_{1.3}^*$, where the subscript denotes the respective high-density limit, see Fig. 3.4. Here, in Figs. 3.10 and 3.11 we examine the impact of the high-density behavior of the effective mass on the zero-temperature EOS. The impact on thermal effects is studied in Sec. 3.4.2.

In Figs. 3.10 and 3.11, the nuclear matter properties are fixed as

$$(K, n_0, B) = (K_{\text{max}}, (n_0, B)_{\text{min}}), \quad (3.12)$$

$$(E_{\text{sym}}, L)/\text{MeV} = (30, 35). \quad (3.13)$$

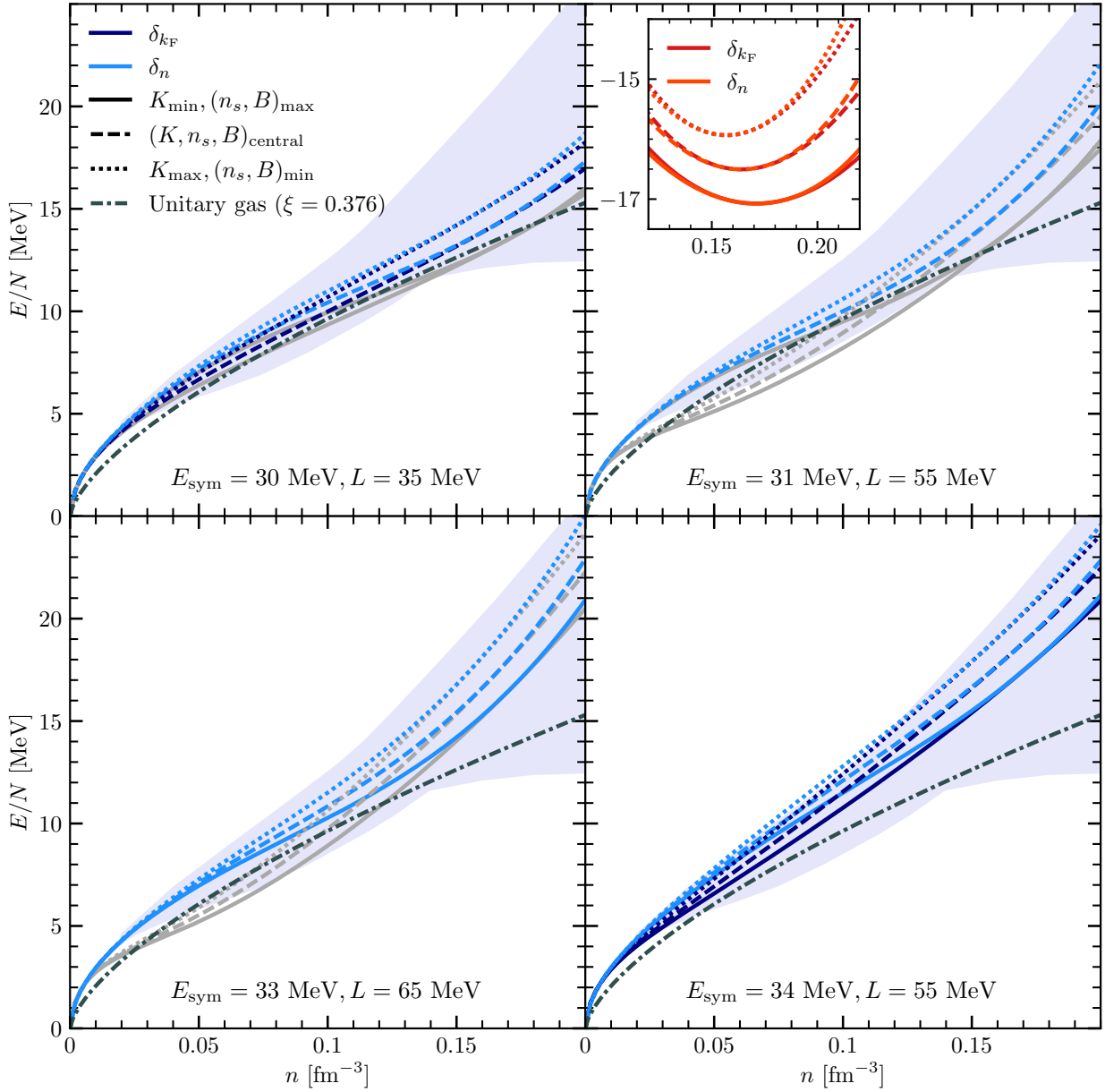


Figure 3.8: Results for the energy per particle of PNMs at nuclear densities. The four panels correspond to the four representative (E_{sym}, L) pairs given by Eq. (3.8). In each panel we show the results obtained from the three (n_0, B, K) triples given by Eqs. (3.9)–(3.11). The light/dark blue lines are for the δ_n/δ_{k_F} functional. All depicted EOSs employ the smallest d available for the respective choice of δ_i ; see Eq. (3.7), the effective mass scenario $m_{1,0}^*$, and the same high-density fits for the pressure (see Fig. 3.9, top panel). In the inset of the second panel, we show the corresponding SNM results. The light blue band in each panel corresponds to the combined chiral EFT results from Fig. 3.1. The anthracite dash-dotted line in each panel is the conjectured lower bound (unitary gas with $\xi = 0.376$) on the PNM energy. All EOSs with energies that violate this bound are excluded and shown as gray lines.

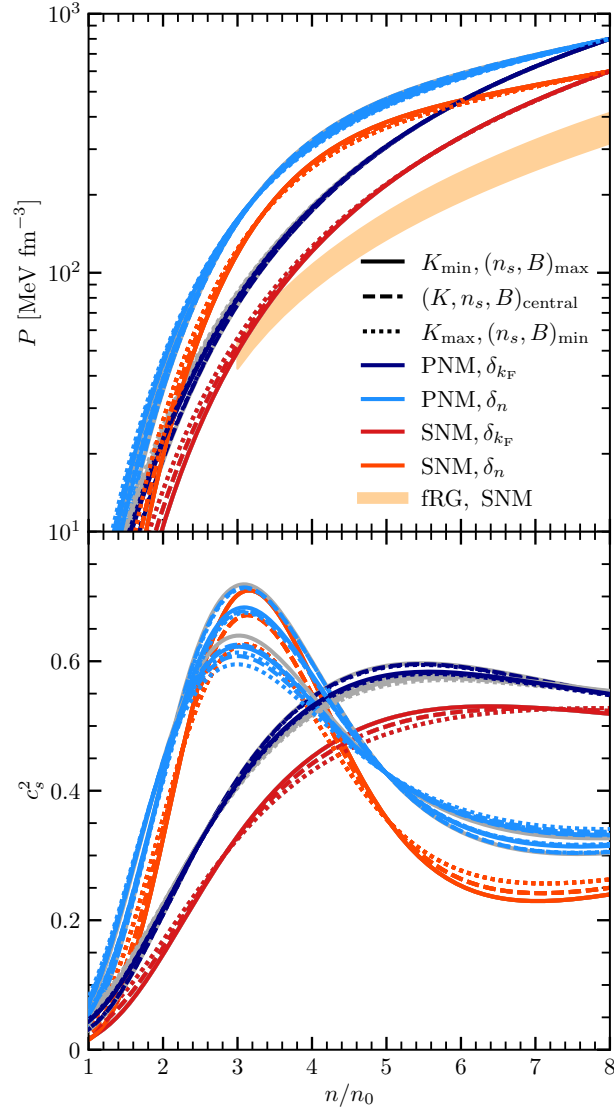


Figure 3.9: High-density analog of Fig. 3.8 for the pressure (upper panel) and the speed of sound (lower panel) of PNM (blue) and SNM (red) as a function of density. The orange band corresponds to the fRG SNM results from Ref. [171].

The high-density input is fixed as specified in Fig. 3.9. We see that the overall influence of the effective mass on the energy and pressure at zero temperature is comparatively small by construction. The speed of sound, as a quantity that is not directly constrained by the fit, is more sensitive to variations of the effective mass. The observed behavior depends on the choice of δ_i , and in each case the results for $m_{1.0}^*$ and $m_{1.3}^*$ are more similar compared to $m_{0.7}^*$. In the case of δ_n the maximum of c_s^2 increases with the high-density limit of the effective mass (i.e., the EOS becomes stiffer), while for δ_{k_F} the speed of sound peak occurs at smaller densities for $m_{0.7}^*$.

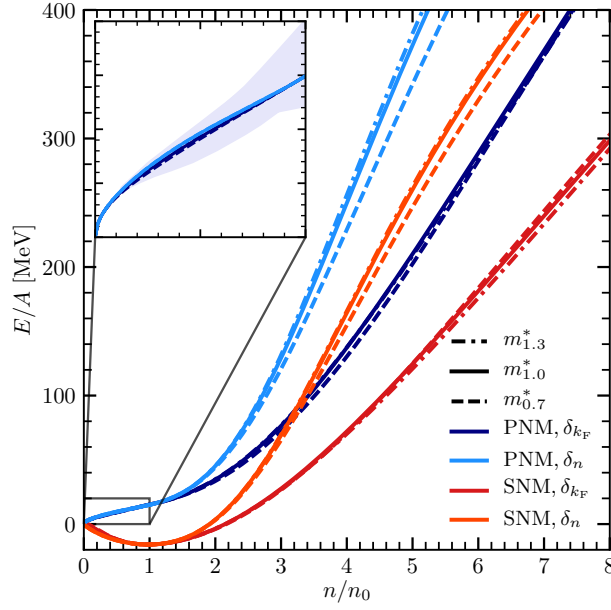


Figure 3.10: Results for the energy per particle of PNM (blue) and SNM (red) as a function of density for the three effective mass scenarios of Fig. 3.4. All depicted EOS employ the smallest d available for the respective choice of δ_i . The nuclear matter properties and high-density input are fixed, see text for details. The light blue band in the inset corresponds to the combined chiral EFT results from Fig. 3.1.

3.3.3 High-density variations

With a careful implementation of the nuclear physics constraints at hand the objective now is to have the EOS functional reproduce the high-density constraints from neutron star observations. That is, the goal is to cover the band for neutron star matter obtained by Raaijmakers *et al.* [126] and have EOS that are consistent with the mass measurements of Antoniadis *et al.* [7] and the 2σ confidence interval of the $2.14 M_\odot$ measurement by Cromartie *et al.* [8], see Sec. 3.1.2. For this, we span a grid of fit points for the pressure of SNM and PNM at $n = 1.28 \text{ fm}^{-3} \approx 8n_0$. We fit the pressure of SNM to values $\{300, 400, 500, 600, 700, 800, 900\} \text{ MeV fm}^{-3}$ and the pressure difference between PNM and SNM to $\{50, 100, 150, 200, 250, 300, 350, 400\} \text{ MeV fm}^{-3}$, so the pressure of PNM ranges from 350 to 1300 MeV fm^{-3} . This results in 56 high-density fit combinations for each low-density and effective mass input. From these, we exclude all EOSs that, after including β -equilibrium and electrons, are not consistent with the Raaijmakers *et al.* bands in Fig. 3.3.

The high-density fRG calculations of SNM by Leonhardt *et al.* [171] (see Sec. 3.1.3) lie on the lower end of the employed fit values for the SNM pressure: $310 \text{ MeV fm}^{-3} \lesssim P_{\text{fRG}}(8n_0) \lesssim 410 \text{ MeV fm}^{-3}$. A lower SNM pressure implies that the pressure of matter in β -equilibrium is small as well. More specifically, the proton fraction increases with the SNM-PNM pressure difference, leading to a decrease of the pressure of matter in β -equilibrium. As a result, enforcing consistency with the fRG results reduces the range for neutron star matter to a great extent, such that the uncertainty band by Raaijmakers *et al.* [126] cannot be fully covered. Therefore, we do not use the fRG band as a strict constraint. The subset of EOSs that are consistent with the fRG calculations is studied further in Sec. 3.4.1.

As an example, representative high-density variations of the energy per particle of PNM and SNM are shown in Fig. 3.12. The corresponding results for the pressure and the speed of sound are displayed in Fig. 3.13. Here, the nuclear matter properties are set to $(K_{\text{max}}, (n_0, B)_{\text{min}})$ and $E_{\text{sym}} = 30 \text{ MeV}$, $L = 35 \text{ MeV}$.

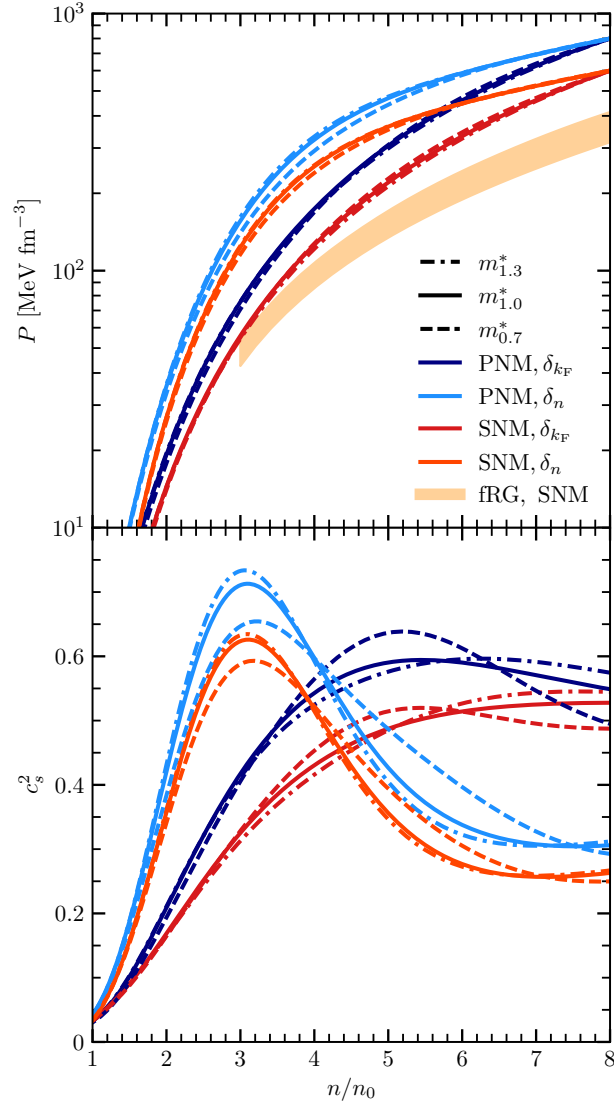


Figure 3.11: Analog of Fig. 3.10 for the pressure (upper panel) and speed of sound (lower panel) of PNM (blue) and SNM (red) as a function of density. The orange band corresponds to the fRG SNM result from Ref. [171].

The effective mass is given by $m_{1.0}^*$, and for each δ_i combination we use the smallest d value from Eq. (3.7). For each δ_i we keep only the EOSs, which are consistent with the constraints from nuclear physics and neutron star observations.

As seen in Fig. 3.12, for SNM the EOSs with δ_n span a much wider energy band that almost entirely encloses the δ_{k_F} energy band. At nuclear densities the pressures of both the δ_n and the δ_{k_F} EOSs lie mostly above the fRG pressure, see the top panel of Fig. 3.13. At high densities on the other hand the δ_n high-density variations encompass the entire fRG band. In contrast, for δ_{k_F} the deviations from the fRG band increase with density.

Compared to SNM, the δ_n and δ_{k_F} energy and pressure bands are of similar size for PNM. Regarding the speed of sound of PNM and SNM, in the bottom panel of Fig. 3.13 one sees that the high-density variations do not lead to significant changes in the systematics for different (δ_i, d) choices; see Fig. 3.6. For both

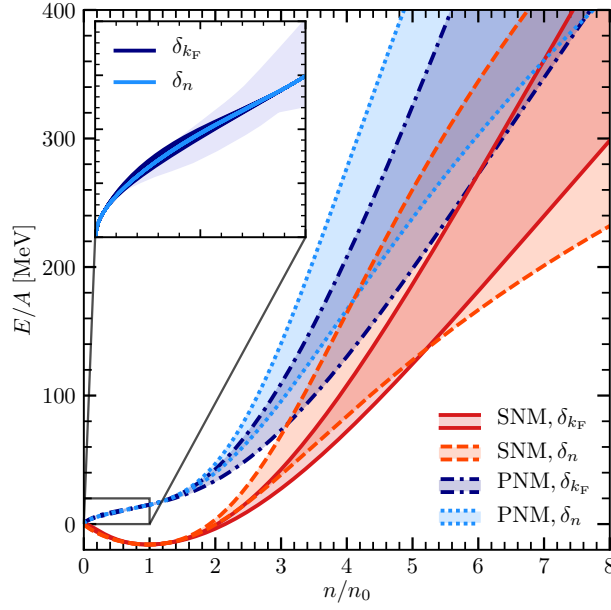


Figure 3.12: High-density variations for the energy per particle of PNM (blue) and SNM (red) as a function of density, see text for details. The bands for the two different δ_i combinations include only EOS that are consistent with neutron star constraints. The d parameter, the effective mass, and the nuclear matter properties are kept fixed. The light blue band in the inset corresponds to the combined chiral EFT results from Fig. 3.1.

δ_i sets, the EOS with largest stiffness regions involve a PNM speed of sound that at its peak is close to $c_s^2 = 0.8$. In Fig. 3.13, for both the PNM and SNM speed of sound the two δ_i sets give nonoverlapping results at high densities. However, one needs to keep in mind the displayed results are for one particular choice of the d parameter, the nuclear matter properties and the effective mass. Varying these reduces the area that is not covered with the specific input used. Plots that involve the full range of the considered parameter variations are shown in the subsequent section.

3.4 Astrophysical equation of state

Here, we examine our results for cold matter in β -equilibrium and study neutron star properties such as the M - R relation and the electron fraction. We take into account the full set of parameter variations of the EOS functional, as discussed in Sec. 3.3. Thermal effects, which are crucial for applications in CCSN and NSM simulations, are analyzed as well.

3.4.1 Neutron star properties

The density of electrons and muons in neutron star matter is equal to the proton density because of local charge neutrality. For simplicity, we neglect muons as this causes only a very small change in the neutron star EOS. The proton fraction x at a given baryon density n is fixed by the requirement of β -equilibrium,

$$\mu_n(n, x) = \mu_p(n, x) + \mu_e(n_e = xn), \quad (3.14)$$

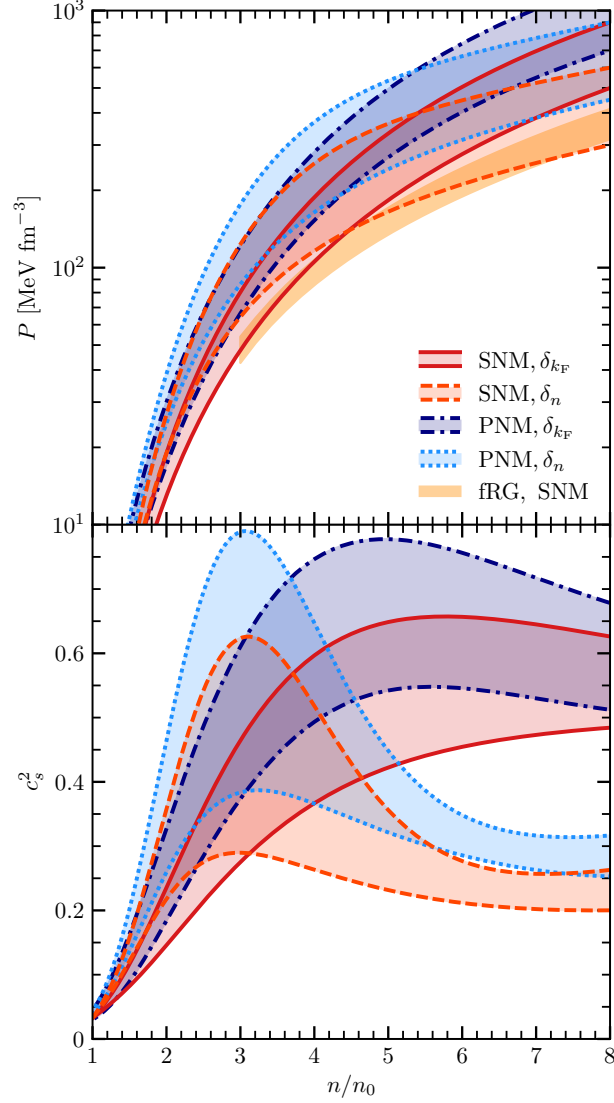


Figure 3.13: Analog of Fig. 3.12 for the pressure (upper panel) and speed of sound (lower panel) of PNM (blue) and SNM (red) as a function of density. The orange band corresponds to the fRG SNM results from Ref. [171].

where $\mu_{n,p,e}$ is the chemical potential of the respective particle species. Electrons can be modeled as an ultrarelativistic degenerate Fermi gas, so the electron pressure is $P_e = E_e/(3V)$, with the electron energy density given by $E_e/V = (3\pi^2 n_e)^{4/3}/(4\pi^2)$. The electron chemical potential reads $\mu_e = (3\pi^2 n_e)^{1/3}$ and the chemical potentials of neutrons and protons are $\mu_{n,p} = \partial_{n_{n,p}} E(n, x)/V + m_{n,p}$.

With the variations of the EOS input and the choices for the functional parameters δ_i and d of Eqs. (3.6) and (3.7) in place, we perform all possible fit combinations to obtain bands for the EOS of matter in β -equilibrium. The neutron star mass-radius (M - R) relation is then obtained by solving the Tolman-Oppenheimer-Volkoff equations [54, 55]. To this end, we implement the Baym, Pethick, Sutherland (BPS) crust from Ref. [319] for densities below $n_{\text{crust}} = 0.08 \text{ fm}^{-3}$, as in Ref. [126]. As discussed in the two previous sections, for each of the δ_i sets we consider four d values, 12 variations of nuclear matter properties, three effective mass scenarios, and 56 high-density fits for the pressure of SNM and PNM, resulting in a set

of 16128 EOS. Among these, we keep only EOSs that

- are consistent with the theoretical PNM uncertainty band and the unitary gas bound for the energy per particle up to 0.2 fm^{-3} ,
- provide masses of neutron stars of at least $1.965 M_{\odot}$ (combined lower bound of the measurements from Ref. [7] and the 2σ interval of Ref. [8]),
- and lie within the 95% credible regions based on the joint analysis of GW170817 and NICER from Raaijmakers *et al.* [126].

The results for the pressure and the speed of sound of neutron star matter are shown in Fig. 3.14. We see that our EOS functional covers almost the entire band for the pressure by Raaijmakers *et al.* [126]. At the high-pressure boundary the agreement is very close, but some of the softer EOSs within the Raaijmakers *et al.* band are not reproduced. This feature can be largely attributed to the fact that we use a strict lower bound for the minimal value of M_{max} whereas Raaijmakers *et al.* have modeled the mass likelihood function for the $2.14 M_{\odot}$ pulsar [8].

In Fig. 3.14, the parts of the different EOSs that correspond to neutron stars with masses below the canonical $1.4 M_{\odot}$ are highlighted in dark green. Their continuation up to the respective maximum mass M_{max} is colored in light green. The central density $n_{1.4}$ for a neutron star with $1.4 M_{\odot}$ lies approximately within $2\text{--}3.5 n_0$. The smallest and largest n_{max} are roughly $4.5 n_0$ and $7.5 n_0$, respectively, where one particular EOS reaches $n_{\text{max}} \approx 7.9 n_0$, very similar to Ref. [4]. Up to $n_{1.4}$, the speed of sound is relatively strongly constrained, but at higher densities a large variety of speed of sound curves is present that covers a range from $c_s^2 \approx 0.2$ to almost the speed of light.

Next, in Fig. 3.15 we show the corresponding results for the pressure-energy density relation and the neutron star M - R diagram. Regarding the M - R relation, compared to our results the band of Raaijmakers *et al.* [126] includes for $M \gtrsim 1.5 M_{\odot}$ neutron stars with slightly smaller radii. This is a direct consequence of the softer EOSs included there, as discussed above. For a $1.4 M_{\odot}$ neutron star we find a radius range of $R_{1.4} = 11.1\text{--}13.6 \text{ km}$, similar to Ref. [126]. Interestingly, compared to Ref. [126] our EOS functional gives lower-mass neutron stars with slightly larger radii as well as larger maximum masses for neutron stars with $12 \lesssim R/\text{km} \lesssim 13$. Further, in Fig. 3.15 we also show the mass-radius band obtained by Hebeler *et al.* [4] using polytropic extrapolations of chiral EFT results. Compared to the other bands, the band by Hebeler *et al.* [4] allows for neutron stars with smaller radii and larger maximum masses. This is mainly because it shows the entire region (100% instead of 95% credible) compatible with the maximum mass constraint.

The density exponents of the functional δ_i mostly influence the stiffness of the EOS. In particular, softer EOSs corresponding to neutron stars with smaller radii mainly involve δ_{k_F} , while δ_n yields stiffer EOSs and larger radii. Moreover, the back-bending of the M - R lines at $M \approx 0.5 M_{\odot}$ is more pronounced for EOSs that use δ_n .

The EOSs for which SNM is consistent with the fRG band by Leonhardt *et al.* [171] are highlighted in orange in Fig. 3.15. More specifically, for the orange EOSs the pressure of SNM starting at $5n_0$ deviates from the fRG band by at most 10%. Compared to the full band, the fRG-consistent neutron star EOSs have lower pressures at energy densities $\varepsilon \gtrsim 800 \text{ MeV fm}^{-3}$, which is a consequence of the relatively low SNM pressures obtained by the fRG calculation. This translates into comparatively larger neutron star radii and smaller maximum masses. Nevertheless, the fRG-consistent EOSs cover a broad range of the pressure-energy density and M - R bands of Raaijmakers *et al.* [126]. Overall, the fRG results for SNM provide viable additional constraints for astrophysical EOS constructions, and incorporating them leads to a considerable narrowing of the uncertainty band for the EOS and the M - R relation. In the future, improved fRG calculations will enable further advancements along these lines.

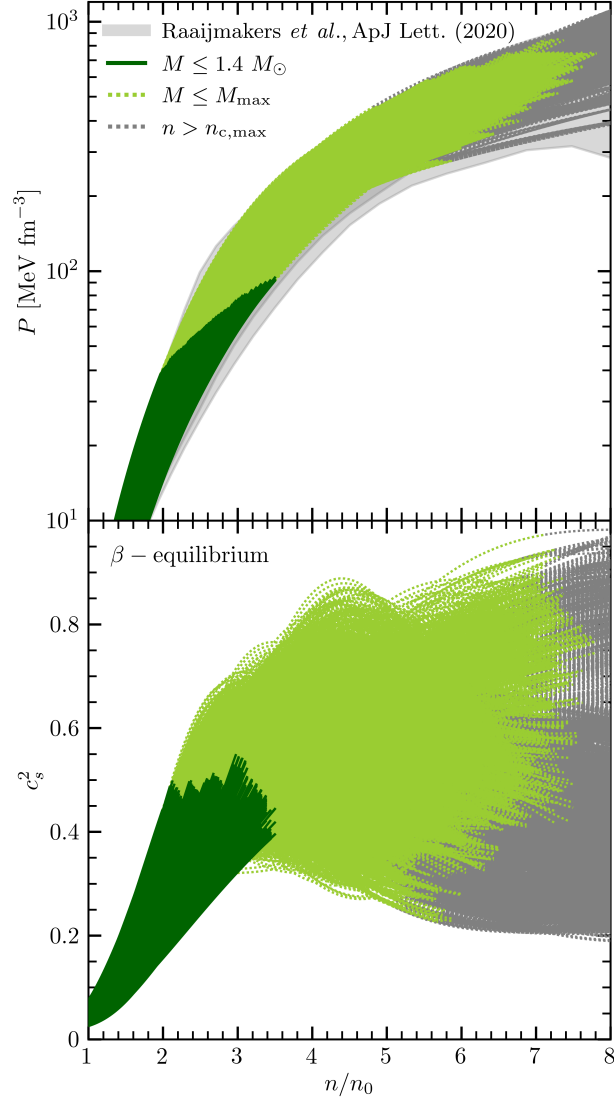


Figure 3.14: Results for the pressure (upper panel) and the speed of sound (lower panel) of matter in β -equilibrium as a function of density. As described in the text, we show all EOSs that fulfill the constraints from nuclear physics and neutron star observations. The color coding indicates the mass of the corresponding neutron star, where dark green corresponds to masses up to $1.4 M_{\odot}$ and light green to higher masses up to the respective maximum mass M_{\max} . Gray lines correspond to the continuation of the EOSs to densities above the central densities $n_{c,\max}$ of the respective heaviest neutron star. The light-gray band depicts the 95% credible region of the neutron star constraints from Raaijmakers *et al.* [126].

Our results for the neutron star maximum mass are examined further in Fig. 3.16 where we plot the number of EOSs that yield a given value of M_{\max} . The distribution in Fig. 3.16 shows a broad peak, which falls off steeply for $M_{\max} \gtrsim 2.35 M_{\odot}$, reaching zero at $M_{\max} \approx 2.6 M_{\odot}$. Our largest maximum masses are only slightly above the model-dependent bound $M_{\max} \lesssim 2.3\text{--}2.4 M_{\odot}$ inferred from GW170817 [88, 301, 302, 89, 90, 303, 304]. Again, in Fig. 3.16 the EOSs that are consistent with the fRG band are highlighted in orange. As discussed above, the fRG constraint implies softer EOSs and thus leads to smaller values of

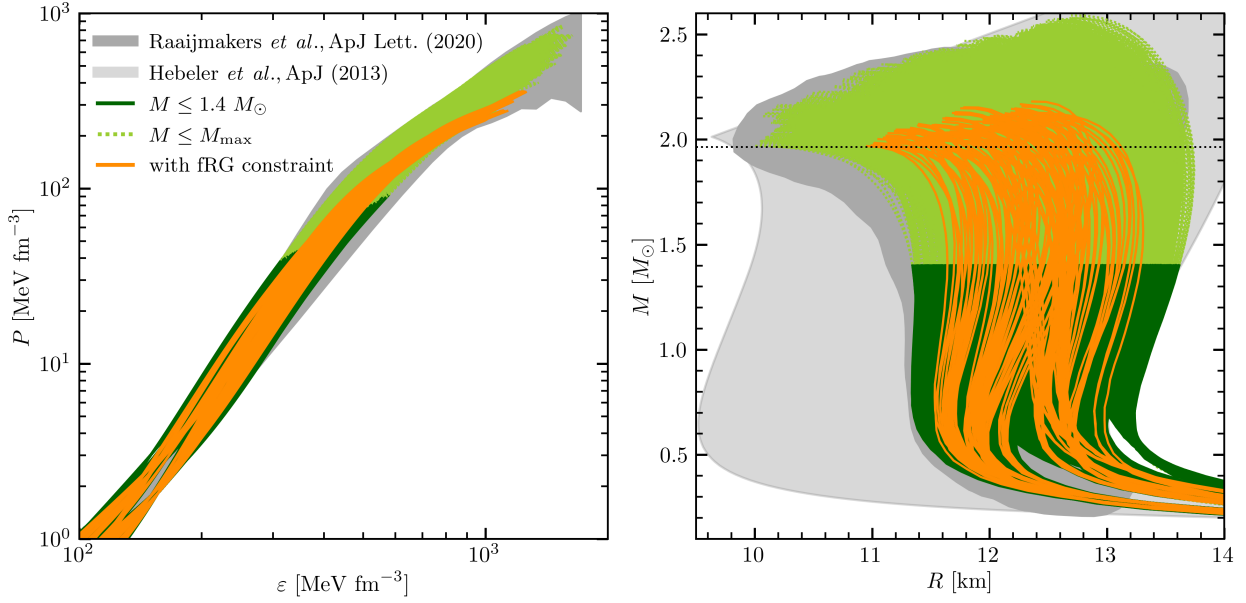


Figure 3.15: Analog of Fig. 3.14 for the pressure-energy density relation (left) and the mass-radius relation (right) of cold neutron stars. The orange lines correspond to EOSs that are consistent with the fRG SNM results from [171], see text for details. The gray band depicts the 95% credible region of the neutron star constraints from Raaijmakers *et al.* [126]. For comparison, in the M - R plot we show also the uncertainty band obtained by Hebeler *et al.* [4] using piecewise polytrope extensions to high densities (light gray band).

the maximum mass with $M_{\max} \lesssim 2.18 M_{\odot}$.

Finally, in Fig. 3.17 we show the electron fraction $Y_e(n)$ in neutron stars as obtained from the different EOS. The density dependence of the electron fraction is strongly related to that of the symmetry energy $S(n)$. Similar to the results for the speed of sound, our $Y_e(n)$ band is fairly narrow up to around saturation density where the electron fraction is given by $Y_e(n_0) \approx (4E_{\text{sym}})^3/3\pi^2 n_0 \approx 0.035\text{--}0.055$ [175]. Above $(2\text{--}3)n_0$, the $Y_e(n)$ band widens considerably, with different EOS given electron fractions between 0 to about 30% in the core of heavy neutron stars. This reflects the difference in energy of PNM to SNM, as a larger symmetry energy implies a higher electron fraction.

3.4.2 Thermal effects

Some EOSs used in NSM simulations start from a cold neutron star EOS and add a thermal part that is parametrized in terms of a density-independent thermal index $\Gamma_{\text{th}} = \text{const.}$, e.g., $\Gamma_{\text{th}} = 1\text{--}2$. The validity of this approximation was studied by Bauswein *et al.* in Ref. [261] who concluded that a consistent treatment of thermal effects beyond the $\Gamma_{\text{th}} = \text{const.}$ approximation is important. As discussed in Sec. 2.4, the thermal contribution to the EOS is governed to a large extent by the nucleon effective mass. Full EOS tables for astrophysical simulations mostly apply a mean-field effective mass that monotonically decreases with density. This, however, is not consistent with microscopic nuclear-matter calculations [262, 263], which show that interaction effects beyond the mean-field approximation are significant. As discussed in Sec. 3.2.1, our EOS functional incorporates such microscopic effective-mass results explicitly.

The temperature dependence of our EOS functional is described solely by the kinetic term, which is modeled as a noninteracting nucleon gas with neutron and proton effective mass $m_n^*(n, x)$ and $m_p^*(n, x)$, see

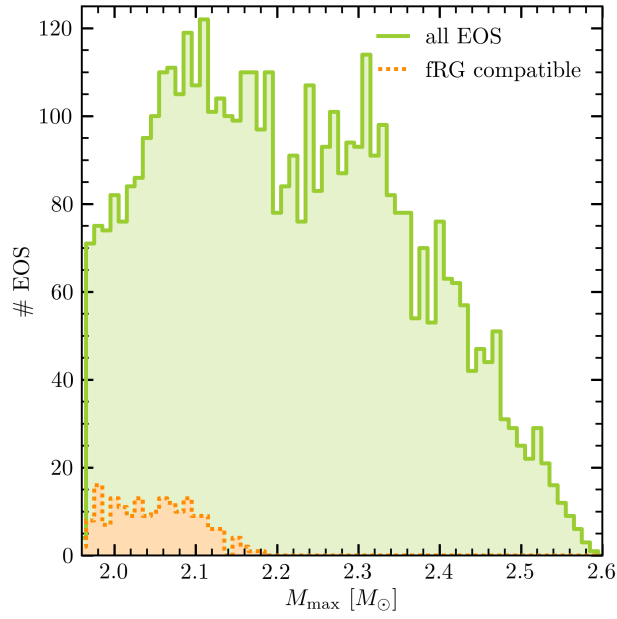


Figure 3.16: Number of EOSs per maximum mass M_{max} corresponding to the mass-radius relation of Fig. 3.15. The orange dotted line corresponds to EOSs that are consistent with the fRG SNM results from Ref. [171].

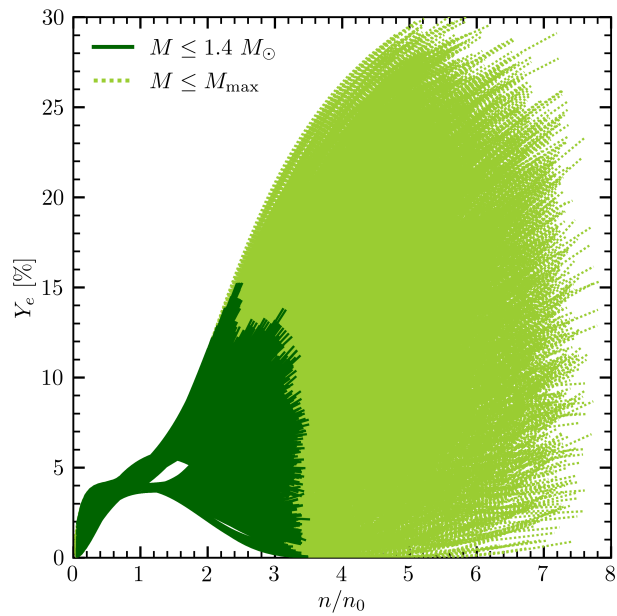


Figure 3.17: Analog of Fig. 3.14 for the electron fraction Y_e as a function of density.

Sec. 3.2.2. From this one arrives at the following equation for the thermal index Γ_{th} of isospin-asymmetric nuclear matter (ANM) with proton fraction x :

$$\Gamma_{\text{th}}(n, x, T) = \frac{5}{3} - n \frac{\sum_t \frac{\varepsilon_{t,\text{th}}(n, x, T)}{m_t^*(n, x)} \frac{\partial m_t^*(n, x)}{\partial n}}{\sum_t \varepsilon_{t,\text{th}}(n, x, T)}, \quad (3.15)$$

where $\varepsilon_{t,\text{th}}(n, x, T) = \varepsilon_t(n, x, T) - \varepsilon_t(n, x, 0)$ is the thermal part of the kinetic energy density of neutrons and protons, respectively. In the context of our EOS functional, Eq. (3.15) is an exact representation of $\Gamma_{\text{th}}(n, x, T)$, i.e., it is equivalent to Eq. (2.10). The T dependence of $\Gamma_{\text{th}}(n, x, T)$ vanishes for $x = 0$ and $x = 1/2$, i.e., for PNM and SNM one obtains the familiar expression given by Eq. (2.17). However, for ANM the thermal index is a temperature-dependent quantity. Consequently, we explore whether the T dependence of Γ_{th} for ANM is a significant effect, and, if the T dependence is small, what is the appropriate temperature-independent approximative expression for the thermal index. For a classical free nucleon gas with $m_n^*(n, x)$ and $m_p^*(n, x)$ one obtains by substituting $3Tn_t/2$ for $\varepsilon_{t,\text{th}}(n, x, T)$ in Eq. (3.15) the expression from Eq. (2.17)

$$\Gamma_{\text{th,classical}}(n, x) = \frac{5}{3} - \sum_t \frac{n_t(n, x)}{m_t^*(n, x)} \frac{\partial m_t^*(n, x)}{\partial n}. \quad (3.16)$$

Comparing the results obtained from Eqs. (3.15) and (3.16) one finds that the classical expression provides a very good approximation, with relative errors well below the 1% level (except at very low $T \lesssim 1$ MeV). For example, averaging over densities $n/n_0 \in [0, 8]$ and the results obtained from the three effective mass scenarios ($m_{0.7}^*$, $m_{1.0}^*$, and $m_{1.3}^*$), the mean relative errors at $T = 10$ MeV are (0.18%, 0.52%, 0.63%) for $x = (0.1, 0.2, 0.3)$. At higher temperatures one is closer to the classical limit, so the errors decrease with T ; at $T = 1$ MeV and $T = 50$ MeV they are (0.22%, 0.61%, 0.85%) and (0.09%, 0.16%, 0.24%), respectively, for $x = (0.1, 0.2, 0.3)$. For each T and x and each effective mass scenario the deviations first increase with density up to $n/n_0 \approx 5-7$, and then decrease again (since the high-density limit of the effective mass is x independent in our approach). Overall, we conclude that $\Gamma_{\text{th,classical}}(n, x)$ provides a very good representation of the temperature dependence of the EOS of ANM.

Our results for the thermal index Γ_{th} of PNM, SNM, and ANM with $x = 0.2$ are shown in Fig. 3.18, where for ANM we show the results obtained from the classical approximation, Eq. (3.16). The density behavior of Γ_{th} is then for each x determined entirely by that of $m_n^*(n, x)$ and $m_p^*(n, x)$. For PNM and SNM, an increasing (decreasing) effective mass implies that Γ_{th} is below (above) the free or unitary Fermi gas value $\Gamma_{\text{th}} = 5/3$, and the thermal index of PNM is larger than that of SNM. For each x , at low densities Γ_{th} first increases with n and then decreases again such that $\Gamma_{\text{th}} = 5/3$ is reached at $n \approx n_0$, corresponding to the minimum of $m_t^*(n, x)$ at around saturation density (see Sec. 3.2.1). The high-density behavior is fixed by the respective effective mass scenario, where the largest deviations from $\Gamma_{\text{th}} = 5/3$ occur for $m_{0.7}^*$ at $n \approx 5.8n_0$ (the $n \rightarrow 0$ limit is $\Gamma_{\text{th}} \rightarrow 5/3$ by construction). The smallest values, e.g., $\Gamma_{\text{th}} \approx 1.25$ at $n \approx 3.7n_0$ for SNM, are obtained for $m_{1.3}^*$.

The detailed description of thermal effects within our EOS functional may have interesting effects in astrophysical applications. In particular, the proto-neutron star contraction in CCSN simulations is largely governed by the T dependence of the EOS [47, 48]. Lower effective masses lead to larger thermal contributions and thus to a larger PNS radius. A faster contraction increases the temperature at the surface of the PNS. As a consequence, neutrinos emitted from the PNS have larger energies, which aids the shock evolution towards a faster explosion. The very high-density regime of the EOS is more important in NSM than in CCSN applications. Investigating the effects of our different high-density effective mass scenarios in NSM simulations may be an interesting subject for future research.

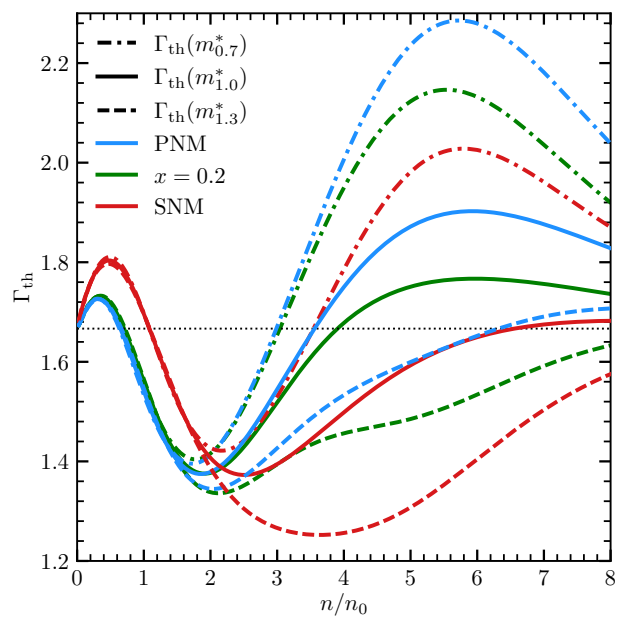


Figure 3.18: Results for the thermal index of PNM (blue), SNM (red), and ANM with $x = 0.2$ (green) as a function of density. The different line types correspond to the three effective mass scenarios, see Sec. 3.2.1. The horizontal gray dotted line corresponds to the thermal index $\Gamma_{\text{th}} = 5/3$ of a free or unitary Fermi gas.

4 Impact of the equation of state in astrophysical applications

Simulations of astrophysical environments such as CCSNe and NSMs require an equation of state that covers a broad range of conditions in density, temperature, and electron fraction. In this chapter, we aim to provide new EOS tables for astrophysical applications that reflect the uncertainties from modern nuclear theory calculations as well as astrophysical observations. This enables the systematic investigation of specific EOS parameters and uncertainties in simulations due to the EOS. To this end, we use the EOS constructed in Ch. 3 for nuclear matter and extend it to inhomogeneous matter based on the liquid-drop model. This EOS construction is implemented by Yeunhwan Lim. We further explore the impact of nuclear matter properties in NSM simulations. This study is based on a previous analysis of EOS effects in CCSN simulations, see Sec. 2.6.2. Here, the simulations of NSMs are conducted by Maximilian Jacobi.

4.1 Set of representative equations of state

For the construction of EOS tables we pick a set of representative EOS from the EOS functional derived in Ch. 3. Our requirements for this set of representative EOS is that it reflects the uncertainties of the mass-radius relation of cold neutron stars and that it enables systematic studies of the influence of the

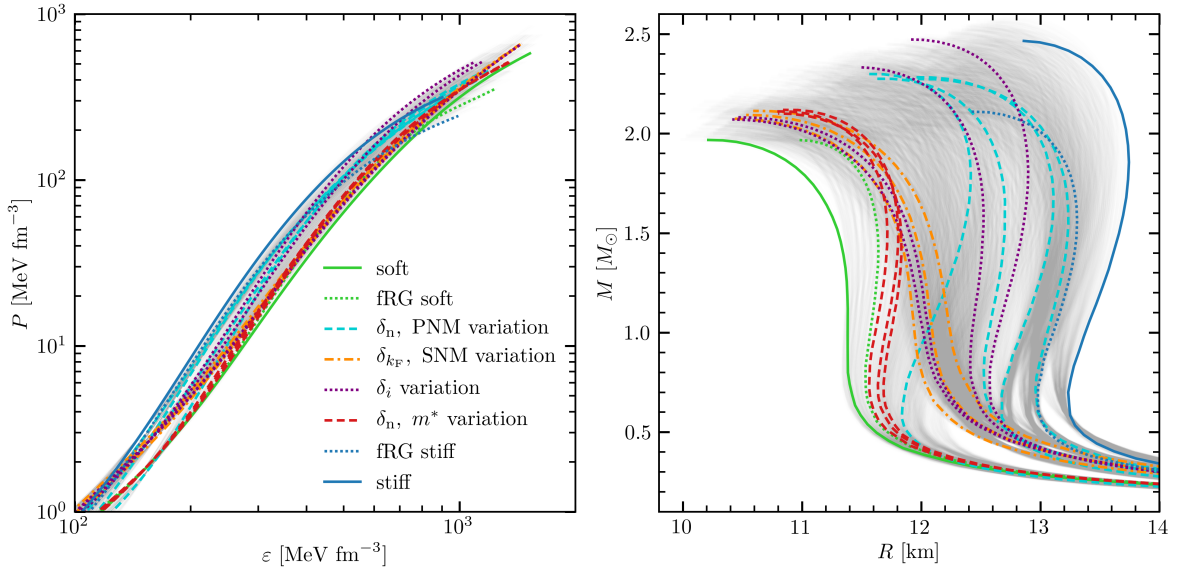


Figure 4.1: Equation of state and mass-radius relation for the set of representative EOSs. We further show all EOS from our EOS functional that are consistent with nuclear theory constraints and observations in light grey, see also Fig. 3.15.

EOS model	δ_i	d	n_0	B	K	E_{sym}	L	m^*	$P_{8n_0}^{\text{SNM}}$	$P_{8n_0}^{\text{PNM}}$	$R_{1.4}$
soft	δ_{k_F}	1	0.157	15.29	255	30	35	$m_{0.7}^*$	600	650	11.34
fRG soft	δ_n	0.6	0.157	15.29	255	30	35	$m_{1.3}^*$	400	650	11.64
PNM 30/35	δ_n	0.4	0.164	15.86	215	30	35	$m_{1.0}^*$	600	800	12.38
PNM 31/55	δ_n	0.4	0.164	15.86	215	31	55	$m_{1.0}^*$	600	800	13.05
PNM 33/65	δ_n	0.4	0.164	15.86	215	33	65	$m_{1.0}^*$	600	800	13.21
PNM 34/55	δ_n	0.4	0.164	15.86	215	34	55	$m_{1.0}^*$	600	800	12.69
SNM min	δ_{k_F}	3	0.171	16.43	175	34	55	$m_{1.0}^*$	800	1050	11.86
SNM mean	δ_{k_F}	3	0.164	15.86	215	34	55	$m_{1.0}^*$	800	1050	12.00
SNM max	δ_{k_F}	3	0.157	15.29	255	34	55	$m_{1.0}^*$	800	1050	12.13
$\delta_{k_F}/d3$	δ_{k_F}	3	0.164	15.86	215	34	55	$m_{1.0}^*$	800	1000	11.72
$\delta_{k_F}/d5$	δ_{k_F}	5	0.164	15.86	215	34	55	$m_{1.0}^*$	800	1000	11.70
$\delta_n/d.4$	δ_n	0.4	0.164	15.86	215	34	55	$m_{1.0}^*$	800	1000	12.7
$\delta_n/d.6$	δ_n	0.6	0.164	15.86	215	34	55	$m_{1.0}^*$	800	1000	12.41
$m_{0.7}^*$	δ_n	0.6	0.157	15.29	255	30	35	$m_{0.7}^*$	600	700	11.83
$m_{1.0}^*$	δ_n	0.6	0.157	15.29	255	30	35	$m_{1.0}^*$	600	700	11.80
$m_{1.3}^*$	δ_n	0.6	0.157	15.29	255	30	35	$m_{1.3}^*$	600	700	11.71
fRG stiff	δ_n	0.2	0.164	15.86	215	33	65	$m_{1.3}^*$	300	700	13.28
stiff	δ_n	0.2	0.157	15.29	255	33	65	$m_{1.3}^*$	500	850	13.61

Table 4.1: EOS parameters and radius of a $1.4 M_\odot$ neutron star for the set of representative EOS. The units are $\text{fm}^{(2-\delta_i)}$ for d , fm^{-3} for n_0 , MeV for B, K, E_{sym}, L , MeV fm^{-3} for the pressure of SNM and PNM at $8n_0$ and km for $R_{1.4}$.

nucleon effective mass m^* and nuclear matter properties like saturation density n_0 , binding energy B , and incompressibility K for SNM, and symmetry energy E_{sym} and slope parameter L for PNM.

The set of representative EOS consists of 18 EOS. The soft and stiff EOS represent the radius uncertainty and, thus, correspond to the EOS that feature the smallest and largest radius of a $1.4 M_\odot$ neutron star out of all possible EOS from our functional. Similar to this, the fRG soft and fRG stiff reflect the radius uncertainty for all EOS that are consistent with the fRG constraint on top of the constraints from nuclear theory and observation, see orange lines in Fig. 3.15. We pick 10 additional EOS to study systematics of the EOS functional and nuclear matter properties. For this, we individually vary PNM parameters, SNM parameters, the density exponents δ_i , and the high density limit of the effective mass m^* . For the PNM variation, we use the four pairs

$$(E_{\text{sym}}, L)/\text{MeV} \in \{(30, 35), (31, 55), (33, 65), (34, 55)\}, \quad (4.1)$$

while all other parameters are fixed to specific values, see Tab. 4.1 for details and the radius of a $1.4 M_\odot$ neutron star for each EOS of the representative set. The names of the EOS are given by "PNM" together with the value for the symmetry energy and slope parameter. For the SNM variation, we use min, mean,

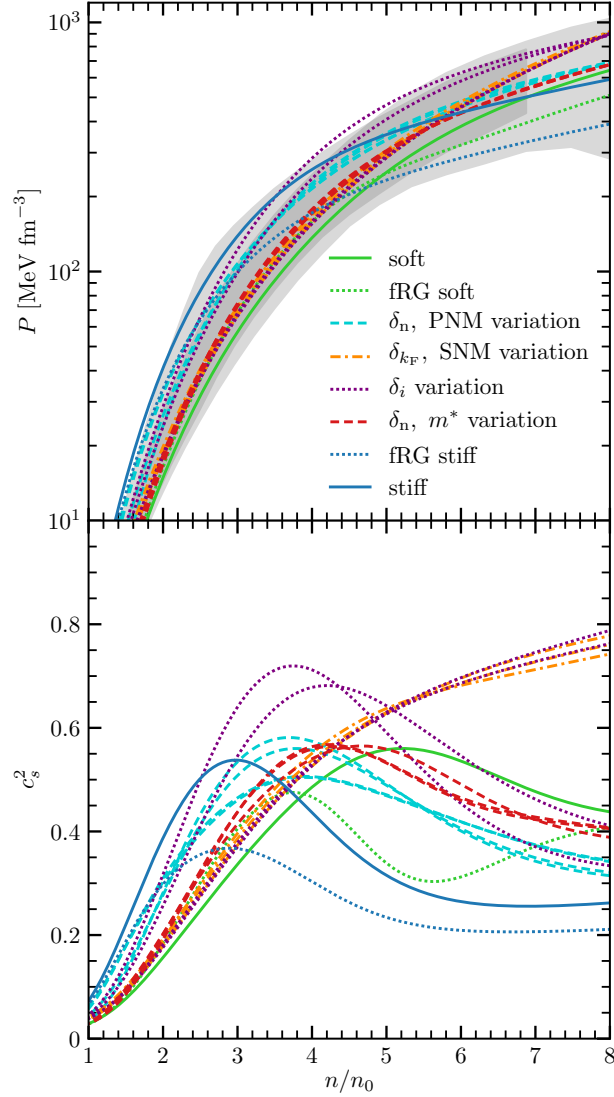


Figure 4.2: Pressure and speed of sound as a function of density for the selection of representative EOS. The gray bands for the pressure depict the 95% credible region of the neutron star matter constraints from Ref. [126].

and max depending on the choice of n_0 , B , and K , i.e.

$$\min \hat{=} (K_{\min}, (n_0, B)_{\max}) = (175 \text{ MeV}, 0.171 \text{ fm}^{-3}, 16.43 \text{ MeV}), \quad (4.2)$$

$$\text{mean} \hat{=} (K, n_0, B)_{\text{mean}} = (215 \text{ MeV}, 0.164 \text{ fm}^{-3}, 15.86 \text{ MeV}), \quad (4.3)$$

$$\max \hat{=} (K_{\max}, (n_0, B)_{\min}) = (255 \text{ MeV}, 0.158 \text{ fm}^{-3}, 15.29 \text{ MeV}). \quad (4.4)$$

For the variation of the density expansion, we choose two EOS with δ_{k_F} and two with δ_n where only the corresponding d value differs for each choice of the exponents. These EOS are then labeled $\delta_{k_F}/d3$, $\delta_{k_F}/d5$, $\delta_n/d.4$, and $\delta_n/d.6$. Lastly, we have three EOS to systematically study the influence of the high-density limit of the effective mass named $m_{0.7}^*$, $m_{1.0}^*$, and $m_{1.3}^*$. In Fig. 4.1, we show the set of representative EOS and the corresponding mass-radius relations. We further depict in light grey all EOS that are consistent

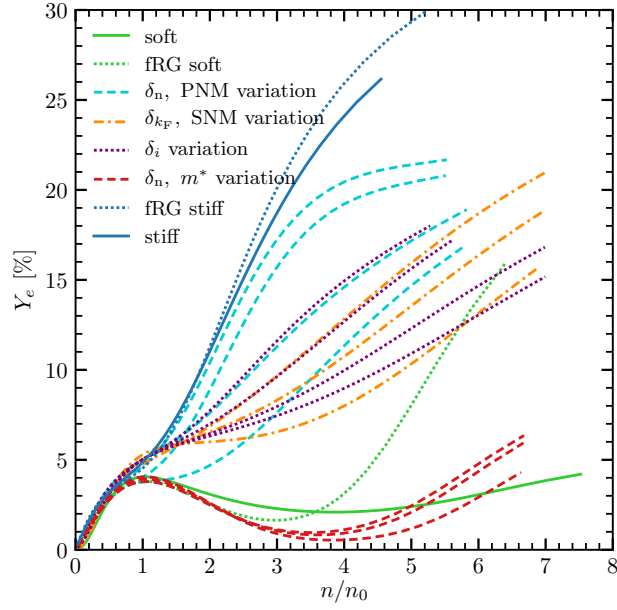


Figure 4.3: Electron fraction as a function of density for the set of representative EOS.

with the constraints from nuclear theory and observation as shown in Fig. 3.15. The chosen EOS are well distributed across the radius uncertainty. As expected, the variation of PNM properties mainly influences the radius of neutron stars and leads to a change of almost 1 km for the radius of a $1.4 M_{\odot}$ neutron star. We find that the density expansion impacts the radius to roughly the same degree and also influences the maximum mass, while SNM properties and the effective mass scenarios result in only a minor change for the radius as well as the maximum mass.

We show the pressure and the speed of sound for neutron star matter as a function of density for the set of representative EOS in Fig. 4.2. The EOS set nicely covers the constraint from Ref. [126] that is shown in gray. We find that those EOS producing large neutron star radii are stiff up to about $4 - 5n_0$ and then become softer at higher densities, while EOS corresponding to small radii are mostly soft in the beginning and become stiff with increasing density to support massive neutron stars. This behavior is also reflected in the speed of sound. Up to roughly $3n_0$, the EOS with large neutron star radii exhibit higher values for the speed of sound, while at densities above $5n_0$ the speed of sound is higher for those EOS that lead to smaller neutron stars. The set of representative EOS shows a wide spread for the electron fraction after twice saturation density as depicted in Fig. 4.3. The electron fraction is strongly influenced by the difference between PNM and SNM such that especially the variations of PNM parameters impacts the electron fraction for neutron star matter.

4.2 Phase diagram of nuclear matter

We calculate the liquid-gas phase transition for asymmetric nuclear matter for the set of representative EOS, see also Sec. 2.5 for a theoretical description on the phase transition. Following Ref. [320], we compute the coexistence boundary via an effective 1-dimensional Maxwell construction, which is easier to solve compared to Eqs. (2.18). In this approach, we set the neutron chemical potential to a specific value, see also Ref. [321] for a similar strategy. This defines the neutron density for a given proton density. Thus, we

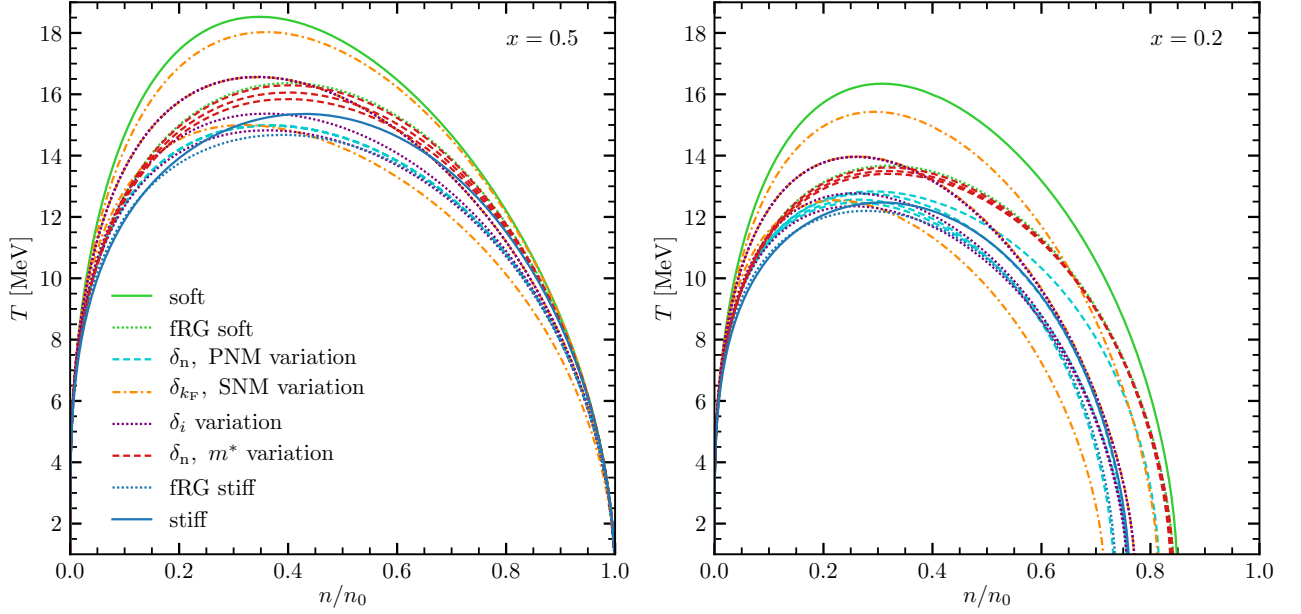


Figure 4.4: Coexistence boundary for the set of representative EOS for $x = 0.5$ (left) and $x = 0.2$ (right).

are able to compute the Maxwell construction for protons only:

$$P(n_{p,g}, T) = P(n_{p,l}, T) , \quad (4.5)$$

$$\mu_{p,g}(n_{p,g}, T) = \mu_{p,l}(n_{p,l}, T) . \quad (4.6)$$

In this case, we have two equations and two unknowns, which are the two proton densities for the liquid and gas phase. After we solved for the proton densities, we can extract the corresponding neutron densities via the fixed neutron chemical potential from the first step. As a result, we have $n_{p,g}$, $n_{p,l}$, $n_{n,g}$, and $n_{n,l}$, which ultimately yields the total density $n = n_n + n_p$ and proton fraction $x = n_p/n$ of the coexistence boundary. The repetition of these steps for different neutron chemical potentials leads to the density of the phase transition for various proton fractions. Similarly, we repeat all steps for different temperatures. To obtain the phase diagram in the density-temperature plane, we interpolate our results for density and proton fraction of the coexistence boundary and extract the values for specific proton fractions at given temperatures.

We depict the coexistence boundary for the set of representative EOS for SNM (left) and neutron-rich matter with $x = 0.2$ (right) in Fig. 4.4. In both cases, we find that the soft EOS shows the largest critical temperature and the fRG soft the smallest. In SNM, the ranges for the critical temperature and critical density are $14.7 - 18.5$ MeV and $0.32 - 0.43 \text{ fm}^{-3}$, respectively. All EOS models end up at the same density n_l of approximately saturation density. As expected, the variation of the effective mass has only a small impact on the phase transition since the EOS below saturation density is almost the same for all m^* scenarios. The critical temperature increases slightly with the high-density limit of the effective mass. The influence of the PNM nuclear matter properties increases when matter becomes more neutron-rich. Consequently, all EOS where only the symmetry energy and slope parameter are changed result in exactly the same phase boundary for SNM, but show a deviation for $x = 0.2$. In particular, a larger symmetry energy leads to a smaller critical temperature with a smaller corresponding critical density, while a smaller slope parameter results in a phase transition that extends to larger densities for. For the two models with the same slope parameter, PNM 31/55 and PNM 34/55, the density of the coexistence boundary are the same at low

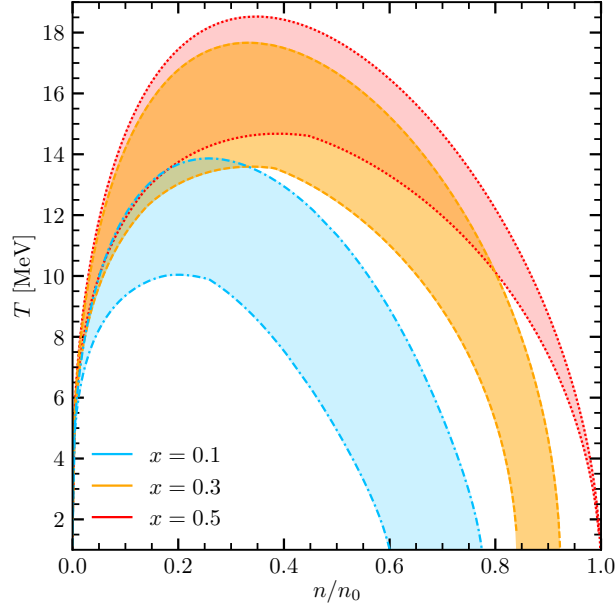


Figure 4.5: Uncertainty of the coexistence boundary for the set of representative EOS and three different proton fractions, $x = 0.1, 0.3, 0.5$.

temperatures. We find a strong correlation of the critical temperature with SNM variations. The critical temperature rises by about 3.5 MeV for both proton fractions when we change the SNM properties from the combination with small incompressibility to the one with large K . The critical density increases as well. Lastly, we analyze the impact of the δ_i variation. The critical density stays almost the same, but the critical temperature is about 2 MeV higher for the EOS models with δ_{k_F} . Here, we see no impact of the d parameter, while for δ_n exponents the larger d value results in a higher critical temperature.

In Fig. 4.5, we show the uncertainty of the phase boundary for the set of representative EOS and three different proton fractions, namely $x = 0.1, 0.3, 0.5$. With increasing proton fraction, the critical temperature as well as the corresponding critical density increase. The difference between two proton fractions becomes larger for smaller proton fractions, i.e. the variation between $x = 0.3$ and $x = 0.5$ is rather small compared to the difference between $x = 0.1$ and $x = 0.3$. The uncertainty of the critical temperature is about 4 MeV for all depicted proton fractions. In particular, for $x = 0.1$ the critical temperature ranges between 10 MeV and 13.9 MeV and the critical density between 0.16 fm^{-3} and 0.26 fm^{-3} . The phase boundary towards dense matter shows a higher deviation for different EOS models when matter is becoming neutron-rich. In fact, for SNM all EOS merge at high roughly saturation density, while for $x = 0.1$ the set of representative EOS covers a density range of almost $0.2n_0$.

4.3 Equation of state construction based on liquid-drop model

There exist several models in order to construct the EOS across a wide range of density, temperature, and proton fraction as present in astrophysical environments. The liquid-drop model and the Thomas Fermi approximation are often used for the EOS for astrophysical applications. Here, we closely follow the description of the LS EOS [275, 276] and employ the liquid-drop model with a single nucleus approximation, see also Ref. [48]. The EOS calculation is performed by Yeunhwan Lim.

4.3.1 Single nucleus approximation

We assume matter to consist of neutrons, protons, alpha particles, one representative heavy nucleus, electrons, positrons, and photons. There are two types of phases, uniform and non-uniform matter. The first one consists of a free gas of nucleons and alpha particles, while in the latter heavy nuclei are formed. We describe this system using Wigner-Seitz cells. Each cell has a volume V_{cell} and is electrostatically neutral. A heavy nucleus is located in the center of a cell and occupies the volume fraction $u = V_N/V_{\text{cell}}$ where V_N is the volume of the nucleus. In the liquid-drop model, heavy nuclei are described as bulk nuclear matter with surface and Coulomb effects. We model the interior of heavy nuclei with constant density n_i and proton fraction x_i . The nucleus is surrounded with a free gas of nucleons and alpha particles. The latter are described as hard spheres of constant volume $V_\alpha = 24 \text{ fm}^{-3}$ that excludes nucleons. Thus, alpha particles occupy the volume fraction $n_\alpha V_\alpha$ in each cell with the alpha particle density n_α . Neutrons and protons outside nuclei with density n_{no} and n_{po} , respectively, are in the remaining volume fraction $u_o = (1 - u)(1 - n_\alpha v_\alpha)$. For consistency, we treat nucleons inside and outside nuclei with the same EOS functional and use the energy density functional and the nucleon effective mass parametrization as introduced in Ch. 3. We further assume matter to be in thermal equilibrium of temperature T .

The total free energy of the system is the sum of the individual constituents

$$F = F_o + F_\alpha + F_h + F_e + F_\gamma . \quad (4.7)$$

We treat leptons and photons as relativistic free gases. The free energy of nucleons outside nuclei is given by

$$F_o = u_o n_o f_B(n_o, x_o, T) \quad \text{with} \quad f_B = E_B/n - T s_B , \quad (4.8)$$

corresponding to our EOS functional. Alpha particles are assumed as non-interacting Boltzman particles as in Lattimer-Swesty with

$$F_\alpha = (1 - u)n_\alpha f_\alpha = (1 - u)n_\alpha(\mu_\alpha - B_\alpha - T) \quad \text{with} \quad \mu_\alpha = T \ln \left[\frac{n_\alpha}{8n_Q} \right], \quad (4.9)$$

where B_α is the binding energy of alpha particles relative to free nucleons and $n_Q = (m_n T/2\pi)^{3/2}$. The pressure of alpha particles is obtained via $P_\alpha = n_\alpha T$.

The free energy of heavy nuclei is the sum of the individual contributions

$$F_h = F_i + F_S + F_C + F_T , \quad (4.10)$$

with the free energy of nucleons inside nuclei $F_i = u n_i f_i$ as given by the EOS functional. The free energy contributions from the surface F_S , Coulomb interaction F_C , and translational energy F_T are finite-size contributions for the description of spherical nuclei and their deformation to pasta phases. In the following, we will explain them in detail.

Surface energy

Inhomogeneous matter is separated into a dense phase corresponding to the nucleus that is surrounded by a dilute phase given by the gas of unbound nucleons and alpha particles. The energy that is stored in the surface between the two phases, i.e. the surface of the nuclei, can be described in terms of the surface area and the surface tension. For spherical nuclei, the surface area is simply given by $4\pi r_N^2$, with the radius of the nucleus r_N , but at higher densities where nuclei are deformed the shape is more involved. To account for these more exotic phases, we parametrize the surface area with the surface shape function $s(u)$ and a generalized nuclear size r_N

$$F_S = \frac{3s(u)}{r_N} \sigma(x_i, T) . \quad (4.11)$$

Following the LS EOS, we do not consider specific shapes such that the surface shape function is an interpolating function that reproduces known limits of the shape of nuclei at low and high densities. To this end, we use $s(u) = u(1 - u)$, which represents spheres at low densities $\lim_{u \rightarrow 0} s(u) = u$ and bubbles at high densities $\lim_{u \rightarrow 1} s(u) = 1 - u$. The surface tension $\sigma(x_i, T)$ depends on the proton fraction inside nuclei x_i and the temperature T . Hereafter, we describe the numerical calculation of the surface tension, which is then approximated with a simple fitting function that is used subsequently for the calculation of the EOS.

For the numerical calculation of the surface tension we consider semi-infinite nuclear matter. In this system, the density varies only along one direction, here we choose the z -axis, while Coulomb effects are ignored. Matter is homogeneous in the other two dimensions. In this description, the surface tension is given by

$$\sigma(x_i, T) = - \int_{-\infty}^{+\infty} [P_o - P(z)] dz . \quad (4.12)$$

The limits at $z \rightarrow \pm\infty$ correspond to the conditions $P(z \rightarrow -\infty) = P_o$ and $P_o = P_i$ for $z \rightarrow +\infty$. We use the finite-range Thomas Fermi model to determine the surface tension for a given EOS. This model is numerically stable and gives the surface tension also as a function of temperature. This model assumes for the interaction energy between nucleons

$$W = -8\pi^3 \int d^3r_1 \int d^3r_2 f(r_{12}/a) \sum_t \left[C_L f_{t_1} f_{t_2} d^3k_{t_1} d^3k_{t_2} + C_U f_{t_1} f_{t_2}' d^3k_{t_1} d^3k_{t_2}' \right] , \quad (4.13)$$

where C_L and C_U are density and momentum dependent functionals between like (L) and unlike (U) particles, $f(r_{12}) = e^{-r_{12}/a}/4\pi r_{12}$ is the effective finite-range function with the distance between two nucleons $r_{12} = |\vec{r}_1 - \vec{r}_2|$, and f_t is the occupation number of a nucleon with isospin $t = (n, p)$,

$$f_t = \frac{1}{1 + \exp(\frac{\varepsilon_t - \mu_t}{T})} , \quad (4.14)$$

with the single particle energy

$$\varepsilon_t = \frac{k^2}{2m_t^*} + V_t , \quad (4.15)$$

as given by our EOS functional. With this, the total energy of the system is $E = K + W$ with the total kinetic energy from neutrons and protons $K = \sum_t \int d^3r \tau_t / 2m_t$. The chemical potential of the nucleons are expressed via the inverse of the Fermi-integral by combining Eq. (4.15) and (4.14)

$$\mu_t = V_t + T F_{1/2}^{-1} \left[2\pi^2 n_t \left(\frac{1}{2m_t^*} \right)^{3/2} \right] . \quad (4.16)$$

We use the Lagrange multiplier method to minimize the free energy density and obtain the surface tension by applying Eq. (4.12).

Similar to the LS EOS, we apply a fitting function for the surface tension given by

$$\sigma(x_i, T) = \sigma_0 h(x_i, T) \frac{2^{1+\lambda} + q}{(1-x)^{-\lambda} + q + x^{-\lambda}} , \quad (4.17)$$

$$h(x_i, T) = \left[1 - \left(\frac{T}{T_c(x_i)} \right)^2 \right]^p . \quad (4.18)$$

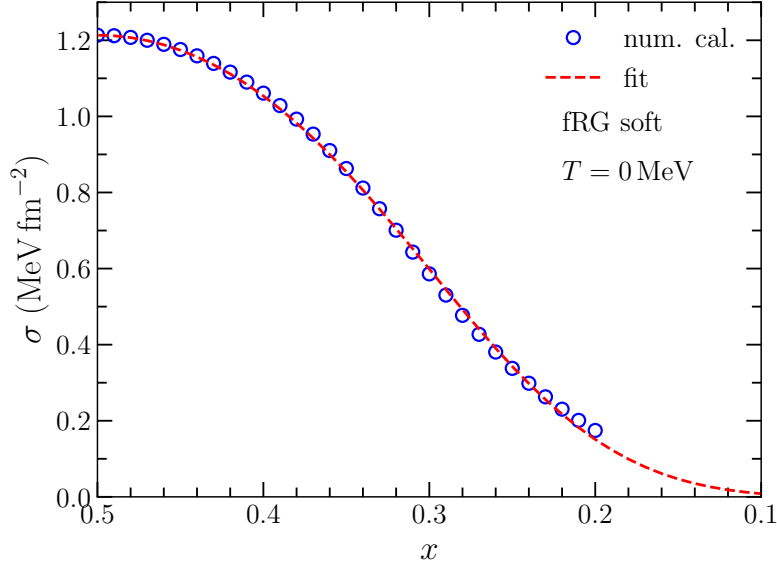


Figure 4.6: Comparison of numerical calculation for the surface tension at $T = 0$ MeV and its fitting function for the fRG soft EOS.

Here, $\sigma_0 = \sigma(x_i = \frac{1}{2}, T = 0)$ is the surface tension of symmetric nuclear matter at zero temperature. This function is only valid for temperatures $T \leq T_c$ as otherwise there are no nuclei. The parameters λ, p, q are determined by fitting the given function to the numerical calculation as explained above. The critical temperature as a function of the proton fraction $T_c(x_i)$ is calculated numerically via solving the equations for the phase transition $P_i = P_o, \mu_{ni} = \mu_{no}, \mu_{pi} = \mu_{po}$. This exact numerical calculation is also fitted via

$$T_c(x) = T_{co}(1 + a\delta^2 + b\delta^4 + c\delta^6) \quad (4.19)$$

where $T_{co} = T_c(x = 0.5)$ is the critical temperature of SNM and $\delta = 1 - 2x$ is the neutron excess.

In Fig. 4.6, we compare our numerical calculation of the surface tension to the fit using Eqs. (4.17) and (4.18) for the fRG soft EOS. We find that the fit function is a suitable approximation to the numerical calculation of the surface tension.

Coulomb energy

For the calculation of the Coulomb energy we assume the charge of the heavy nucleus at the center of the Wigner-Seitz cell and electrons outside of the nucleus. Then, the free energy associated with Coulomb interactions is given by

$$F_C = \frac{4\pi e^2}{5} (x_i n_i r_N)^2 c(u), \quad (4.20)$$

where $c(u)$ is the coulomb shape function and e the electron charge. Since the Coulomb and surface energy are the only contributions that depend on the nuclear size r_N , the minimization of the total free energy with respect to the nuclear size results in the relation $F_S = 2F_C$, which is the nuclear virial theorem. We use this theorem to express the nuclear size as a function of the surface and coulomb shape function. This yields for the sum of the Coulomb and surface free energy

$$F_S + F_C = \beta [c(u)s(u)^2]^{1/3} \equiv \beta \mathcal{D} \quad \text{with} \quad \beta = 9 \left[\frac{\pi e^2}{15} \right]^{1/3} (x_i n_i \sigma(x_i, T))^{2/3} \quad (4.21)$$

Similar to the surface shape function, the coulomb shape function $c(u)$ needs to reproduce known limits. At low densities where nuclei are spherical, the nuclei occupy only a small volume fraction of the cell, such that $\lim_{u \rightarrow 0} c(u) = uD(u)$ with $D(u) = 1 - 3u^{1/3}/2 + u/2$. Just below saturation density the nuclei are deformed to low-density spherical bubbles inside dense nuclear matter. This limit is represented by replacing u with $1 - u$ and, thus, $\lim_{u \rightarrow 1} c(u) = (1 - u)D(1 - u)$. Between both limits, other non-spherical shapes of nuclei minimize the free energy. However, for constructing an EOS with the liquid-drop model, it is practical to use a continuous shape function that approximates the pasta phases rather than treating them explicitly. We use the same shape function as implemented in the LS EOS,

$$\mathcal{D}(u) = u(1 - u) \frac{(1 - u)D^{1/3}(u) + uD^{1/3}(1 - u)}{u^2 + (1 - u)^2 + 0.6u^2(1 - u)^2}, \quad (4.22)$$

where D is given as introduced above.

Translational free energy

The translational energy accounts for the fact that the heavy nucleus is free to move within the Wigner-Seitz cell. In this case, the translational free energy is given as

$$F_T = \frac{u(1 - u)n_i}{A_o} (\mu_T - T)h(x_i, T) \quad \text{with} \quad \mu_T = T \ln \left(\frac{u(1 - u)n_i}{n_Q A^{5/2}} \right), \quad (4.23)$$

with the temperature dependent factor $h(x_i, T)$ from Eq. (4.18) and the average mass number A that we set to a constant $A = A_o = 60$ as in the LS EOS.

4.3.2 Equilibrium conditions

To calculate the EOS at a given baryon density n , proton fraction x , and temperature T , we minimize the free energy with respect to the following variables: density of heavy nucleus n_i , proton fraction of heavy nucleus x_i , density of unbound neutrons n_{no} , density of unbound protons n_{po} , density of alpha particles n_α , and volume fraction of a heavy nucleus u . The system of equations to solve for these variables is

$$n = un_i + (1 - u) [4n_\alpha + (n_{no} + n_{po})(1 - n_\alpha v_\alpha)], \quad (4.24)$$

$$nY_e = un_i x_i + (1 - u) [2n_\alpha + n_{po}(1 - n_\alpha v_\alpha)], \quad (4.25)$$

$$0 = P_i - B_1 - P_o - P_\alpha, \quad (4.26)$$

$$0 = \mu_{ni} - B_2 - \mu_{no}, \quad (4.27)$$

$$0 = \mu_{pi} - B_3 - \mu_{po}, \quad (4.28)$$

$$\mu_\alpha = B_\alpha + 2(\mu_{no} + \mu_{po}) - v_\alpha P_o. \quad (4.29)$$

The first two equations refer to baryon number conservation and charge neutrality, respectively. The three conditions that are equal to zero are obtained from derivatives with respect to the volume fraction and density and proton fraction inside nuclei. The last equation for the chemical potential of alpha particles reflects that alpha particles are in chemical equilibrium with unbound neutrons and protons including a

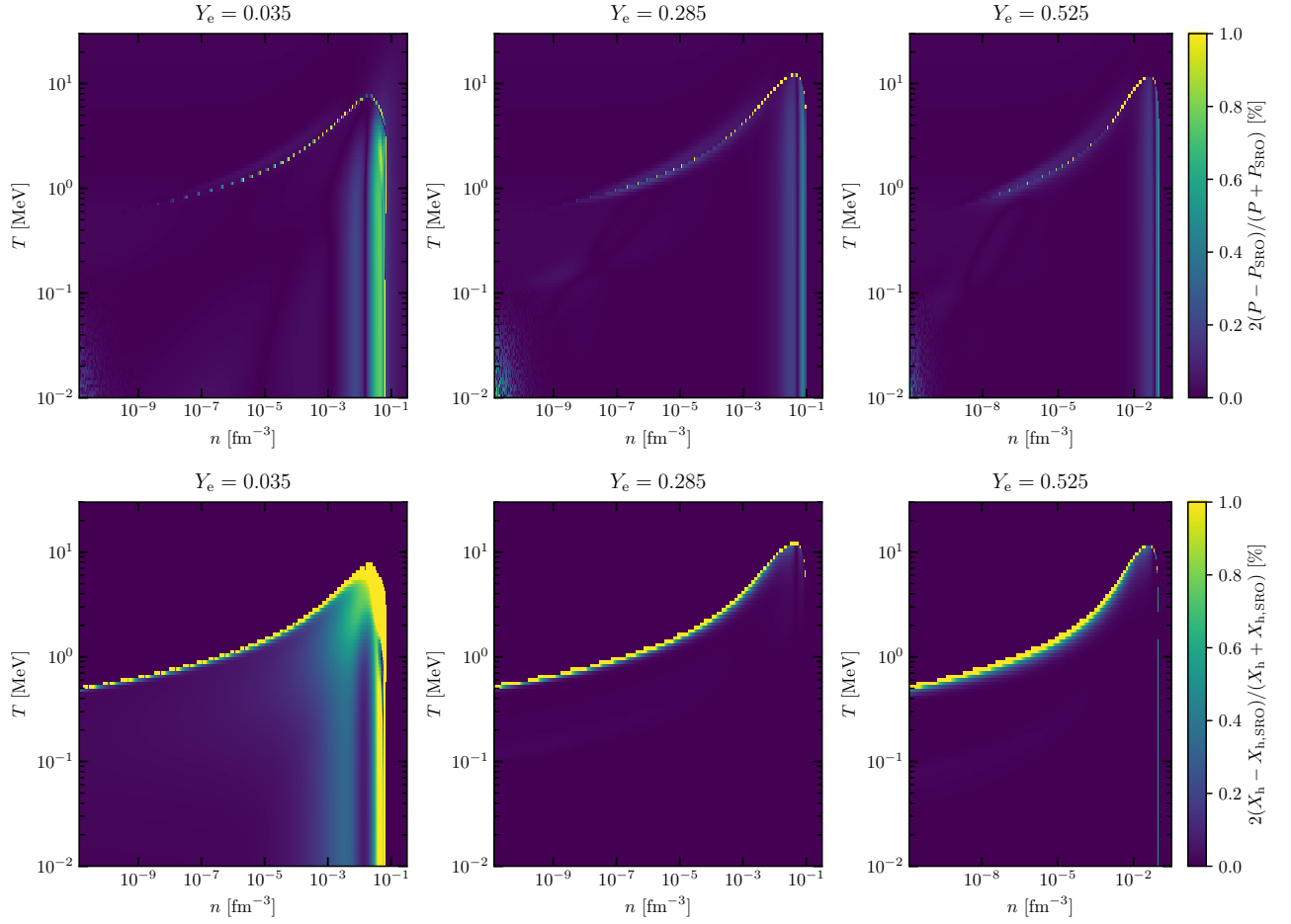


Figure 4.7: Relative difference for the pressure (upper panels) and the fraction of heavy nuclei (lower panels) for three different electron fractions for the LS220 EOS between our EOS calculation and the table computed with the SRO code from Refs. [48, 289].

excluded volume correction. We further used the definitions

$$B_1 = \frac{\partial \hat{F}}{\partial u} - \frac{n_i}{u} \frac{\partial \hat{F}}{\partial n_i}, \quad (4.30)$$

$$B_2 = \frac{1}{u} \left[\frac{x_i}{n_i} \frac{\partial \hat{F}}{\partial x_i} - \frac{\partial \hat{F}}{\partial n_i} \right], \quad (4.31)$$

$$B_3 = -\frac{1}{u} \left[\frac{1 - x_i}{n_i} \frac{\partial \hat{F}}{\partial x_i} + \frac{\partial \hat{F}}{\partial n_i} \right], \quad (4.32)$$

with $\hat{F} = F_S + F_C + F_T$. The solution of this system of equation gives the equilibrium values of the independent variables at a given n, x, T . This then enables the calculation of thermodynamic quantities like the pressure and entropy for the specific condition.

4.3.3 Comparison with Lattimer-Swesty equation of state

We benchmark the EOS construction with the SRO code from Refs. [48, 289] for the LS220 parametrisation as both codes are based on the LS EOS, see also Sec. 2.6. To this end, we calculate an EOS table using the fit parameters of the LS220 EOS and compare all quantities that are necessary for a CCSN simulation. We show the relative difference for the pressure and the fraction of heavy nuclei in Fig. 4.7 for three different electron fractions from very neutron rich up to symmetric matter. The color coding refers to the relative difference between our calculation and the result from the SRO code over the entire density and temperature space of the respective EOS tables. The agreement between the two tables is excellent. We only see differences around the phase transition. This is expected because the treatment of the phase transition is different for the SRO code. In our case, the decision whether uniform or non-uniform matter is present at a given density, temperature, and electron fraction is based on the Maxwell construction as described above. In the SRO code, matter is considered uniform or non-uniform depending on which system results in a lower free energy.

We also compared our results with the LS220 EOS table from Ref. [322], which is constructed using the original LS code from Ref. [323]. We find that in general the relative difference at the phase transition is smaller. Note that low densities and temperatures are calculated via the Timmes EOS [324] for the LS EOS table from Ref. [322]. Consequently, we do find larger differences in these regions. For a comparison between the LS220 EOS from the SRO code and the original LS code, see also Ref. [48].

To validate the implementation of our new EOS functional for the description of unbound nucleons and bulk matter inside nuclei, we compare thermodynamic quantities including the pressure and chemical potentials at different conditions in the n, x, T space. We further find that the phase boundary calculation from the EOS table construction agrees with the computation using our EOS functional, see Sec. 4.2. We conclude that the new EOS and effective mass parametrization are correctly implemented.

4.4 Impact of equation of state in astrophysical simulations

With the implementation of the EOS construction for inhomogeneous matter at hand, we are now able to compute EOS tables for our set of representative EOS to perform CCSN and NSM simulations. This step is currently in progress. Here, we report on a study on the impact of nuclear matter properties in NSM simulations that is mostly based on the analysis of EOS effects in CCSN simulations from Ref. [47]. The NSM simulations are performed by Maximilian Jacobi, see also Refs. [325, 326].

4.4.1 Neutron star mergers

There are many aspects of the nuclear EOS that have an influence on the merger dynamics such as the detailed density dependence of the pressure, thermal effects, and the dependence on the composition. Many studies aim to quantify nuclear physics uncertainties in numerical simulations by employing a small sample of different EOS models, see e.g. Refs. [327, 28, 328], thereby varying many of the above mentioned aspects at the same time. While this approach is useful to reveal correlations with the general stiffness of the EOS, the impact of its specific features cannot be studied this way. Only a few works have focused on the dependence of neutron star mergers on individual aspects of the EOS. For example, Ref. [329] investigated the impact of the slope of the symmetry energy on the post-merger dynamics, while Refs. [261, 330, 331] investigated the temperature dependence by changing the thermal pressure independently from the cold EOS.

In this work, we individually vary different nuclear matter properties in 3D general relativistic simulations of merging binary neutron stars. We use the EOS from the study of EOS effects in CCSN simulations,

EOS	$m^*(n_0)/m_n$	B	K	E_{sym}	L	n_0	$\tilde{\Lambda}$	$R_{1.4}$
LS175 [†]	1.0	16.0	175	29.3	73.7	0.155	358.9	12.1
LS220 [†]	1.0	16.0	220	29.3	73.7	0.155	606.2	12.7
LS255 [†]	1.0	16.0	255	29.3	73.7	0.155	661.1	13.0
$m_{0.8}^*$	0.8	16.0	220	29.3	79.3	0.155	698.4	12.9
m_{S}^*	0.634	16.0	220	29.3	86.5	0.155	765.4	13.2
$(m^*, K)_{\text{S}}$	0.634	16.0	281	29.3	86.5	0.155	975.0	13.5
$(m^*, K, E_{\text{sym}})_{\text{S}}$	0.634	16.0	281	36.9	109.3	0.155	1090.5	14.1
SkShen	0.634	16.3	281	36.9	109.4	0.145	1295.5	14.5
Shen	0.634	16.3	281	36.9	110.8	0.145	1220.8	14.5

Table 4.2: The nuclear matter parameters B , K , E_{sym} , and L are given in MeV, the saturation density n_0 is given in fm^{-3} and the radius of a $1.4 M_{\odot}$ neutron star is given in km. The value of the tidal deformability $\tilde{\Lambda}$ refers to the neutron star masses used in the simulations, $1.365 M_{\odot}$.

which we discussed in Sec. 2.6.2. We add two additional EOS computed with the SRO code where only the incompressibility is changed, labelled LS175[†] and LS255[†]. This set of EOS enables us to study the impact of the effective nucleon mass, the incompressibility, the symmetry energy and the saturation point separately. The nuclear matter properties, tidal deformability $\tilde{\Lambda}$, and the radius of a $1.4 M_{\odot}$ neutron star are summarized in Tab. 4.2. The simulations of Maximilian Jacobi to model binary neutron star systems are carried out in the framework of the `EinsteinToolkit` suite [332, 333], which is based on the `Carpet` computational toolkit [334]. To handle general relativistic hydrodynamics we employ the `WhiskyTHC` code [335, 336, 337]. We perform one simulation per EOS, where each model initially consists of two $1.365 M_{\odot}$ irrotational neutron stars on quasi circular orbits with initial separation of 45 km. This combination corresponds to a chirp mass of $1.188 M_{\odot}$ and is compatible with the GW source of GW170817.

The time evolution of the maximum density inside the neutron star is shown in Fig. 4.8. The newly formed remnant is in a highly deformed state and is initially oscillating, which is imprinted in the maximum density. In the model LS175[†], a black hole is formed immediately after merger, while for LS220[†], the remnant oscillates several times before it collapses. In both cases, the lower incompressibility reduces the pressure at high density and the merged object is not able to support its mass against gravitational collapse. In other models the pressure in the center of the neutron star is large enough to stop the contraction of the remnant before a black hole is formed. In general, the final central density is larger for EOS with lower pressures at high density. In LS255[†], the dependency of the pressure on density is steeper due to the higher incompressibility such that the contraction of the remnant stops already after 10 ms. The remnant in the simulations $m_{0.8}^*$ and m_{S}^* on the other hand keep contracting for longer, which is visible due to the increase in central density. Increasing the symmetry energy shows almost no effect on the density in the center of the remnant. Changing the binding energy and saturation density (SkShen) results in a lower central density and initially in a lower remnant temperature.

The lower panel of Fig. 4.8 shows the evolution of the average temperature inside the remnant as a function of time. In LS220[†], the remnant is heated up much more than in the non-collapsing cases due to the increasingly violent oscillations. In the case of the non-collapsing remnants the average temperature is correlated with the maximum density because stiffer EOS result in a less violent merger and reduced

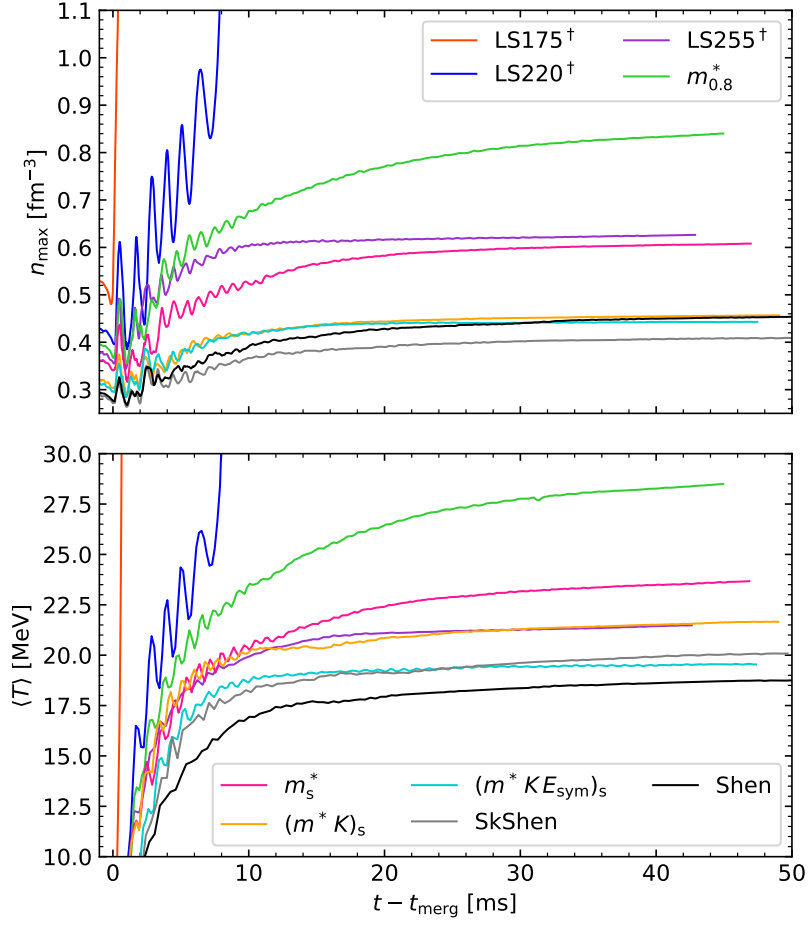


Figure 4.8: Maximum density (upper panel) and average remnant temperature (lower panel) as a function of time after merger.

shock heating. However, comparing LS255[†] with m_s^* and $(m^*, K)_s$ shows a deviation from this trend. The central density in the model LS255[†] is higher than in m_s^* and $(m^*, K)_s$, but the average remnant temperature is lower than in m_s^* and similar to $(m^*, K)_s$. This is because of the larger values of Γ_{th} for models with lower effective mass, which increases the shock heating efficiency, see also [330]. In general, the implications due to the increased incompressibility for LS255[†] are seen as well when comparing m_s^* and $(m^*, K)_s$. Unlike in the models $(m^*, K)_s$ and $(m^*, K, E_{\text{sym}})_s$, the average remnant temperature in SkShen keeps increasing and is thus eventually larger than in $(m^*, K, E_{\text{sym}})_s$. Compared to the original Shen EOS, SkShen leads to a lower central density, which can be attributed to smaller pressures above $2n_0$ for SkShen. The average remnant temperature is larger in SkShen because it has a larger thermal index than the Shen EOS. Nevertheless, the remnant evolution for the SkShen and Shen is remarkably similar. In total, the central densities of the remnant vary between $\sim 2.5 - 5n_0$ at the end of the simulation.

5 Constraining neutron-star matter with microscopic and macroscopic collisions

So far, the equation of state for neutron star matter is constrained by nuclear theory calculations and astrophysical observations. Terrestrial heavy-ion collision experiments also probe dense matter, see Sec. 2.3. In this work, we use Bayesian inference to combine data from nuclear theory, astrophysical observations of neutron stars, and results from HIC experiments that were performed at the Schwerionensynchrotron 18 (SIS-18) accelerator located at the GSI Helmholtz Centre for Heavy Ion Research in Darmstadt to further constrain the EOS in a density range for which theoretical calculations become less reliable. This work was performed in collaboration with Peter T. H. Pang, Ingo Tews, and others and is published in Ref. [163]. My contribution has focused on the implementation of EOS constraints from information of HIC experiments. Additionally, in Sec. 5.6, we combine our findings for the constraints from heavy-ion collisions with the EOS functional derived in Ch. 3.

At densities below $1-2n_0$, the EOS and its theoretical uncertainty can be obtained from microscopic calculations based on chiral EFT of QCD [4, 167, 168, 169, 170, 73]. To probe dense matter beyond these densities, further approaches, based on experimental and observational data, are necessary. A very promising tool is the multi-messenger astrophysics analysis of neutron stars and their collisions, which provides access to dense neutron-rich matter not accessible in terrestrial experiments at present. In recent years, the advent of GW astronomy [66] and new electromagnetic (EM) observations of neutron stars [136, 122, 121], including the NICER mission of NASA [122, 121], led to new constraints on the EOS [67, 68, 69, 70, 150, 71, 72, 151, 124, 152]. However, these observations mainly probe the EOS at densities $\gtrsim 2n_0$ and still carry considerable uncertainties, reflected in the ranges for predictions of neutron-star radii. More precise or new complementary information are required to reduce the uncertainties further. The gap between our current knowledge of the EOS stemming from nuclear theory and experiment at low densities and astrophysical observations of neutron stars at higher densities can be bridged by HIC experiments. These experiments, performed with heavy-ion beam energies of up to 2 GeV per nucleon, probe the nuclear EOS mainly in a density range of $1-2n_0$ at present [246, 249, 256], representing a new source of information [338].

5.1 Nuclear theory input

Our analysis starts with a set of 15,000 EOSs that are constrained by nuclear theory calculations at low densities from Ingo Tews. In particular, we employ calculations using local chiral EFT interactions [168, 177]. Based on local chiral two- and three-nucleon interactions, we use quantum Monte Carlo methods, which are among the most precise many-body methods to solve the nuclear many-body problem [198]. The 15,000 EOSs are sampled such that they span the theoretical uncertainty range of the chiral EFT calculation. The breakdown scale of the chiral EFT expansion was estimated to be $\sim 500-600$ MeV [170]. Therefore, we constrain our EOS set using chiral EFT input only up to $1.5n_0$ (corresponding to Fermi momenta of the order of 400 MeV) but a variation within $1-2n_0$ shows no substantial impact on our final results for neutron-star radii [339], see also Tab. 5.1. Applying constraints from chiral EFT only up to $1n_0$ allows

for a broader and stiffer EOS prior at higher densities since information up to $1.5n_0$ is discarded. As a consequence, the EOSs including HIC only and to a lesser extent the combination of HIC and observational constraints become stiffer leading to an increase of neutron-star radii. This effect is larger when using a natural instead of a uniform prior in radius.

Table 5.1: Comparison of the 95% credible interval for the pressure [MeV fm^{-3}] and radius [km] of neutron stars when including only HIC experiments, only astrophysical observations, or the combined HIC and astrophysics results for chiral EFT constraints up to $1.5n_0$ and up to $1n_0$, and for using a natural and uniform prior on $R_{1.4}$. We find that differences for pressures and neutron-star radii are small between both prior choices when Astro+HIC data constraints are employed.

		Natural prior on $R_{1.4}$					
P/R	Chiral EFT up to $1.5n_0$			Chiral EFT up to $1n_0$			
	HIC only	Astro only	Astro+HIC	HIC only	Astro only	Astro+HIC	
$1.0n_0$	$2.05^{+0.49}_{-0.45}$	$2.00^{+0.52}_{-0.49}$	$2.11^{+0.49}_{-0.52}$	$1.95^{+0.51}_{-0.39}$	$1.87^{+0.51}_{-0.41}$	$1.95^{+0.50}_{-0.43}$	
$1.5n_0$	$6.06^{+1.85}_{-2.04}$	$5.84^{+1.96}_{-2.26}$	$6.25^{+1.90}_{-2.26}$	$10.77^{+29.80}_{-8.81}$	$8.98^{+8.41}_{-4.30}$	$9.12^{+6.66}_{-4.36}$	
$2.0n_0$	$19.47^{+33.63}_{-11.67}$	$18.44^{+16.24}_{-9.69}$	$19.07^{+15.27}_{-10.53}$	$33.02^{+76.25}_{-31.06}$	$26.11^{+24.36}_{-17.81}$	$26.21^{+21.85}_{-17.16}$	
$2.5n_0$	$47.78^{+75.96}_{-32.96}$	$45.05^{+39.80}_{-19.62}$	$45.43^{+40.41}_{-19.11}$	$68.31^{+114.74}_{-66.35}$	$54.19^{+38.50}_{-20.67}$	$54.33^{+35.54}_{-21.69}$	
$1.0M_\odot$	$11.89^{+0.79}_{-0.98}$	$11.76^{+0.65}_{-0.71}$	$11.88^{+0.57}_{-0.76}$	$12.68^{+1.44}_{-1.41}$	$12.36^{+0.95}_{-0.90}$	$12.40^{+0.85}_{-0.89}$	
$1.4M_\odot$	$12.06^{+1.13}_{-1.18}$	$11.94^{+0.79}_{-0.78}$	$12.01^{+0.78}_{-0.77}$	$12.96^{+1.87}_{-1.84}$	$12.53^{+1.22}_{-1.03}$	$12.56^{+1.07}_{-1.01}$	
$1.6M_\odot$	$12.11^{+1.33}_{-1.33}$	$11.98^{+0.93}_{-0.79}$	$12.03^{+0.98}_{-0.75}$	$13.05^{+2.11}_{-2.08}$	$12.55^{+1.31}_{-1.10}$	$12.57^{+1.22}_{-1.04}$	
$2.0M_\odot$	$12.19^{+1.71}_{-1.59}$	$11.88^{+1.23}_{-1.10}$	$11.91^{+1.24}_{-1.11}$	$13.21^{+2.53}_{-2.38}$	$12.32^{+1.58}_{-1.49}$	$12.33^{+1.56}_{-1.44}$	
		Uniform prior on $R_{1.4}$					
P/R	Chiral EFT up to $1.5n_0$			Chiral EFT up to $1n_0$			
	HIC only	Astro only	Astro+HIC	HIC only	Astro only	Astro+HIC	
$1.0n_0$	$2.05^{+0.46}_{-0.54}$	$1.92^{+0.64}_{-0.45}$	$2.18^{+0.43}_{-0.68}$	$1.98^{+0.49}_{-0.40}$	$1.90^{+0.52}_{-0.43}$	$2.00^{+0.49}_{-0.46}$	
$1.5n_0$	$6.12^{+1.75}_{-2.43}$	$5.56^{+2.45}_{-2.15}$	$6.57^{+1.66}_{-2.92}$	$9.11^{+42.6}_{-7.53}$	$8.22^{+6.51}_{-5.53}$	$8.58^{+6.62}_{-5.70}$	
$2.0n_0$	$17.04^{+46.81}_{-12.56}$	$18.19^{+27.15}_{-12.37}$	$19.93^{+29.61}_{-12.96}$	$23.84^{+100.12}_{-22.25}$	$22.56^{+21.12}_{-18.76}$	$23.45^{+21.97}_{-18.10}$	
$2.5n_0$	$38.39^{+98.48}_{-34.37}$	$44.28^{+47.06}_{-24.88}$	$47.03^{+52.26}_{-22.44}$	$48.34^{+154.87}_{-46.75}$	$46.39^{+38.20}_{-31.12}$	$47.89^{+37.10}_{-32.47}$	
$1.0M_\odot$	$11.70^{+1.25}_{-2.23}$	$11.72^{+0.91}_{-0.89}$	$11.96^{+0.78}_{-1.02}$	$12.27^{+1.92}_{-3.01}$	$12.15^{+1.07}_{-1.39}$	$12.25^{+1.04}_{-1.41}$	
$1.4M_\odot$	$11.81^{+1.62}_{-2.30}$	$11.90^{+1.18}_{-0.92}$	$12.08^{+1.18}_{-0.94}$	$12.32^{+2.60}_{-2.89}$	$12.22^{+1.31}_{-1.42}$	$12.33^{+1.26}_{-1.52}$	
$1.6M_\odot$	$11.81^{+1.86}_{-2.33}$	$11.94^{+1.37}_{-0.96}$	$12.10^{+1.34}_{-1.02}$	$12.29^{+2.93}_{-2.87}$	$12.20^{+1.44}_{-1.43}$	$12.30^{+1.42}_{-1.50}$	
$2.0M_\odot$	$12.37^{+1.82}_{-2.69}$	$11.82^{+1.71}_{-1.27}$	$11.97^{+1.80}_{-1.27}$	$12.92^{+3.04}_{-3.22}$	$11.88^{+1.85}_{-1.57}$	$11.94^{+1.85}_{-1.59}$	

We extend each EOS above $1.5n_0$ using an extrapolation in the speed of sound (c_s) in neutron-star matter [340], see also Greif *et al.* [176]. To construct the neutron-star EOS set, we first extend our chiral EFT calculation to β -equilibrium and add a crust [341]. Above $1.5n_0$ density, we sample a set of six randomly distributed points in the speed of sound plane at baryon densities between $1.5n_0$ and $12n_0$, enforcing $0 \leq c_s \leq 1$ at each point. A variation of the number of sampled points between 5-10 does not

impact our findings. We then connect these points by line segments, reconstruct the EOS, and solve the Tolman-Oppenheimer-Volkoff equations to extract neutron-star properties. Additionally, for each EOS we construct a partner EOS that includes a segment with vanishing speed of sound to explicitly simulate strong first-order phase transitions. We sample the onset density and width of this segment randomly.

Our EOS set includes 15,000 different EOS samples where the prior on the radii of neutron stars is naturally determined by the EOS expansion scheme. We have explicitly checked the differences among a prior uniform in the radius of a typical $1.4M_{\odot}$ neutron star and the “natural” prior and found only minor changes up to around 5% once astrophysical and HIC data are included, see Tab. 5.1.

The extrapolation to high densities is only constrained by causality ($c_s \leq 1$) and stability of neutron-star matter ($c_s \geq 0$). In contrast to Refs. [68, 69], we do not take into account any information at asymptotically high densities from perturbative QCD calculations. In addition, at this level we require all EOSs in the prior to support neutron stars with masses of at least $1.9M_{\odot}$, to remove EOSs that only support neutron stars with maximum masses well below the lower limit from the combined observations of heavy pulsars [7, 342, 9]. Hence, this lower bound ensures that the resulting EOS prior has reasonable support for massive-pulsar observations that we include at the first state of our Bayesian framework [72]). These general assumptions lead to a broad uncertainty for the EOS at higher densities (see Fig. 5.1A), as well as for neutron-star masses and radii (see Fig. 5.2A). The EOS prior is then used to analyse astrophysical observations and HIC experiments.

5.2 Multi-messenger astrophysics information

To constrain the set of EOSs derived from chiral EFT with astrophysical data, a multi-step Bayesian multi-messenger framework [72, 343] has been used in which results from individual steps are used as prior for the next part of the analysis [72], see Fig. 5.3. Here, each EOS is analyzed with respect to its agreement with a variety of observational data. First, we incorporate constraints on the maximum mass of neutron stars. For this, we implement the mass measurements of the heavy radio pulsars PSR J0348+0432 [7] and PSR J1614-2230 [342]. We do not include the mass measurement of PSR J0740+6620 [9] since we make use of the NICER and XMM mass-radius information of PSR J0740+6620 [124, 123] at a later stage. This procedure avoids double counting. The combination of these observations [72, 344] of high-mass neutron stars provides a lower bound on the maximum mass of neutron stars. In contrast, an upper bound of the maximum mass is obtained from the observation of the merger remnant of the neutron-star merger GW170817 [89]. Among other arguments, the observation of a bright, red kilonova component and the observation of a short gamma-ray burst 2 seconds after the merger of the two neutron stars indicate that the remnant experienced a delayed ($\mathcal{O}(100\text{ms})$) collapse to a black hole, so that an upper limit on the maximum mass can be derived. The combined estimate of the maximum mass, $2.21^{+0.10}_{-0.13}M_{\odot}$ at 68% uncertainty, already provides important information about the internal structure of neutron stars and disfavors both too stiff and too soft EOSs, i.e., EOSs with too large and too small pressures, respectively.

Next, NICER’s mass and radius measurement of PSR J0030+0451 [122] and PSR J0740+6620 [124, 123] are incorporated. In addition to NICER, the XMM-Newton telescope [345, 346] has been used for the analysis of PSR J0740+6620 [124] to improve the total flux measurement. For PSR J0740+6620, we average over the results obtained by Miller *et al.* [124] and Riley *et al.* [123], while for PSR J0030+0451 we only use results of Miller *et al.* [122].

Next, GW information from the two neutron-star mergers GW170817 [66] and GW190425 [157] are analysed with Bayesian inference techniques by matching the observed GW data with theoretical GW models that depend on neutron-star properties. Here, a GW model [347] is used that is an improved version of the main waveform model employed by the LIGO/Virgo Collaboration for the study of GW170817 [299] and GW190425 [157]. Similarly to the GW analysis, we also include information from the kilonova

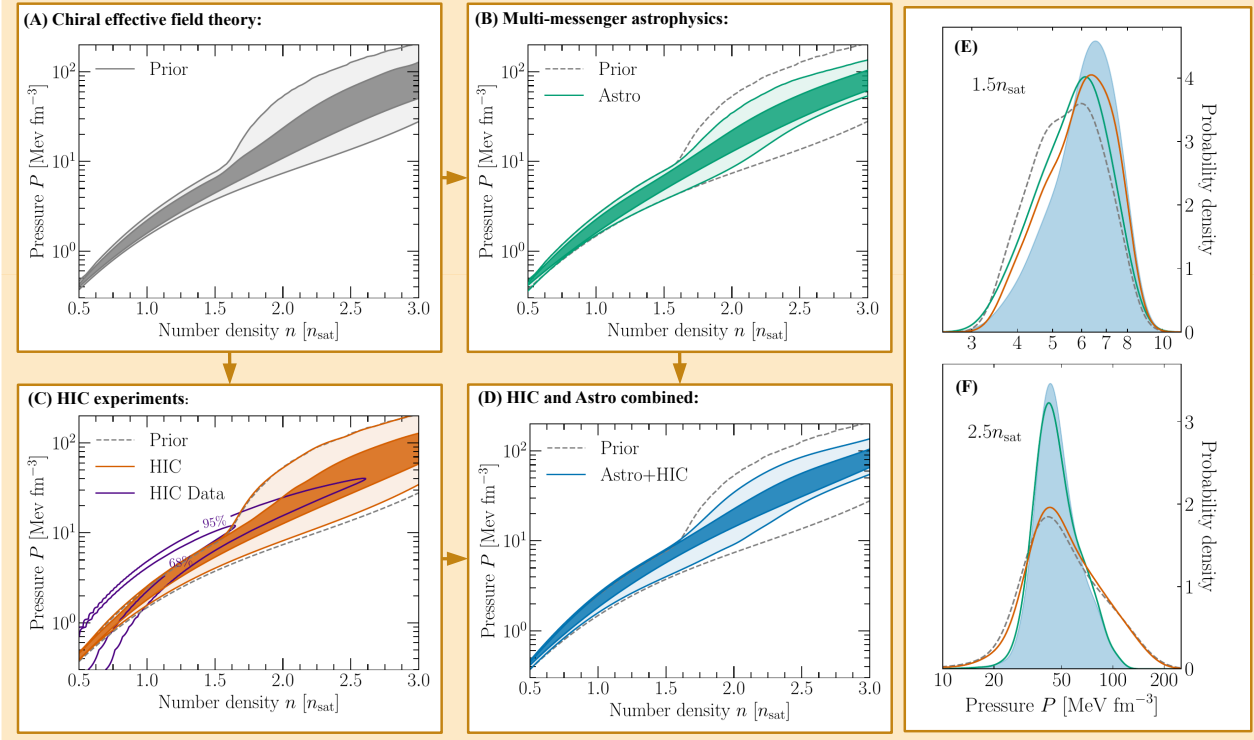


Figure 5.1: Evolution of the pressure as a function of baryon number density for the EOS prior (A, gray), when including only data from multi-messenger neutron-star observations (B, green), when including only HIC data (C, orange), and when combining both (D, blue). The shading corresponds to the 95% and 68% credible intervals (lightest to darkest). The impact of the HIC experimental constraint (HIC Data, purple lines at 95% and 68%) on the EOS is shown in panel C. In panels (B) through (D), we show the 95% prior bound for comparison (gray dashed lines). We also show posterior distributions for the pressure at $1.5n_0$ and $2.5n_0$ at different stages of our analysis (E, F), where the combined Astro+HIC region is light-blue shaded.

AT2017gfo [136] associated with the GW signal. To test the robustness of the GW analysis, we have explored a number of different GW models and found only a minimal impact on the final EOS constraint [72].

The above astrophysical information leads to important constraints on the neutron-star EOS, as shown in Fig. 5.1B. The constraints are strongest above $1.5n_0$, where the extrapolation in the speed of sound is used for the EOSs. The high-density astrophysical constraints affect mostly the high-mass region in the mass-radius plane and exclude the stiffest EOSs that lead to the largest radii, see Fig. 5.2B.

5.3 Data from heavy-ion collision experiments

To further constrain the EOS, we implement data from HIC experiments. The FOPI [249] and ASY-EOS [256] experiments performed at GSI provide information respectively on the symmetric nuclear matter EOS, i.e., matter with the same amount of protons and neutrons, and on the symmetry energy, which describes the energy cost of changing protons into neutrons in nuclear matter. For both experiments, ^{197}Au nuclei were collided at relativistic energies (0.4 to 1.5 GeV/nucleon), forming an expanding fireball in the collision region. This expansion is dictated by the achieved compression and therefore depends on the EOS of hot and dense matter. Due to the initial neutron-to-proton asymmetry of the Au-Au system, the

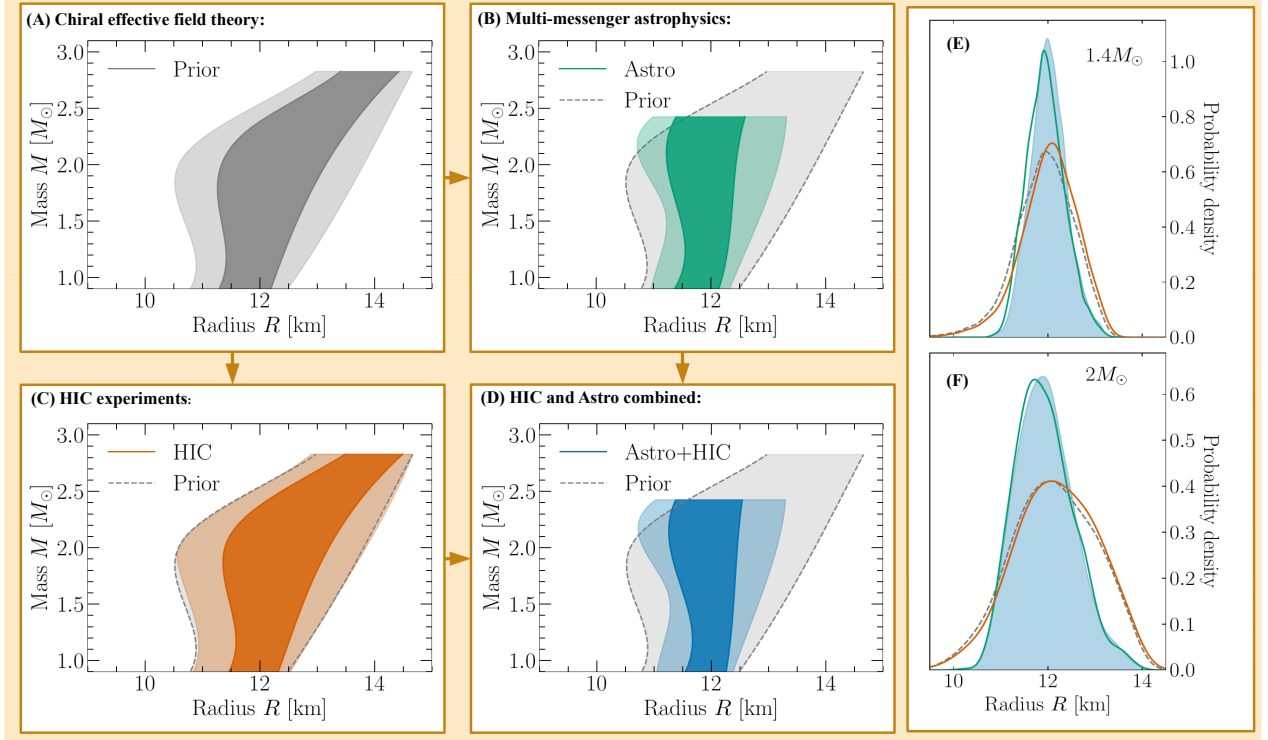


Figure 5.2: We show the 95% and 68% credible ranges for the neutron-star radius across various masses (up to the 95% upper bound on the maximum allowed mass, as only few EOSs support mass beyond that, which would result in an unrepresentative credible range) for the prior (A, gray), when including only multi-messenger constraints (B, green), when including only HIC experiment data (C, orange), and for the joint constraint (D, blue). We show the prior 95% contour in panels (B)-(D) for comparison. Posterior distributions for the radii of $1.4M_{\odot}$ and $2M_{\odot}$ stars are given at different stages of our analysis (E, F), where the combined Astro+HIC region is light-blue shaded.

expansion of the emitted nucleons is sensitive to the nuclear symmetry energy. Constraints on the symmetry energy (from ASY-EOS) can be translated into a constraint on the pressure of neutron-star matter as a function of the baryon density when empirical information on symmetric nuclear matter from experiments (FOPI) with atomic nuclei is used.

Using FOPI data on the elliptic flow in gold-gold collisions between 400 MeV and 1.5 GeV/nucleon, thanks to the broad acceptance of the detector, an enhanced precision in the determination of the EOS could be achieved. Including the full rapidity and transverse momentum dependence of the elliptic flow of protons and heavier isotopes [249] in the analysis with the Isospin-QMD (IQMD) transport model, the incompressibility was determined as $K = 190 \pm 30$ MeV. This result was confirmed by interpreting the same data with three Skyrme energy-density functionals introduced into the ultrarelativistic QMD (UrQMD) transport model [229], leading to $K = 220 \pm 40$ MeV. The interval of confidence used in the present study, $K = 200 \pm 25$ MeV, reflects both predictions. The densities probed were estimated to range between $1-3n_0$ by analyzing the densities effective in building the elliptic flow in IQMD simulations [249]. We note that the value of K has very little influence on the observables measured by ASY-EOS to extract the symmetry energy [348]. Note that the constraints deduced from the analysis of elliptic flow are compatible with earlier findings of the Kaon Spectrometer (KaoS) Collaboration obtained from comparisons of QMD

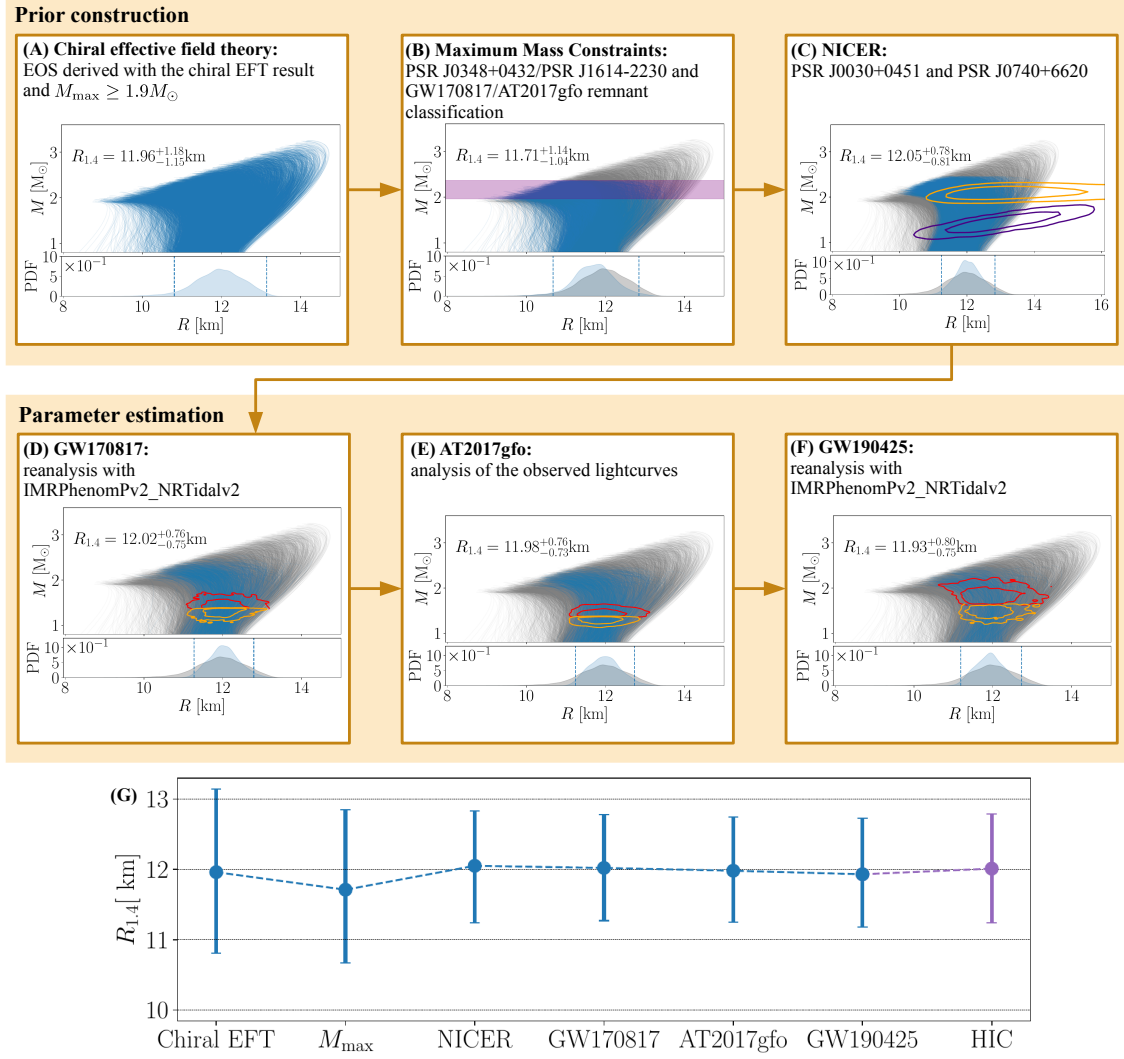


Figure 5.3: In each panel (except for panel A), EOSs within (outside of) 95% credible interval are shown as blue (gray) lines. Lower panels indicate the probability distribution function (PDF) for the radius of a $1.4M_{\odot}$ neutron star, with the 95% confidence range indicated by dashed lines, in panels (B)-(F) the prior from panel (A) is shown in grey. (A) The EOS prior set constrained by chiral EFT calculations up to $1.5n_0$ and $M_{\max} \geq 1.9M_{\odot}$. (B) The EOS set restricted by incorporating information from mass measurements of PSR J0348+0432, PSR J1614-2230, and the maximum-mass constraints obtained from GW170817/AT2017gfo. The 95% confidence interval of the maximum mass posterior probability distribution is shown by the purple band. (C) The EOS set further restricted by the NICER mass-radius measurement of PSR J0030+0451 (purple contours at 68% and 95% confidence) and PSR J0740+6620 (orange contours at 68% and 95% confidence). Note that the latter shows the average of the results obtained by Miller *et al.* [124] and Riley *et al.* [123]. (D) Further restrictions on the EOS set from a reanalysis of the GW170817 using Bayesian inference. Contours at 68% and 95% confidence show the mass-radius measurements of the primary (red) and secondary (orange) neutron stars. (E) We use the chirp mass, mass ratio, and the EOSs as Bayesian prior for our analysis of AT2017gfo. (F) Further restrictions by analysing GW190425. Again, contours at 68% and 95% confidence show the mass-radius measurements of the primary (red) and secondary (orange) neutron stars. (G) The radius constraint at each step of this analysis with 95% confidence ranges. The radius constraint after including HIC experimental data is also shown.

predictions with experimental K^+ meson production yields from gold-gold and carbon-carbon collisions performed at GSI between 0.6 and 1.5 GeV/nucleon [349, 350].

The ASY-EOS experiment was performed at GSI in Darmstadt, studying collisions of gold nuclei of 400 MeV/nucleon incident energy and gold targets. The description of the experiment and the analysis with the UrQMD transport model are given in detail in Russotto *et al.* [256]. ASY-EOS benefited from the Large-Area Neutron Detector (LAND) [351] permitting the detection of neutrons and charged particles within the same acceptance. Its isotopic resolution in this experiment was not sufficient to uniquely identify protons. Elliptic flow ratios were, therefore, determined for neutrons with respect to all charged particles within the LAND acceptance. We note that for the selected collisions and angular region, the yield of charged particles consists of light isotopes, mainly protons (around 50%) according to FOPI data for the same reaction. Confronted with UrQMD transport model predictions (and confirmed with other models, IQMD [251] and Tübingen QMD (TüQMD) [348]), the resulting flow ratio enabled deducing a constraint for the symmetry energy, which is so far the most precise for supra-saturation densities obtained from HICs. As indicated by QMD model predictions, densities probed by the elliptic flow ratio in the ASY-EOS experiment extend up to about $2n_0$.

5.3.1 Implementation of nuclear equation of state constraints from heavy-ion collisions

For analysing the experimental elliptic flow data, an EOS functional needs to be fed into the QMD simulations for both symmetric and asymmetric nuclear matter. For the analysis of the FOPI experiment, symmetric nuclear matter has been parameterised with

$$\frac{E}{A}(n, 0) = \frac{3}{5} \left(\frac{n}{n_0} \right)^{2/3} E_F + \frac{\alpha n}{2n_0} + \frac{\beta}{\gamma + 1} \left(\frac{n}{n_0} \right)^\gamma, \quad (5.1)$$

with the saturation density n_0 , the Fermi energy E_F , and where the parameters α , β , and γ are fixed by the incompressibility K , the binding energy B of symmetric nuclear matter at n_0 , and the condition that the pressure of symmetric nuclear matter is zero at saturation density:

$$\alpha = -2 \left(\frac{K + \frac{6E_F}{5}}{9(\gamma - 1)} + \frac{2}{5} E_F \right), \quad \beta = \left(K + \frac{6}{5} E_F \right) \frac{\gamma + 1}{9\gamma(\gamma - 1)}, \quad \gamma = \frac{K + \frac{6E_F}{5}}{9 \left(\frac{E_F}{5} + B \right)}. \quad (5.2)$$

In the ASY-EOS analysis, the symmetry energy as a function of density has been parameterised as

$$S(n) = E_{\text{kin},0} \left(\frac{n}{n_0} \right)^{2/3} + E_{\text{pot},0} \left(\frac{n}{n_0} \right)^{\gamma_{\text{asy}}}. \quad (5.3)$$

At saturation density, the kinetic part has been set to $E_{\text{kin},0} = 12$ MeV and $E_{\text{pot},0} = E_{\text{sym}} - E_{\text{kin},0}$. The parameter γ_{asy} was extracted from fits to experimental data of the p_t dependence of the elliptic flow ratio of neutrons over charged particles around mid-rapidity. In particular, this results in $\gamma_{\text{asy}} = 0.68 \pm 0.19$ for $E_{\text{sym}} = 31$ MeV and $\gamma_{\text{asy}} = 0.72 \pm 0.19$ for $E_{\text{sym}} = 34$ MeV. In Fig. 5.4, we compare the constraint from the HIC experiments (red area) with various microscopic neutron matter calculations as introduced in Sec. 3.1.1. Overall, they are in good agreement for $n \gtrsim n_0$, but the HIC constraint also allows rather low energies at smaller densities. This behavior can be attributed to the simple form of the parametrization for the symmetry energy (Eq. (5.3)) and the fact that the uncertainty of γ_{asy} is density independent. Here, we interpolate γ_{asy} assuming a linear function with E_{sym} , where the uncertainty is chosen to be 0.19 independent of E_{sym} . In Fig. 5.5, we have studied the behavior of γ_{asy} as a function of S_0 for two different QMD models. In particular, we compare the results from the UrQMD model that is used in the analysis of

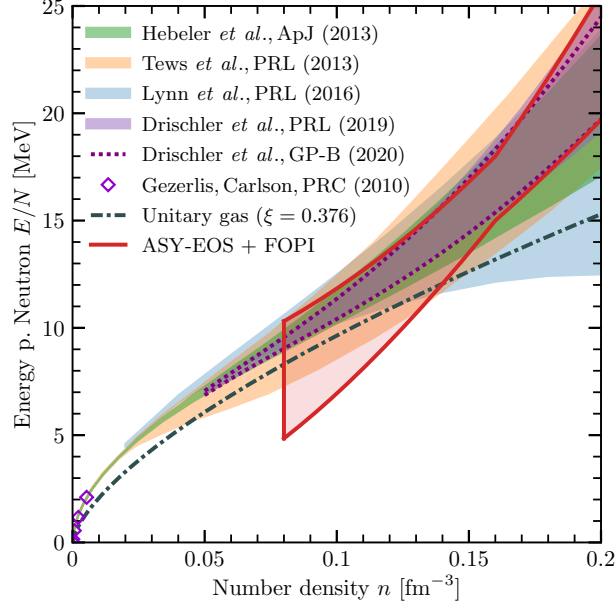


Figure 5.4: Energy per particle E/N of neutron matter as a function of density n for various many-body calculations using chiral EFT interactions from Hebeler et al. [4], Tews et al. [167], Lynn et al. (used here) [168], Drischler et al. PRL [169] and GP-B [170], and low-density quantum Monte Carlo results from Gezerlis and Carlson [291]. We also show the energy per particle of a unitary Fermi gas of neutrons, which has been proposed as a lower bound for the energy of neutron matter [235]. Finally, we compare the theoretical results with the constraint from the ASY-EOS and FOPI experiments (red), which is used as a constraint for neutron matter in the main work.

the ASY-EOS experiment with new simulations using the IQMD model. The red line indicates the mean value for γ_{asy} along the linear interpolation for the chosen range of S_0 that is used in this work. Overall, the models are in good agreement with each other and we conclude that the linear interpolation in the E_{sym} range is suitable.

The pressure constraint is given by the density derivative of the energy per particle,

$$P(n, \delta) = n^2 \frac{\partial E/A(n, \delta)}{\partial n}, \quad (5.4)$$

and depends on n , δ , n_0 , B , K , and E_{sym} . We enforce this constraint only at densities where the experiment is sensitive. The density region of the HIC constraint is set by the sensitivity of the neutrons-over-charged-particles flow ratio determined for the ASY-EOS experiment [256]. This sensitivity curve covers the density range from $0.5n_0$ up to $3n_0$ and peaks between n_0 and $\sim 2n_0$, where the experiment is most sensitive.

Neutron-star matter is composed of neutrons, protons, electrons, and muons in β -equilibrium. In order to apply the ASY-EOS constraint to neutron stars, we need to determine the proton fraction $x_{\text{ASY-EOS}}$ accordingly. For simplicity, we neglect muons because they only have a small impact on the neutron-star EOS in the considered density range. Then, the density of electrons is equal to the proton density due to local charge neutrality, and the proton fraction x at a given baryon density n is fixed by the β -equilibrium condition.

The final pressure constraint is obtained using $E_F = 37$ MeV and by varying the parameters n_0 , B , K , and E_{sym} within specific ranges. For the parameters describing symmetric nuclear matter, we use the values

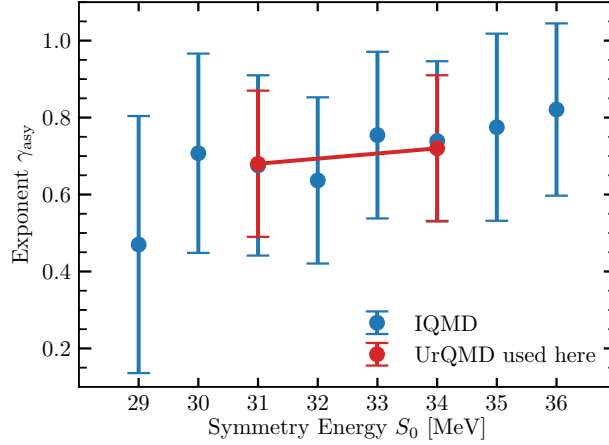


Figure 5.5: We show the exponent γ_{asy} of the density dependence of the potential part of the symmetry energy, see Eq. (5.3), as deduced from the analysis of ASY-EOS experimental data using the UrQMD model used in this work [256] (red points) and new simulations from the IQMD model (blue points). The red line indicates the mean value for γ_{asy} along the linear interpolation for the chosen range of S_0 .

consistent with the FOPI analysis given by $n_0 = 0.16 \text{ fm}^{-3}$, $B = 16 \text{ MeV}$, and a Gaussian distribution for K with $K = 200 \pm 25 \text{ MeV}$ at 1σ . Regarding E_{sym} , we apply a uniform prior in the range from 31 – 34 MeV.

In addition to the GSI experiments, we include constraints on the pressure of symmetric nuclear matter at larger densities obtained from model calculations of Danielewicz *et al.* [246] that were used to analyze experimental data from LBL and BNL in which ^{197}Au nuclei were collided at energies up to 10 GeV/nucleon. A comparison of this constraints together with the allowed range from FOPI and calculations from chiral EFT for the pressure of symmetric nuclear matter is shown in Fig. 5.6.

The results from Danielewicz *et al.* are sensitive to higher densities, 2-4.5 n_0 , but we only include their constraints up to 3 n_0 where the sensitivity of the ASY-EOS experiment ends, i.e. we disregard all parameter sets, which lead to a pressure that is not consistent with their constraint. This excludes the highest values for the incompressibility K from the FOPI distribution and also influences symmetric matter at smaller densities, which depends on the range of K . However, both experimental constraints are in very good agreement with each other. We find that the inclusion of this additional constraint has only minimal impact, but keep it to ensure the completeness of our study; see HIC-only results in Tab. 5.2. Note that the uncertainty band from FOPI is smaller than the theoretical one because the empirical saturation point used for extracting the experimental results has smaller uncertainties compared to theoretical estimates from chiral EFT.

In Fig. 5.1C, we show the combined HIC experimental constraints (labelled HIC Data) at 68% and 95% credibility as well as the resulting posterior distribution for the neutron-star EOS. We find that the HIC constraints tend to prefer EOSs stiffer than the ones favoured by astrophysical observations, i.e., EOSs that have higher pressures at densities up to 2 n_0 , see Fig. 5.1C and Fig. 5.1E. We note that results of the ASY-EOS experiment, in their sub-saturation density extension, are compatible with recent experimental findings from isobaric analog states supplemented with additional constraints from neutron-skin data [242], HICs using isospin-diffusion observables measured in mid-peripheral collisions of Sn isotopes [241], and other nuclear structure information [352, 353]. More recently, the $S\pi\text{rit}$ campaign at RIKEN has identified spectral yield ratios of charged pions in collisions of various tin isotopes near threshold as sensitive probes of the slope of the symmetry energy near and beyond nuclear saturation density [257]. The obtained value

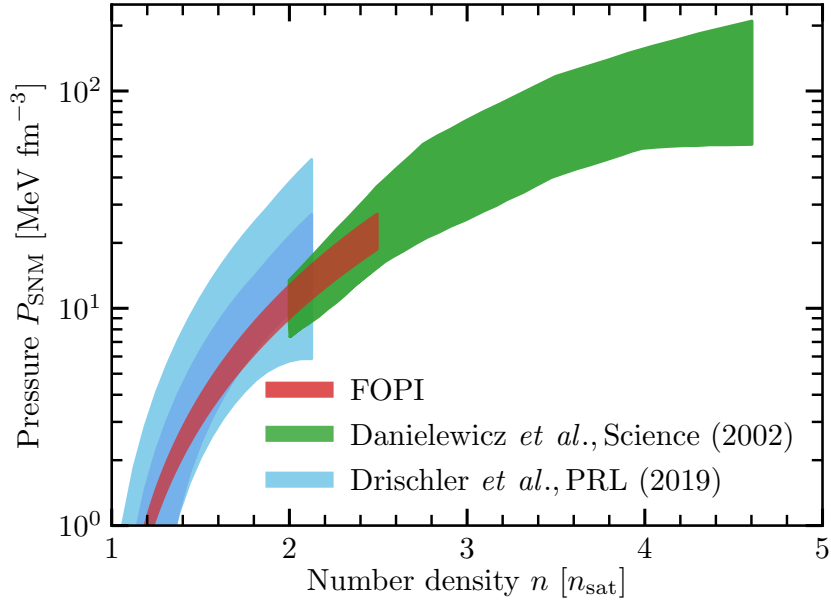


Figure 5.6: The pressure band from the FOPI experiment [249] at the 1σ level (red) for the incompressibility is consistent with the chiral EFT constraint from Drischler *et al.* [169, 171] at $N^2\text{LO}$ (light blue) and $N^3\text{LO}$ (dark blue). Between $2\text{-}3n_0$, we additionally constrain the FOPI results with the constraint from Danielewicz *et al.* [246] (green), which has no statistical interpretation.

Table 5.2: Comparison of the 95% credible interval for the pressure [MeV fm^{-3}] and radius [km] of neutron stars when including only HIC experiments and for combined HIC and astrophysics results with and without the inclusion of the constraint from Danielewicz *et al.* [246].

P/R	With Danielewicz <i>et al.</i> [246]		Without Danielewicz <i>et al.</i> [246]	
	HIC only	Astro+HIC	HIC only	Astro+HIC
$1.0n_0$	$2.05^{+0.49}_{-0.45}$	$2.11^{+0.49}_{-0.52}$	$2.06^{+0.49}_{-0.45}$	$2.11^{+0.48}_{-0.52}$
$1.5n_0$	$6.06^{+1.85}_{-2.04}$	$6.25^{+1.90}_{-2.26}$	$6.08^{+1.83}_{-2.04}$	$6.25^{+1.89}_{-2.23}$
$2.0n_0$	$19.47^{+33.63}_{-11.67}$	$19.07^{+15.27}_{-10.53}$	$19.35^{+33.66}_{-10.71}$	$19.05^{+15.33}_{-10.27}$
$2.5n_0$	$47.78^{+75.96}_{-32.96}$	$45.43^{+40.41}_{-19.11}$	$47.59^{+79.68}_{-27.46}$	$45.57^{+40.87}_{-18.89}$
$1.0M_\odot$	$11.89^{+0.79}_{-0.98}$	$11.88^{+0.57}_{-0.76}$	$11.89^{+0.79}_{-0.98}$	$11.88^{+0.56}_{-0.78}$
$1.4M_\odot$	$12.06^{+1.13}_{-1.18}$	$12.01^{+0.78}_{-0.77}$	$12.06^{+1.12}_{-1.19}$	$12.01^{+0.78}_{-0.77}$
$1.6M_\odot$	$12.11^{+1.33}_{-1.33}$	$12.03^{+0.98}_{-0.75}$	$12.11^{+1.32}_{-1.34}$	$12.03^{+0.92}_{-0.80}$
$2.0M_\odot$	$12.19^{+1.71}_{-1.59}$	$11.91^{+1.24}_{-1.11}$	$12.18^{+1.70}_{-1.61}$	$11.91^{+1.17}_{-1.15}$

Table 5.3: Comparison of the 95% credible interval for the pressure [MeV fm^{-3}] and radius [km] of neutron stars when including only HIC results, only astrophysical observations, and for combined HIC and astrophysics results for different EOS extension schemes used, namely the speed-of-sound extension that is used in this work and the piecewise-polytrope extension.

P/R	Speed-of-sound extension			Piecewise-polytrope extension		
	HIC only	Astro only	Astro+HIC	HIC only	Astro only	Astro+HIC
$1.0n_0$	$2.05^{+0.49}_{-0.45}$	$2.00^{+0.52}_{-0.49}$	$2.11^{+0.49}_{-0.52}$	$2.06^{+0.49}_{-0.44}$	$1.96^{+0.54}_{-0.45}$	$2.10^{+0.49}_{-0.51}$
$1.5n_0$	$6.06^{+1.85}_{-2.04}$	$5.84^{+1.96}_{-2.26}$	$6.25^{+1.90}_{-2.26}$	$6.06^{+1.85}_{-1.96}$	$5.66^{+2.15}_{-2.00}$	$6.20^{+1.93}_{-2.17}$
$2.0n_0$	$19.47^{+33.63}_{-11.67}$	$18.44^{+16.24}_{-9.69}$	$19.07^{+15.27}_{-10.53}$	$19.00^{+17.6}_{-8.34}$	$18.96^{+15.40}_{-8.40}$	$19.64^{+15.83}_{-8.60}$
$2.5n_0$	$47.78^{+75.96}_{-32.96}$	$45.05^{+39.80}_{-19.62}$	$45.43^{+40.41}_{-19.11}$	$43.72^{+39.81}_{-18.98}$	$44.77^{+35.36}_{-18.86}$	$45.27^{+36.77}_{-18.00}$
$1.0M_\odot$	$11.89^{+0.79}_{-0.98}$	$11.76^{+0.65}_{-0.71}$	$11.88^{+0.57}_{-0.76}$	$11.90^{+0.74}_{-0.89}$	$11.80^{+0.70}_{-0.69}$	$11.92^{+0.67}_{-0.71}$
$1.4M_\odot$	$12.06^{+1.13}_{-1.18}$	$11.94^{+0.79}_{-0.78}$	$12.01^{+0.78}_{-0.77}$	$12.02^{+0.96}_{-1.01}$	$11.97^{+0.84}_{-0.77}$	$12.05^{+0.83}_{-0.79}$
$1.6M_\odot$	$12.11^{+1.33}_{-1.33}$	$11.98^{+0.93}_{-0.79}$	$12.03^{+0.98}_{-0.75}$	$12.05^{+1.11}_{-1.11}$	$12.01^{+0.94}_{-0.83}$	$12.07^{+0.95}_{-0.84}$
$2.0M_\odot$	$12.19^{+1.71}_{-1.59}$	$11.88^{+1.23}_{-1.10}$	$11.91^{+1.24}_{-1.11}$	$12.02^{+1.35}_{-1.39}$	$11.88^{+1.22}_{-1.11}$	$11.92^{+1.32}_{-1.08}$

is compatible with the ASY-EOS result but currently offers no additional strong constraint due to its large uncertainty [257, 354].

5.3.2 Uncertainty studies

The HIC pressure-density constraint includes various sources of uncertainties including systematic and statistical uncertainties of the experiments and the analysis of its data [249, 256]. We have explicitly checked the robustness of our results when varying the details of the analysis and employed models, and generally found that our results do not significantly depend on individual model choices. In Tab. 5.3, we analyze variations due to the extension scheme of the equation of state to high densities. Here, we compare the speed-of-sound extension with the piecewise-polytrope scheme that extends the EOS beyond $1.5n_0$ with five polytropic segments with randomly chosen transition densities and polytropic indices, see e.g. [4, 176]. The differences of the pressure estimates between the two EOS extension schemes is less than 3% and the difference between the radius estimates is less than 0.5%.

In addition, we check the impact of the EOS parametrization for symmetric nuclear matter in Tab. 5.4. We compare the functional form from FOPI used in this work, see Eq. (5.1), with a general Taylor expansion for symmetric nuclear matter with the same values for the saturation point and the incompressibility but including the third-order parameter $Q = -150 \pm 250 \text{ MeV}$ at 1σ using a Gaussian distribution. We find that our results are robust with respect to a variation of this parameterisation and the impact of this choice is at the 5% level for pressures and 1% level for radii.

Our results show also no significant changes when using a more conservative choice for the proton fraction, see Tab. 5.5. In particular, there are only small changes when computing the proton fraction for the HIC constraints using the EOS functional introduced by the ASY-EOS analysis ($x_{\text{ASY-EOS}}$) and allowing the proton fraction to be within the rather large range $0 \leq x \leq 0.1$ in the density range set by the ASY-EOS experiment.

The recent NICER constraint for the radius of J0740+6220 [124, 123] prefers a stiffer EOS, which agrees well with the constraint from HIC experiments, see Tab. 5.6. As a consequence, the impact of including

Table 5.4: Comparison of the 95% credible interval for the pressure [MeV fm^{-3}] and radius [km] of neutron stars when including only HIC experiments and for combined HIC and astrophysics results for two parameterisations of symmetric nuclear matter. We compare the functional form from FOPI used in this work, see Eq. (5.1), with a general Taylor expansion for symmetric nuclear matter including the third-order parameter $Q = -150 \pm 250 \text{ MeV}$ at 1σ using a Gaussian distribution.

P/R	SNM form used here		Taylor expansion	
	HIC only	Astro+HIC	HIC only	Astro+HIC
$1.0n_0$	$2.05^{+0.49}_{-0.45}$	$2.11^{+0.49}_{-0.52}$	$1.95^{+0.52}_{-0.44}$	$2.01^{+0.51}_{-0.47}$
$1.5n_0$	$6.06^{+1.85}_{-2.04}$	$6.25^{+1.90}_{-2.26}$	$5.61^{+2.04}_{-2.00}$	$5.87^{+1.99}_{-2.14}$
$2.0n_0$	$19.47^{+33.63}_{-11.67}$	$19.07^{+15.27}_{-10.53}$	$18.80^{+32.63}_{-12.89}$	$18.72^{+16.57}_{-9.34}$
$2.5n_0$	$47.78^{+75.96}_{-32.96}$	$45.43^{+40.41}_{-19.11}$	$47.58^{+77.40}_{-31.93}$	$45.66^{+41.66}_{-19.19}$
$1.0M_\odot$	$11.89^{+0.79}_{-0.98}$	$11.88^{+0.57}_{-0.76}$	$11.77^{+0.84}_{-0.97}$	$11.79^{+0.60}_{-0.71}$
$1.4M_\odot$	$12.06^{+1.13}_{-1.18}$	$12.01^{+0.78}_{-0.77}$	$11.98^{+1.16}_{-1.18}$	$11.97^{+0.77}_{-0.74}$
$1.6M_\odot$	$12.11^{+1.33}_{-1.33}$	$12.03^{+0.98}_{-0.75}$	$12.05^{+1.32}_{-1.37}$	$12.00^{+0.90}_{-0.78}$
$2.0M_\odot$	$12.19^{+1.71}_{-1.59}$	$11.91^{+1.24}_{-1.11}$	$12.13^{+1.73}_{-1.61}$	$11.92^{+1.23}_{-1.10}$

Table 5.5: Comparison of the 95% credible interval for the pressure [MeV fm^{-3}] and radius [km] of neutron stars when including only HIC experiments and for combined HIC and astrophysics results for two choices for the proton fraction in β -equilibrium. We compare our main results that are based on the computation using the EOS functional introduced by the ASY-EOS analysis ($x_{\text{ASY-EOS}}$) with a more conservative choice that constrains the proton fraction to be within the range $0 \leq x \leq 0.1$.

P/R	$x_{\text{ASY-EOS}}$		$0 \leq x \leq 0.1$	
	HIC only	Astro+HIC	HIC only	Astro+HIC
$1.0n_0$	$2.05^{+0.49}_{-0.45}$	$2.11^{+0.49}_{-0.52}$	$2.05^{+0.50}_{-0.45}$	$2.10^{+0.48}_{-0.52}$
$1.5n_0$	$6.06^{+1.85}_{-2.04}$	$6.25^{+1.90}_{-2.26}$	$6.02^{+1.89}_{-2.04}$	$6.23^{+1.81}_{-2.31}$
$2.0n_0$	$19.47^{+33.63}_{-11.67}$	$19.07^{+15.27}_{-10.53}$	$19.32^{+33.95}_{-11.05}$	$19.00^{+14.74}_{-10.54}$
$2.5n_0$	$47.78^{+75.96}_{-32.96}$	$45.43^{+40.41}_{-19.11}$	$48.00^{+78.57}_{-34.40}$	$45.48^{+39.96}_{-19.28}$
$1.0M_\odot$	$11.89^{+0.79}_{-0.98}$	$11.88^{+0.57}_{-0.76}$	$11.88^{+0.79}_{-0.98}$	$11.87^{+0.59}_{-0.75}$
$1.4M_\odot$	$12.06^{+1.13}_{-1.18}$	$12.01^{+0.78}_{-0.77}$	$12.05^{+1.14}_{-1.17}$	$12.00^{+0.77}_{-0.77}$
$1.6M_\odot$	$12.11^{+1.33}_{-1.33}$	$12.03^{+0.98}_{-0.75}$	$12.10^{+1.31}_{-1.36}$	$12.03^{+0.91}_{-0.79}$
$2.0M_\odot$	$12.19^{+1.71}_{-1.59}$	$11.91^{+1.24}_{-1.11}$	$12.18^{+1.70}_{-1.61}$	$11.90^{+1.22}_{-1.14}$

Table 5.6: Comparison of the 95% credible interval for the pressure [MeV fm^{-3}] and radius [km] of neutron stars when including only HIC results, only astrophysical observations, and for combined HIC and astrophysics results when we include the combined mass-radius measurement from NICER [124, 123] or only the radio mass measurement from Ref. [9].

P/R	HIC only	Using Ref. [124, 123] for J0740+6220		Using Ref. [9] for J0740+6220	
		Astro only	Astro+HIC	Astro only	Astro+HIC
$1.0n_0$	$2.05^{+0.49}_{-0.45}$	$2.00^{+0.52}_{-0.49}$	$2.11^{+0.49}_{-0.52}$	$1.95^{+0.55}_{-0.45}$	$2.08^{+0.49}_{-0.53}$
$1.5n_0$	$6.06^{+1.85}_{-2.04}$	$5.84^{+1.96}_{-2.26}$	$6.25^{+1.90}_{-2.26}$	$5.63^{+2.16}_{-2.05}$	$6.14^{+1.93}_{-2.28}$
$2.0n_0$	$19.47^{+33.63}_{-11.67}$	$18.44^{+16.24}_{-9.69}$	$19.07^{+15.27}_{-10.53}$	$17.46^{+15.66}_{-9.27}$	$18.32^{+14.87}_{-9.60}$
$2.5n_0$	$47.78^{+75.96}_{-32.96}$	$45.05^{+39.80}_{-19.62}$	$45.43^{+40.41}_{-19.11}$	$42.23^{+41.75}_{-20.47}$	$43.22^{+42.66}_{-19.18}$
$1.0M_\odot$	$11.89^{+0.79}_{-0.98}$	$11.76^{+0.65}_{-0.71}$	$11.88^{+0.57}_{-0.76}$	$11.68^{+0.71}_{-0.74}$	$11.82^{+0.68}_{-0.78}$
$1.4M_\odot$	$12.06^{+1.13}_{-1.18}$	$11.94^{+0.79}_{-0.78}$	$12.01^{+0.78}_{-0.77}$	$11.83^{+0.86}_{-0.86}$	$11.94^{+0.87}_{-0.83}$
$1.6M_\odot$	$12.11^{+1.33}_{-1.33}$	$11.98^{+0.93}_{-0.79}$	$12.03^{+0.98}_{-0.75}$	$11.87^{+1.01}_{-0.93}$	$11.95^{+1.01}_{-0.91}$
$2.0M_\odot$	$12.19^{+1.71}_{-1.59}$	$11.88^{+1.23}_{-1.10}$	$11.91^{+1.24}_{-1.11}$	$11.74^{+1.44}_{-1.25}$	$11.77^{+1.42}_{-1.23}$

the HIC constraint is smaller compared to using only the radio mass measurement from Ref. [9] since the tension between the HIC information and the observational constraints decreased.

When extracting the HIC constraint on neutron-star matter, we vary nuclear matter properties, such as the incompressibility parameter and the symmetry energy at n_0 , according to the measurements from FOPI and ASY-EOS. We have explicitly checked that increasing these uncertainties in agreement with theoretical estimates [73] only leads to minor changes of our final results, see Tab. 5.7. In particular, we extend the range for the symmetry energy at saturation density to $S_0 = 30 - 35$ MeV by extrapolating γ_{asy} linearly. We use Gaussian distributions for n_0 , B , and K describing symmetric nuclear matter and vary these parameters within their empirical ranges (at 1σ): $n_0 = 0.164 \pm 0.007 \text{ fm}^{-3}$, $B = 15.86 \pm 0.57$ MeV [169] and $K = 215 \pm 40$ MeV from microscopic calculations [169, 228, 226], which is in good agreement with the FOPI results.

To enforce the ASY-EOS constraints only at densities where the experiment is sensitive, we use the sensitivity curve for neutrons and charged particles (n/ch) [256] as a prior for the probed density range. This curve is shown in Fig. 5.7 together with the neutron-over-proton (n/p) sensitivity curves for 400 MeV/nucleon incident energy from Russotto et al. [256] and the density curve reported by Le Fèvre et al. [249] for the sensitivity of the elliptic flow of protons in Au+Au collisions at 1 GeV/nucleon. These curves mainly differ in their peak density. The n/ch sensitivity corresponding to the ASY-EOS results peaks at the lowest density around saturation density. Thus, the HIC information as used in this work offers a constraint only in this density range. We have checked the variation of our results for alternative choices of the sensitivity curve [256] in Tab. 5.8. In particular, we compare our standard results using the neutron over charged particles (n/ch) sensitivity curve [256] with the neutron over proton (n/p) sensitivity from Russotto et al. [256], which peaks at $1.5n_0$. We find that our results are robust and differences for both sensitivity curves are small. Additionally, we compare the results to calculations where the ASY-EOS data is implemented using a uniform prior in density between $1-2n_0$ (labelled Window). For the latter choice, we generally find larger pressures and larger neutron-star radii because the n/ch and n/p sensitivity curves decrease rapidly after their maxima at 1 and $1.5n_0$, lowering the impact of the ASY-EOS constraint at higher

Table 5.7: Comparison of the 95% credible interval for the pressure [MeV fm^{-3}] and radius [km] of neutron stars when using ranges for nuclear matter properties as published for the FOPI and ASY-EOS experiments [256, 249] and when inflating the uncertainties according to theoretical calculations for including only information from HIC experiments and for the combined HIC and astrophysics information.

P/R	HIC parameters		Enlarged variations	
	HIC only	Astro+HIC	HIC only	Astro+HIC
$1.0n_0$	$2.05^{+0.49}_{-0.45}$	$2.11^{+0.49}_{-0.52}$	$2.05^{+0.50}_{-0.45}$	$2.09^{+0.47}_{-0.52}$
$1.5n_0$	$6.06^{+1.85}_{-2.04}$	$6.25^{+1.90}_{-2.26}$	$6.00^{+1.90}_{-2.00}$	$6.18^{+1.88}_{-2.25}$
$2.0n_0$	$19.47^{+33.63}_{-11.67}$	$19.07^{+15.27}_{-10.53}$	$19.34^{+35.65}_{-11.54}$	$18.98^{+14.97}_{-9.92}$
$2.5n_0$	$47.78^{+75.96}_{-32.96}$	$45.43^{+40.41}_{-19.11}$	$47.36^{+81.44}_{-28.09}$	$45.49^{+40.05}_{-20.58}$
$1.0M_\odot$	$11.89^{+0.79}_{-0.98}$	$11.88^{+0.57}_{-0.76}$	$11.87^{+0.81}_{-0.97}$	$11.86^{+0.58}_{-0.78}$
$1.4M_\odot$	$12.06^{+1.13}_{-1.18}$	$12.01^{+0.78}_{-0.77}$	$12.05^{+1.12}_{-1.20}$	$12.00^{+0.75}_{-0.80}$
$1.6M_\odot$	$12.11^{+1.33}_{-1.33}$	$12.03^{+0.98}_{-0.75}$	$12.10^{+1.35}_{-1.32}$	$12.03^{+0.92}_{-0.80}$
$2.0M_\odot$	$12.19^{+1.71}_{-1.59}$	$11.91^{+1.24}_{-1.11}$	$12.17^{+1.70}_{-1.62}$	$11.91^{+1.23}_{-1.15}$

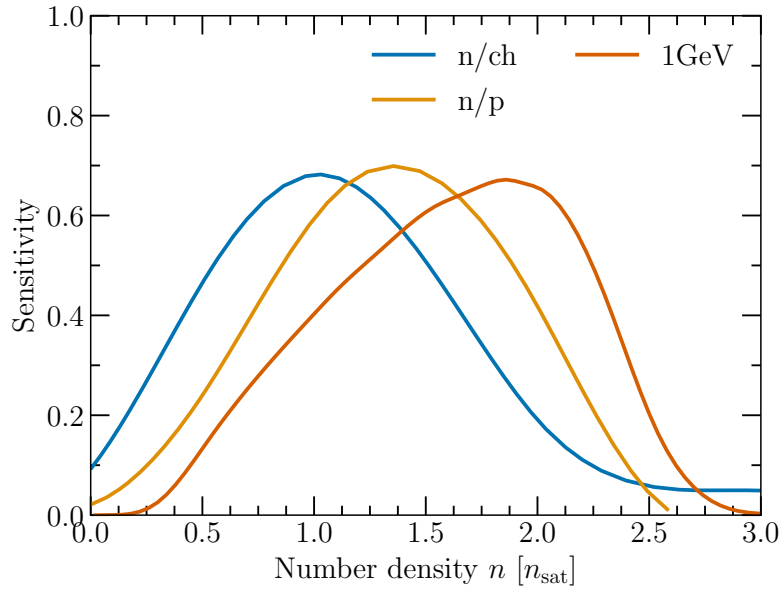


Figure 5.7: We show three sensitivity-to-density curves for different observables and incident energies. In particular, the neutron-over-charged-particle (n/ch, used here) and the neutron-over-proton (n/p) sensitivity curves for 400 MeV/nucleon incident energy from Russotto et al. [256] are compared with the density curve reported by Le Fèvre et al. [249] for the sensitivity of the elliptic flow of protons in Au+Au collisions at 1 GeV/nucleon.

densities. However, differences for radii and pressures remain small once Astro+HIC data is included.

Table 5.8: Comparison of the 95% credible interval for the pressure [MeV fm^{-3}] and radius [km] of neutron stars when including only HIC experiments and for combined HIC and astrophysics results for our standard results using the neutron over charged particles (n/ch) sensitivity curve [256] with the neutron over proton (n/p) sensitivity from Russotto et al. [256] and calculations where the ASY-EOS data is implemented using a uniform prior in density between $1-2n_0$ (labelled Window).

P/R	n/ch sensitivity		n/p sensitivity		Window $1-2n_0$	
	HIC only	Astro+HIC	HIC only	Astro+HIC	HIC only	Astro+HIC
$1.0n_0$	$2.05^{+0.49}_{-0.45}$	$2.11^{+0.49}_{-0.52}$	$2.10^{+0.45}_{-0.49}$	$2.13^{+0.46}_{-0.54}$	$2.23^{+0.32}_{-0.50}$	$2.28^{+0.35}_{-0.55}$
$1.5n_0$	$6.06^{+1.85}_{-2.04}$	$6.25^{+1.90}_{-2.26}$	$6.23^{+1.68}_{-2.16}$	$6.34^{+1.83}_{-2.30}$	$6.76^{+1.15}_{-2.13}$	$6.93^{+1.39}_{-2.17}$
$2.0n_0$	$19.47^{+33.63}_{-11.67}$	$19.07^{+15.27}_{-10.53}$	$19.62^{+33.36}_{-10.81}$	$19.20^{+15.42}_{-9.21}$	$21.41^{+30.60}_{-9.02}$	$20.59^{+16.10}_{-8.36}$
$2.5n_0$	$47.78^{+75.96}_{-32.96}$	$45.43^{+40.41}_{-19.11}$	$47.61^{+79.33}_{-32.61}$	$45.62^{+40.81}_{-18.61}$	$54.71^{+66.27}_{-36.26}$	$48.60^{+39.47}_{-19.32}$
$1.0M_\odot$	$11.89^{+0.79}_{-0.98}$	$11.88^{+0.57}_{-0.76}$	$11.92^{+0.78}_{-0.95}$	$11.91^{+0.61}_{-0.73}$	$12.09^{+0.59}_{-0.63}$	$12.06^{+0.48}_{-0.56}$
$1.4M_\odot$	$12.06^{+1.13}_{-1.18}$	$12.01^{+0.78}_{-0.77}$	$12.09^{+1.12}_{-1.14}$	$12.02^{+0.78}_{-0.76}$	$12.26^{+0.96}_{-0.84}$	$12.17^{+0.73}_{-0.60}$
$1.6M_\odot$	$12.11^{+1.33}_{-1.33}$	$12.03^{+0.98}_{-0.75}$	$12.13^{+1.31}_{-1.30}$	$12.05^{+0.91}_{-0.79}$	$12.33^{+1.14}_{-1.05}$	$12.19^{+0.81}_{-0.76}$
$2.0M_\odot$	$12.19^{+1.71}_{-1.59}$	$11.91^{+1.24}_{-1.11}$	$12.20^{+1.68}_{-1.60}$	$11.91^{+1.25}_{-1.11}$	$12.42^{+1.44}_{-1.48}$	$12.06^{+1.14}_{-1.20}$

5.4 Combination of the astrophysical and heavy-ion collision constraints

The experimental and observational EOS constraints are combined via Bayesian inference. The EOS posterior is given by

$$\begin{aligned}
 p(\text{EOS}|\text{MMA}, \text{HIC}) &\propto p(\text{HIC}|\text{EOS}) \\
 &\times p(\text{MMA}|\text{EOS})p(\text{EOS}) \\
 &= p(\text{HIC}|\text{EOS})p(\text{EOS}|\text{MMA}) \\
 &\equiv \mathcal{L}_{\text{HIC}}(\text{EOS})\mathcal{P}_{\text{MMA}}(\text{EOS}),
 \end{aligned} \tag{5.5}$$

where MMA denotes multi-messenger astrophysics, $\mathcal{L}_{\text{HIC}}(\text{EOS})$ is the likelihood of the HIC measurements for a given EOS, and $\mathcal{P}_{\text{MMA}}(\text{EOS})$ is the posterior probability distribution on the EOS based on the multi-messenger observations, which acts as prior for this analysis. From the HIC experiments we obtain a posterior of the pressure at a given density, $p(P|n, \text{HIC})$. By combining this with the distribution of probed densities from the neutrons-over-charged particles sensitivity curve [256], $p(n|\text{HIC})$, the joint posterior $p(n, P|\text{HIC}) = p(P|n, \text{HIC})p(n|\text{HIC})$ is obtained. Therefore, the relative faithfulness of the experimental results at various densities is accounted for. The likelihood $\mathcal{L}_{\text{HIC}}(\text{EOS})$ is given by

$$\begin{aligned}
 \mathcal{L}_{\text{HIC}}(\text{EOS}) &= \int dn dP p(\text{HIC}|n, P)p(n, P|\text{EOS}) \\
 &\propto \int dn dP p(n, P|\text{HIC})p(n, P|\text{EOS}) \\
 &\propto \int dn dP p(n, P|\text{HIC})\delta(P - P(n, \text{EOS})) \\
 &= \int dn P(n, P = P(n; \text{EOS})|\text{HIC}),
 \end{aligned} \tag{5.6}$$

where we used that the pressure is a function of density for a given EOS.

Table 5.9: Comparison of the pressure in MeV fm^{-3} at $1.5n_0$ and the radius in km of a $1.4M_\odot$ neutron star (median with the 95% credible interval) when including only astrophysical constraints, only HIC experimental data, and for the combination of both.

	Prior	Astro only	HIC only	Astro + HIC
$P_{1.5n_0}$	$5.59^{+2.04}_{-1.97}$	$5.84^{+1.95}_{-2.26}$	$6.06^{+1.85}_{-2.04}$	$6.25^{+1.90}_{-2.26}$
$R_{1.4}$	$11.96^{+1.18}_{-1.15}$	$11.93^{+0.80}_{-0.75}$	$12.06^{+1.13}_{-1.18}$	$12.01^{+0.78}_{-0.77}$

5.5 Combining information from micro- and macroscopic collisions

The final EOS constraints are obtained through the combination of both the HIC information and astrophysical multi-messenger observations, see Fig. 5.1D. While the multi-messenger data rules out the most extreme EOS behavior, the HIC data favors larger pressures around $1-1.5n_0$, where the experimental sensitivity is highest. This is similar to the effect of recent NICER observations on the EOS [124, 152]. Hence, the two complementary approaches, HIC experiments and astrophysical observations show a remarkable agreement, cf. Fig. 5.1E. At low densities, HIC results have a clear impact on the total posterior for the EOS, while the EOS at higher densities ($\gtrsim 2n_0$) is mostly determined by astrophysical observations. At these densities, HIC results deviate only mildly from the prior, see Fig. 5.1F. This is also reflected in the radii of neutron stars shown in Fig. 5.2E and Fig. 5.2F. Because astrophysical observations mainly probe neutron stars with $M \gtrsim 1.4M_\odot$, for which the probed densities are higher, HIC information influences the radii of these neutron stars to a smaller degree. The radius of low-mass stars with $M \sim 1.0M_\odot$, on the other hand, is also constrained by HIC information. Our final result for a typical 1.4 solar mass neutron star is $12.01^{+0.37}_{-0.38}$ km at 68% uncertainty ($12.01^{+0.78}_{-0.77}$ km at 95% uncertainty), see Tab. 5.9. Comparing this value to the result without any HIC information, $11.93^{+0.39}_{-0.41}$ km at 68% confidence, highlights the benefit of combining these various sources of information in a statistically robust framework. Finally, we quantify the possibility for the presence of a strong first-order phase transition to a new phase of QCD matter in the core of neutron stars. For this, we calculate the Bayes factor in favor of the presence of such a phase transition against its absence, and find it to be $0.419 \pm 0.012 < 1$. Therefore, its presence is slightly disfavoured given current astrophysical and experimental data.

The interdisciplinary analysis of EOS constraints from HIC experiments and multi-messenger astrophysics shows remarkable agreement between the two, and provides important information to constrain the nuclear EOS at supra-saturation densities. Going forward, it is important that both statistic and systematic sources of uncertainty for HIC experiments are further improved. For example, the impact of choosing different Quantum Molecular Dynamics (QMD) models when analyzing HIC experiments needs to be further investigated (see Fig. 5.5, 5.7), and advancing HIC experiments to probe higher densities, above $2-3n_0$, will be key. From Tab. 5.10, we find that for all exploratory setups, HIC data is showing a stronger impact on the EOS constraint than the current setup. The result with a density cutoff is showing a significant decrease in uncertainty compared to the result of this work. Therefore, to achieve a stronger constraint on the EOS, improvements to the low-density part of the HIC constraint will be most important. Combining the latter with a reduction of experimental uncertainties, data from HICs has great potential to provide complimentary EOS information, bridging nuclear theory and astrophysical observations. In the next few years, the ASY-EOS-II and Compressed Baryonic Matter (CBM) Experiments at the upcoming Facility for Antiproton and Ion Research (FAIR) at GSI will provide a unique opportunity to study nuclear matter at densities probed in the core of neutron stars and their mergers, and might detect new phases of QCD matter, possibly involving hyperons and, ultimately, the transition to a deconfined quark matter phase at

Table 5.10: Comparison of the 95% credible interval for the pressure [MeV fm^{-3}] and the radius [km] of a neutron star when including only HIC experiments and for combined HIC and astrophysics results for different future improvements. In particular, we show the results with the 1 GeV sensitivity curve (see Fig. 5.7) applied to the current measurement (second column), when additionally halving the uncertainty on γ_{asy} (third column), and when using a lower cutoff density of $1n_0$ instead of $0.5n_0$ (fourth column).

P/R	Current setup		1 GeV sensitivity		1 GeV sensitivity and halved uncertainty on HIC		1 GeV sensitivity with a $1n_0$ lower cutoff	
	HIC only	Astro+HIC	HIC only	Astro+HIC	HIC only	Astro+HIC	HIC only	Astro+HIC
$1.0n_0$	$2.05^{+0.49}_{-0.45}$	$2.11^{+0.49}_{-0.52}$	$2.10^{+0.49}_{-0.45}$	$2.13^{+0.47}_{-0.53}$	$2.12^{+0.43}_{-0.48}$	$2.16^{+0.43}_{-0.55}$	$2.07^{+0.48}_{-0.45}$	$2.12^{+0.47}_{-0.53}$
$1.5n_0$	$6.06^{+1.85}_{-2.04}$	$6.25^{+1.90}_{-2.26}$	$6.20^{+1.71}_{-2.13}$	$6.35^{+1.80}_{-2.31}$	$5.84^{+1.96}_{-2.26}$	$6.44^{+1.77}_{-2.21}$	$6.11^{+1.80}_{-2.02}$	$6.33^{+1.82}_{-2.33}$
$2.0n_0$	$19.47^{+33.63}_{-11.67}$	$19.07^{+15.27}_{-10.53}$	$19.42^{+28.90}_{-11.69}$	$19.14^{+14.24}_{-8.97}$	$19.73^{+29.32}_{-11.49}$	$19.32^{+13.93}_{-8.74}$	$18.66^{+22.18}_{-8.65}$	$18.52^{+11.08}_{-7.04}$
$2.5n_0$	$47.78^{+75.96}_{-32.96}$	$45.43^{+40.41}_{-19.11}$	$47.13^{+75.65}_{-27.86}$	$45.3^{+40.52}_{-17.24}$	$48.20^{+78.30}_{-24.83}$	$45.73^{+38.03}_{-18.47}$	$44.31^{+60.85}_{-21.23}$	$43.30^{+31.65}_{-15.92}$
$1.0M_{\odot}$	$11.89^{+0.79}_{-0.98}$	$11.88^{+0.57}_{-0.76}$	$11.91^{+0.74}_{-0.93}$	$11.91^{+0.55}_{-0.76}$	$11.96^{+0.72}_{-0.85}$	$11.94^{+0.54}_{-0.71}$	$11.85^{+0.66}_{-0.78}$	$11.85^{+0.55}_{-0.70}$
$1.4M_{\odot}$	$12.06^{+1.13}_{-1.18}$	$12.01^{+0.78}_{-0.77}$	$12.08^{+1.09}_{-1.10}$	$12.02^{+0.76}_{-0.73}$	$12.11^{+1.07}_{-1.01}$	$12.04^{+0.72}_{-0.71}$	$11.97^{+0.95}_{-0.85}$	$11.96^{+0.66}_{-0.67}$
$1.6M_{\odot}$	$12.11^{+1.33}_{-1.33}$	$12.03^{+0.98}_{-0.75}$	$12.12^{+1.30}_{-1.24}$	$12.04^{+0.88}_{-0.75}$	$12.15^{+1.26}_{-1.16}$	$12.06^{+0.85}_{-0.74}$	$11.99^{+1.14}_{-0.95}$	$11.96^{+0.79}_{-0.66}$
$2.0M_{\odot}$	$12.19^{+1.71}_{-1.59}$	$11.91^{+1.24}_{-1.11}$	$12.17^{+1.71}_{-1.51}$	$11.90^{+1.21}_{-1.10}$	$12.18^{+1.66}_{-1.46}$	$11.92^{+1.19}_{-1.07}$	$11.93^{+1.61}_{-1.32}$	$11.79^{+1.08}_{-0.95}$

the highest densities (see, e.g., Orsaria *et al.* [355], Brandes *et al.* [356]). Together with experiments at the Rare Isotope Beam Facility (RIBF) at RIKEN in Japan and the Nuclotron-based Ion Collider fAcility (NICA) in Russia, the robust combination of experimental HIC constraints and astrophysical observations has the potential to revolutionise our understanding of the EOS.

5.6 Impact of information from heavy-ion collisions on equation of state functional

In this section, we combine the constraints from HIC data with our EOS functional from Ch. 3. To this end, we use the HIC information as an additional constraint for PNM. The parameter ranges for the nuclear matter properties and the exponent γ_{asy} stay in principle the same, but their implementation changes in a statistical manner. In the study of the present chapter, we use Bayesian methods, which allows us to implement the parameter of the HIC constraint with the corresponding statistical interpretation. For our EOS functional we use clear cuts, i.e. if the pressure is above the predicted pressure of a particular constraint, we neglect the EOS. In general, this leads to stricter constraints as more EOS are ruled out.

To implement the information from HICs consistently, we set the nuclear matter properties to the same ranges as for our EOS functional, namely $n_0 = 0.164 \pm 0.007 \text{ fm}^{-3}$, $B = 15.86 \pm 0.57 \text{ MeV}$, $K = 215 \pm 40 \text{ MeV}$ and $E_{\text{sym}} = 32 \pm 2 \text{ MeV}$. For γ_{asy} , we use the 1σ and 2σ intervals to analyze how much our findings depend on the uncertainty of the HIC data. The resulting constraint is incorporated in the density range defined by the full width at half maximum criterion, which corresponds for the n/ch sensitivity curve to $n = 0.056 - 0.278 \text{ fm}^{-3}$. In general, the HIC constraint is slightly enlarged compared to the implementation in the Bayesian framework (cf. Fig. 5.4), since we use enlarged ranges for the nuclear matter properties to be consistent with our EOS functional.

In Fig. 5.8, we show all EOS for the allowed ranges of the EOS functional (see also Fig. 3.15 for details) and highlight EOS that are consistent with the HIC experiments for the 1 and 2σ uncertainty. The HIC information rules out mostly soft EOS due to the high slope parameter estimated by the HIC experiments. Some stiff EOS are also not consistent with the HIC constraint, especially for the 1σ uncertainty for γ_{asy} . Central densities of the remaining EOS reach only up to about $6n_0$. The new information is able to drastically reduce the EOS uncertainty at low densities, while at higher energy densities a broad range is still covered. This leads to a radius uncertainty of a canonical neutron star of $R_{1.4M_\odot} = 12.6 - 13.2 \text{ km}$ ($12.6 - 13.4 \text{ km}$) for the 1σ (2σ) uncertainty. Since the HIC constraint does not influence the high density part of the EOS to a high degree, the mass-radius relation spreads out with increasing mass, which results in a broad range for allowed maximum masses.

The speed of sound for EOS consistent with the HIC information spans a rather narrow band up to roughly $2n_0$, see Fig. 5.9 (left panel). At higher density that are not sensitive to the HIC experiments, allowed values for the speed of sound only barely exceed $0.7c^2$. Regarding the electron fraction (right panel), we find that for most EOS Y_e increases with density reaching the highest values within the total EOS functional range. Neutron stars with a very neutron-rich core and only a small proton fraction are mostly ruled out by the HIC data. Only a few EOS within the 2σ uncertainty lead to proton fraction below 5 percent in the center of the neutron star.

We conclude that the constraints from HIC experiments have a significant impact on our EOS functional, which is in contrast to our findings within the Bayesian multi-messenger framework. There are two main factors for this. First, for the implementation in the EOS functional, we use clear cuts, i.e. we disregard all EOS that are not consistent with the pressure for neutron matter obtained from the HIC data at any density for the 1 or 2σ experimental uncertainty. Second, we use the HIC constraint at a specific density window and do not take into account the relative faithfulness of the experiment over the density range as

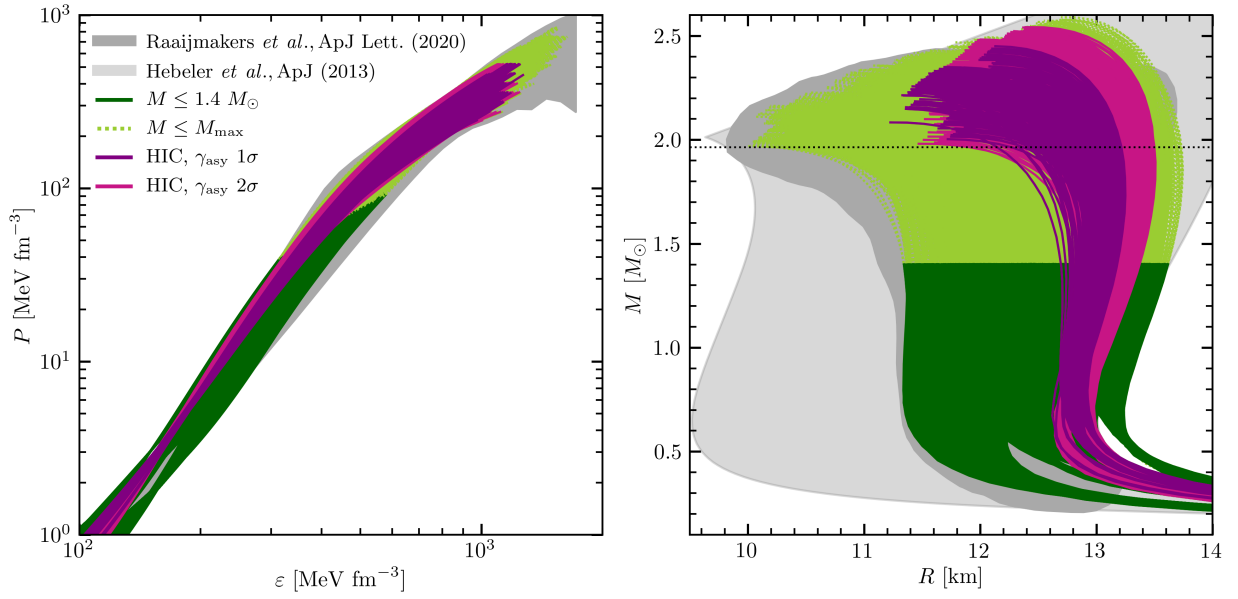


Figure 5.8: Pressure versus energy density (left) and mass-radius relationship (right) for the EOS functional with and without including information from HIC experiments. The constraint from HIC data is implemented with 1σ and 2σ uncertainty for the total experimental error. The color coding for the entire EOS set of the EOS functional indicates the mass of the corresponding neutron star, where dark green corresponds to masses up to $1.4 M_\odot$ and light green to higher masses up to the respective maximum mass M_{max} . The gray band depicts the 95% credible region of the neutron star constraints from Raaijmakers *et al.* [126]. For comparison, in the M - R plot we show also the uncertainty band obtained by Hebel *et al.* [4] using piecewise polytrope extensions to high densities (light gray band).

done in the Bayesian framework. We have already seen in the analysis of Tab. 5.8 that the window method results in a larger influence of HIC constraints on the EOS.

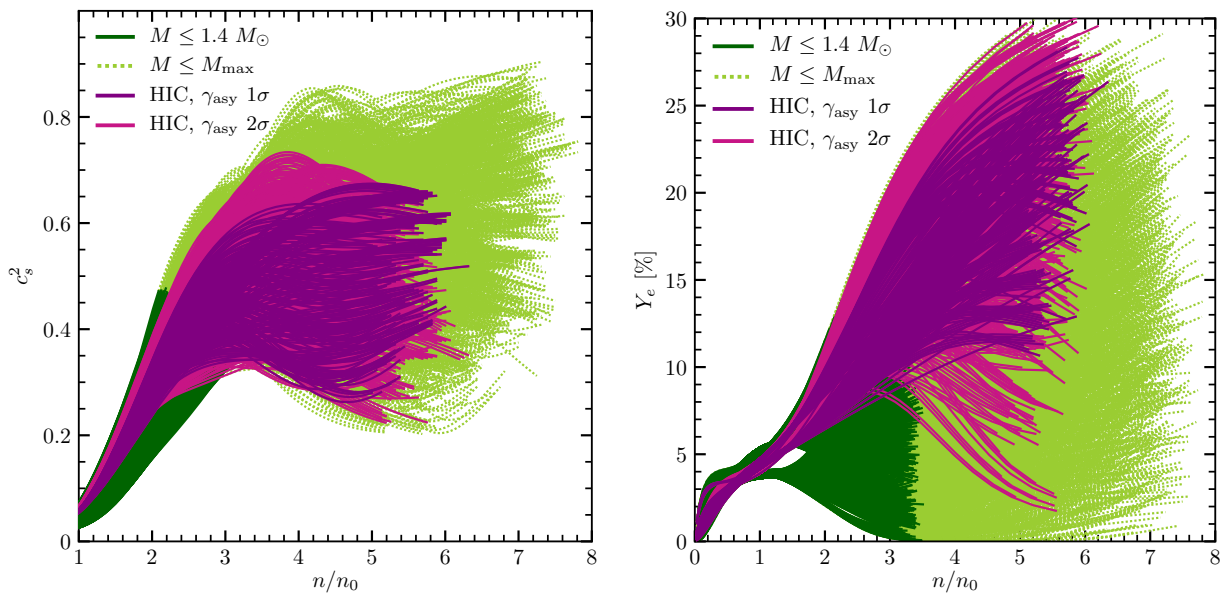


Figure 5.9: Analog of Fig. 5.8 for the speed of sound (left) and the electron fraction Y_e (right) as a function of density.

6 Summary and outlook

In this thesis, we explored the equation of state for hot and dense matter to improve our understanding of matter inside neutron star cores and the mechanisms behind astrophysical phenomena such as CCSNe and NSMs. In particular, we developed a new energy density functional for astrophysical applications consistent with recent estimates from nuclear theory and observations. The EOS is a key microphysics input in simulations of CCSNe and NSMs, but so far most phenomenological EOS that are suitable for simulations are not in agreement with current constraints. We further performed an interdisciplinary study on the EOS of cold neutron stars by combining our knowledge from nuclear theory and astrophysical observation with information from HICs. This work also indicated future needs for HIC experiments in order to provide more stringent constraints on the properties of dense matter.

Regarding the new EOS functional for application in CCSN and NSM simulations, we used constraints from various chiral-EFT based calculations of neutron matter and nuclear matter, from astrophysical observations, and (to a lesser extent) results from a recent QCD-based fRG study of high-density matter. In particular, the EOSs obtained from our functional are consistent with recent mass measurements of heavy neutron stars and the joint analysis of observational data from GW170817 and NICER from Raaijmakers *et al.* [126]. We have modeled the kinetic part of the EOS as a noninteracting nucleon gas with density-dependent effective mass. The effective mass is a key quantity that determines the temperature dependence of the EOS and governs the PNS contraction in CCSN simulations. The careful implementation of microscopic results for the nucleon effective mass in our EOS functional is a novelty compared to previous constructions of astrophysical EOS. The description of the interaction part in our approach represents an improvement over traditional EOS functionals as well. That is, we have modeled the interaction part not as a sum of density monomials but as a sum of density-dependent rational functions to ensure a stable EOS functional under variations of the low- and high-density input. We have fitted the parameters of the interaction part to the combination of state-of-the-art neutron matter calculations and observational constraints. From this, we have derived a comprehensive uncertainty band for neutron star matter. Our EOS predict that the radius of a canonical $1.4 M_{\odot}$ neutron star lies in the range $R_{1.4} = 11.1\text{--}13.6$ km. The fRG results of Leonhardt *et al.* [171] and of heavy-ion collisions [249, 256] provide an additional constraint that leads to a significant reduction in the radius uncertainty of neutron stars. Overall, our EOS functional represents a significant step towards a microscopic description of the complete uncertainty range of the dense matter EOS for astrophysical simulations. Future work will be targeted at further refinements of the EOS functional, including the careful consideration of possible phase-transition effects on the dense matter EOS. In addition, the implementation of an uncertainty band for the nucleon effective mass based on microscopic calculations up to twice saturation density is useful to capture thermal effects in CCSN simulations where central densities are oftentimes in this range. Regarding the fit parameters of the EOS functional, we have seen in subsequent studies that a larger flexibility of nuclear matter properties via a sampling can be beneficial to extend the range of possible EOS. As soon as the parameter space of possible EOS is largely reduced by future constraints on the EOS, a refinement of the chosen combination of nuclear matter properties might be necessary.

From the novel EOS functional, we chose a set of representative EOS that covers the radius uncertainty of a $1.4 M_{\odot}$ neutron star. This set consists of 18 EOS and permits systematic studies of individual nuclear matter

properties. We calculated the coexistence boundary of the liquid-gas phase transition in nuclear matter via an effective one dimensional Maxwell construction and found that for SNM the critical temperature varies between 14.7 and 18.5 MeV and the critical density between $0.32 - 0.43 \text{ fm}^{-3}$. In general, the variation of the SNM properties, incompressibility, binding energy, and saturation density result in the largest deviation for the critical temperature. PNM properties like the symmetry energy and the slope parameter only show an impact for asymmetric matter. In collaboration with Yeunhwan Lim, we started to compute EOS tables based on the liquid drop model with a single nucleus approximation where the EOS functional is used for the description of bulk nuclear matter inside nuclei as well as of unbound neutrons and protons surrounding the nuclei. These EOS tables are suited for direct use in CCSN as well as NSM simulations. For further developments, we conclude from the experience with CCSN simulations that the implementation of a nuclear statistical equilibrium rather than a single nucleus approximation results in a more realistic evolution at lower densities and temperatures.

In addition to the improvements on the EOS for astrophysical applications, we conducted an interdisciplinary analysis of EOS constraints from HIC experiments and multi-messenger astrophysics that showed a remarkable agreement between the two and provided important information to constrain the nuclear EOS at supra-saturation densities. In fact, we analyzed the EOS and neutron-star properties by extending our Bayesian multi-messenger astrophysics framework to include information from the FOPI and the ASY-EOS experimental campaigns that were performed at the Schwerionensynchrotron 18 accelerator located at the GSI Helmholtz Centre for Heavy Ion Research. The combination of these experiments provides new constraints for neutron-rich matter in the density range around $1-2n_0$. We also included the EOS constraint from Danielewicz *et al.* [246] for symmetric nuclear matter obtained from HIC experiments at the Bevalac accelerator at Lawrence Berkeley National Laboratory and the Alternating Gradient Synchrotron at Brookhaven National Laboratory. We found that the HIC data favors larger pressures around $1-1.5n_0$, for which the experimental sensitivity is highest. This is similar to the effect of recent NICER observations on the EOS. Hence, the two complementary approaches, HIC experiments and astrophysical observations, show a remarkable agreement. At higher densities, $\gtrsim 2n_0$, the EOS is mostly determined by astrophysical observations. Our final result for a typical $1.4M_\odot$ neutron star is $12.01^{+0.37}_{-0.38}$ km at 68% uncertainty ($12.01^{+0.78}_{-0.77}$ km at 95% uncertainty). From systematic studies of the robustness of our results, we concluded that for future constraints it will be key for HIC experiments to probe higher densities above $2-3n_0$ and to reduce experimental uncertainties. In particular, the systematic investigation of different QMD models is essential to provide meaningful uncertainties for the constraints from HIC experiments. Once these challenges are solved, information from HIC experiments are a promising tool to advance our understanding of dense matter as present in neutron star cores. In future studies, also the nuclear theory input can be adjusted to include various microscopic calculations, which ultimately leads to a broader prior.

Overall, we live in an exciting era where we expect lots of new constraints on the mass-radius relation from astrophysical observations. Consequently, all frameworks that are set up need to be flexible in order to infer stringent constraints for the EOS including information from complementary sources.

Bibliography

- [1] Haensel, P., Potekhin, A. Y. & Yakovlev, D. G. *Neutron Stars 1* (Springer, New York, 2007).
- [2] Heiselberg, H. & Pandharipande, V. Recent progress in neutron star theory. *Annu. Rev. Nucl. Part. Sci.* **50**, 481 (2000).
- [3] Lattimer, J. M. The nuclear equation of state and neutron star masses. *Annu. Rev. Nucl. Part. Sci.* **62**, 485 (2012).
- [4] Hebeler, K., Lattimer, J. M., Pethick, C. J. & Schwenk, A. Equation of state and neutron star properties constrained by nuclear physics and observation. *Astrophys. J.* **773**, 11 (2013).
- [5] Steiner, A. W., Lattimer, J. M. & Brown, E. F. The Neutron Star Mass-Radius Relation and the Equation of State of Dense Matter. *Astrophys. J.* **765**, L5 (2013).
- [6] Demorest, P., Pennucci, T., Ransom, S., Roberts, M. & Hessels, J. Shapiro Delay Measurement of a Two Solar Mass Neutron Star. *Nature* **467**, 1081 (2010).
- [7] Antoniadis, J. *et al.* A Massive Pulsar in a Compact Relativistic Binary. *Science* **340**, 1233232 (2013).
- [8] Cromartie, H. T. *et al.* Relativistic Shapiro delay measurements of an extremely massive millisecond pulsar. *Nature Astron.* **4**, 72 (2019).
- [9] Fonseca, E. *et al.* Refined Mass and Geometric Measurements of the High-mass PSR J0740+6620. *Astrophys. J. Lett.* **915**, L12 (2021).
- [10] Shapiro, S. L. & Teukolsky, S. A. *Black Holes, White Dwarfs and Neutron Stars: The Physics of Compact Objects* (Wiley, 2008).
- [11] Lattimer, J. M. & Prakash, M. The physics of neutron stars. *Science* **304**, 536 (2004).
- [12] Rezzolla, L., Pizzochero, P., Jones, D. I., Rea, N. & Vidaña, I. (eds.) *The Physics and Astrophysics of Neutron Stars* (Springer, 2018).
- [13] Annala, E., Gorda, T., Kurkela, A., Nättilä, J. & Vuorinen, A. Evidence for quark-matter cores in massive neutron stars. *Nature Phys.* **16**, 907–910 (2020).
- [14] Lindblom, L. Determining the nuclear equation of state from neutron-star masses and radii. *Astrophys. J.* **398**, 569 (1992).
- [15] Janka, H. T., Langanke, K., Marek, A., Martínez-Pinedo, G. & Müller, B. Theory of core-collapse supernovae. *Phys. Rept.* **442**, 38 (2007).
- [16] Burkert, A., Janka, H.-T., Lesch, H., Heckmann, N. & Hetznecker, H. *Supernovae und kosmische Gammablitz: Ursachen und Folgen von Sternexplosionen* (Spektrum Akademischer Verlag, 2011).

-
- [17] Janka, H.-T. Explosion mechanisms of core-collapse supernovae. *Annu. Rev. Nucl. Part. Sci.* **62**, 407 (2012).
- [18] Janka, H. T. *et al.* Core-collapse supernovae: Reflections and directions. *Prog. Theor. Exp. Phys.* **2012**, 01A309 (2012).
- [19] Burrows, A. Colloquium: Perspectives on core-collapse supernova theory. *Rev. Mod. Phys.* **85**, 245 (2013).
- [20] Burbidge, E. M., Burbidge, G. R., Fowler, W. A. & Hoyle, F. Synthesis of the elements in stars. *Rev. Mod. Phys.* **29**, 547 (1957).
- [21] Cameron, A. G. W. Nuclear reactions in stars and nucleogenesis. *Publ. Astron. Soc. Pac.* **69**, 201 (1957).
- [22] Arnould, M., Goriely, S. & Takahashi, K. The r-process of stellar nucleosynthesis: Astrophysics and nuclear physics achievements and mysteries. *Phys. Rep.* **450**, 97 (2007).
- [23] Winkler, P. F. Sn 1006: a thousand-year perspective. *Proceedings of the International Astronomical Union* **2**, 301 (2006).
- [24] Hamacher, D. W. Are supernovae recorded in indigenous astronomical traditions? (2014).
- [25] Sathyaprakash, B. S. & Schutz, B. F. Physics, Astrophysics and Cosmology with Gravitational Waves. *Living Rev. Rel.* **12**, 2 (2009).
- [26] Andersson, N. *et al.* Gravitational waves from neutron stars: Promises and challenges. *Gen. Rel. Grav.* **43**, 409 (2011).
- [27] Metzger, B. D. Kilonovae. *Living Rev. Rel.* **20**, 3 (2017).
- [28] Radice, D. *et al.* Binary Neutron Star Mergers: Mass Ejection, Electromagnetic Counterparts and Nucleosynthesis. *Astrophys. J.* **869**, 130 (2018).
- [29] Shibata, M. & Hotokezaka, K. Merger and mass ejection of neutron star binaries. *Annu. Rev. Nucl. Part. Sci.* **69**, 41 (2019).
- [30] Fujibayashi, S. *et al.* Mass ejection from disks surrounding a low-mass black hole: Viscous neutrino-radiation hydrodynamics simulation in full general relativity. *Phys. Rev. D* **101** (2020).
- [31] Fujibayashi, S. *et al.* Comprehensive study of mass ejection and nucleosynthesis in binary neutron star mergers leaving short-lived massive neutron stars. *Astrophys. J.* **942**, 39 (2023).
- [32] Lattimer, J. M. & Schramm, D. N. Black-hole-neutron-star collisions. *Astrophys. J. Lett.* **192**, L145 (1974).
- [33] Lattimer, J. M., Mackie, F., Ravenhall, D. G. & Schramm, D. N. The decompression of cold neutron star matter. *Astrophys. J.* **213**, 225 (1977).
- [34] Meyer, B. S. Decompression of Initially Cold Neutron Star Matter: A Mechanism for the r-Process? *Astrophys. J.* **343**, 254 (1989).
- [35] Freiburghaus, C., Rosswog, S. & Thielemann, F.-K. R-Process in Neutron Star Mergers. *Astrophys. J. Lett.* **525**, L121 (1999).

-
- [36] Metzger, B. *et al.* Electromagnetic Counterparts of Compact Object Mergers Powered by the Radioactive Decay of R-process Nuclei. *Mon. Not. Roy. Astron. Soc.* **406**, 2650 (2010).
- [37] Goriely, S., Bauswein, A. & Janka, H.-T. r-process Nucleosynthesis in Dynamically Ejected Matter of Neutron Star Mergers. *Astrophys. J. Lett.* **738**, L32 (2011).
- [38] Korobkin, O., Rosswog, S., Arcones, A. & Winteler, C. On the astrophysical robustness of the neutron star merger r-process. *Mon. Not. Roy. Astron. Soc.* **426**, 1940 (2012).
- [39] Wanajo, S. *et al.* Production of all the r-process nuclides in the dynamical ejecta of neutron star mergers. *Astrophys. J.* **789**, L39 (2014).
- [40] Just, O., Bauswein, A., Ardevol-Pulpillo, R., Goriely, S. & Janka, H. T. Comprehensive nucleosynthesis analysis for ejecta of compact binary mergers. *Mon. Not. Roy. Astron. Soc.* **448**, 541 (2015).
- [41] Bovard, L. *et al.* r-process nucleosynthesis from matter ejected in binary neutron star mergers. *Phys. Rev.* **D96**, 124005 (2017).
- [42] Kullmann, I. *et al.* Dynamical ejecta of neutron star mergers with nucleonic weak processes i: nucleosynthesis. *Mon. Not. Roy. Astron. Soc.* **510**, 2804 (2021).
- [43] Côté, B. *et al.* Neutron star mergers might not be the only source of r-process elements in the milky way. *Astrophys. J.* **875**, 106 (2019).
- [44] Hubble Space Telescope by NASA. http://hubblesite.org/image/1823/news_release/2005-37 (2005). Last check: October 9, 2018.
- [45] LIGO and Virgo observatories detect neutron star smash-ups. <https://www.psu.edu/news/research/story/ligo-and-virgo-observatories-detect-neutron-star-smash-ups/>. Last check: January 10, 2023.
- [46] Krüger, T., Tews, I., Hebeler, K. & Schwenk, A. Neutron matter from chiral effective field theory interactions. *Phys. Rev. C* **88**, 025802 (2013).
- [47] Yasin, H., Schäfer, S., Arcones, A. & Schwenk, A. Equation of state effects in core-collapse supernovae. *Phys. Rev. Lett.* **124**, 092701 (2020).
- [48] Schneider, A. S., Roberts, L. F. & Ott, C. D. Open-source nuclear equation of state framework based on the liquid-drop model with skyrme interaction. *Phys. Rev. C* **96**, 065802 (2017).
- [49] Landau, L. D. On the theory of stars. *Phys. Z. Sowjetunion* **1**, 285 (1932).
- [50] Chadwick, J. Possible Existence of a Neutron. *Nature* **129**, 312 (1932).
- [51] Baade, W. & Zwicky, F. Cosmic Rays from Super-Novae. *Proc. National Akad. Sci.* **20**, 259 (1934).
- [52] Baade, W. & Zwicky, F. On Super-Novae. *Proc. National Akad. Sci.* **20**, 254 (1934).
- [53] Baade, W. & Zwicky, F. Remarks on Super-Novae and Cosmic Rays. *Phys. Rev.* **46**, 76 (1934).
- [54] Tolman, R. C. Static Solutions of Einstein's Field Equations for Spheres of Fluid. *Phys. Rev.* **55**, 364 (1939).
- [55] Oppenheimer, J. R. & Volkoff, G. M. On Massive Neutron Cores. *Phys. Rev.* **55**, 374 (1939).

-
- [56] Hewish, A., Bell, S. J., Pilkington, J. D. H., Scott, P. F. & Collins, R. A. Observation of a Rapidly Pulsating Radio Source. *Nature* **217**, 709 (1968).
- [57] Hewish, A. & Okoye, S. E. Evidence for an unusual source of high radio brightness temperature in the crab nebula. *Nature* **207**, 59 (1965).
- [58] Large, M. I., Vaughan, A. E. & Mills, B. Y. A pulsar supernova association? *Nature* **220**, 340 (1968).
- [59] Staelin, D. H. & Reifenstein, E. C. Pulsating radio sources near the crab nebula. *Science* **162**, 1481 (1968).
- [60] Comella, J. M., Craft, H. D., Lovelace, R. V. E., Sutton, J. M. & T., G. L. Crab nebula pulsar np 0532. *Nature* **221**, 453 (1969).
- [61] Blinnikov, S. I., Imshennik, V. S. & Nadyozhin, D. K. The neutrino radiation of collapsing stellar cores and the neutrino burst detected from SN 1987A. *Astrophys. Space Sci.* **150**, 273 (1988).
- [62] Manchester, R. N., Hobbs, G. B., Teoh, A. & Hobbs, M. The Australia Telescope National Facility pulsar catalogue. *Astron. J.* **129**, 1993 (2005).
- [63] ATNF Pulsar Catalogue. <http://www.atnf.csiro.au/research/pulsar/psrcat/>. Last check: Dezember 28, 2022.
- [64] Hulse, R. & Taylor, J. Discovery of a pulsar in a binary system. *Astrophys. J.* **195**, L51 (1975).
- [65] Abbott, B. P. *et al.* Observation of Gravitational Waves from a Binary Black Hole Merger. *Phys. Rev. Lett.* **116**, 061102 (2016).
- [66] Abbott, B. P. *et al.* GW170817: Observation of gravitational waves from a binary neutron star inspiral. *Phys. Rev. Lett.* **119**, 161101 (2017).
- [67] Bauswein, A., Just, O., Janka, H. T. & Stergioulas, N. Neutron-star radius constraints from GW170817 and future detections. *Astrophys. J.* **850**, L34 (2017).
- [68] Annala, E., Gorda, T., Kurkela, A. & Vuorinen, A. Gravitational-wave constraints on the neutron-star-matter equation of state. *Phys. Rev. Lett.* **120**, 172703 (2018).
- [69] Most, E. R., Weih, L. R., Rezzolla, L. & Schaffner-Bielich, J. New constraints on radii and tidal deformabilities of neutron stars from GW170817. *Phys. Rev. Lett.* **120**, 261103 (2018).
- [70] Abbott, B. P. *et al.* GW170817: Measurements of neutron star radii and equation of state. *Phys. Rev. Lett.* **121**, 161101 (2018).
- [71] Capano, C. D. *et al.* Stringent constraints on neutron-star radii from multimessenger observations and nuclear theory. *Nature Astron.* **4**, 625 (2020).
- [72] Dietrich, T. *et al.* New Constraints on the Supranuclear Equation of State and the Hubble Constant from Nuclear Physics – Multi-Messenger Astronomy. *Science* **370**, 1450 (2020).
- [73] Huth, S., Wellenhofer, C. & Schwenk, A. New equations of state constrained by nuclear physics, observations, and qcd calculations of high-density nuclear matter. *Phys. Rev. C* **103**, 025803 (2021).
- [74] Woosley, S. & Janka, H. T. The physics of core-collapse supernovae. *Nature Phys.* **1**, 147 (2005).

-
- [75] Colgate, S. A. & White, R. H. The Hydrodynamic Behavior of Supernovae Explosions. *Astrophys. J.* **143**, 626 (1966).
- [76] Bethe, H. A. & Wilson, J. R. Revival of a stalled supernova shock by neutrino heating. *Astrophys. J.* **295**, 14 (1985).
- [77] Newton, W. G. A taste of pasta? *Nature Phys.* **9**, 396–397 (2013).
- [78] Watts, A. L. *et al.* Dense matter with eXTP. *Sci. China Phys. Mech. Astron.* **62**, 29503 (2018).
- [79] Pethick, C. J., Akmal, A., Pandharipande, V. R. & Ravenhall, D. G. Neutron star structure (1999).
- [80] Negele, J. W. & Vautherin, D. Neutron star matter at subnuclear densities. *Nucl. Phys.* **A207**, 298 (1973).
- [81] Burgio, G., Schulze, H.-J., Vidaña, I. & Wei, J.-B. Neutron stars and the nuclear equation of state. *Prog. Part. Nucl. Phys.* **120**, 103879 (2021).
- [82] Adam, C., Martín-Caro, A. G., Huidobro, M., Vázquez, R. & Wereszczynski, A. Kaon condensation in skyrmion matter and compact stars (2022).
- [83] Tolos, L. Strange mesons in nuclei and neutron stars. *EPJ Web of Conferences* **271**, 09002 (2022).
- [84] Sedrakian, A., Li, J. J. & Weber, F. Heavy baryons in compact stars (2022).
- [85] Kochankovski, H., Ramos, A. & Tolos, L. Equation of state for hot hyperonic neutron star matter. *Mon. Not. Roy. Astron. Soc.* **517**, 507 (2022).
- [86] Baym, G. & Pethick, C. Neutron stars. *Annu. Rev. Nucl. Sci.* **25**, 27 (1975).
- [87] Lattimer, J. M. & Prakash, M. Neutron star observations: Prognosis for equation of state constraints. *Phys. Rep.* **442**, 109 – 165 (2007).
- [88] Margalit, B. & Metzger, B. D. Constraining the maximum mass of neutron stars from multi-messenger observations of GW170817. *Astrophys. J.* **850**, L19 (2017).
- [89] Rezzolla, L., Most, E. R. & Weih, L. R. Using gravitational-wave observations and quasi-universal relations to constrain the maximum mass of neutron stars. *Astrophys. J.* **852**, L25 (2018).
- [90] Shibata, M., Zhou, E., Kiuchi, K. & Fujibayashi, S. Constraint on the maximum mass of neutron stars using GW170817 event. *Phys. Rev. D* **100** (2019).
- [91] Most, E. R., Papenfort, L. J., Weih, L. R. & Rezzolla, L. A lower bound on the maximum mass if the secondary in GW190814 was once a rapidly spinning neutron star. *Monthly Notices of the Royal Astronomical Society: Letters* **499**, L82 (2020).
- [92] Lattimer, J. M. & Prakash, M. Neutron star structure and the equation of state. *Astrophys. J.* **550**, 426 (2001).
- [93] Glendenning, N. K. *Compact Stars: Nuclear Physics, Particle Physics, and General Relativity*. Astronomy and Astrophysics Library (Springer New York, 2000), 2nd edn.
- [94] Misner, C. W., Thorne, K. S. & Wheeler, J. A. *Gravitation* (W. H. Freeman and Company, San Francisco, 1973).

-
- [95] Greif, S. K. *Constraining the radius of neutron stars through the moment of inertia*. Master's thesis, Technische Universität Darmstadt (2016).
- [96] Greif, S. K. *Constraining the nuclear equation of state from nuclear physics and neutron star observations*. Ph.D. thesis, Technische Universität Darmstadt, Darmstadt (2019).
- [97] Kramer, M. *et al.* Tests of general relativity from timing the double pulsar. *Science* **314**, 97 (2006).
- [98] Lattimer, J. M. Observed neutron star masses. <https://stellarcollapse.org/nsmasses>. Accessed September 16, 2016.
- [99] Lattimer, J. M. & Prakash, M. Ultimate energy density of observable cold baryonic matter. *Phys. Rev. Lett.* **94**, 111101 (2005).
- [100] STAIRS, I. H. Pulsar timing observations and tests of general relativity in double-neutron-star binaries. In *The Ninth Marcel Grossmann Meeting, 1753–1754* (World Scientific Publishing Company, 2002).
- [101] Damour, T. & Deruelle, N. General relativistic celestial mechanics of binary systems. I. The post-Newtonian motion. *Ann. Inst. Henri Poincaré Phys. Théor* **43**, 107 (1985).
- [102] Damour, T. & Taylor, J. H. Strong field tests of relativistic gravity and binary pulsars. *Phys. Rev.* **D45**, 1840 (1992).
- [103] Stairs, I. H. Testing general relativity with pulsar timing. *Living Rev. Rel.* **6** (2003).
- [104] P. Freire. https://www3.mpifr-bonn.mpg.de/staff/pfreire/NS_masses.html. Last check: December 28, 2022.
- [105] Watts, A. L. *et al.* Colloquium: Measuring the neutron star equation of state using x-ray timing. *Rev. Mod. Phys.* **88**, 021001 (2016).
- [106] Gendreau, K. C. *et al.* The Neutron star Interior Composition Explorer (NICER): design and development. In *Space Telescopes and Instrumentation 2016: Ultraviolet to Gamma Ray*, vol. 9905, 99051H. International Society for Optics and Photonics (SPIE, 2016).
- [107] Lo, K. H., Miller, M. C., Bhattacharyya, S. & Lamb, F. K. Determining neutron star masses and radii using energy-resolved waveforms of x-ray burst oscillations. *Astrophys. J.* **776**, 19 (2013).
- [108] Psaltis, D., Özel, F. & Chakrabarty, D. Prospects for measuring neutron-star masses and radii with x-ray pulse profile modeling. *Astrophys. J.* **787**, 136 (2014).
- [109] Miller, M. C. & Lamb, F. K. Bounds on the compactness of neutron stars from brightness oscillations during x-ray bursts. *Astrophys. J.* **499**, L37 (1998).
- [110] Poutanen, J. & Gierlinski, M. On the nature of the x-ray emission from the accreting millisecond pulsar SAX j1808.4-3658. *Mon. Not. Roy. Astron. Soc.* **343**, 1301 (2003).
- [111] Poutanen, J. & Beloborodov, A. M. Pulse profiles of millisecond pulsars and their fourier amplitudes. *Mon. Not. Roy. Astron. Soc.* **373**, 836 (2006).
- [112] Cadeau, C., Morsink, S. M., Leahy, D. & Campbell, S. S. Light curves for rapidly rotating neutron stars. *Astrophys. J.* **654**, 458 (2007).

-
- [113] Morsink, S. M., Leahy, D. A., Cadeau, C. & Braga, J. The oblate schwarzschild approximation for light curves of rapidly rotating neutron stars. *Astrophys. J.* **663**, 1244 (2007).
- [114] Bauböck, M., Berti, E., Psaltis, D. & Özel, F. Relations between neutron-star parameters in the hartle-thorne approximation. *Astrophys. J.* **777**, 68 (2013).
- [115] AlGendy, M. & Morsink, S. M. Universality of the acceleration due to gravity on the surface of a rapidly rotating neutron star. *Astrophys. J.* **791**, 78 (2014).
- [116] Psaltis, D. & Özel, F. Pulse profiles from spinning neutron stars in the hartle-thorne approximation. *Astrophys. J.* **792**, 87 (2014).
- [117] Nättilä, J. & Pihajoki, P. Radiation from rapidly rotating oblate neutron stars. *Astron. Astrophys.* **615**, A50 (2018).
- [118] Watts, A. L. Constraining the neutron star equation of state using Pulse Profile Modeling. *AIP Conf. Proc.* **2127**, 020008 (2019).
- [119] Zhang, S. *et al.* The enhanced x-ray timing and polarimetry mission—eXTP. *Sci. China Phys. Mech. Astron.* **62** (2018).
- [120] Ray, P. S. *et al.* STROBE-X: A probe-class mission for x-ray spectroscopy and timing on timescales from microseconds to years (2018).
- [121] Riley, T. E. *et al.* A NICER view of PSR J0030+0451: Millisecond pulsar parameter estimation. *Astrophys. J. Lett.* **887**, L21 (2019).
- [122] Miller, M. C. *et al.* PSR J0030+0451 mass and radius from NICER data and implications for the properties of neutron star matter. *Astrophys. J. Lett.* **887**, L24 (2019).
- [123] Riley, T. E. *et al.* A NICER view of the massive pulsar PSR j0740+6620 informed by radio timing and XMM-newton spectroscopy. *Astrophys. J. Lett.* **918**, L27 (2021).
- [124] Miller, M. C. *et al.* The radius of PSR J0740+6620 from NICER and XMM-newton data. *Astrophys. J. Lett.* **918**, L28 (2021).
- [125] Raaijmakers, G. *et al.* A NICER view of PSR J0030+0451: Implications for the dense matter equation of state. *Astrophys. J. Lett.* **887**, L22 (2019).
- [126] Raaijmakers, G. *et al.* Constraining the dense matter equation of state with joint analysis of NICER and LIGO/Virgo measurements. *Astrophys. J.* **893**, L21 (2020).
- [127] Raaijmakers, G. *et al.* Constraints on the dense matter equation of state and neutron star properties from NICER’s mass–radius estimate of PSR J0740+6620 and multimessenger observations. *Astrophys. J. Lett.* **918**, L29 (2021).
- [128] Einstein, A. Über Gravitationswellen. *Sitzungsber. Preuss. Akad. Wiss. Berlin (Math. Phys.)* **1918**, 154 (1918).
- [129] Einstein, A. The Field Equations of Gravitation. *Sitzungsber. Preuss. Akad. Wiss. Berlin (Math. Phys.)* **1915**, 844 (1915).
- [130] Einstein, A. Approximative Integration of the Field Equations of Gravitation. *Sitzungsber. Preuss. Akad. Wiss. Berlin (Math. Phys.)* **1916**, 688 (1916).

-
- [131] Schutz, B. F. Determining the Hubble Constant from Gravitational Wave Observations. *Nature* **323**, 310 (1986).
- [132] Schutz, B. F. Gravitational wave sources and their detectability. *Class. Quant. Grav.* **6**, 1761 (1989).
- [133] Cutler, C. *et al.* The last three minutes: Issues in gravitational-wave measurements of coalescing compact binaries. *Phys. Rev. Lett.* **70**, 2984 (1993).
- [134] Camenzind, M. *Compact Objects in Astrophysics: White Dwarfs, Neutron Stars and Black Holes*. Astronomy and Astrophysics Library (Springer Berlin Heidelberg, 2007).
- [135] Cutler, C. & Thorne, K. S. An overview of gravitational-wave sources (2002).
- [136] Abbott, B. P. *et al.* Gravitational Waves and Gamma-Rays from a Binary Neutron Star Merger: GW170817 and GRB 170817A. *Astrophys. J.* **848**, L13 (2017).
- [137] Abbott, B. P. *et al.* LIGO: The Laser interferometer gravitational-wave observatory. *Rept. Prog. Phys.* **72**, 076901 (2009).
- [138] Harry, G. M. Advanced LIGO: The next generation of gravitational wave detectors. *Class. Quant. Grav.* **27**, 084006 (2010).
- [139] Giazotto, A. The Virgo Project: A Wide Band Antenna for Gravitational Wave Detection. *Nucl. Instrum. Meth. A* **289**, 518 (1990).
- [140] Acernese, F. *et al.* Advanced Virgo: a second-generation interferometric gravitational wave detector. *Class. Quant. Grav.* **32**, 024001 (2015).
- [141] Coleman Miller, M. & Yunes, N. The new frontier of gravitational waves. *Nature* **568**, 469 (2019).
- [142] Will, C. M. The confrontation between general relativity and experiment. *Living Rev. Rel.* **17** (2014).
- [143] Flanagan, E. E. & Hinderer, T. Constraining neutron star tidal Love numbers with gravitational wave detectors. *Phys. Rev. D* **77**, 021502 (2008).
- [144] Peters, P. C. & Mathews, J. Gravitational radiation from point masses in a Keplerian orbit. *Phys. Rev.* **131**, 435 (1963).
- [145] Hinderer, T. Tidal Love numbers of neutron stars. *Astrophys. J.* **677**, 1216 (2008).
- [146] Punturo, M. *et al.* The Einstein Telescope: A third-generation gravitational wave observatory. *Class. Quant. Grav.* **27**, 194002 (2010).
- [147] Hild, S. Beyond the Second Generation of Laser-Interferometric Gravitational Wave Observatories. *Class. Quant. Grav.* **29**, 124006 (2012).
- [148] Martynov, D. *et al.* Exploring the sensitivity of gravitational wave detectors to neutron star physics. *Phys. Rev. D* **99** (2019).
- [149] Reitze, D. *et al.* Cosmic Explorer: The U.S. Contribution to Gravitational-Wave Astronomy beyond LIGO (2019).
- [150] Radice, D. & Dai, L. Multimessenger Parameter Estimation of GW170817. *Eur. Phys. J.* **A55**, 50 (2019).

-
- [151] Legred, I., Chatziioannou, K., Essick, R., Han, S. & Landry, P. Impact of the PSR J0740+6620 radius constraint on the properties of high-density matter. *Phys. Rev. D* **104**, 063003 (2021).
- [152] Raaijmakers, G. *et al.* Constraints on the dense matter equation of state and neutron star properties from NICER’s mass-radius estimate of PSR J0740+6620 and multimessenger observations. *Astrophys. J. Lett.* **918**, L29 (2021).
- [153] Rosswog, S. *et al.* The first direct double neutron star merger detection: implications for cosmic nucleosynthesis. *Astron. Astrophys.* **615**, A132 (2018).
- [154] Kawaguchi, K., Shibata, M. & Tanaka, M. Radiative transfer simulation for the optical and near-infrared electromagnetic counterparts to GW170817. *Astrophys. J. Letters* **865**, L21 (2018).
- [155] Kasliwal, M. M. *et al.* Spitzer mid-infrared detections of neutron star merger GW170817 suggests synthesis of the heaviest elements. *Mon. Not. Roy. Astron. Soc. Lett.* **510**, L7 (2019).
- [156] Krishnan, V. V. *et al.* Lense-thirring frame dragging induced by a fast-rotating white dwarf in a binary pulsar system. *Science* **367**, 577 (2020).
- [157] Abbott, B. P. *et al.* GW190425: Observation of a Compact Binary Coalescence with Total Mass $\sim 3.4M_{\odot}$. *Astrophys. J. Lett.* **892**, L3 (2020).
- [158] Dudi, R. *et al.* Investigating GW190425 with numerical-relativity simulations (2021).
- [159] Coughlin, M. W. *et al.* GROWTH on S190425z: Searching thousands of square degrees to identify an optical or infrared counterpart to a binary neutron star merger with the Zwicky Transient Facility and Palomar Gattini IR. *Astrophys. J. Lett.* **885**, L19 (2019).
- [160] Steeghs, D. *et al.* LIGO/Virgo S190425z: GOTO observations. *GRB Coordinates Network* **24224**, 1 (2019).
- [161] Han, M. Z. *et al.* Is GW190425 consistent with being a neutron star–black hole merger? *Astrophys. J. Letters* **891**, L5 (2020).
- [162] Kyutoku, K. *et al.* On the possibility of GW190425 being a black hole–neutron star binary merger. *Astrophys. J.* **890**, L4 (2020).
- [163] Huth, S. *et al.* Constraining neutron-star matter with microscopic and macroscopic collisions. *Nature* **606**, 276 (2022).
- [164] Margetis, S., Safarik, K. & Villalobos Baillie, O. Strangeness production in heavy-ion collisions. *Annu. Rev. Nucl. Part. Sci.* **50**, 299 (2000).
- [165] Aarts, G. *et al.* Phase transitions in particle physics – results and perspectives from lattice quantum chromo-dynamics (2023).
- [166] Drischler, C., Holt, J. & Wellenhofer, C. Chiral effective field theory and the high-density nuclear equation of state. *Annu. Rev. Nucl. Part. Sci.* **71**, 403 (2021).
- [167] Tews, I., Krüger, T., Hebeler, K. & Schwenk, A. Neutron Matter at Next-to-Next-to-Next-to-Leading Order in Chiral Effective Field Theory. *Phys. Rev. Lett.* **110**, 032504 (2013).
- [168] Lynn, J. E. *et al.* Chiral Three-Nucleon Interactions in Light Nuclei, Neutron- α Scattering, and Neutron Matter. *Phys. Rev. Lett.* **116**, 062501 (2016).

-
- [169] Drischler, C., Hebeler, K. & Schwenk, A. Chiral interactions up to next-to-next-to-next-to-leading order and nuclear saturation. *Phys. Rev. Lett.* **122**, 042501 (2019).
- [170] Drischler, C., Furnstahl, R. J., Melendez, J. A. & Phillips, D. R. How well do we know the neutron-matter equation of state at the densities inside neutron stars? A bayesian approach with correlated uncertainties. *Phys. Rev. Lett.* **125** (2020).
- [171] Leonhardt, M. *et al.* Symmetric nuclear matter from the strong interaction. *Phys. Rev. Lett.* **125**, 142502 (2020).
- [172] Braun, J. & Schallmo, B. Zero-temperature thermodynamics of dense asymmetric strong-interaction matter. *Phys. Rev. D* **106**, 076010 (2022).
- [173] Kurkela, A., Romatschke, P. & Vuorinen, A. Cold quark matter. *Phys. Rev. D* **81** (2010).
- [174] Fraga, E. S., Kurkela, A. & Vuorinen, A. Interacting quark matter equation of state for compact stars. *Astrophys. J.* **781**, L25 (2014).
- [175] Hebeler, K., Lattimer, J. M., Pethick, C. J. & Schwenk, A. Constraints on Neutron Star Radii Based on Chiral Effective Field Theory Interactions. *Phys. Rev. Lett.* **105**, 161102 (2010).
- [176] Greif, S. K., Raaijmakers, G., Hebeler, K., Schwenk, A. & Watts, A. L. Equation of state sensitivities when inferring neutron star and dense matter properties. *Mon. Not. Roy. Astron. Soc.* **485**, 5363 (2019).
- [177] Tews, I., Carlson, J., Gandolfi, S. & Reddy, S. Constraining the speed of sound inside neutron stars with chiral effective field theory interactions and observations. *Astrophys. J.* **860**, 149 (2018).
- [178] Workman, R. L. *et al.* Review of Particle Physics. *Prog. Theor. Exp. Phys.* **2022**, 083C01 (2022).
- [179] Hinchliffe, I. & Manohar, A. The QCD coupling constant. *Annu. Rev. Nucl. Part. Sci.* **50**, 643 (2000).
- [180] Bethke, S. Experimental tests of asymptotic freedom. *Prog. Part. Nucl. Phys.* **58**, 351 (2007).
- [181] Machleidt, R. & Entem, D. R. Chiral effective field theory and nuclear forces. *Phys. Rep.* **503**, 1 (2011).
- [182] Kaplan, D. B. Five lectures on effective field theory. In *Lectures delivered at the 17th National Nuclear Physics Summer School 2015, Berkeley, June 6-17, 2005* (2005).
- [183] Entem, D. R. & Machleidt, R. Accurate charge-dependent nucleon-nucleon potential at fourth order of chiral perturbation theory. *Phys. Rev. C* **68**, 041001(R) (2003).
- [184] Epelbaum, E., Hammer, H. W. & Meißner, U. G. Modern Theory of Nuclear Forces. *Rev. Mod. Phys.* **81**, 1773 (2009).
- [185] Epelbaum, E. Nuclear Forces from Chiral Effective Field Theory: A Primer (2010).
- [186] Weinberg, S. Phenomenological Lagrangians. *Physica A* **96**, 327 (1979).
- [187] Weinberg, S. Nuclear forces from chiral Lagrangians. *Phys. Lett. B* **251**, 288 (1990).
- [188] Weinberg, S. Effective chiral Lagrangians for nucleon - pion interactions and nuclear forces. *Nucl. Phys. B* **363**, 3 (1991).

-
- [189] Weinberg, S. Three-body interactions among nucleons and pions. *Phys. Lett. B* **295**, 114 (1992).
- [190] Epelbaum, E. Nuclear Chiral EFT in the Precision Era (2016).
- [191] Holt, J. D., Menéndez, J., Simonis, J. & Schwenk, A. Three-nucleon forces and spectroscopy of neutron-rich calcium isotopes. *Phys. Rev. C* **90**, 024312 (2014).
- [192] Tichai, A., Langhammer, J., Binder, S. & Roth, R. Hartree-Fock many-body perturbation theory for nuclear ground-states. *Phys. Lett. B* **756**, 283 (2016).
- [193] Tichai, A., Roth, R. & Duguet, T. Many-body perturbation theories for finite nuclei. *Front. Phys.* **8** (2020).
- [194] Tsukiyama, K., Bogner, S. K. & Schwenk, A. In-medium Similarity Renormalization Group for Nuclei. *Phys. Rev. Lett.* **106**, 222502 (2011).
- [195] Hergert, H., Bogner, S. K., Morris, T. D., Schwenk, A. & Tsukiyama, K. The In-Medium Similarity Renormalization Group: A Novel Ab Initio Method for Nuclei. *Phys. Rept.* **621**, 165 (2016).
- [196] Dickhoff, W. H. & Barbieri, C. Selfconsistent Green's function method for nuclei and nuclear matter. *Prog. Part. Nucl. Phys.* **52**, 377 (2004).
- [197] Gezerlis, A. *et al.* Quantum Monte Carlo Calculations with Chiral Effective Field Theory Interactions. *Phys. Rev. Lett.* **111**, 032501 (2013).
- [198] Carlson, J. *et al.* Quantum Monte Carlo methods for nuclear physics. *Rev. Mod. Phys.* **87**, 1067 (2015).
- [199] Lynn, J. E., Tews, I., Gandolfi, S. & Lovato, A. Quantum Monte Carlo Methods in Nuclear Physics: Recent Advances. *Ann. Rev. Nucl. Part. Sci.* **69**, 279 (2019).
- [200] Hagen, G., Papenbrock, T., Hjorth-Jensen, M. & Dean, D. J. Coupled-cluster computations of atomic nuclei. *Rep. Prog. Phys.* **77**, 096302 (2014).
- [201] Binder, S., Langhammer, J., Calci, A. & Roth, R. Ab initio path to heavy nuclei. *Phys. Lett. B* **736**, 119 (2014).
- [202] Hebeler, K., Holt, J. D., Menéndez, J. & Schwenk, A. Nuclear forces and their impact on neutron-rich nuclei and neutron-rich matter. *Annu. Rev. Nucl. Part. Sci.* **65**, 457 (2015).
- [203] Wetterich, C. Exact evolution equation for the effective potential. *Phys. Lett. B* **301**, 90 (1993).
- [204] Cyrol, A. K., Fister, L., Mitter, M., Pawłowski, J. M. & Strodthoff, N. Landau gauge yang-mills correlation functions. *Phys. Rev. D* **94**, 054005 (2016).
- [205] Wilson, K. G. Renormalization group and critical phenomena. 1. Renormalization group and the Kadanoff scaling picture. *Phys. Rev. B* **4**, 3174 (1971).
- [206] Wilson, K. G. Renormalization group and critical phenomena. 2. Phase space cell analysis of critical behavior. *Phys. Rev. B* **4**, 3184 (1971).
- [207] Wilson, K. G. Confinement of quarks. *Phys. Rev. D* **10**, 2445 (1974).

-
- [208] Peskin, M. E. & Schroeder, D. V. *An Introduction to quantum field theory* (Addison-Wesley, Reading, USA, 1995).
- [209] Gies, H. *Introduction to the Functional RG and Applications to Gauge Theories*, 287 (Springer Berlin Heidelberg, Berlin, Heidelberg, 2012).
- [210] Bedaque, P. & Steiner, A. W. Sound velocity bound and neutron stars. *Phys. Rev. Lett.* **114** (2015).
- [211] Gorda, T., Kurkela, A., Romatschke, P., Säppi, S. & Vuorinen, A. Next-to-next-to-next-to-leading order pressure of cold quark matter: Leading logarithm. *Phys. Rev. Lett.* **121**, 202701 (2018).
- [212] Gorda, T., Kurkela, A., Paatelainen, R., Säppi, S. & Vuorinen, A. Soft interactions in cold quark matter. *Phys. Rev. Lett.* **127** (2021).
- [213] Most, E. R., Weih, L. R., Rezzolla, L. & Schaffner-Bielich, J. New constraints on radii and tidal deformabilities of neutron stars from GW170817. *Phys. Rev. Lett.* **120** (2018).
- [214] Annala, E. *et al.* Multimessenger constraints for ultradense matter. *Phys. Rev. X* **12** (2022).
- [215] Somasundaram, R., Tews, I. & Margueron, J. Perturbative QCD and the neutron star equation of state (2022).
- [216] Altiparmak, S., Ecker, C. & Rezzolla, L. On the sound speed in neutron stars. *Astrophys. J. Lett.* **939**, L34 (2022).
- [217] Fujimoto, Y., Fukushima, K., McLerran, L. D. & Praszalowicz, M. Trace anomaly as signature of conformality in neutron stars. *Phys. Rev. Lett.* **129**, 252702 (2022).
- [218] Marczenko, M., McLerran, L., Redlich, K. & Sasaki, C. Reaching percolation and conformal limits in neutron stars (2022).
- [219] Ecker, C. & Rezzolla, L. A general, scale-independent description of the sound speed in neutron stars. *Astrophys. J. Lett.* **939**, L35 (2022).
- [220] Ecker, C. & Rezzolla, L. Impact of large-mass constraints on the properties of neutron stars. *Mon. Not. Roy. Astron. Soc.* **519**, 2615 (2022).
- [221] Jiang, J. L., Ecker, C. & Rezzolla, L. Bayesian analysis of neutron-star properties with parameterized equations of state: the role of the likelihood functions (2022).
- [222] Gorda, T., Hebel, A., Kurkela, A., Schwenk, A. & Vuorinen, A. Constraints on strong phase transitions in neutron stars (2022).
- [223] Komoltsev, O. & Kurkela, A. How perturbative QCD constrains the equation of state at neutron-star densities. *Phys. Rev. Lett.* **128** (2022).
- [224] Gorda, T., Komoltsev, O. & Kurkela, A. Ab-initio QCD calculations impact the inference of the neutron-star-matter equation of state (2022).
- [225] Lattimer, J. M. & Lim, Y. Constraining the Symmetry Parameters of the Nuclear Interaction. *Astrophys. J.* **771**, 51 (2013).
- [226] Drischler, C., Hebel, K. & Schwenk, A. Asymmetric nuclear matter based on chiral two- and three-nucleon interactions. *Phys. Rev. C* **93**, 054314 (2016).

-
- [227] Bertsch, G. F. & Bingham, D. Estimating parameter uncertainty in binding-energy models by the frequency-domain bootstrap. *Phys. Rev. Lett.* **119**, 252501 (2017).
- [228] Hebeler, K., Bogner, S. K., Furnstahl, R. J., Nogga, A. & Schwenk, A. Improved nuclear matter calculations from chiral low-momentum interactions. *Phys. Rev. C* **83**, 031301(R) (2011).
- [229] Wang, Y. *et al.* Determination of the nuclear incompressibility from the rapidity-dependent elliptic flow in heavy-ion collisions at beam energies 0.4 A –1.0 A GeV. *Phys. Lett. B* **778**, 207 (2018).
- [230] Garg, U. & Colò, G. The compression-mode giant resonances and nuclear incompressibility. *Prog. Part. Nucl. Phys.* **101**, 55–95 (2018).
- [231] Stone, J. R., Stone, N. J. & Moszkowski, S. A. Incompressibility in finite nuclei and nuclear matter. *Phys. Rev. C* **89**, 044316 (2014).
- [232] Grams, G., Somasundaram, R., Margueron, J. & Khan, E. Nuclear incompressibility and sound speed in uniform matter and finite nuclei (2022).
- [233] Lattimer, J. M. Constraints on nuclear symmetry energy parameters. *Particles* **6**, 30–56 (2023).
- [234] Gandolfi, S., Carlson, J. & Reddy, S. The maximum mass and radius of neutron stars and the nuclear symmetry energy. *Phys. Rev. C* **85**, 032801(R) (2012).
- [235] Tews, I., Lattimer, J. M., Ohnishi, A. & Kolomeitsev, E. E. Symmetry Parameter Constraints from a Lower Bound on Neutron-matter Energy. *Astrophys. J.* **848**, 105 (2017).
- [236] Kortelainen, T., M. Lesinski *et al.* Nuclear energy density optimization. *Phys. Rev. C* **82**, 024313 (2010).
- [237] Trippa, L., Colo, G. & Vigezzi, E. The Giant Dipole Resonance as a quantitative constraint on the symmetry energy. *Phys. Rev. C* **77**, 061304 (2008).
- [238] Chen, L. W., Ko, C. M., Li, B. A. & Xu, J. Density slope of the nuclear symmetry energy from the neutron skin thickness of heavy nuclei. *Phys. Rev. C* **82**, 024321 (2010).
- [239] Tamii, A. *et al.* Complete electric dipole response and the neutron skin in ^{208}Pb . *Phys. Rev. Lett.* **107**, 062502 (2011).
- [240] Roca-Maza, X. *et al.* Electric dipole polarizability in ^{208}pb : Insights from the droplet model. *Phys. Rev. C* **88**, 024316 (2013).
- [241] Tsang, M. B. *et al.* Constraints on the density dependence of the symmetry energy. *Phys. Rev. Lett.* **102**, 122701 (2009).
- [242] Danielewicz, P. & Lee, J. Symmetry energy II: Isobaric analog states. *Nucl. Phys. A* **922**, 1 (2014).
- [243] Adhikari, D. *et al.* Accurate Determination of the Neutron Skin Thickness of ^{208}Pb through Parity-Violation in Electron Scattering. *Phys. Rev. Lett.* **126**, 172502 (2021).
- [244] Reed, B. T., Fattoyev, F. J., Horowitz, C. J. & Piekarewicz, J. Implications of PREX-II on the equation of state of neutron-rich matter. *Phys. Rev. Lett.* **126**, 172503 (2021).
- [245] Chen, L. W. *et al.* *Nuclear Matter at High Density and Equation of State*, 183–285 (Springer Nature Singapore, Singapore, 2022).

-
- [246] Danielewicz, P., Lacey, R. & Lynch, W. G. Determination of the equation of state of dense matter. *Science* **298**, 1592 (2002).
- [247] Fuchs, C. & Wolter, H. H. Modelization of the EOS. *Eur. Phys. J. A* **30**, 5 (2006).
- [248] Zhang, Y. *et al.* Progress of quantum molecular dynamics model and its applications in heavy ion collisions. *Front. Phys. (Beijing)* **15**, 54301 (2020).
- [249] Le Fèvre, A., Leifels, Y., Reisdorf, W., Aichelin, J. & Hartnack, C. Constraining the nuclear matter equation of state around twice saturation density. *Nucl. Phys. A* **945**, 112 (2016).
- [250] Reisdorf, W. *et al.* Systematics of azimuthal asymmetries in heavy ion collisions in the 1 A GeV regime. *Nucl. Phys. A* **876**, 1 (2012).
- [251] Hartnack, C. *et al.* Modeling the many body dynamics of heavy ion collisions: Present status and future perspective. *Eur. Phys. J. A* **1**, 151 (1998).
- [252] Le Fèvre, A., Leifels, Y., Hartnack, C. & Aichelin, J. Origin of elliptic flow and its dependence on the equation of state in heavy ion reactions at intermediate energies. *Phys. Rev. C* **98**, 034901 (2018).
- [253] Tsang, M. B. *et al.* Constraints on the symmetry energy and neutron skins from experiments and theory. *Phys. Rev. C* **86**, 015803 (2012).
- [254] Horowitz, C. J. *et al.* A way forward in the study of the symmetry energy: experiment, theory, and observation. *J. Phys. G: Nucl. Part. Phys.* **41**, 093001 (2014).
- [255] Russotto, P. *et al.* Symmetry energy from elliptic flow in 197Au+197Au. *Phys. Lett. B* **697**, 471 (2011).
- [256] Russotto, P. *et al.* Results of the ASY-EOS experiment at GSI: The symmetry energy at suprasaturation density. *Phys. Rev. C* **94**, 034608 (2016).
- [257] Estee, J. *et al.* Probing the Symmetry Energy with the Spectral Pion Ratio. *Phys. Rev. Lett.* **126**, 162701 (2021).
- [258] Fischer, T. *et al.* The state of matter in simulations of core-collapse supernovae – Reflections and recent developments. *Publ. Astron. Soc. Austral.* **34**, 67 (2017).
- [259] Baiotti, L. & Rezzolla, L. Binary neutron star mergers: a review of Einstein’s richest laboratory. *Rept. Prog. Phys.* **80**, 096901 (2017).
- [260] Endrizzi, A. *et al.* Thermodynamics conditions of matter in the neutrino decoupling region during neutron star mergers. *Eur. Phys. J. A* **56** (2020).
- [261] Bauswein, A., Janka, H.-T. & Oechslin, R. Testing approximations of thermal effects in neutron star merger simulations. *Phys. Rev. D* **82**, 084043 (2010).
- [262] Carbone, A. & Schwenk, A. Ab initio constraints on thermal effects of the nuclear equation of state. *Phys. Rev. C* **100**, 025805 (2019).
- [263] Keller, J., Wellenhofer, C., Hebeler, K. & Schwenk, A. Neutron matter at finite temperature based on chiral effective field theory interactions. *Phys. Rev. C* **103** (2021).

-
- [264] Hebeler, K., Duguet, T., Lesinski, T. & Schwenk, A. Non-empirical pairing energy functional in nuclear matter and finite nuclei. *Phys. Rev. C* **80**, 044321 (2009).
- [265] Siemens, P. J. Liquid–gas phase transition in nuclear matter. *Nature* **305**, 410 (1983).
- [266] Pochodzalla, J. *et al.* Probing the nuclear liquid-gas phase transition. *Phys. Rev. Lett.* **75**, 1040 (1995).
- [267] Finn, J. E. *et al.* Nuclear fragment mass yields from high-energy proton-nucleus interactions. *Phys. Rev. Lett.* **49**, 1321 (1982).
- [268] Karnaukhov, V. A. *et al.* Critical temperature for the nuclear liquid-gas phase transition (from multifragmentation and fission). *Phys. Atom. Nucl.* **71**, 2067 (2008).
- [269] Rios, A., Polls, A. & Vidaña, I. Hot neutron matter from a Self-Consistent Green’s Functions approach. *Phys. Rev. C* **79**, 025802 (2009).
- [270] Somà, V. & Bozek, P. Thermodynamic properties of nuclear matter with three-body forces. *Phys. Rev. C* **80**, 025803 (2009).
- [271] Holt, J. W., Kaiser, N. & Weise, W. Nuclear chiral dynamics and thermodynamics. *Prog. Part. Nucl. Phys.* **73**, 35 (2013).
- [272] Carbone, A., Polls, A. & Rios, A. Microscopic Predictions of the Nuclear Matter Liquid-Gas Phase Transition. *Phys. Rev.* **C98**, 025804 (2018).
- [273] Bacca, S. *et al.* Neutrino processes in partially degenerate neutron matter. *Astrophys. J.* **758**, 34 (2012).
- [274] Keller, J., Hebeler, K. & Schwenk, A. Nuclear equation of state for arbitrary proton fraction and temperature based on chiral effective field theory and a gaussian process emulator (2022).
- [275] Lattimer, J. M., Pethick, C. J., Ravenhall, D. G. & Lamb, D. Q. Physical properties of hot, dense matter: The general case. *Nucl. Phys. A* **432**, 646 (1985).
- [276] Lattimer, J. M. & Swesty, F. D. A generalized equation of state for hot, dense matter. *Nucl. Phys. A* **535**, 331 (1991).
- [277] Baym, G., Bethe, H. A. & Pethick, C. J. Neutron star matter. *Nucl. Phys. A* **175**, 225–271 (1971).
- [278] Shen, H., Toki, H., Oyamatsu, K. & Sumiyoshi, K. Relativistic equation of state of nuclear matter for supernova and neutron star. *Nucl. Phys. A* **637**, 435 (1998).
- [279] Shen, H., Toki, H., Oyamatsu, K. & Sumiyoshi, K. Relativistic equation of state of nuclear matter for supernova explosion. *Prog. Theor. Phys.* **100**, 1013 (1998).
- [280] Shen, H., Toki, H., Oyamatsu, K. & Sumiyoshi, K. Relativistic equation of state for core-collapse supernova simulations. *Astrophys. J. Suppl.* **197**, 20 (2011).
- [281] Oyamatsu, K. Nuclear shapes in the inner crust of a neutron star. *Nucl. Phys. A* **561**, 431 (1993).
- [282] Hempel, M. & Schaffner-Bielich, J. A statistical model for a complete supernova equation of state. *Nucl. Phys. A* **837**, 210–254 (2010).

-
- [283] Steiner, A. W., Hempel, M. & Fischer, T. Core-collapse supernova equations of state based on neutron star observations. *Astrophys. J.* **774**, 17 (2013).
- [284] Typel, S., Ropke, G., Klahn, T., Blaschke, D. & Wolter, H. H. Composition and thermodynamics of nuclear matter with light clusters. *Phys. Rev.* **C81**, 015803 (2010).
- [285] Todd-Rutel, B. G. & Piekarewicz, J. Neutron-rich nuclei and neutron stars: A new accurately calibrated interaction for the study of neutron-rich matter. *Phys. Rev. Lett.* **95** (2005).
- [286] Hempel, M., Fischer, T., Schaffner-Bielich, J. & Liebendörfer, M. New equations of state in simulations of core-collapse supernovae. *Astrophys. J.* **748**, 70 (2012).
- [287] Chabanat, E., Bonche, P., Haensel, P., Meyer, J. & Schaeffer, R. A Skyrme parametrization from subnuclear to neutron star densities. 2. Nuclei far from stabilities. *Nucl. Phys. A* **635**, 231 (1998).
- [288] Tews, I., Gandolfi, S., Gezerlis, A. & Schwenk, A. Quantum monte carlo calculations of neutron matter with chiral three-body forces. *Phys. Rev. C* **93**, 024305 (2016).
- [289] Schneider, A. S., Roberts, L. F. & Ott, C. D. <https://bitbucket.org/andschn/sroeos> (2018).
- [290] Bogner, S. K., Furnstahl, R. J. & Schwenk, A. From low-momentum interactions to nuclear structure. *Prog. Part. Nucl. Phys.* **65**, 94 (2010).
- [291] Gezerlis, A. & Carlson, J. Low-density neutron matter. *Phys. Rev. C* **81**, 025803 (2010).
- [292] Ku, M. J. H., Sommer, A. T., Cheuk, L. W. & Zwierlein, M. W. Revealing the superfluid lambda transition in the universal thermodynamics of a unitary fermi gas. *Science* **335**, 563 (2012).
- [293] Roca-Maza, X. *et al.* The neutron skin thickness from the measured electric dipole polarizability in ^{68}Ni , ^{120}Sn , and ^{208}Pb . *Phys. Rev. C* **92**, 064304 (2015).
- [294] Hagen, G. *et al.* Neutron and weak-charge distributions of the ^{48}Ca nucleus. *Nature Phys.* **12**, 186 (2016).
- [295] Birkhan, J. *et al.* Electric dipole polarizability of ^{48}Ca and implications for the neutron skin. *Phys. Rev. Lett.* **118**, 252501 (2017).
- [296] Kaufmann, S. *et al.* Charge Radius of the Short-Lived ^{68}Ni and Correlation with the Dipole Polarizability. *Phys. Rev. Lett.* **124**, 132502 (2020).
- [297] BUQEYE collaboration. <https://buqeye.github.io/software/> (2020).
- [298] Lattimer, J. M. Symmetry energy in nuclei and neutron stars. *Nucl. Phys. A* **928**, 276 (2014).
- [299] Abbott, B. P. *et al.* Properties of the binary neutron star merger GW170817. *Phys. Rev. X* **9**, 011001 (2019).
- [300] Abbott, B. P. *et al.* Multi-messenger observations of a binary neutron star merger. *Astrophys. J. Lett.* **848**, L12 (2017).
- [301] Shibata, M. *et al.* Modeling GW170817 based on numerical relativity and its implications. *Phys. Rev. D* **96** (2017).

-
- [302] Ruiz, M., Shapiro, S. L. & Tsokaros, A. Gw170817, general relativistic magnetohydrodynamic simulations, and the neutron star maximum mass. *Phys. Rev. D* **97** (2018).
- [303] Ai, A., Gao, H. & Zhang, B. What constraints on the neutron star maximum mass can one pose from GW170817 observations? *Astrophys. J.* **893**, 146 (2020).
- [304] Abbott, B. P. *et al.* Model comparison from ligo–virgo data on gw170817’s binary components and consequences for the merger remnant. *Classic. Quant. Grav.* **37**, 045006 (2020).
- [305] Shao, D. S. *et al.* Estimating the maximum gravitational mass of nonrotating neutron stars from the GW170817/GRB170817A/AT2017gfo observation. *Phys. Rev. D* **101**, 063029 (2020).
- [306] Kurkela, A., Fraga, E. S., Schaffner-Bielich, J. & Vuorinen, A. Constraining neutron star matter with Quantum Chromodynamics. *Astrophys. J.* **789**, 127 (2014).
- [307] Klos, P., Carbone, A., Hebeler, K., Menéndez, J. & Schwenk, A. Uncertainties in constraining low-energy constants from ${}^3\text{H}$ β decay. *Eur. Phys. J. A* **53**, 168 (2017). [Erratum: *Eur. Phys. J. A* **54**, 76 (2018)].
- [308] Buraczynski, M., Ismail, N. & Gezerlis, A. Nonperturbative extraction of the effective mass in neutron matter. *Phys. Rev. Lett.* **122**, 152701 (2019).
- [309] Wellenhofer, C., Holt, J. W., Kaiser, N. & Weise, W. Nuclear thermodynamics from chiral low-momentum interactions. *Phys. Rev. C* **89**, 064009 (2014).
- [310] Sjöberg, O. On the landau effective mass in asymmetric nuclear matter. *Nucl. Phys. A* **265**, 511 (1976).
- [311] van Dalen, E. N. E., Fuchs, C. & Faessler, A. Effective nucleon masses in symmetric and asymmetric nuclear matter. *Phys. Rev. Lett.* **95**, 022302 (2005).
- [312] Li, A., Hu, J. N., Shang, X. L. & Zuo, W. Nonrelativistic nucleon effective masses in nuclear matter: Brueckner-hartree-fock model versus relativistic hartree-fock model. *Phys. Rev. C* **93**, 015803 (2016).
- [313] Li, B. A., Cai, B. J., Chen, L. W. & Xu, J. Nucleon effective masses in neutron-rich matter. *Prog. Part. Nucl. Phys.* **99**, 29 (2018).
- [314] Wellenhofer, C., Holt, J. W. & Kaiser, N. Divergence of the isospin-asymmetry expansion of the nuclear equation of state in many-body perturbation theory. *Phys. Rev. C* **93**, 055802 (2016).
- [315] Wellenhofer, C., Holt, J. W. & Kaiser, N. Thermodynamics of isospin-asymmetric nuclear matter from chiral effective field theory. *Phys. Rev. C* **92**, 015801 (2015).
- [316] Lim, Y. & Holt, J. W. Structure of neutron star crusts from new skyrme effective interactions constrained by chiral effective field theory. *Phys. Rev. C* **95**, 065805 (2017).
- [317] Lim, Y. & Holt, J. W. Neutron star tidal deformabilities constrained by nuclear theory and experiment. *Phys. Rev. Lett.* **121**, 062701 (2018).
- [318] Wellenhofer, C. Zero-temperature limit and statistical quasiparticles in many-body perturbation theory. *Phys. Rev. C* **99**, 065811 (2019).
- [319] Baym, G., Pethick, C. & Sutherland, P. The Ground state of matter at high densities: Equation of state and stellar models. *Astrophys. J.* **170**, 299 (1971).

-
- [320] Ducoin, C., Chomaz, P. & Gulminelli, F. Role of isospin in the nuclear liquid–gas phase transition. *Nucl. Phys. A* **771**, 68 (2006).
- [321] Wu, C. & Ren, Z. Liquid-gas phase transition in hot asymmetric nuclear matter. *Phys. Rev. C* **83**, 044605 (2011).
- [322] O’Connor, E. P. <https://stellarcollapse.org/equationofstate.html> (2016).
- [323] Lattimer, J. M. & Swesty, F. D. <http://www.astro.sunysb.edu/dswesty/lseos.html> (1993).
- [324] Timmes, F. X. & Arnett, D. The accuracy, consistency, and speed of five equations of state for stellar hydrodynamics. *Astrophys. J. Suppl.* **125**, 277 (1999).
- [325] Jacobi, M., Guercilena, F. M., Arcones, A., Huth, S. & Schwenk, A. *In preparation* (2023).
- [326] Jacobi, M. *Neutron star mergers: Mass ejection and the role of the nuclear equation of state*. Ph.D. thesis, Technische Universität Darmstadt, Darmstadt. In preparation.
- [327] Sekiguchi, Y., Kiuchi, K., Kyutoku, K., Shibata, M. & Taniguchi, K. Dynamical mass ejection from the merger of asymmetric binary neutron stars: Radiation-hydrodynamics study in general relativity. *Phys. Rev.* **D93**, 124046 (2016).
- [328] Nedora, V. *et al.* Dynamical ejecta synchrotron emission as a possible contributor to the changing behaviour of grb170817a afterglow. *Mon. Not. Roy. Astron. Soc.* **506**, 5908 (2021).
- [329] Most, E. R. & Raithel, C. A. Impact of the nuclear symmetry energy on the post-merger phase of a binary neutron star coalescence. *Phys. Rev. D* **104**, 124012 (2021).
- [330] Hotokezaka, K. *et al.* The mass ejection from the merger of binary neutron stars. *Phys. Rev.* **D87**, 024001 (2013).
- [331] Raithel, C. A., Paschalidis, V. & Özel, F. Realistic finite-temperature effects in neutron star merger simulations. *Phys. Rev. D* **104**, 063016 (2021).
- [332] Zlochower, Y. *et al.* The einstein toolkit (2022).
- [333] Löffler, F. *et al.* The einstein toolkit: A community computational infrastructure for relativistic astrophysics. *Class. Quant. Grav.* **29**, 115001 (2012).
- [334] Goodale, T. *et al.* In *Vector and Parallel Processing–VECPAR’2002*, vol. 2565 (2003).
- [335] Radice, D. & Rezzolla, L. THC: a new high-order finite-difference high-resolution shock-capturing code for special-relativistic hydrodynamics. *Astron. Astrophys.* **547**, A26 (2012).
- [336] Radice, D., Rezzolla, L. & Galeazzi, F. Beyond second-order convergence in simulations of binary neutron stars in full general-relativity. *Mon. Not. Roy. Astron. Soc.* **437**, L46 (2014).
- [337] Radice, D., Rezzolla, L. & Galeazzi, F. High-Order Fully General-Relativistic Hydrodynamics: new Approaches and Tests. *Class. Quant. Grav.* **31**, 075012 (2014).
- [338] Tsang, M. B., Lynch, W. G., Danielewicz, P. & Tsang, C. Y. Symmetry energy constraints from GW170817 and laboratory experiments. *Phys. Lett. B* **795**, 533 (2019).

-
- [339] Essick, R., Tews, I., Landry, P., Reddy, S. & Holz, D. E. Direct Astrophysical Tests of Chiral Effective Field Theory at Supranuclear Densities. *Phys. Rev. C* **102**, 055803 (2020).
- [340] Tews, I., Margueron, J. & Reddy, S. Critical examination of constraints on the equation of state of dense matter obtained from GW170817. *Phys. Rev.* **98**, 045804 (2018).
- [341] Tews, I. Spectrum of shear modes in the neutron-star crust: Estimating the nuclear-physics uncertainties. *Phys. Rev. C* **95**, 015803 (2017).
- [342] Arzoumanian, Z. *et al.* The NANOGrav 11-year Data Set: High-precision timing of 45 Millisecond Pulsars. *Astrophys. J. Suppl.* **235**, 37 (2018).
- [343] Pang, P. T. H. *et al.* Nuclear physics multimessenger astrophysics constraints on the neutron star equation of state: Adding NICER's PSR J0740+6620 measurement. *Astrophys. J.* **922**, 14 (2021).
- [344] Tews, I. *et al.* On the Nature of GW190814 and Its Impact on the Understanding of Supranuclear Matter. *Astrophys. J. Lett.* **908**, L1 (2021).
- [345] Strüder, L. *et al.* The European Photon Imaging Camera on XMM-Newton: The pn-CCD camera. *Astron. Astrophys.* **365**, L18 (2001).
- [346] Turner, M. J. L. *et al.* The European Photon Imaging Camera on XMM-Newton: The MOS cameras. *Astron. Astrophys.* **365**, L27 (2001).
- [347] Dietrich, T. *et al.* Improving the NRTidal model for binary neutron star systems. *Phys. Rev. D* **100**, 044003 (2019).
- [348] Cozma, M. D. Feasibility of constraining the curvature parameter of the symmetry energy using elliptic flow data. *Eur. Phys. J. A* **54**, 40 (2018).
- [349] Sturm, C. *et al.* Evidence for a soft nuclear equation of state from kaon production in heavy ion collisions. *Phys. Rev. Lett.* **86**, 39 (2001).
- [350] Fuchs, C. *et al.* The Nuclear equation of state probed by K⁺ production in heavy ion collisions. *J. Phys. G* **28**, 1615 (2002).
- [351] Blaich, T. *et al.* A large area detector for high-energy neutrons. *Nucl. Instrum. Meth. A* **314**, 136 (1992).
- [352] Zhang, Z. & Chen, L. W. Constraining the symmetry energy at subsaturation densities using isotope binding energy difference and neutron skin thickness. *Phys. Lett. B* **726**, 234 (2013).
- [353] Brown, B. A. Constraints on the skyrme equations of state from properties of doubly magic nuclei. *Phys. Rev. Lett.* **111**, 232502 (2013).
- [354] Yong, G. C. Symmetry energy extracted from the $S_{\pi\text{rit}}$ pion data in Sn+Sn systems (2021).
- [355] Orsaria, M. G. *et al.* Phase transitions in neutron stars and their links to gravitational waves. *J. Phys. G* **46**, 073002 (2019).
- [356] Brandes, L., Kaiser, N. & Weise, W. Fluctuations and phases in baryonic matter. *Eur. Phys. J. A* **57**, 243 (2021).

Acknowledgments

The last years have been very formative for me, not only physics-wise, but also on a personal level. As I write these lines, I remember countless moments full of laughter and joy. I am grateful for everybody who participated in my journey in one way or another.

First of all, I want to thank Achim Schwenk for his continuous support since I started my Bachelor thesis seven years ago. You still surprise me with your profound knowledge of physics even beyond your direct research interests and I highly appreciated your insights and ideas for new projects. I am deeply grateful for the opportunities to participate in numerous conferences, workshops, and summer schools and for nominating me for several awards. Your efforts for gender equality have influenced me and many others a lot. Thank you for providing a safe space and for your flexibility about working while being a mom of twins.

I want to thank Almudena Arcones for being such a supportive collaborator over the years and for reviewing this thesis. I enjoyed working with you a lot! I learned many things about nuclear astrophysics and you always created a comfortable working environment.

I would like to thank my collaborators Kshitij Agarwal, Mattia Bulla, Michael Coughlin, Tim Dietrich, Maximilian Jakobi, Arnaud Le Fèvre, Yeunhwan Lim, Peter Pang, Gerard Navó, Ingo Tews, Wolfgang Trautmann, Chris Van Den Broeck, and Corbinian Wellenhofer for countless fruitful discussions. I am especially grateful for Ingo, Peter, and Tim with whom even two hours of frustration about line numbers and multi-section bibliographies right before submission are not too bad. It's a pity that we haven't all met in person yet.

I am very grateful for Ingo Tews, Tyler Gorda, Matthias Heinz, Yeunhwan Lim, Gerard Navó, Benedikt Schallmo, and Achim Schwenk for helpful feedback and comments on this thesis. Also, thank you Tim for quick and informative answers to any questions related to neutron star mergers.

A big thank you goes to all former and current members of the strongint group. You are one of the main reasons why I had such a good time in the last seven years. I remember with great pleasure countless coffee breaks, DPG meetings, Wednesday evenings, discussions about the coffee-machine theft and the best Hogwarts house, and many more. I want to thank Svenja Greif who challenged my views on many things and Catharina Brase and Matthias Heinz for numerous virtual coffee breaks since the pandemic.

Thank you, Stephanie Müller, for your help with countless administrative questions and tasks. I always enjoyed talking to you!

I am also thankful for the support by the Deutsche Forschungsgemeinschaft (DFG, German Research Foundation) – Project-ID 279384907 – SFB 1245, especially for the SFB workshops and the ongoing effort on gender equality.

I am deeply grateful for my family for the encouragement and support throughout my entire life. I want to thank especially my mom, my dad, and my in-laws Ulrike, Werner, and Patrick for taking such good care of my kids. Without you this thesis wouldn't even be halfway done.

Lukas, thank you for loving me just the way I am, despite my perfectionism and my knowing-it-all-ness. It is the best feeling that our family always comes first for you, that I can count on you and trust you blindly.

You are the best dad to our children and make having twins as easy as it can be. Ben and Theo, you bring so much joy in my life. Every time you laugh the world stands still for a moment and I (almost) forget the sleepless nights. You will always be my babies even when you are old enough to read this. My heart is almost exploding out of love, happiness, and pride that the three of you are my family.

Curriculum Vitae

Name	Sabrina Huth
Date of birth	01.10.1993
Place of birth	Lich
Citizenship	German

Education

Nov 18 – present	Doctoral studies, Theoretical Nuclear Physics, Technische Universität Darmstadt Supervisor: Prof. Ph.D. Achim Schwenk
Oct 19 – Sep 21	Master studies in Energy Science and Engineering (part time), Technische Universität Darmstadt
Oct 16 – Oct 18	Master studies in Physics, Technische Universität Darmstadt Thesis: <i>Equation of state effects in core-collapse supernovae</i> Supervisor: Prof. Ph.D. Achim Schwenk Degree: Master of Science, Grade: 1,04
Oct 13 – Sep 16	Bachelor studies in Physics, Technische Universität Darmstadt Thesis: <i>Investigation of thermal effects on the equation of state and radii of neutron stars</i> Supervisor: Prof. Ph.D. Achim Schwenk Degree: Bachelor of Science, Grade: 2,16

Erklärungen laut Promotionsordnung

§ 8 Abs. 1 lit. c PromO

Ich versichere hiermit, dass die elektronische Version meiner Dissertation mit der schriftlichen Version übereinstimmt.

§ 8 Abs. 1 lit. d PromO

Ich versichere hiermit, dass zu einem vorherigen Zeitpunkt noch keine Promotion versucht wurde. In diesem Fall sind nähere Angaben über Zeitpunkt, Hochschule, Dissertationsthema und Ergebnis dieses Versuchs mitzuteilen.

§ 9 Abs. 1 PromO

Ich versichere hiermit, dass die vorliegende Dissertation selbstständig und nur unter Verwendung der angegebenen Quellen verfasst wurde.

§ 9 Abs. 2 PromO

Die Arbeit hat bisher noch nicht zu Prüfungszwecken gedient.

Darmstadt, 7. Februar 2023

S. Huth